AIIM

Association for Information and Image Management

1100 Wayne Avenue, Suite 1100
Silver Spring, Maryland 20910

301/587-8202

Centimeter

Inches

MANUFACTURED TO AIIM STANDARDS
BY APPLIED IMAGE, INC.

1 of 2

EGG-[redacted]-2700

INEL BNCT Research Program
Annual Report
1992

Edited by
J. R. Venhuizen

Published May 1993

Idaho National Engineering Laboratory
EG&G Idaho, Inc.
Idaho Falls, Idaho 83415

Prepared for the
U.S. Department of Energy
Office of Energy Research (ER)
Under DOE Idaho Field Office
Contract DE-AC07-76ID01570

MASTER

DISTRIBUTION OF THIS DOCUMENT IS UNLIMITED

ABSTRACT

This report is a summary of the progress and research produced for the Idaho National Engineering Laboratory Boron Neutron Capture Therapy (BNCT) Research Program for calendar year 1992. Contributions from all the principal investigators about their individual projects are included, specifically, chemistry (pituitary tumor targeting compounds, boron drug development including liposomes, lipoproteins, and carboranylalanine derivatives), pharmacology (murine screenings, toxicity testing, inductively coupled plasma-atomic emission spectroscopy (ICP-AES) analysis of biological samples), physics (radiation dosimetry software, neutron beam and filter design, neutron beam measurement dosimetry), and radiation biology (small and large animal models tissue studies and efficacy studies). Information on the potential toxicity of borocaptate sodium and boronophenylalanine is presented, results of 21 spontaneous-tumor-bearing dogs that have been treated with BNCT at the Brookhaven National Laboratory (BNL) Medical Research Reactor (BMRR) are discussed, and predictions for an epithermal-neutron beam at the Georgia Tech Research Reactor (GTRR) are shown. Cellular-level boron detection and localization by secondary ion mass spectrometry, sputter-initiated resonance ionization spectroscopy, low atomization resonance ionization spectroscopy, and alpha track are presented. Boron detection by ICP-AES is discussed in detail. Several boron carrying drugs exhibiting good tumor uptake are described. Significant progress in the potential of treating pituitary tumors with BNCT is presented. Measurement of the epithermal-neutron flux at BNL and comparison to predictions are shown. Calculations comparing the GTRR and BMRR epithermal-neutron beams are also presented.

CONTENTS

ABSTRACT iii

ACRONYMS AND ABBREVIATIONS xiii

INTRODUCTION, *Dr. Ron Dorn* 1

- Boron Drug Development 1
- Pituitary Tumor Evaluation 2
- Boron Localization Screening 2
- Drug Stability, Pharmacology, and Toxicity 2
- Treatment Protocol Development 2
- Noninvasive Boron Quantification 2
- Analytical Dosimetry 3
- Analysis of Boron in Biological Samples 3
- Intra- and Intercellular Boron Analysis 3
- Georgia Tech Research Reactor (GTRR) Physics Support 4
- Research Reactor/Accelerator Physics Support 4

CARBORANYLALANINE AND LDL DEVELOPMENT AND EVALUATION, *Dr. Steve Kahl* 5

BORONATED LIPOSOME DEVELOPMENT AND EVALUATION, *Dr. Fred Hawthorne* 12

PITUITARY TUMOR EVALUATION, *Dr. Barry Albertson, Dr. Steve Binney* 20

BORON LOCALIZATION SCREENING, *Dr. Cathy Elstad* 25

PHARMACOLOGY AND TOXICOLOGY OF BORON DELIVERY AGENTS, *Dr. Tom Latham* 35

TREATMENT PROTOCOL DEVELOPMENT, *Dr. Pat Gavin* 42

NONINVASIVE BORON QUANTIFICATION, *Dr. Marty Schweizer and Ken Bradshaw* 50

ANALYTICAL DOSIMETRY, *Dr. Dave Nigg and Floyd Wheeler* 59

IMPLEMENTATION OF A SINGLE PARTICLE HIGH-LET IRRADIATION SYSTEM, *Dr. John Nelson and Dr. Leslie Braby* 70

ANALYSES OF BORON IN BIOLOGICAL SAMPLES, *Dr. Bill Bauer* 78

SECONDARY ION MASS SPECTROMETRY (SIMS), *Dr. Victor Chia* 108

ALPHA TRACK-ETCH, *Dr. Clive Nelson* 119

RESONANCE IONIZATION SPECTROSCOPY, SIRIS AND LARIS, *Dr. Heinrich Arlinghaus* 125

NEUTRON BEAM MEASUREMENT DOSIMETRY,
Dr. Yale Harker, Dr. Pete Randolph, and Cecelia Amaro 142

GTRR PHYSICS SUPPORT, *Dr. Dave Nigg and Floyd Wheeler* 150

REFERENCES 158

FIGURES

1. Low density lipoprotein 5

2. Cutaway view of a small unilamellar vesicle 12

3. Synthesis of [2-$B_{10}H_9CO$]-(II) 14

4. X-ray crystal structure of [2-$B_{10}H_9CO$]-(II) 14

5. Transformations of [2-$B_{10}H_9CO$]-(II) 15

6. Synthesis of $[B_{20}H_{18}]^{2-}$(IV) and reduction to $[B_{20}H_{18}]^{4-}$(V) 15

7. Synthesis of a substituted *nido*-carborane (XVIII) 17

8. Murine tissue boron concentrations from delivery of boron salts by liposomes. 19

9. The amino acid sequence of oCRH is shown with the conjugated carborane cage ($^{10}B_{10}$) 21

10. c-AMP dose response after a 10 minute exposure of AtT-20 cells to varying concentrations of oCRH 22

11. c-AMP response of AtT-20 cells to oCRH carborane CRH, or carborane cage alone at various concentrations 22

12. AtT-20 cell survival after five days following exposure to varying gamma doses in the reactor thermal column 23

13. Comparison of AtT-20 cells with and without irradiation 23

14. *In vitro* uptake of boron by B16-BL6 murine melanoma cells exposed for six hours to increasing concentrations of BPA in the culture medium 28

15. *In vitro* uptake of boron by B16-BL6 murine melanoma cells cultured in medium formulated with normal or low levels of tyrosine and phenylalamine and exposed to increasing concentrations of BPA 28

16. Growth of B16-BL6 murine melanoma cells on day five of *in vitro* culture with increasing concentrations of BPA in culture medium 29

17. PAL enzymatic activity against Phe and BPA 29

18. Biodistribution of boron 6 and 12 hours after intraperitoneal injection into mice of BPA 30

19. Biodistribution of boron 6 and 12 hours after intravenous injection of 200 μL of BPA into the dilated lateral tail vein of unanesthetized mice 30

20. Radioactivity levels in tumor tissue through time after intraperitoneal injection of an ^{125}I-labelled boron compound 32

21. Biodistribution of boron in tumor and blood after intravenous injection of 200 μL of liposomal-encapsulated $Na_2n\text{-}B_{20}H_{18}$ 32

22. Biodistribution of boron in tumor, blood, and brain after intravenous injection of 200 μL of liposomal-encapsulated $Na_3B_{20}H_{17}NH_3$ 33

23. BPA elicited cardiovascular lablity in an open-chest, artificially-ventilated rat 39

24. CT image of an intra-axial tumor located in the right temporal lobe with ring enhancement 42

25. MRI of an extra-axial tumor located in the left temporal lobe 43

26. Changes in blood boron levels over time in intracranial tumors, blood, and normal brain 46

27. Radiation-induced, subclinical changes in the brain of a dog treated with BNCT 46

28. Comparison of survival of dogs with nonmeningioma brain tumors with BNCT and with augmented conventional cobalt (^{60}Co+) radiation therapy 47

29. Comparison of survival of dogs with all tumor types with BNCT, augmented conventional cobalt (^{60}Co+) radiation therapy, and symptomatic or no treatment 47

30. MRI of a dog with a tumor located in the right temporal lobe, pretreatment image 48

31. MRI of the same dog as in Figure 30, three weeks following BNCT 48

32. Hair loss and hair color change in a dog following BNCT 49

33. Structure of BSH anion and ^{11}B COSY spectrum 50

34. Birdcage coil 52

35. 20.5 MHz boron-11 spectrum of BSH in canine head 52

36. Normalized BSH in dog head and blood 53

37. Three-dimensional projection sequence 53

38. Boron sagittal image showing the homogeneous limits of the bird cage boron coil 54

39. Comparison of boron signal intensity from different tissues of equal volumes after end of infusion 55

40. T2 weighted axial proton images show gliosarcoma development over nine days post inoculation 56

41. Axial boron image and proton image (same proton image day, Figure 40) 56

42. Boron axial of "Boo" 58

43. Boron axial of "Sally" 58

44. Flow diagram for BNCT neutron particle transport and microdosimetry analysis 60

45. Axial MRI of a Labrador Retriever head showing B-spline outlines of the brain and outer head surface 62

46. Three-dimensional Labrador head reconstruction using the B-spline surface fitting method 63

47. Three-dimensional reconstruction of the canine brain and eyes using the B-spline surface fitting method 63

48. Illustration of the algorithm used for flux tallies in the subelement Monte Carlo method 65

49. Calculated thermal-neutron flux contours in an axial plane for the B-spline Labrador retriever head model, positioned in the BMRR epithermal-neutron beam 65

50. Calculated proton-recoil physical dose contours in an axial plane for the B-spline Labrador Retriever head model, positioned in the BMRR epithermal-neutron beam 66

51. Calculated photon-induced physical dose contours in an axial plane for the B-spline Labrador Retriever head model positioned in the BMRR epithermal-neutron beam 66

52. Calculated physical dose-depth profiles along the beam centerline for the B-spline Labrador Retriever head model 67

53. Schematic diagram of the single particle irradiator 71

54. Image of a 7-8 μm beam made by placing a piece of radiachromic film on the Mylar® surface of the culture dish, opening the shutter, and exposing it to a large number of particles 72

55. Although SVEC4-10 cells appear quite similar to many other cell lines, their growth appears to be poorly regulated and the cultures become overgrown at relatively low densities 74

56. X-ray survival data for SVEC-10 cells relative to CHO cells 74

57. Cells are typsinized, plated at low density (~5 cells/mm^2), and allowed to attach firmly to the Mylar® bottom of the dish 75

58. Set of images, assembled from one of the time-lapse sequences, demonstrating both the precision movement of the motor-controlled stage and the quality of the growth environment within the incubator 77

59. Comparison of boron analysis results in blood serum and plasma using prompt-γ analysis and ICP-AES 87

60. Comparison of boron concentrations in tissue samples determined by prompt-γ analysis and acid digestion, and ICP-AES with internal standardization 87

61. Comparison of a conventional continuous aspiration ICP-AES and FIA-ICP-AES for 1 μg B/mL solution 94

62. Typical calibration by FIA-ICP-AES from 0-4 μg B/mL (ppm) standards with an NIST calibration check. Values indicate the % RSD for the replicate injections 94

63. Elimination of B in an atypical dog following administration of BSH. Each point represents the mean of the DCP-AES analysis and ICP-AES and prompt γ performed at a later date 99

64. Schematic of modification to ICP-AES sample introduction system for the *in-situ* generation of methoxyborate 102

65. Effect of the carrier flow rate (represented as psi of back pressure) on the peak area and peak width at 20% of the maximum height 104

66. Representative peak shapes obtained from repeated analysis of 5, 10, and 15-ng boron standards 106

67. A schematic diagram of a Cameca IMS-4f 109

68. A schematic diagram of a TFS™ TOF-SIMS Surface Analyzer 109

69. Boron calibration curve in agarose 110

70. Boron calibration curve in gelatin 111

71. SIMS depth profiles of boron in rat brain matrix 112

72. Boron calibration curve in rat brain matrix 112

73. Biological tissue preparation 113

74. Total secondary ion image of silica beads 114

75. Total secondary ion image of dog skin 115

76. Total boron ion image of dog skin 115

77. Boron calibration curves of BSH and boric acid in brain homogenate and gelatin 117

78. SIMS depth profiles of boron in the liver of an infused BSH rat and control rat 117

79. Boron secondary ion image of liver tissue from the infused rat. Insert shows an optical micrograph of the freeze-dried liver section prepared at DUMC 118

80. Potassium secondary ion image of liver tissue from the infused rat 118

81. Alpha tracks from the radioactive isotope of Lead-210 (^{210}Pb) in three types of nuclear track detecting film: A - LR115-3, B - CN-1 and C - CR-39; ~ 400X 121

82. Distribution of tracks in CN-1 films from $^{10}B(n,\alpha)^{7}Li$ reactions in A, cerebral gray matter and B, cerebral white matter; ~ 400X 123

83. Distribution of tracks in CN-1 films from $^{10}B(n,\alpha)^{7}Li$ reactions in dog brain 123

84. Demonstration of the SIRIS element selectivity 126

85. Simplified energy level diagrams illustrating the photoionization of neutral atoms 127

86. Diagram of the experimental arrangement to measure boron in tissues with SIRIS and LARIS 129

87. Ion-induced electron image of a 600 mesh (42 μm grid spacing) hexagonal Cu grid 130

88. LARIS image of a 400 mesh, 50% transparency (63.5 μm spacing) Cu grid 131

89. Correlation of boron signals from identical BSH doped gelatin samples using SIRIS and LARIS 132

90. Position/concentration measurements using SIRIS in retina tissue section of control animal in which no BSH infusion was performed 134

91. Photomicrograph (middle left), ion-induced electron image (bottom right) and boron SIRIS (top left and right) and LARIS (bottom left) signal in BSSB infused rat kidney 135

92. Photomicrograph (middle) and LARIS images (right) of BSSB infused rat kidney 136

93. Boron concentration along two orthogonal tracks in BSSB rat brain (left) 137

94. Boron LARIS concentration along two orthogonal tracks in BSSB infused rat tumor (left) 139

95. Photomicrograph (left), ion-induced electron image (top right), and SIRIS boron image (bottom right) of a tumor section 140

96. Photomicrograph (upper) and LARIS image (lower) of BSSB infused rat tumor. The sampling interval was 20 μm 140

97. BMRR epithermal-beam neutron spectrum before core modification 143

98. BMRR epithermal-beam neutron spectrum after core modification 143

99. Thermal neutron flux distribution as a function of depth in the cylindrical phantom 146

100. Epithermal-neutron flux distribution as a function of depth in the cylindrical phantom 146

101. Thermal and epithermal-neutron flux distributions as a function of depth in the ellipsoid phantom (INEL measurements compared with BNL measurements and calculations) 147

102. Thermal and epithermal-neutron flux distributions as a function of depth in the ellipsoid phantom (INEL measurements compared with INEL calculations) 148

103. Gamma dose distribution in ellipsoid phantom 148

104. Conceptual epithermal-neutron facility at the GTRR 152

105. Comparison of BMRR and GTRR neutron beam spectrum 152

106. Comparison of BMRR and GTRR neutron beam angular distributions 153

107. Lucite canine-head phantom 154

108. Calculated physical absorbed dose-depth results along beam centerline 156

109. Tumor RBE dose-depth profiles for GTRR and BMRR 157

TABLES

1. LDL reconstitutions with alkyl and aryl carboranes 7

2. LDL reconstitutions - double filter experiment 8

3. Boron content *in vivo* following ECC-lipoprotein injection 9

4. Effect of PAL on tumor levels of boron 31

5. Tumor-bearing subjects in BSH biodistribution study 45

6. Particle beams available for single-cell irradiation studies 73

7. Spike recovery data for 10 to 20 microgram spikes to tissue samples prior to acid bomb digestion 81

8. Effect of varying the acid content of the standards 82

9. Analysis results with Sc spiked to previously digested samples for use as an internal standard to quantitate B 83

10. Results for tissue digestions with Sc and Y as internal standards 84

11. Typical ICP-AES boron analysis results of tissue samples from a dog that had been administered B in the form of $Na_2B_{12}H_{11}SH$ 85

12. Replicate acid bomb digestions of the same tongue samples, including matrix spiked digestions, demonstrating the effects of sample inhomogeneity on the accuracy and precision of the B analysis 86

13. Results from the ICP-AES determination of B in tissues digests with different digestions methods. Values in μg B/g ± standard deviation determined from replicate digestions and analyses 90

14. Percent recoveries of scandium spiked to each sample as a recovery standard. Values represent the average recovery ± standard deviation of replicate digestions 92

15. Results of an initial study comparing slurry nebulization and acid digestion of whole blood spiked with either BSH or tetraborate. Analysis was by ICP-AES 97

16. Effect of blood volume on the recovery of B by DCP-AES with slurry sample introduction 97

17. Comparison of typical results for B analysis by prompt γ, DCP-AES and ICP-AES 98

18. Mean % errors for whole blood B analysis by prompt γ, ICP-AES and DCP-AES 99

19. ICP-AES parameters for the determination of boron as methoxyborate 102

20. The dependance of the quantity of water and sulfuric acid on the measurable boron from the *in-situ* formation of methoxyborate 105

21. Comparison of tissue sample analysis results from standard ICP-AES and DCP-AES with methoxyborate generation 107

22. Cameca instrument conditions used for Gelatin and Agarose analyses 110

23. BMRR epithermal beam parameters - integral flux and dose values 144

24. BMRR epithermal beam measurements and calculations, after modification 145

25. Peak thermal neutron flux data 147

26. Integral parameters - GTRR conceptual design 154

ACRONYMS AND ABBREVIATIONS

AA	Atomic absorption
AAS	Atomic absorption spectroscopy
AES	Atomic emission spectroscopy
BAE	Boric acid equivalent
BMRR	Brookhaven Medical Research Reactor
BNL	Brookhaven National Laboratory
BNCT	Boron Neutron Capture Therapy
BOPP	Water-soluble boronated porphyrin
BPA	Boronophenylalanine
BSH	Borocaptate Sodium ($Na_2B_{12}H_{11}SH$)
cAMP	cyclic adenosine monophosphate
CAR	Carboranylalanine
CAT	computerized axial tomography
CE&A	Charles Evans & Associates
COSY	Correlation spectroscopy
CSF	Cerebrospinal fluid
CT	Computed tomography
CVM	College of Veterinary Medicine
D-MEM	Dulbecco's modified eagle medium
D-PBS	Dulbecco's phosphate buffered saline
DCP-AES	Direct coupled plasma-atomic emission spectroscopy
DME	Dulbecco's modification of Eagle's minimum essential medium
DOE	Department of Energy
DUMC	Duke University Medical Center
ECC	Elaidyl carborane carboxylate
EDTA	Ethylenediaminetetraacetic acid
FBS	Fetal bovine serum
FIA	Flow injection analysis
FOV	Field of view
GFAAS	Graphite furnace atomic absorption spectroscopy
GTRR	Georgia Institute of Technology Research Reactor
ICP-AAS	Inductively coupled plasma-atomic absorption spectroscopy
ICP-AES	Inductively coupled plasma-atomic emission spectroscopy
INEL	Idaho National Engineering Laboratory
IR	Infrared
IRC	Idaho Research Center
ISU	Idaho State University
LARIS	Low atomization resonance ionization spectroscopy
LDL	Low density lipoproteins
LET	Linear energy transfer
MRI	Magnetic resonance imaging
MRS	Magnetic resonance spectroscopy
MTD	Maximum tolerated dose
MTT	3-[4,5-dimethylthiazole-2-yl]-2,5-diphenyltetrazolium bromide; thiazolyl blue

NCT	Neutron Capture Therapy
oCRH	Ovine corticotrophin
OHSU	Oregon Health Sciences University
ORSU	Oregon State University
PAL	Phenylalanine ammonia lyase
PHE	Phenylalanine
PI	Principal Investigator
PMT	Photomultiplier tube
PNL	Pacific Northwest Laboratory
RBE	Relative biological effectiveness
RIS	Resonance ion spectroscopy
ROI	Region-of-interest
RPD	Relative percent differences
RSD	Relative standard deviation
s	standard deviation of the sample
S/N	Signal-to-noise
SEM	Standard error of mean
SIMS	Secondary ion mass spectrometry
SIRIS	Sputter-initiated resonance ionization spectroscopy
TLD	Thermoluminescent dosimeter
TOF	Time of flight
UCLA	University of California, Los Angeles
UCSF	University of California, San Francisco
UofT	University of Tennessee
UofU	University of Utah
UV	Ultraviolet
VIS	Visible
WSU	Washington State University

INEL BNCT RESEARCH PROGRAM ANNUAL REPORT 1992

INTRODUCTION

Dr. Ron Dorn, Medical Consultant, Mountain States Tumor Institute and Idaho National Engineering Laboratory

The Idaho National Engineering Laboratory (INEL) Boron Neutron Capture Therapy (BNCT) Research Program was initially funded in 1987 with a goal of providing the scientific and technological basis for using of BNCT in the treatment of human malignant brain tumors. The principal of BNCT for cancer involves a two step process: (a) selective tumor absorption of a boronated compound, and (b) capture of thermal neutrons by the ^{10}B nuclei, promoting a fission reaction which yields alpha particles, gamma rays and ^{7}Li nuclei. The energetic alphas, with high linear energy transfer (LET), damage tissue within about one cell diameter, thereby theoretically providing selective destruction of the tumor.[1] Although the potentials of BNCT were suggested forty years ago by Sweet et al.[2] only within the past decade has there been serious international research efforts towards its maturation and clinical deployment. The first years of the INEL BNCT Research program successfully produced break-through research in several important areas in BNCT, including large animal model development, inductively coupled plasma-atomic emission spectroscopy (ICP-AES) analysis of boron concentration in biological samples, boron magnetic resonance imaging (MRI) and spectroscopy (MRS), intra-cellular boron analysis, and analytical dosimetry for BNCT. Following these successes, the INEL BNCT Research Program was reconfigured to begin focusing on boron drug development, boron localization screening, drug stability, pharmacology and toxicity, treatment protocol development, and supporting technology development while maintaining progress and refinement in the technical support activities.

1992 was a year of considerable challenge and success for the INEL BNCT Research Program. It was named the National Center for BNCT Measurement and Development by the Department of Energy (DOE). Remarkable progress was achieved throughout the research programs. This annual report will review the current status of all the various components of the INEL BNCT Research Program and the experimental results and developments of the past year. This introduction will provide a brief overview of the program achievements of the past year.

Boron Drug Development

Researchers under the direction of Dr. Steve Kahl, University of California at San Francisco (UCSF), made significant progress this year in the development of carboranylalanine and low-density lipoproteins (LDLs) as potential agents for BNCT. They determined that simple carborane esters can successfully replace the cholesterol core of LDLs. This boronated LDL can be measured in tissue using ICP-AES with appropriate digestion procedures. Collaboration with researchers in Helsinki has shown high localization of technetium tagged LDL in recurrent glioblastoma multiforme. Stereo-selective synthesis of carboranylalanine has been successfully developed, and initial *in vitro* tests in collaboration with Brookhaven National Laboratory (BNL) have shown high efficacy.

Boronated liposome research, under the direction of Dr. Fred Hawthorne at the University of California at Los Angeles (UCLA), has shown the concept of boronated liposomes to be valid. New compound synthesis has taken top priority as initial boron compounds carried to the tumor with liposomes tend to wash out quickly. Several exciting new boron compounds including $(2\text{-}B_{10}H_9NCO)^{2-}$ have been developed and successfully incorporated into liposomes.

Twenty-five screening studies with ten different compounds and four tumor lines have been carried out in cooperation with the group at Washington State University (WSU). Plans for the immediate future include combining the boron compound $(B_{20}H_{17}NH_3)^{3-}$ with liposomes that contain boron in the liposomal structure itself. Such a combination holds great promise for a significant increase and retention in the boron deposited within the tumor cells.

Pituitary Tumor Evaluation

Under the direction of Dr. Barry Albertson at Oregon Health Sciences University (OHSU), carborane cages supplied by Dr. Fred Hawthorne from UCLA have been successfully conjugated with ovine corticotrophin releasing hormone (oCRH). This conjugate has shown retention of biological activity. Experiments using this compound in AtT-20 cells have shown successful BNCT lethality. Optimization of this exciting system is underway for potential use in pituitary tumors.

Boron Localization Screening

An extensive program in the assessment of new boron compounds is under the direction of Dr. Cathy Elstad at WSU. Several murine and rat tumor models are used for the *in vivo* localization screening of boron compounds, including boronophenylalanine (BPA), liposomes, and LDLs. Two to three *in vivo* assays are being carried out per month with each assay involving 50 animals, 6 per time point. Using these models, several studies with regard to enhancement of BPA uptake via diet restriction or phenylalanine ammonia-lyase (PAL) preparation have been performed. Optimization of tumor uptake of boronated liposomes and LDLs are currently being studied, including using multiple administration.

Drug Stability, Pharmacology, and Toxicity

Under the direction of Dr. Tom LaHann at Idaho State University (ISU), progress has been made towards the establishment of a tiered toxicology program for all BNCT agents. Prior to the use of a boronated compound for BNCT in humans, safety of the compound must be established, including identification of major adverse effects, clinical use side affects, and identification of side affects that would preclude the use of the compound in clinical trials The BNCT compounds BPA and borocaptate sodium (BSH) have been investigated this past year. A BSH dose of equal to or greater than 625 mg/kg body weight has been found to be lethal in a rat model as a result of cardiovascular system collapse. The current recommendation, therefore, is for BSH dosing in humans to remain under 200 mg/kg while further data is collected. Initial studies of BPA have indicated that this drug appears to be safer from a toxicological viewpoint than BSH.

Treatment Protocol Development

The highly successful large animal model studies have continued under the direction of Dr. Pat Gavin at WSU. A useful review of the development of this model and important experimental results from the first years of its use are contained in this section of this report. One highlight of these studies has been the treatment of a total of 21 dogs with spontaneous brain tumors with BNCT using BSH. These studies have shown very good results with good tumor response and control, better than with conventional treatment, and using only one treatment fraction. This data continues to support the promise of neutron capture therapy (NCT) for the treatment of brain tumors.

Noninvasive Boron Quantification

One of the more exciting developments in the initial years of the INEL BNCT Research Program was the establishment of the technology for MRI and MRS of boron *in vivo*. This past year, under the direction of Dr. Marty Schweizer and Ken Bradshaw at the University of Utah (UofU), this technology has been significantly refined with a development of a rapid 3-D projection reconstruction technique resulting in

good image quality with a 5–8 minute data acquisition time. This section of the report describes *in vivo* studies with dogs demonstrating drug pharmacokinetic data and good imaging of boron *in vivo* with 1.5 cm voxel size. Work continues to further refine this technology for more rapid data acquisition and improved resolution.

Analytical Dosimetry

INEL researchers Floyd Wheeler, Dan Wessol, and Dr. Dave Nigg have successfully developed analytical methods and software for performing detailed radiation transport and dosimetry calculations for BNCT. During the past year, efforts in this task have been directed towards refinement of methods for computation of macroscopic absorbed doses. This section of the report also contains an excellent summary and discussion of BNCT analytical dosimetry, illustrating the need for this technology, technical approaches for meeting this need, and an overview of BNCT microdosimetry.

Also within this section is a summary and discussion of the implementation of a single particle hi-LET radiation system at Pacific Northwest Laboratory (PNL) under the direction of Drs. John Nelson and Les Braby. Data from this system is necessary to allow prediction of the biological effects of small numbers of hi-LET particles. The technical demands of the development of this system as well as its capabilities and initial results are illustrated.

Analysis of Boron in Biological Samples

Under the direction of Dr. Bill Bauer at INEL, the INEL BNCT Research Program continues to provide valuable support to the world BNCT research community in the use of ICP-AES analysis of boron content in biological samples. In addition to reviewing this activity over the past year, this portion of the report provides an overview of the development of this technology within the INEL BNCT Research Program. Contained in this section is also an excellent and detailed discussion of the refinement of this technology in the areas of sample preparation that allows analysis of nanogram levels of boron in samples as small as 1-10 milligrams. With these refinements, boron detectability in a 5-milligram sample is down to approximately 0.2 nanogram boron per milligram, with a practical limit of 0.6 nanogram boron per milligram.

Intra- and Intercellular Boron Analysis

During the initial years of the INEL BNCT Research Program, the feasibility of a secondary ion mass spectroscopy (SIMS) for the detection and localization of boron at the cellular level was determined. Work has continued this past year under the direction of Dr. Victor Chia at Charles Evans and Associates into further refinement of this technology. As outlined in this report, improvement in sample preparation has been a major thrust of the activity within this area during 1992.

Researchers at ISU under the direction of Dr. Clive Nelson have been investigating the refinement of alpha-track-etch for intra- and intercellular boron analysis. They have determined that CN-1 film can be used to determine the distribution and concentration of ^{10}B in brain tumors and surrounding tissue.

The final section in the area of intra- and intercellular boron analysis comes from Atom Sciences, Inc. under the direction of Dr. Heinrich Arlinghaus. These researchers in the INEL BNCT Research Program have been investigating the use of sputter-initiated resonance ionization spectroscopy (SIRIS) and laser atomization resonance ionization spectroscopy (LARIS). A summary of experiments in both of these technologies is contained within the report, which clearly demonstrates that the SIRIS/LARIS is suited for quantitation and imaging of trace elements, including boron, in biological tissue sections.

Georgia Tech Research Reactor (GTRR) Physics Support

A major accomplishment during the first years of the INEL BNCT Research Program was the design and construction of an epithermal-neutron beam at the Brookhaven Medical Research Reactor (BMRR) in a cooperative effort between BNL and INEL. This neutron beam has been used extensively for BNCT research activities by INEL, BNL, and other researchers. It is clear that further development of BNCT up to and including clinical trials will require an improved epithermal-neutron beam. The theoretical advantages of an improved epithermal-neutron beam are described in this section. This past year, the INEL BNCT Research Program, under the direction of Dr. Dave Nigg and Floyd Wheeler, has extensively investigated the potential for developing such an improved beam at GTRR. Data strongly supporting the development of such a facility at GTRR is presented in this section.

Research Reactor/Accelerator Physics Support

In 1992, the BMRR core was modified to increase the intensity of the epithermal-neutron beam. As a result, recharacterization of the beam to confirm neutron spectrum changes, etc., was undertaken. This section of the report summarizes this recharacterization with the conclusion that the core modification did, in fact, increase the free beam intensity of BMRR by 49% with no significant alteration in the shape of the epithermal-neutron spectrum. The net increase in beam intensity through the defining apertures used for our large animal model studies was 28%. Further details concerning the characterization of the new BMRR beam are included in this report. Noteworthy was the fact that there is excellent consistency between the INEL dosimetry model and measurements.

Everyone in the INEL BNCT Research Program (National Center for BNCT Measurement and Development) remains committed to the successful development of BNCT and its promise for the treatment of malignant tumors in humans. This annual report provides an overview of progress to this end and summarizes a firm foundation for clinical trials in the United States.

CARBORANYLALANINE AND LDL DEVELOPMENT AND EVALUATION

Dr. Steve Kahl, Principal Investigator (PI), University of California, San Francisco, Department of Pharmaceutical Chemistry

Major progress toward the development of boronated LDL and the boronated amino acid carboranylalanine for site selective boron drug delivery has been made during the past year by researchers at UCSF. This enhances possibilities for future application of these approaches to clinical studies of BNCT. These approaches are part of an intensive effort by researchers at UCSF to develop site selective boron drugs for the treatment of a variety of human cancers.

LDL Development

One of the major differences between cancer cells and normal cells is the rate of metabolism of LDL. LDL is the principal cholesterol transport protein in human plasma and is found in an average concentration range of 150-250 mg/dL in normal human adults in the U.S. The term LDL is actually misleading; the term refers to a range of spherical particles of 17-25 nanometer diameter and having a density of between 1.019 and 1.063 g/mL. A schematic cartoon of the organization of the LDL particle is shown in Figure 1. Each particle contains a non-polar core, composed chiefly of long chain fatty acid esters of cholesterol, and a polar coat consisting of phospholipid and unesterified cholesterol, and a single copy of a protein known as apoprotein B-100 (apo B-100). Seventy-five percent of the total cholesterol in LDL is in the cholesterol ester core of LDL, while the remaining 25% is not esterified and is found embedded in the phospholipid coat. It is estimated that an average of 1500-2000 molecules of cholesterol ester are present in each particle core, and the particles are roughly one-half cholesterol ester by weight. The apo B-100 surface protein is large, about 550,000 molecular weight, and is probably wound around throughout the surface of the particle, providing approximately 20% of the total mass of the particle. This protein is recognized by specific,

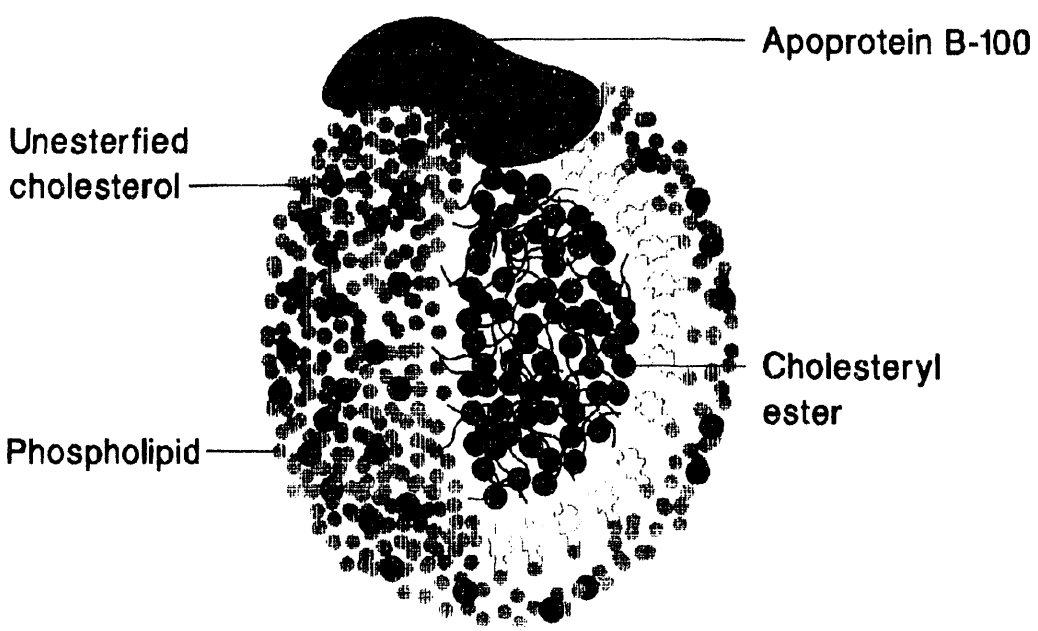

Figure 1. Low density lipoprotein.

high-affinity receptors clustered in regions of the target cell plasma membranes known as clathrin coated pits. After LDL binds to these receptors, the particle-receptor complex is brought into the cell by endocytosis. The bound LDL is transported to the intracellular lysosomes where the LDL is broken down. The receptor is usually recycled to the cell surface to pick up more cholesterol. This recycling process is believed to occur about 250 times during the 20 hour half-life of the receptor. In the lysosome, the particle is exposed to a multitude of enzymes which degrade the LDL protein to amino acids and hydrolyze the esters to free cholesterol for storage and use by the cell. Approximately 45% of the plasma LDL pool in normal humans is catabolized daily. Of this, about 2/3 enters cells through this receptor-mediated pathway; the remaining 1/3 is catabolized by non-specific pathways involving various kinds of macrophage or "scavenger cells."

Cells require cholesterol chiefly for the construction of new membrane. Both normal and cancerous cells obtain about 90% of their cholesterol requirements by importation, as described above. However, rapidly proliferating cells, such as cancer cells, require increased amounts of cholesterol over surrounding normal cells. A logical consequence of this is that cancer cells have high LDL requirements and higher LDL receptor activity than normal cells. A number of research groups have reported experimental cholesterol flux measurements in various types of cancers consistent with this hypothesis. In some cases, this differential rate in cholesterol flux is 20 times higher in cancer cells than in normal fibroblasts. LDL receptor activity in gliomas has been found to be significantly elevated, making LDL an ideal drug delivery agent for treatment of gliomas since the LDL particle is much too large to pass the normal blood-brain-barrier.

LDLs possess several potential advantages as drug delivery vehicles. They are "natural" body components and, as such, are able to survive in tissue or plasma for significant time periods. The small particle size allows diffusion from the vascular to the extravascular compartments of the body. Intracellular uptake *via* receptor-mediated endocytosis permits the contents of LDL particles to enter the interior of cells, an important factor when considering drug delivery vehicles for BNCT, since the boron fission reaction is much more effective in cell killing if the boron is located inter- rather than extracellularly. The oily core of LDL provides a favorable domain for lipophilic drugs and prodrugs.

Researchers at UCSF and elsewhere have demonstrated that the LDL core components can be partly or even totally replaced with lipophilic drugs. And, finally, receptor-mediated LDL uptake is significantly enhanced in certain pathophysiologic states, providing the potential to selectively administer boronated LDL to such cells.

In principle, then, if the cholesterol ester core of LDL could be replaced by a similarly hydrophobic boron compound, the receptor-mediated uptake of boronated LDL could provide a "Trojan horse"-like mechanism for the selective delivery of boron to tumor cells. This is a stealth-type effect since, in principle, the reconstituted boron-loaded LDL should appear to the body and behave 'normal' LDL.

The UCSF group has previously pioneered and developed a method by which the cholesterol esters can be stripped from human LDL and replaced by a series of long chain unsaturated fatty alcohol esters of 1,2-carborane carboxylic acid. The carborane is a polyhedral molecule consisting of 10 boron and 2 carbon atoms with each of the 12 atoms linked to single hydrogen atom. Its closed cage "ball-like" nature renders it more or less inert and non-toxic. Of the several dozen esters evaluated, it was found that the elaidyl ester could be reconstituted to the highest degree. Indeed, calculations based on the boron content of the resultant boronated LDL showed that an average 2000-3000 molecules of the ester could be placed in the LDL core. Using cell culture techniques and the BMRR beam, it was shown that the reconstituted LDL apparently entered cultured cancer cells *via* the normal receptor-mediated process, and that the boron internalized by this process provided very potent

sensitization to the beam of thermal neutrons. When sufficient cells were cultured in the presence of boronated LDL to enable independent measurement of their boron content, an average intracellular boron content of ~240 ppm was determined. This concentration is far higher than that from any other known boron delivery system and is an order of magnitude greater than that needed for therapy.

One focus of the present year's work has been to determine whether simple commercially available carboranes would behave in a similar fashion. Simple alkyl and aryl carboranes were evaluated for their ability to replace cholesterol in LDL. Table 1 presents a representative sample of the results of these studies.

It is clear from these data that some of the compounds reconstitute very efficiently while others do not. Hexyl and allyl carborane, both viscous liquids at room temperature, provide boronated LDL with substantial boron/protein ratios and exceed elaidyl carborane carboxylate (ECC) in that respect. Carborane compounds, which are more highly crystalline, such as phenyl carborane, reconstitute very poorly.

Before attempting small animal experiments with boronated LDL, it was necessary to demonstrate that inductively coupled plasma-atomic emission spectrometry (ICP-AES) could be used to accurately measure the boron content of tissues from animal treated with boronated LDL. All previous work had relied upon using prompt gamma spectrometry to measure boron. Prompt gamma techniques lack the sensitivity required for ppm and sub-ppm boron measurement in small samples, and requires the use of a nuclear reactor as a neutron source. The boron compounds used in the LDL work are both more stable and more lipophilic than those previously evaluated using ICP-AES, and would likely be in a more difficult matrix than others examined. This proved to be the case; ICP-AES and prompt gamma boron determinations of the same samples were often widely divergent. However, INEL researchers headed by Dr. Bill Bauer were able to overcome this difficulty by using a more vigorous sample digestion process for the LDL samples. Although some additional modification of this process may still be required for accurate boron measurement in very hydrophobic environments such as brain tissue, the general concordance between the two techniques is currently at about 90% (data not shown).

Another series of experiments was designed to evaluate the integrity of the boronated LDL in solution. Other investigators had suggested that the reconstitution process somehow altered the LDL particles and caused them to aggregate. Although these studies did not use boronated LDL, the possible effects of such a process on the use of boronated LDL for BNCT required that

Table 1. LDL reconstitutions with alkyl and aryl carboranes.

Compound	Ave. μg B/g	Ave. μg protein/g	Ave. μg B/μg protein
1-hexyl carborane	94.4 ± 8	660 ± 15	0.71 ± .05
1-allyl carborane	75.8 ± 25	671 ± 100	0.55 ± .11
1-butenyl carborane	13.3 ± 4	508 ± 100	0.13 ± .04
1-phenyl carborane	11.8 ± 7	492 ± 60	0.11 ± .06
1-methyl carborane	7.8 ± 2	224 ± 13	0.11 ± .06
meta carborane	4.4 ± 1	511 ± 60	0.04 ± .02

UCSF researchers evaluate this phenomenon. This was carried out by performing a second filtration of the LDL through a 0.45 micron filter in order to determine whether such a process would selectively remove highly aggregated material. The results of this study are presented in Table 2.

Several observations may be made regarding these values. The singly filtered samples all have ratios within experimental error of ratios for these compounds reported previously with the single exception of 1-allyl carborane, which usually has a large standard deviation. These numbers confirm a previous assertion that only 1-hexyl- and, perhaps, 1-allyl-carborane are viable candidates among the alkyl and aryl for LDL insertion for tumor boron delivery. Elaidyl carborane carboxylate has been the standard for all previous *in vitro* work, and the boron/protein ratio reported here is consistent with values for a number of previous samples used in cell culture. It is also clear from these data that a second filtration step has a relatively minor effect on the overall boron/protein ratio of the boronated LDL. Indeed, in each of the pairs of ratios, both values are within experimental error of each other. However, the raw data (not shown) indicate an interesting effect. For the better reconstituting compounds, i.e., hexyl, allyl and ECC, the absolute boron content is reduced by approximately 10% during the second filtration, and in each case, so, too, is the absolute protein content. However, for less efficient reconstituters such as methyl, butenyl and phenyl, the change in boron content varies widely while the protein content decreases by 10-15%. This is further confirmation that these compounds are unsuitable for LDL incorporation and disrupt the LDL in a presently unknown fashion.

Following the choice of ECC as the boron carrier and the verification of ICP-AES as an accurate boron measurement techniques, animal distribution experiments were begun in collaboration with the group at WSU. In these experiments, mice bearing the B16-BL6 murine melanoma were given a single 400 µL dose of ECC-LDL by tail vein injection. The boron content of the solution was found to be 180 µg/mL by ICP-AES, so the total administered dose was 95 µg boron per animal (or 4.75 mg/kg assuming a 20g animal). This dose is small by comparison with that used in studies with other compounds, and is limited by the injection volume and by the protein content of the solution. Tissues were obtained at sacrifice from 6 animals each at 6, 12 and 24 hour intervals. The results are presented in Table 3.

It is clear from this preliminary experiment that some partitioning of LDL among the organs takes place and does so on a fairly rapid time frame. Tumor and blood boron content are roughly parallel over time while brain uptake is quite small as expected and is characterized by large relative percentage errors. Liver and spleen uptake are large, as expected on the basis of normal LDL receptor populations in these organs.

Table 2. LDL reconstitutions - double filter experiment.

	µgB/µg Protein	
Compound	Single filtered	Double filtered
1-hexyl carborane	0.71 ± 0.05	0.68 ± 0.04
1-allyl carborane	0.34 ± 0.10	0.30 ± 0.04
ECC	0.25 ± 0.02	0.22 ± 0.02
1-methyl carborane	0.21 ± 0.05	0.39 ± 0.15
1-phenyl carborane	0.15 ± 0.05	0.14 ± 0.04
1-butenyl carborane	0.06 ± 0.02	0.09 ± 0.03

Table 3. Table 3. Boron content *in vivo* following ECC-lipoprotein injection.

	Organ boron content (μg/g)		
	6 hr	12 hr	24 hr
Tumor	5.37 ± 2.32	3.65 ± 1.78	4.11 ± 0.56
Blood	5.92 ± 0.53	3.48 ± 1.61	3.07 ± 0.30
Brain	1.02 ± 0.21	0.72 ± 0.22	0.75 ± 0.31
Skin	3.39 ± 1.09	1.71 ± 0.73	2.46 ± 0.93
Liver	28.09 ± 3.86	15.25 ± 9.37	11.18 ± 6.22
Spleen	26.69 ± 4.30	19.89 ± 13.55	16.16 ± 8.72
Kidney	5.27 ± 0.33	2.78 ± 1.26	2.79 ± 1.01
Muscle	2.46 ± 0.69	1.48 ± 0.66	1.01 ± 0.33

Several other series of similar animal experiments were performed. By lengthening the time from injection to sacrifice, it was possible to examine boronated LDL distribution out to 72 hours. From these data (not shown), it is clear that boronated LDL is cleared from tumor fairly rapidly, i.e., by about 24-36 hours. Blood and tumor levels are identical within experimental error at all time points. It is clear from these data that murine models are not suitable for evaluating the biodistribution of boronated human LDL. This is not surprising because, although the murine LDL receptor recognizes the human apo B-100 protein, the mouse does not utilize LDL as its primary cholesterol transport lipoprotein. The B16-BL6 may also not be the ideal tumor model to use. Future studies will examine the *in vitro* uptake of boronated LDL in a variety of cell lines, including human tumor lines, in order to determine whether another tumor might give a more suitable model. Such studies will also aid in choosing a better animal model. The likely choice is the rabbit whose lipoprotein metabolism is much more like that of humans.

In collaboration with a group of neurosurgeons and neurologists at the Helsinki University Hospital in Helsinki, Finland, the UCSF group has recently demonstrated conclusively the potential for using LDL as a boron drug carrier. Six patients with recurrent glioblastoma have been evaluated for the ability of radiolabeled LDL to bind to their tumors. LDL was isolated from the blood of each patient prior to surgery and tagged with ^{99m}Tc. The radiolabeled LDL was reinjected and each patient was scanned using a gamma camera just prior to surgery. In each case, the recurrent tumor was clearly and definitively outlined; these enhanced areas correlated directly with tumor location determined at the time of surgery. Although it was not possible to quantitate the degree of uptake, it is clear that high-grade recurrent gliomas have very active LDL receptor populations, and that radiolabeled LDL is excluded from the normal brain. These exciting results indicate the true potential of LDL for BNCT treatment of gliomas.

The UCSF compound development group has also made major progress toward the stereoselective synthesis and testing of a boronated amino acid known as carboranylalanine—nicknamed Car—in keeping with the standard, three letter amino acid abbreviation system. The incorporation of boronated amino acid analogues of phenylalanine (Phe) *via* the accentuated aromatic-amino acid uptake activity present in melanotic melanoma cells is one of the most attractive strategies for site-specific boron delivery of boron compounds to neoplastic cells. Moreover, the successful synthesis of such compounds would permit their incorporation into a wide variety of small peptides whose naturally

occurring congeners are known to be taken up by various types of cancers.

In 1958 Snyder et al. noted the potential use of metabolic mechanisms for localizing boron in tumors, and synthesized BPA with the specific purpose of using the aromatic amino acid transport system to load melanomas with boron for BNCT. The advantages to tumor targeting through known metabolic differences are that the uptake system can be manipulated through rational biochemical strategies. If a tumor cell requires a particular metabolite, for example phenylalanine, and a boronated analog can be used to exploit this requirement, other sources of the natural substrates may be blocked to enhance uptake of the boronated mimic. Phenylalanine is known to be actively taken up by melanin-producing cells for use in the production of melanin. Very little is known regarding the biochemical specificity of this uptake system. It seems likely that such a system has the phenyl ring as a minimal structural requirement, but the extent to which the presence or absence of phenolic hydroxyls influences amino acid transport kinetics is entirely unknown. It is clear, however, that the system is stereospecific and will only accept the (L)-stereoisomer. Successful suppression of melanoma *in vivo* and *in vitro* reported by Coderre and coworkers, and by Mishima and coworkers using (L)-BPA, suggests strongly that the strategy of using boronated false substrates for boron delivery should be explored more fully in other aromatic-amino acid analogue systems.

Mishima and coworkers have actively exploited this rationale using BPA to treat hamsters, pigs, and recently several human patients with BNCT. It appears that their strategy was successful at least insofar as loading the tumors with sufficient boron to permit NCT, but it seems unlikely that BPA is actually incorporated covalently into melanin. Rather, it would appear that a transient accumulation of BPA occurs that depends upon the recognition of BPA as an aromatic amino acid. Coderre and Glass in a series of excellent studies have shown that L-BPA is selectively accumulated by Harding-Passey melanomas in mice and that this accumulation, although transient, is sufficient to demonstrate a clear therapeutic gain in BNCT of mice treated with BPA.

Several lines of reasoning strongly support the concept of developing an amino acid delivery system in which the aromatic phenyl ring of phenylalanine has been replaced by a carborane cage. First, this amino acid contains 46.8% boron by weight compared to 5.2% for BPA (i.e., on a molar basis, it is nine times more effective as a boron carrier). Second, the icosahedral carborane cage is extremely resistant to chemical degradation, unlike the dihydroxyboryl group which is somewhat sensitive to both strong acid and strong base. Third, the carborane group is essentially nontoxic in the absence of thermal neutrons; carborane derivatives are characterized by LD_{50} in the 2000-3000 mg/kg region in rats and mice.

Computer modeling studies carried out at UCSF have been used to compare Phe and Car, and have definitively shown that they are nearly bioisosteric. The apex-to-apex distance in the carborane cage is nearly the same as the C(1) - C(4) distance in the phenyl ring of phenylalanine. The volume swept out by a freely rotating phenyl ring is thus almost coincident with the volume occupied by the carborane cage. On this basis, replacement of Phe by Car in a small peptide, where conformational freedom is likely in solution, is expected to have little or no effect on the biological specificity of the peptide and may well increase the plasma half-life of such a peptide by resistance to the body's peptidase.

Carboranylalanine Development

After a great deal of effort, researchers at UCSF have succeeded in developing a stereoselective synthesis of carboranylalanine. This synthetic strategy utilizes a carboranyl oxazolidone enolate, and allows the synthetic chemist to synthesize either the (L) or (D) form of Car depending upon the stereochemistry of the heterocyclic template. It also has the advantage over other approaches of ease of purification of possible contaminating diastereoisomers and presents a general access route to other interesting

homologs of carboranylalanine. The precise experimental details are beyond the scope of this document, but it can be fairly stated that this synthetic success represents a significant step in the development of tumor directed boronated amino acids and peptides.

In collaboration with Dr. Brenda Laster at BNL, a preliminary *in vitro* evaluation of carboranylalanine has been carried out using a method which was developed jointly and recently published.[3] This simple technique provides information regarding the intra- and extracellular location and concentration of boron and also allows measurement of biological efficacy by the evaluation of survival curves obtained following thermal neutron irradiation. Concomitantly, an indication of compound toxicity can be obtained from the plating efficiency of unirradiated control cells. Briefly, cells are grown for one mitotic cycle (~16 hours) in the presence of the boron-containing compound to be tested and then irradiated in the presence of the same compound. Similar irradiations are also carried out after a thorough washing of the cells and suspension in boron-free media. Biological response is then compared to that obtained after irradiation of cells in known amounts of boric acid ($H_3{}^{10}BO_3$), in which a homogeneous intra- and extracellular distribution is assumed. A comparison of results indicates whether a test compound is taken into the cell, whether it is retained or bound despite washings, and how much is present in terms of known amounts of boric acid (boric acid equivalents or BAE).

Preliminary experiments using this technique suggest that L-carboranylalanine will be a very effective intracellular neutron-sensitizer with very minimal toxicity. B-16 melanoma cells were incubated for 16 hours with a racemic mixture of Car which contained unenriched boron, that is, ^{10}B at its naturally abundant level of ~20% total boron. Prompt gamma analysis of the media gave a ^{10}B-concentration of 5.6 ± 0.6 ppm, or a total boron concentration of ~28 μg/mL. Cells were then washed 3 times with boron-free media and irradiated with thermal neutrons for varying times. Cell survival was obtained through clonogenic assay, and a cell survival curve was constructed. Analysis of this curve gave a D_0 value (time required to reduce survival by a factor of 1/e) of 1.2 minutes when normalized to 95% - ^{10}B. In other words, if 95% ^{10}B-enriched carborane had been used in the amino acid and incubated at the same amino acid concentration (~65-70 μg/mL or 0.16 mM), a 63% reduction in cell survival for each 1.2 minutes of irradiation would have been obtained. Comparison with $H_3{}^{10}BO_3$ experiments produced a BAE of 12, meaning this compound was 12 times as efficient as a similar concentration of $H_3{}^{10}BO_3$. This result, added to the fact that these cells were thoroughly washed before irradiation, suggests strongly that Car is taken up and retained by these melanoma cells. In fact, on a boron weight basis, Car appears by this assay to be approximately as efficacious as the best boronated porphyrin, BOPP. Furthermore, this experiment used racemic Car; one would expect the enantiomerically pure L-Car to be the active form which would further increase the BAE by a factor of two. Moreover, the nearly identical plating efficiencies of controls (73%) and Car-treated cells (71%) demonstrates that Car at these doses is essentially non-toxic.

Future studies with the Car system will include scale-up of the synthesis, production and testing of ^{10}B-labelled stereoisomers and insertion into small peptides.

BORONATED LIPOSOME DEVELOPMENT AND EVALUATION

Dr. Fred Hawthorne, PI, University California, Los Angeles, Department of Chemistry and Biochemistry

The boronated liposome development and evaluation effort consists of two separate tasks. The first is the development of new boron compounds and the synthesis of known boron species with BNCT potential. These compounds are then encapsulated within liposomes for the second task: biodistribution testing in tumor-bearing mice, which examines the potential for the liposomes and their contents to concentrate boron in cancerous tissues.

The team at UCLA (Drs. Kenneth Shelly and Debra Feakes) under the direction of Dr. Hawthorne combines the synthesis of known but previously uninvestigated boron compounds with the development of new boron chemistry to produce a variety of boron agents with BNCT potential. These researchers also produce the boron-containing liposomes for biological screenings that determine the boron localization. The primary liposome biodistribution experiments and liposome characterizations are performed under the direction of Dr. Paul Schmidt at Vestar, Inc. (a private firm specializing in the pharmaceutical applications of liposomes) San Dimas, CA; with the assistance of Dr. Gary Fujii and Teresa Krisch, A.H.T. Further liposome murine experiments are performed at WSU by Dr. Cathy Elstad.

Background

One of the more pressing problems in BNCT has been the development of effective strategies for the localization of boron within tumor tissue. The primary difficulties to be overcome are specific delivery of therapeutic quantities of boron to tumor, while sparing normal tissues, and toxicity of the boron agent delivered. Liposomes, which have been studied extensively as drug delivery systems, present a novel approach for the solution to these problems and are a new and innovative method for the delivery of boron for BNCT.

Liposomes (small unilamellar vesicles) are microscopic spheroidal structures composed of a phospholipid bilayer membrane enclosing an aqueous core (Figure 2). The utility of liposomes as drug delivery systems arises from their ability to encapsulate water-soluble compounds in the aqueous core or to dissolve hydrophobic compounds within the lipid membrane. The liposomal

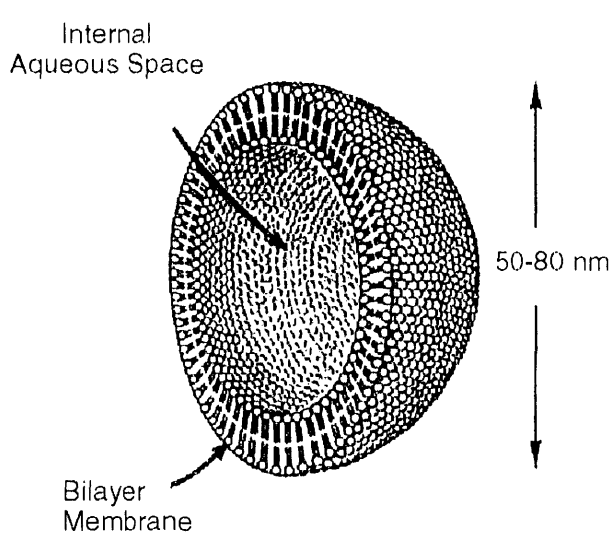

Figure 2. Cutaway view of a small unilamellar vesicle.

delivery of drugs, when successful, has several attractive consequences. Sequestering the effector species in vesicles can provide it with an extended circulation lifetime, thereby increasing its opportunity to be taken up by tissue. The liposome also offers protection for the occluded species from attack by normal physiological agents *in vivo* and reduces potential toxic effects (the liposome constituents themselves are non-toxic). Liposomes can deliver their contents directly to the interior of cells, where their therapeutic utility is maximized. Since selective delivery and cell entry is provided by the liposome, the encapsulated species need not have a natural affinity for the targeted tumor cells, thus making this method amenable to a wide variety of effector molecules.

Previous research at Vestar has demonstrated that suitable liposomes of a particular size and composition will preferentially deliver their contents to tumor cells in animals and humans such that the tumor levels of effector molecules are 5-10 times that of normal tissue, including blood. Researchers at UCLA, in collaboration with Vestar, Inc. have investigated the potential of such liposomes to deliver therapeutic quantities of boron to tumors. The results of the initial studies (1988-1991) demonstrated that liposomes are a viable boron delivery system for BNCT.

Liposomes were shown to be capable of encapsulating borane anions, as their soluble sodium salts, in the high concentration required to deliver a sufficient quantity of boron in a reasonable dose volume. These high concentrations, while much greater than normally attempted in liposomes, were stably encapsulated with only negligible leakage over a period of months. The extended circulation lifetime and tumor selectivity provided by the liposomes permitted the use of relatively small doses of boron to produce significant boron concentrations in tumor. The relatively simple borane anions initially studied, which normally exhibit brief circulation lifetimes and no tumor selectivity, were selectively delivered to tumors in mice by the liposomes. Perhaps the most significant finding was the importance of the chemical reactivity of the delivered boron species. Although simple, inert, non-specific boron compounds were selectively delivered by the liposome to tumor, they were flushed out after a few hours since they had no characteristics to retain them within the tumor cells. Greater success was achieved with boron compounds that had the ability to chemically react with intracellular components, thereby anchoring the boron within the tumor.

The recent focus of attention in boronated liposome development research has centered on two primary aspects: (a) the production of new boron-rich drugs with functional groups or chemical reactivity suitable for tumor retention after liposomal delivery, and (b) the biological testing of these compounds, encapsulated in liposomes, in rapid preliminary screening experiments in mice to determine tumor delivery and retention of boron.

Compound Development

Most of the compound development research at UCLA has involved the production of boron-rich species based upon the ten-boron unit $[B_{10}H_{10}]^{2-}$ (**I**), first synthesized in Hawthorne's laboratory 30 years ago. This ion was chosen for its high boron content, ease of preparation, stability, and rich derivative chemistry. A convenient new method has been developed (Figure 3) to functionalize (**I**) by its reaction with oxalyl chloride to produce the carbonyl derivative $[2\text{-}B_{10}H_9CO]^-$ (**II**). Unlike most other derivatization reactions known for (**I**), carbonylation proceeded smoothly under mild conditions and afforded a high yield of a single pure product. The structure of (**II**) was determined by x-ray crystallography and is displayed in Figure 4. The reactivity of (**II**) enabled its coupling to other organic structures and also provided simple routes to a variety of new substituted $[B_{10}H_{10}]^{2-}$ species as shown in Figure 5.

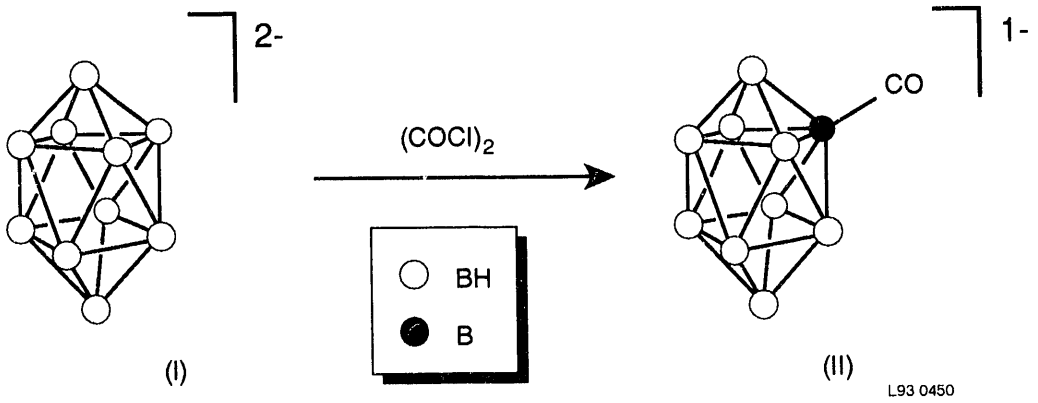

Figure 3. Synthesis of $[2\text{-}B_{10}H_9CO]$-(II).

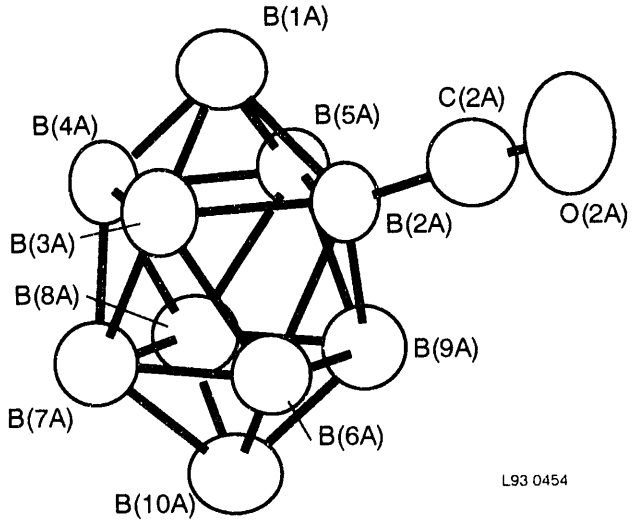

Figure 4. X-ray crystal structure of $[2\text{-}B_{10}H_9CO]$-(II).

The most important transformation of (**II**) was its conversion to the isocyanate $[2\text{-}B_{10}H_9NCO]^{2-}$ (**III**), which was also structurally characterized. This species, although quite stable in aqueous solution, was reactive with nucleophiles such as amines to form urea linkages. This reactivity was presumed to be responsible for the behavior of (**III**) when it was delivered by liposomes *in vivo*. For example, RNH_2 in Figure 5 could represent an intracellular protein residue, thereby binding the boron cage within the cell.

Further compound development studies have dealt with twenty-boron species formed by the coupling of two $[B_{10}H_{10}]^{2-}$ ions (Figure 6). Oxidation of (**I**) produces $[B_{20}H_{18}]^{2-}$ (**IV**), a boron framework that is reactive with nucleophiles and has been shown previously to be retained within tumor cells. Reduction of (**IV**) produces $[B_{20}H_{18}]^{4-}$ (**V**), which may undergo chemical substitutions analogous to those described above for $[B_{10}H_{10}]^{2-}$. The carbonylation of $[B_{20}H_{18}]^{4-}$, unlike the carbonylation of $[B_{10}H_{10}]^{2-}$, does not afford a single pure product, but produces what is believed to be two different isomers. Conversion to the isocyanate derivative, $[B_{20}H_{19}NCO]^{3-}$ (**VI**), has been achieved; though once again, problems with isomerization must be eradicated. These reactions are currently under investigation.

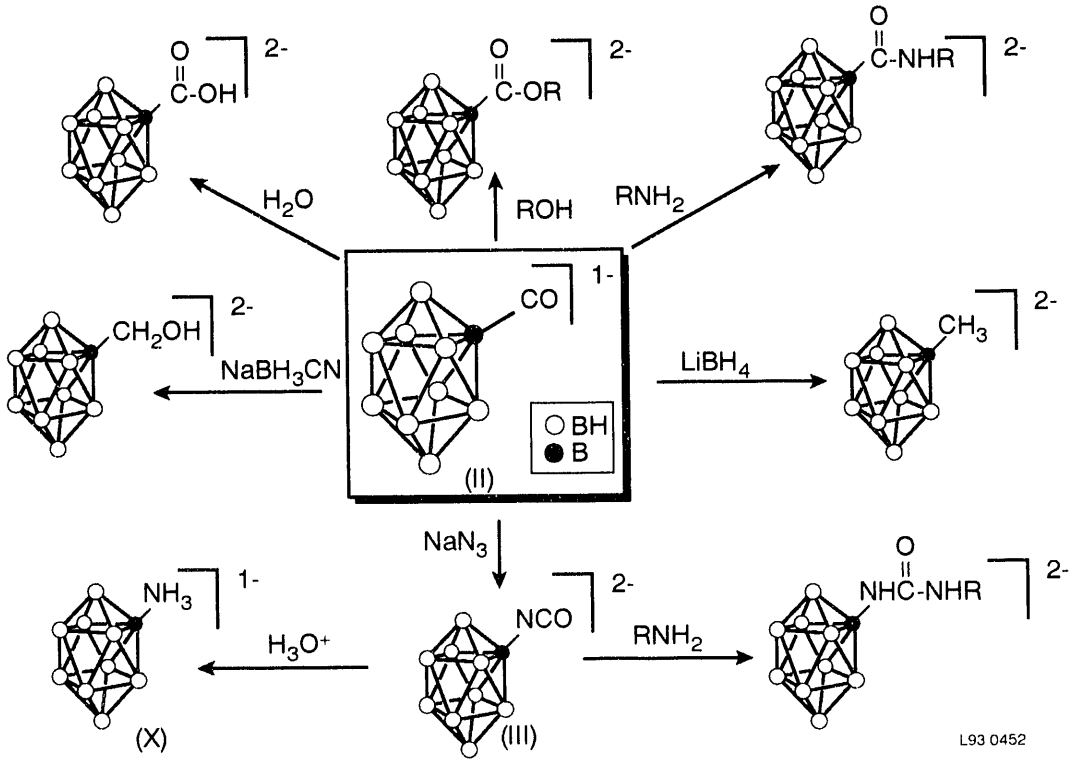

Figure 5. Transformations of $[2\text{-}B_{10}H_9CO]$-(II).

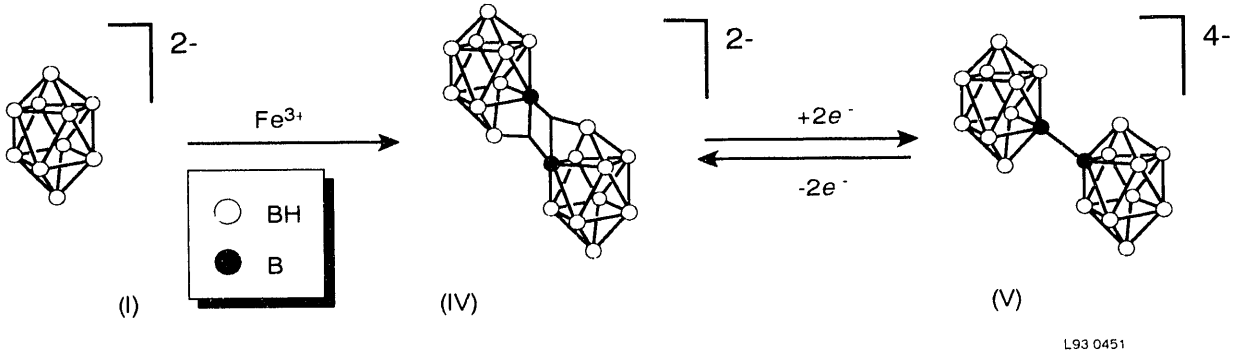

Figure 6. Synthesis of $[B_{20}H_{18}]^{2-}$(IV) and reduction to $[B_{20}H_{18}]^{4-}$(V).

One of the most promising series of compounds are those derived from the nucleophilic substitution of $[B_{20}H_{18}]^{2-}$. The first compound in this series, $[B_{20}H_{17}OH]^{4-}$(**VII**), was developed by Hawthorne in 1963. This compound was investigated to ensure that the tumor retention observed for the $[B_{20}H_{18}]^{2-}$ species was a result of the reactivity of $[B_{20}H_{18}]^{2-}$ and not a result of its hydrolysis product, $[B_{20}H_{17}OH]^{4-}$, which could form at physiological pH. The hydrolysis compound was not retained by the tumor, but was cleared rapidly from all tissues, ensuring the necessity of *in vivo* reactivity for tumor retention.

In an analogous reaction, the amine derivative of $[B_{20}H_{18}]^{4-}$, $[B_{20}H_{17}NH_3]^{3-}$ (**VIII**), was synthesized. This compound has demonstrated one of the most promising biodistributions to date. Detailed investigation of this compound with respect to the unsubstituted species, $[B_{20}H_{19}]^{3-}$ (**IX**), and the hydroxy substituted compound, $[B_{20}H_{17}OH]^{4-}$, has demonstrated that the amine compound is oxidized almost 0.5 V *more readily* than the other two compounds. The ability to oxidize *in vivo* to a more reactive species is the most likely explanation for the high tumor retention demonstrated by this compound. In order to establish whether the oxidation to a more reactive species was responsible for the observed tumor retention, rather than the amine functionality, the known $[2\text{-}B_{10}H_9NH_3]^-$ (**X**) species was synthesized and the biodistribution determined. The amine oxidation product, $[B_{20}H_{17}NH_3]^-$ (**XI**), as well as the known hydroxy oxidation product, $[B_{20}H_{17}OH]^{2-}$ (**XII**), are currently being synthesized for *in vivo* screening. Additionally, other reduced amine substituted compounds have been synthesized and will be studied in future screenings. These include the ethylenediamine derivative, $[B_{20}H_{17}NH_2CH_2CH_2NH_2]^{3-}$ (**XIII**), and the benzylamine derivative, $[B_{20}H_{17}NH_2C_6H_5]^{3-}$ (**XIV**).

Nucleophilic attack of $[B_{20}H_{18}]^{2-}$ by other anions, such as $[CN]^-$, $[SH]^-$ and $[C\int CH]^-$ has been investigated. The resulting compounds $[B_{20}H_{17}CN]^{4-}$ (**XV**), $[B_{20}H_{17}SH]^{4-}$ (**XVI**), and $[B_{20}H_{17}C\int CH]^{4-}$ (**XVII**), respectively, have been observed spectroscopically and will be isolated for future *in vivo* screenings.

The compounds discussed thus far have been water-soluble compounds which are encapsulated as hyperosmotic solutions in the aqueous core of the liposomes. Addition of relatively small amounts of boron to the lipid constituents of the liposome should increase the boron concentration delivered by the liposomes dramatically, provided suitable compounds can be obtained. Carborane cages, $C_2B_{10}H_{12}$, are one of the most versatile boron building blocks known. They have a rich derivative chemistry based on the ability to functionalize the carbon atoms of the cage structure. The substituted carboranes are quite lipophilic. Additionally, they can be decomposed to a *nido* structure characterized by a polar head group and increased hydrophilicity (Figure 7). Substitution of the carborane with a long hydrophobic side chain, preferably one similar in length to the phospholipid constituent, followed by degradation, should provide a structure which will embed itself within the lipid constituents of the liposome without significantly diminishing the stability of the liposome bilayer.

A suitable compound, $K^+[C_2B_9H_{10}(CH_2)_{15}CH_3]^-$ (**XVIII**), has been synthesized. This compound is derived from a carborane substituted at one carbon by a 16 carbon chain. The carborane is degraded to form the product characterized by a hydrophilic head group, the *nido*-carborane, and a hydrophobic tail, the 16 carbon chain. This compound has been successfully embedded into the liposomes, resulting in approximately 1.5% added boron, and the biodistribution determined.

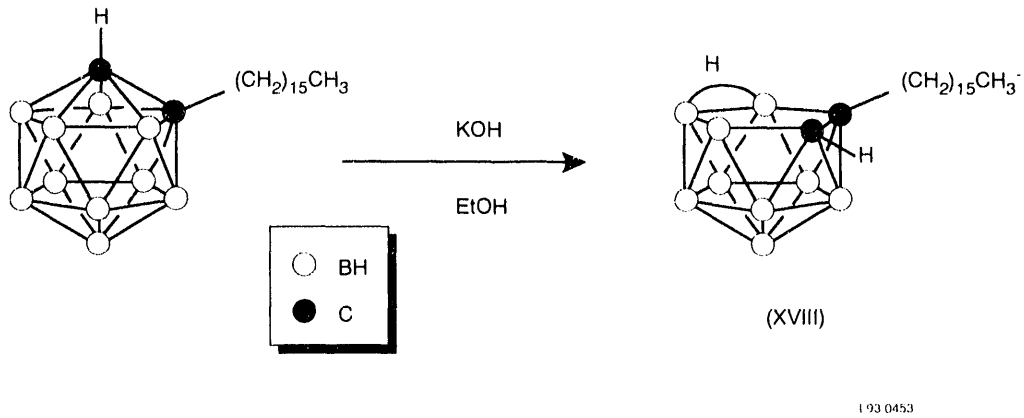

Figure 7. Synthesis of a substituted *nido*-carborane (XVIII).

Liposome Encapsulation and Biodistribution Results

Since September 1991, a total of 25 screenings have been performed utilizing 10 compounds and 4 tumor lines. Screenings with EMT6 murine adenocarcinoma were performed at Vestar, Inc. Researchers at WSU performed screenings with B16-BL6 murine melanoma, P1798 murine lymphosarcoma, and most recently, Lewis Lung murine carcinoma (see below under Boron Localization Screening). Although the B16-BL6 murine melanoma tumor line did not appear to take up the liposomes, results from both the EMT6 murine adenocarcinoma and P1798 murine lymphosarcoma indicated significant uptake and provided analogous results. No analyses have been obtained for the Lewis Lung murine carcinoma to date. All compounds screened, since the inception of this project in 1988, have been screened in the EMT6 murine adenocarcinoma tumor line and all biodistributions included in this section will be from that line.

The best biodistribution results are characterized by high initial tumor boron concentration (>15 μg boron/g tissue). The initial concentration should increase or remain at the same level throughout the time period. Other tissue boron concentrations (blood, liver, and spleen) should decrease throughout the time period and result in low final boron concentrations, thus providing high tumor boron to tissue boron ratios (>3) while maintaining significant tumor boron concentrations. Results previously obtained indicated that compounds possessing the potential to react with intracellular protein constituents were retained within the tumor cells. This working hypothesis was the basis of the compounds chosen for examination during the past year.

The first boron compound ever encapsulated into liposomes (1988) was $Na_2B_{10}H_{10}$ (**I**). This species was chosen because it is conveniently prepared in high yield from decaborane, and its sodium salt is relatively inert and known to be nontoxic. Although the compound showed no retention in any tissues over the time period, the biodistribution did show that liposomes could deliver non-tumor-specific boron compounds to tumor cells. The biodistribution of $Na_2B_{10}H_{10}$ (**I**)is shown in Figure 8A as a comparison to the more exciting biodistribution obtained this year from liposomes containing $Na_2B_{10}H_9NCO$ (**III**, Figure 8B).

Compared to its unsubstituted precursor, the boron delivered by $Na_2B_{10}H_9NCO$ (**III**) was retained by the tumor to a much greater degree. Since the only difference between the two compounds is the amine reactive isocyanate moiety, the proposed intracellular protein reaction appears to be substantiated. Further studies will employ twenty-boron species containing the isocyanate functionality.

The amine derivative of $[B_{20}H_{18}]^{4-}$ (**IV**), $Na_3B_{20}H_{17}NH_3$ (**VIII**), exhibited the biodistribution displayed in Figure 8C. This compound produced the most exciting results obtained for an encapsulated species to date. It is the only encapsulated compound studied which continued to accumulate tumor boron over approximately 30 hours. The tumor boron concentration after 48 hours (25.4 μg boron/g tissue) is approximately equal to that observed after 6 hours (27.0 μg boron/g tissue).

Two reactivity schemes have been proposed for the retention of $Na_3B_{20}H_{17}NH_3$ in tumor cells. The first is based on the ability of the $[B_{20}H_{17}NH_3]^{3-}$ to oxidize to a more reactive species, $[B_{20}H_{17}NH_3]^{-}$. The second is based on the ability of the $-NH_3$ group to react directly with intracellular residues. To test whether the second scheme was correct, an analogous known ten-boron compound, $NaB_{10}H_9NH_3$ (**X**), was synthesized and the biodistribution determined (Figure 8D).

The $NaB_{10}H_9NH_3$ species was cleared rapidly from all tissues, including tumor. This result supported the proposal of the *in vivo* oxidation of $Na_3B_{20}H_{17}NH_3$ to the more reactive $NaB_{20}H_{17}NH_3$, as does the ease of oxidation determined by cyclic voltammetry, as discussed previously.

Recently, the biodistribution of liposomes containing approximately 1.5% added boron in the liposome bilayer in the form of $K^+[C_2B_9H_{10}(CH_2)_{15}CH_3]^-$ was determined (Figure 8E). The liposomes encapsulated a saline buffer solution in the aqueous core. The biodistribution of this compound showed accumulation of tumor boron over a period of approximately 24 hours. The 48-hour tumor boron concentration (25.2 μg boron/g tissue) was *higher* than the 6-hour tumor boron concentration (22.2 μg boron/g tissue). These values were achieved at significantly lower injected doses than those used for the water-soluble boron compounds discussed above. Further studies will utilize the boron lipid bilayer enhancement in tandem with the encapsulation of boron compounds in the aqueous core of the liposomes.

Conclusions

Although the biodistributions of all compounds examined in the past year have not been included, compounds producing exciting results, both as potential therapeutic agents and as mechanistic information, have been presented. Biodistribution data has been obtained which substantiates our current working hypothesis: Compounds possessing the potential to react with intracellular protein residues will be retained by the tumor. The identification of water-soluble compounds providing therapeutic levels of boron in tumor has been accomplished, specifically the $Na_3B_{20}H_{17}NH_3$ compound. A means of increasing the boron levels introduced to the system by doping the bilayer membrane of liposomes already capable of incorporating high concentrations of boron has been developed and is being implemented in future investigations.

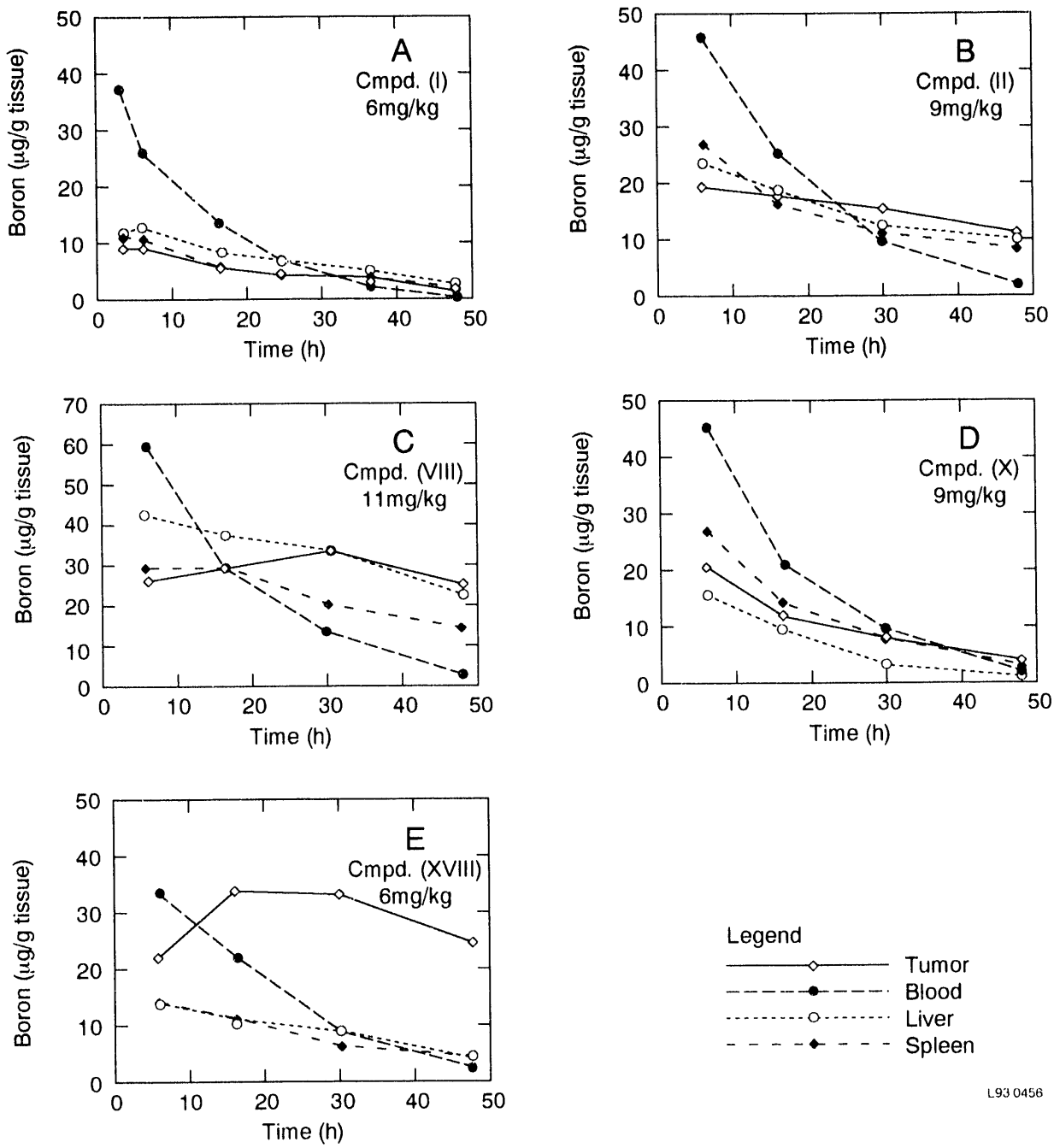

Figure 8. Murine tissue boron concentrations from delivery of boron salts by liposomes. (Injected doses expressed as milligrams boron per kilogram body weight.)

PITUITARY TUMOR EVALUATION

Dr. Barry Albertson, PI, Oregon Health Sciences University, Division of Endocrinology, Diabetes, and Clinical Nutrition, Department of Medicine; Dr. Steve Binney, PI, Oregon State University, Department of Nuclear Engineering

Pituitary tumors comprise approximately 15% of all intracranial tumors.[4] The clinical presentation of these tumors is diverse; morbidity and mortality can be high. Current treatment modalities include conventional x-irradiation and/or neurosurgery, but are inadequate for the most part. Neither are uniformly successful and both are relatively nonspecific. However, several features of these tumors make them ideal candidates for BNCT. First, the tumors are localized in the pituitary gland, rarely metastasizing to other areas of the body. Second, they are rarely larger than 2 cm in diameter. Third, the tumors are outside the blood-brain-barrier. And fourth, the pituitary tumor cells contain cellular membrane receptors that bind and internalize specific hypothalamic polypeptide releasing hormones. The ability to target ^{10}B containing compounds to these pituitary tumor cells with releasing hormones and subsequently kill these cells with BNCT is currently being evaluated in pituitary tumor cells *in vitro* by OHSU researchers.

Chemicals and Reagents

Rodent pituitary tumor cells (AtT-20) were obtained from the American Type Culture Center, Rockville, MD. Cells are cultured in Dulbecco's Modified Eagle Medium (D-MEM) (Gibco Labs, Grand Island, NY) with antibiotics added (penicillin/streptomycin) and 10% fetal bovine serum (FBS) (Gibco). All cell washings are performed with sterile Dulbecco's phosphate buffered saline (D-PBS) (Gibco) in 10 mL conical centrifuge tubes (Corning Labs, Corning, NY). Cells are harvested from T-150 culture flasks (Corning) with a rubber policeman, or from six-well cell culture dishes (Corning) with trypsin/ethylenediaminetetraacetic acid (EDTA) (0.05%/0.53 mM) (Versene, 1:5000) (Gibco). Cells are irradiated in sterile, 20 mL polypropylene scintillation vials. After several washings, cells are counted on a hemocytometer after staining with the supravital stain Trypan blue (Sigma Chemical Co, St. Louis, MO) using an Olympus CK2 inverted microscope.

Cell Irradiation Facility

Cell irradiations are conducted in the thermal column of the ORSU 1 MW Mark II TRIGA Reactor. Three stringers of the graphite thermal column have been removed resulting in a 10 cm x 30 cm cross sectional irradiation port. The innermost end of this region is filled with a bismuth shielding assembly which holds the cell samples, followed by a 50 cm long graphite plug. The thermal neutron and gamma ray fields in the thermal column fall off exponentially with relaxation lengths of 30 and 80 cm, respectively. For these measurements, the rear bismuth shield and graphite plug were absent.

Bare and Cd-covered gold foils were used to measure the thermal and epithermal neutron fluxes at the sample location. These values are 5.2×10^{10} n-cm^{-2}-s^{-1} and 9.2×10^{8} n-cm^{-2}-s^{-1}-Δu, respectively, at 1 MW. The fast neutron flux, measured in a single unshielded graphite stringer using indium threshold foils,[5] is 1.5×10^{8} n-cm^{-2}-s^{-1}. Thus, a reasonably pure thermal neutron beam has been achieved: $\phi_{th}/\phi_{epi} = 56$; $\phi_{th}/\phi_{fast} = 350$.

Gamma ray dose was measured with thermoluminescent dosimeters (TLD)-400s (CaF_2:Mn). The gamma dose rate at 1 MW in the cell sample was 1.1 cGy/s. The ratio of gamma dose to the thermal neutron fluence was 2.0×10^{-11} cGy-cm^2.

Carborane Cage Synthesis and Releasing Hormone Conjugation

$^{10}B_{10}$ carborane cages have been synthesized, purified, and supplied by Dr. Hawthorne, UCLA. The uniqueness of the carborane cage lies in the

incorporation of two carbon atoms combined as an integral part of the cage with an attached acetate reactive group and positioned so that the "cage" can be conjugated via the acetate to protein or polypeptide molecules such as oCRH. The conjugation of the cage is carried out using a classic peptide linkage, thereby joining the reactive carbonyl group on the carborane cage to the amino terminal serine residue of oCRH. These synthetic steps and the final high pressure liquid chromatography purification of the conjugate are performed by Dr. Harry Chen, ERRB, NICHD, National Institute of Health, Bethesda, MD (Figure 9).

Experimental Cell Line (AtT-20)

The AtT-20 rat pituitary corticotroph tumor cell line, established in 1953 by Furth et al.,[6] responds to CRH in a dose dependent fashion with the production of the intracellular second messenger, cyclic adenosine monophosphate (cAMP) (Figure 10).

Retention of Biological Activity of Carborane-CRH

Carborane conjugated oCRH has been shown to retain biological activity, evaluated by the ability to stimulate the production of intracellular levels of cAMP when compared to equimolar concentrations of pure oCRH in *in vitro* experiments using the AtT-20 cell line (Figure 11).

Experimental Paradigm

AtT-20 cells are incubated in a water-jacketed CO_2 incubator in the presence of oCRH, carborane conjugated oCRH, or unconjugated carborane cage and oCRH. After a specified length of time the cells are washed in D-PBS, removed from the T-150 culture flasks using a rubber policeman, and placed into sterile, plastic cell irradiation vials. The vials are positioned in the thermal column as described above. The cells are exposed for up to 10 minutes at different reactor powers. The cell vials are subsequently removed, cell media aspirated after centrifugation (800 rpm for 10 minutes), the cells washed in D-PBS, and replated in T-50 culture flasks in D-MEM with 10% FBS. Cell viability is assessed over time using trypan blue.

Reactor Dosimetry

AtT-20 cells in D-MEM were placed in sterile 20 mL scintillation vials and irradiated under different radiation dose protocols to determine the maximal gamma and/or neutron dose that AtT-20 cells in our *in vitro* paradigm can withstand. The cells were washed and subcultured in D-MEM for five days. Live AtT-20 cells (those that are attached to the plastic culture dish and exclude trypan blue) were removed from the dish using Versene and counted in a hemocytometer. The results of this pilot experiment are shown in Figure 12.

BNCT Effect on AtT-20 Cells

AtT-20 cells were preincubated with oCRH (5×10^{-7} M) or carborane conjugated oCRH analog (5×10^{-7} M) for 18 hours at 37 C, washed with D-PBS, and irradiated for four minutes at 500 kW (representing a gamma and neutron dose that does not appreciably harm the cells) as derived from Figure 12. The cells were removed from the thermal column, washed twice with D-PBS, and subcultured in T-50 flasks with D-MEM-10% FBS for eight days. Cell survivability was assessed at that time using trypan blue. The results are shown in Figure 13.

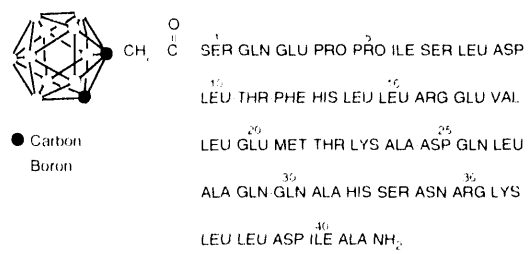

Figure 9. The amino acid sequence of oCRH is shown with the conjugated carborane cage ($^{10}B_{10}$).

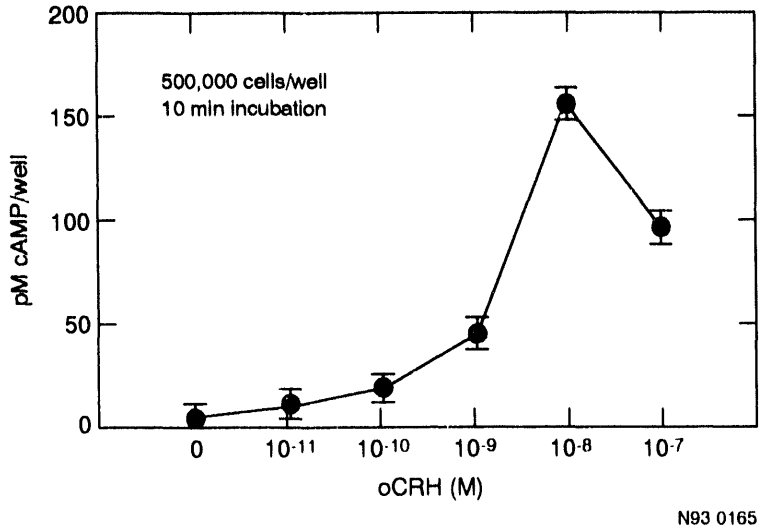

Figure 10. c-AMP dose response after a 10 minute exposure of AtT-20 cells to varying concentrations of oCRH. (5 x 10^5 AtT-20 cells were plated in 12-well culture dishes in D-MEM-10% FBS. cAMP was measured using radioimmunoassy with antisera provided by National Hormone and Pituitary Agency, NIAMD, Baltimore, MD. Each point represents the mean $\pm$ 1 standard deviation of triplicate wells.)

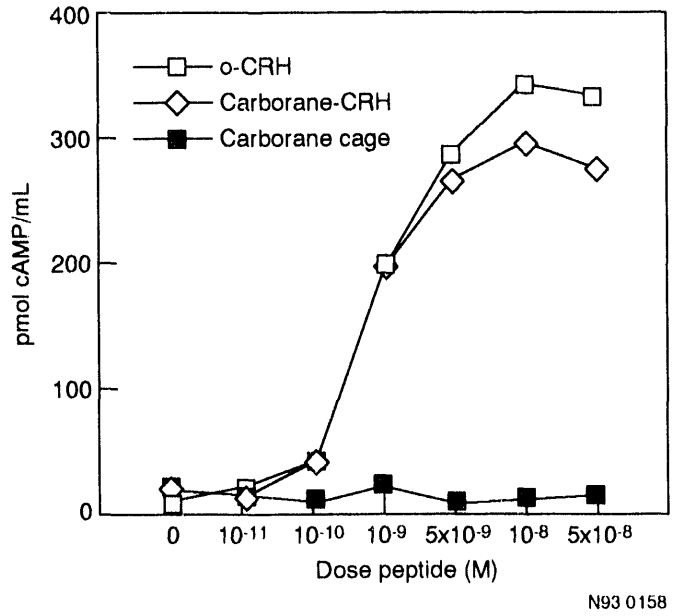

Figure 11. c-AMP response of AtT-20 cells to oCRH carborane CRH, or carborane cage alone at various concentrations. (Dose of peptide, carborane-CRH, or cage alone ranges from 10^{-11} to 5 x 10^{-8}M. Dicomoles of c-AMP produced by 5 x 10^5 cells cultured in 12-well culture dishes per mL is shown on the Y-axis.)

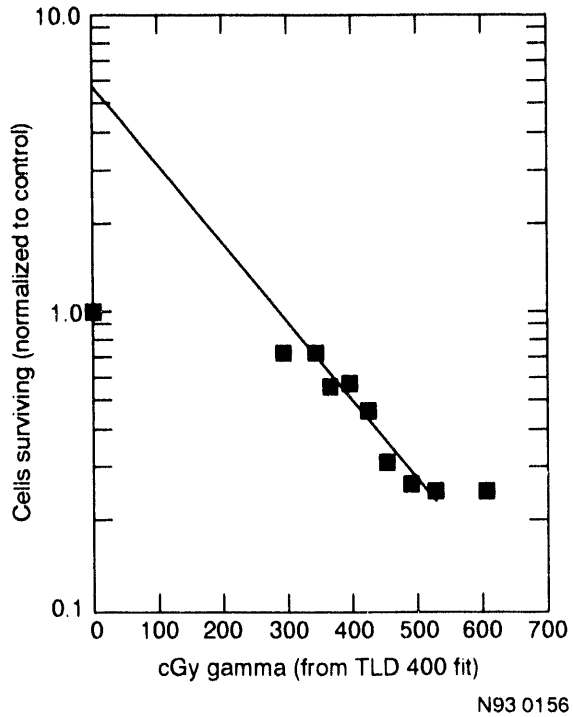

Figure 12. AtT-20 cell survival after five days following exposure to varying gamma doses in the reactor thermal column. (The data suggests that the 1/e dose for the AtT-20 cells was 170 cGy with an extrapolation number of 5.5. The initial AtT-20 cell number at day 0 was 5 x 10^6.)

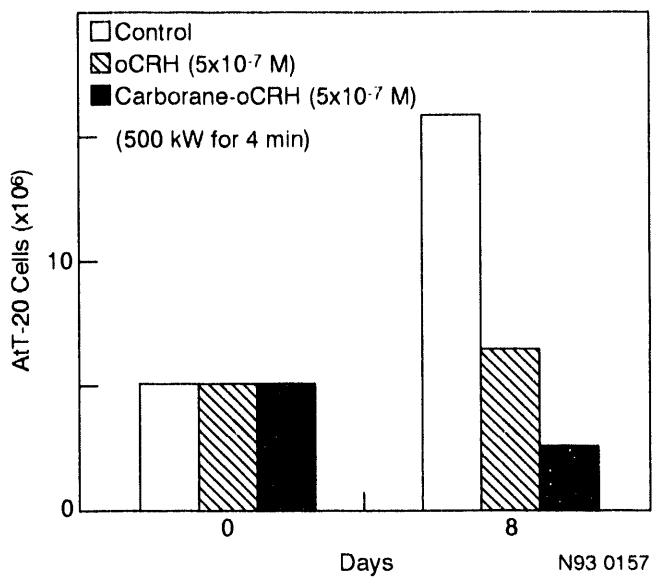

Figure 13. Comparison of AtT-20 cells with and without irradiation. (Control AtT-20 cells receiving no irradiation grew over an 8-day period from 5x10^6 cells/flask to approximately 18x10^6 cells/flask. Cells pre-incubated in the presence of 5 x 10^{-7} M oCRH grew over the same period of time from 5 x 10^6 to 6.5 x 10^6 cells. However, cells preincubated with carborane -oCRH decreased in number from day 0 to 2.5 X 10^6 cells (day 8), suggesting a BNCT effect.)

Conclusions

These preliminary data suggest that pituitary tumor cells can be killed using BNCT by linking enriched boron to hypothalamic releasing hormones. Strategies to decrease even further the contaminating gamma dose delivered to the AtT-20 cells are being tested. Cell loading experiments are currently under way (in conjunction with cellular boron quantitation using ICP-MS and radio-iodine labelling of the carborane-CRH conjugate) to maximize the amount of carborane cage retained by the pituitary tumor cells so that the tumor cell to nontumor cell ^{10}B ratios are as high as possible. These studies will provide important insight into the design of *in vivo* experiments using rodents and subhuman primates to demonstrate the efficacy of BNCT for the treatment of pituitary tumors in humans.

BORON LOCALIZATION SCREENING

Dr. Cathy Elstad, PI, Washington State University, College of Pharmacy

Researchers in the College of Pharmacy at WSU are critically evaluating the effectiveness of potential boron compounds for BNCT. Goals of this research are two-fold: (a) to develop and utilize standardized *in vitro* and *in vivo* assays to quantify boron uptake by tumor cells, and (b) to investigate mechanisms to enhance preferential uptake of boron by tumor cells and, thus, optimize BNCT. Screening of boron compounds for use in BNCT will help determine which boron compounds will have potential for greatest impact on the treatment of human cancer. In addition, identification of alterable factors influencing boron uptake could have a significant impact on BNCT.

Methods

A crucial requirement for effective BNCT of cancer is the selective localization of high concentrations of boron in tumor tissue relative to adjacent normal tissue. Because normal tissues are included within the activating neutron field during therapy, optimal BNCT efficacy requires higher boron accumulation in the tumor than in the surrounding normal host tissues. In addition, preferential intracellular loading of boron into tumor cells is essential because of the short range of the fission fragments produced by BNCT. Researchers at the College of Pharmacy have developed *in vivo* and *in vitro* assays to evaluate boron pharmacokinetics and distribution in normal cells and tumor cells after exposure to selected boron-delivery compounds. Concurrent investigations also evaluate potential cytotoxicity of these compounds on normal cells and tumor cells. These studies presently target tumor systems that are typically not responsive to conventional means of cancer therapy (e.g., surgery, chemotherapy, or radiation therapy) but are possible candidates for BNCT. Melanoma, glioma, lymphosarcoma, and carcinoma tumor systems are currently being investigated for boron uptake. These studies utilize rodent tumors (tumors derived from mice or rats) to facilitate large-scale, rapid, and cost-effective experiments that can have important consequences for large animal research and for potential future human clinical trials. The well characterized, malignant BL6 variant of the B16 murine (mouse-derived) melanoma is being evaluated for boron uptake. Investigations using BL6, a highly invasive and highly metastatic tumor cell, will significantly contribute to the evaluation of BNCT for human malignant melanoma and deep-seated metastatic melanoma lesions. The incidence of melanoma is rapidly increasing and the prognosis for survival is poor due to the refractory nature of the tumor to conventional cancer therapies, emphasizing the urgent need for investigations of the effectiveness of BNCT for treating this cancer. Rat RG2 glioma tumors are used to model the potential effectiveness of BNCT for treating deep-seated brain tumors, especially invasive brain tumors which are inoperable and resistant to other treatment modalities. Murine P1798 lymphosarcoma and murine Lewis lung carcinoma tumor systems are assayed *in vivo* and *in vitro* for boron uptake to facilitate boron compound formulation by other INEL BNCT researchers. These tumor systems grow rapidly *in vitro* and *in vivo* and are well vascularized and "fatty" in appearance *in vivo*. Liposomal and low density lipoprotein boron-delivery vehicles have been tested in these murine tumors. Future *in vivo* and *in vitro* assays will be expanded to encompass different tumor models; such as canine and human tumors in nude or immunocompromised mice. Studies utilizing these latter tumor systems will provide valuable preliminary data to guide both large animal and human studies.

Boron compounds and delivery vehicles screened in assays are those which theoretically demonstrate most potential for BNCT. BPA is one such compound. BPA was originally synthesized as a melanin precursor and phenylalanine amino acid analog. BPA is used as a screening reference in melanoma investigations, since phenylalanine is required by melanoma cells as a precursor for

both protein synthesis and melanin production. BPA has been extensively studied and characterized in clinical trials in Japan and pharmacokinetic trials in the U.S. and Australia. Liposome and LDL boron delivery mechanisms are also being evaluated in current investigations. Both of these delivery vehicles preferentially target well-vascularized tumors with short replication or generation times. These tumors have greater requirements for membrane components (e.g., fatty acids) than do tumors and normal tissues which are slower growing. Liposomes and LDLs provide those membrane components and, therefore, should preferentially accumulate in these faster growing tumors. Evidence that liposomes and LDLs are selectively targeted to tumors has been previously reported in the scientific literature.[7-30] For example, the preferential delivery of several conventional chemotherapeutic drugs—such as adriamycin or doxorubicin—to tumors is enhanced after liposomal encapsulation of the chemotherapeutic drug compared to free or unencapsulated drug.

Using the tumor systems described above, the *in vivo* and *in vitro* studies of this project utilize up-to-date tissue culture technologies and small animals—primarily mice—to screen and compare boron compounds and boron-delivery vehicles for preferential uptake into tumor tissue and to determine cytotoxicity of these compounds on normal and tumor tissues. Prior to screening boron compounds *in vivo* and *in vitro* for uptake by tumor cells, compounds are also tested *in vitro* for cytotoxicity against normal cells and tumor cells. Compounds that are cytotoxic to normal cells *in vitro* may also be cytotoxic to normal tissues *in vivo*, with subsequent detrimental effects to the host, which could negate any beneficial effects of BNCT. For *in vitro* cytotoxicity assays, cell cultures are exposed to increasing concentrations of boron compounds. After incubation with the compound, cell viability and numbers are monitored by one of two standard tissue culture methods: (a) trypan blue exclusion or (b) 3-[4,5-dimethylthiazole-2-yl]-2,5-diphenyltetrazolium bromide; thiazolyl blue (MTT)-dye reduction, during which living cells convert tetrazolium into a blue formazan product which is measured spectrophotometrically at 570 nm. *In vitro* cytotoxicity assays have recently been initiated and indicate no cytotoxicity for boron compounds subsequently screened *in vitro* and *in vivo*. For *in vitro* screening assays, boron compounds are added to confluent cultures of tumor cells. Cultures are subsequently harvested in triplicate 6, 12, and 24 hours later and analyzed for boron by ICP-AES. Results of these *in vitro* screening assays are pending.

For *in vivo* assays, boron compounds are currently screened in specific-pathogen-free, female mice. Mice are inoculated subcutaneously into the dorsal hip with 1-2 million tumor cells. Approximately, 1-2 weeks later, unanesthetized tumor-bearing mice are inoculated with 200 µL of boron compound into either the dilated tail vein or intraperitoneally. Optimal routes of boron administration (intravenous, intraperitoneal, vs oral delivery and multiple dose injections) will be evaluated in future assays. Following injection of boron compound, mice are sacrificed through a 72-hour time interval. At each time point, tissues are collected and analyzed by ICP-AES for boron content by other INEL BNCT researchers. Collected tissues include tumor, blood, liver, spleen, brain, muscle, kidney, and skin. Of particular interest are tumor boron levels and tumor-to-normal tissue boron ratios. The animal model (e.g., mouse, rat, immunocompromised mouse or rat) used in *in vivo* assays will change for future assays depending on the tumor system. Two to three routine *in vivo* boron-delivery assays are conducted each month. Each of these assays involves approximately 50 animals, 6 animals per time point. For selected compounds, attempts are made to preferentially enhance boron uptake by the tumor versus adjacent normal host tissues—for example, by short-term phenylalanine and tyrosine deprivation.

BPA Screenings

Researchers at the WSU College of Pharmacy have shown that selected boronated compounds do accumulate both *in vitro* and *in vivo* in tumor cells. Several of these compounds accumulate to therapeutic levels for BNCT or to levels that are comparable to, or higher than, those previously

reported in the scientific literature. *In vitro* uptake of boron by BL6 melanoma cells increases with increasing levels of BPA (Figure 14). Data indicate that this uptake may be enhanced by restricting two amino acids, tyrosine and phenylalanine. Tyrosine and phenylalanine can be restricted *via* medium formulation for *in vitro* assays, *via* diet for *in vivo* assays, or enzymatically with the enzyme PAL for both *in vitro* and *in vivo* assays. When BL6 is cultured *in vitro* in medium formulated with low levels of tyrosine and phenylalanine, boron uptake is dramatically increased (Figure 15). This increased uptake is not due to any growth modulatory effects of BPA, since growth is generally not affected by exposure of BL6 to exogenous BPA in either normal medium or medium restricted in tyrosine and phenylalanine (Figure 16). Rather, in theory, this increased boron uptake by BL6 melanoma cells is because these tumor cells are "starved" for phenylalanine. Once exposed to phenylalanine in the form of BPA, these "starved" or restricted cells rapidly accumulate BPA, thus increasing tumor-associated levels of boron.

In vitro incubation of BL6 cells with PAL 1–4 hours prior to exposure to BPA has also been investigated as another mechanism to enhance boron uptake via tyrosine and phenylalanine restriction. PAL is an amino acid degrading enzyme which catalyzes the deamination of phenylalanine to cinnamic acid and tyrosine to coumaric acid. Experiments indicate that levels of phenylalanine and tyrosine in culture medium are reduced by PAL and that BPA is not degraded by this enzyme (Figure 17). *In vitro* growth of BL6 is normal after exposure to 0.025 units of PAL. Analysis by ICP-AES of boron uptake by these cells is pending.

Beron also accumulates *in vivo* in tumor tissue after intraperitoneal injection into mice of 750 mg BPA/kg body weight as a slurry (Figure 18). Tumor levels of boron approach 2.5 µg B/g tumor at 6 and 12 hours postinjection. When mice are inoculated intravenously into the dilated tail vein with 100 µg BPA/mL of physiological saline, boron levels in the tumor averaged 0.8 µg B/g tumor 6 and 12 hours postinjection (Figure 19). Present investigations are continuing to evaluate different routes of boron delivery (e.g., intraperitoneal versus intravenous). For BPA, these studies are important since the solubility of BPA has been dramatically increased by dissolving the compound in 0.5 M Tris buffer, which has been shown in *in vivo* studies to be nontoxic. In Tris buffer, College of Pharmacy researchers have shown that 10 mg/mL of BPA can be dissolved, compared to 0.1 mg/mL in water or saline, a 100-fold increase. College of Pharmacy researchers further hypothesized that this *in vivo* boron accumulation into tumor tissue could be enhanced by restricting tyrosine and phenylalanine in the diet or by using PAL to reduce free phenylalanine and tyrosine in the plasma of tumor-bearing mice. Initial studies indicated that tumor levels of boron are not greater in mice fed a diet low in tyrosine and phenylalanine compared to tumor levels in mice fed a normal diet. However, due to inconsistencies in the low tyrosine and phenylalanine diet, this experiment has been repeated and will be re-evaluated. To determine the effect of pretreatment with PAL on *in vivo* boron uptake by tumor tissue, tumor-bearing mice were injected intravenously into the dilated lateral tail vein with 1–4 mg of BPA dissolved in 0.5 M Tris buffer. One half of the mice were pretreated intravenously with PAL (0.2 units/mouse) one hour prior to BPA injection. Tissue and blood samples were collected 6 and 24 hours after BPA injection. Blood amino acid analyses indicate that phenylalanine and tyrosine are 23% and 18%, respectively, lower in PAL-treated mice compared to untreated mice. BPA did not interfere with these amino acid analyses. More importantly, results indicate that PAL pretreatment does enhance uptake of boron into tumor tissue (Table 4). Further experiments have been conducted to optimize PAL-modulated BPA uptake. Results of these studies are pending.

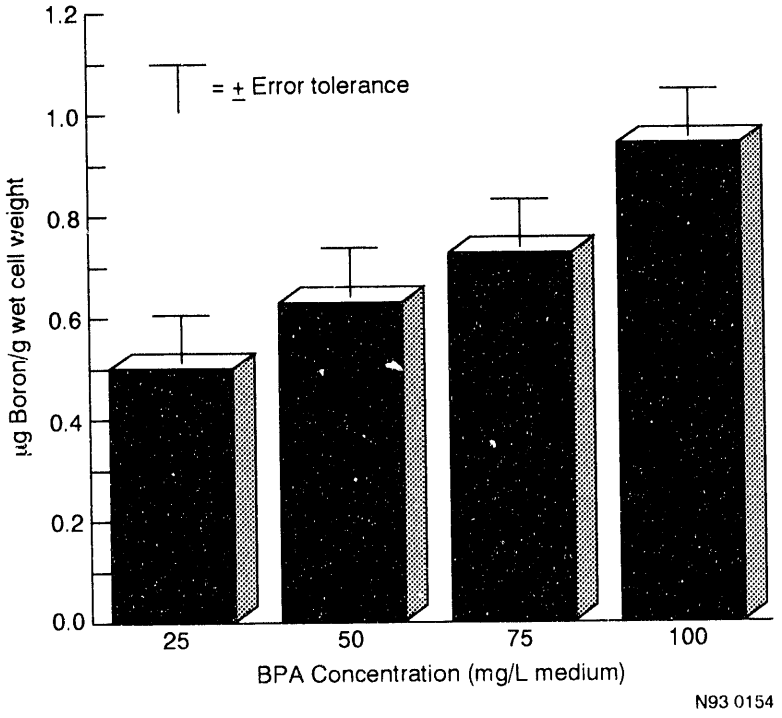

Figure 14. *In vitro* uptake of boron by B16-BL6 murine melanoma cells exposed for six hours to increasing concentrations of BPA in the culture medium.

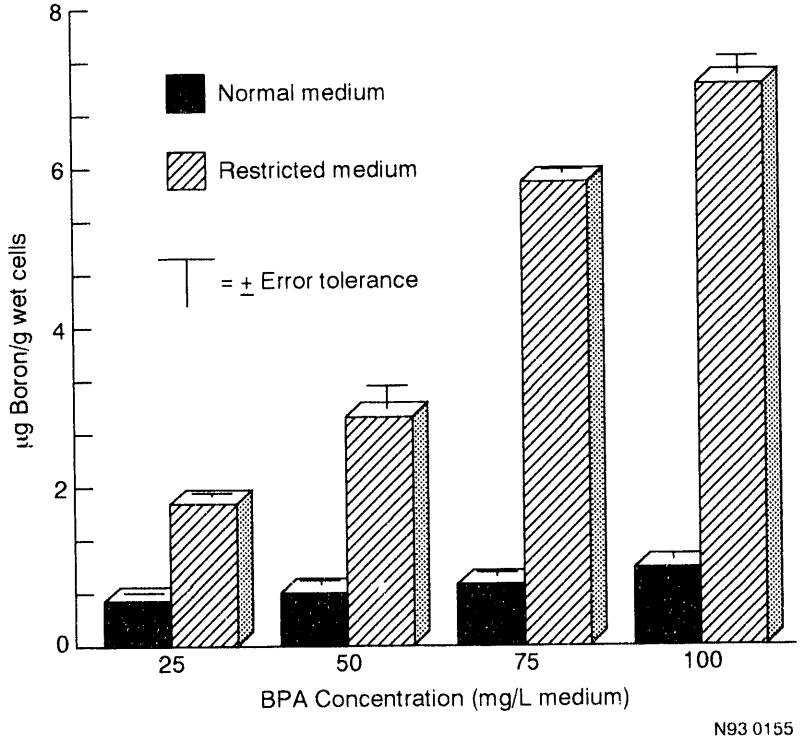

Figure 15. *In vitro* uptake of boron by B16-BL6 murine melanoma cells cultured in medium formulated with normal or low levels of tyrosine and phenylalanine and exposed to increasing concentrations of BPA.

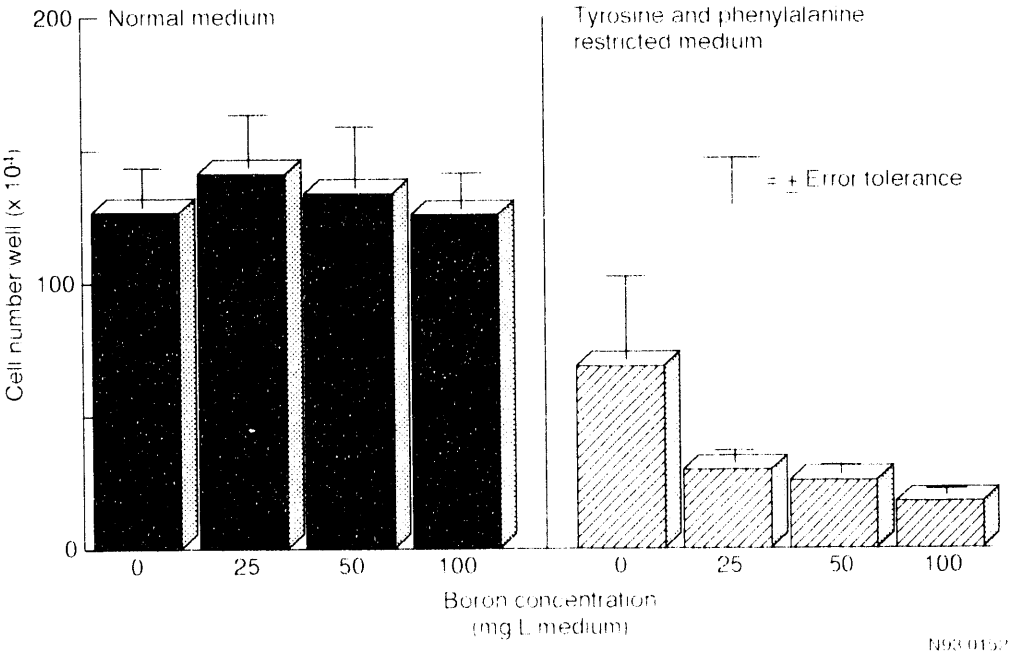

Figure 16. Growth of B16 BL6 murine melanoma cells on day five of *in vitro* culture with increasing concentrations of BPA in culture medium.

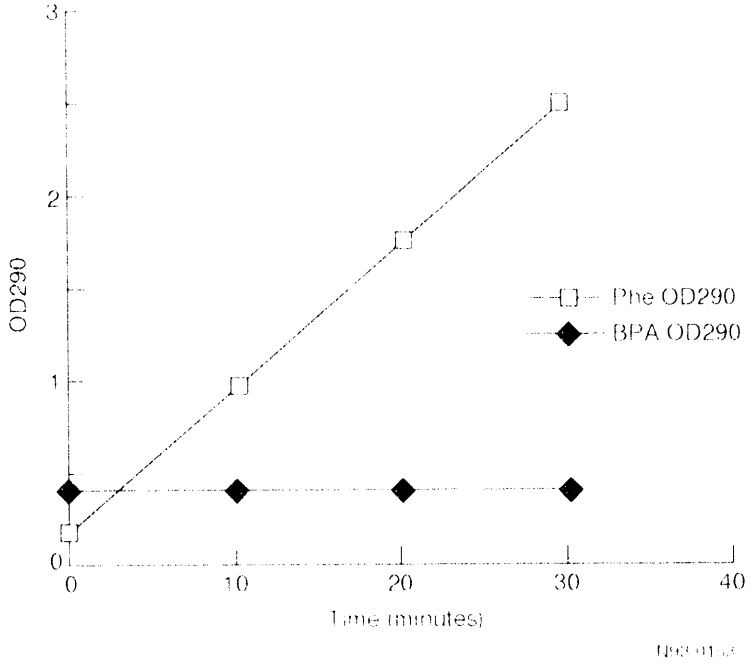

Figure 17. PAL enzymatic activity against Phe and BPA.

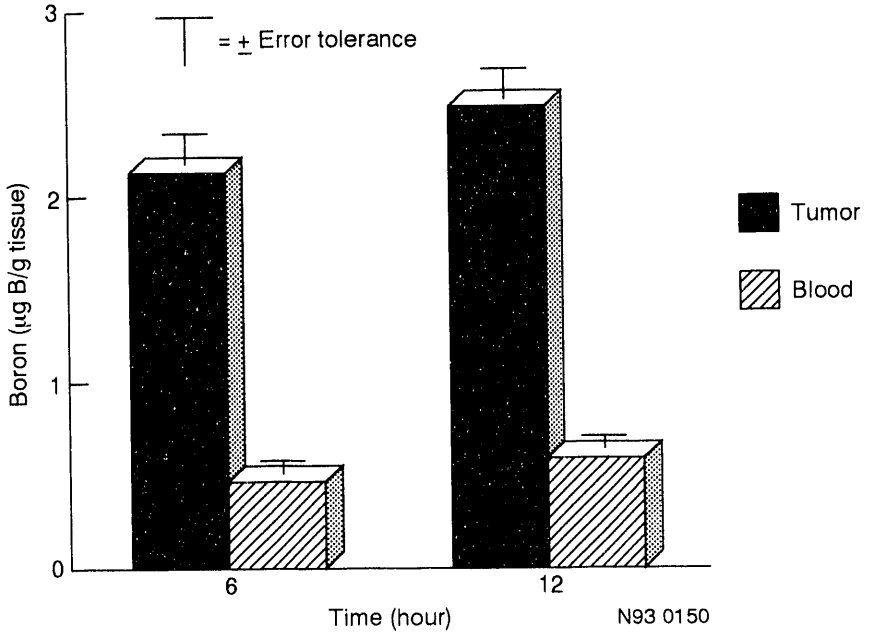

Figure 18. Biodistribution of boron 6 and 12 hours after intraperitoneal injection into mice of BPA.

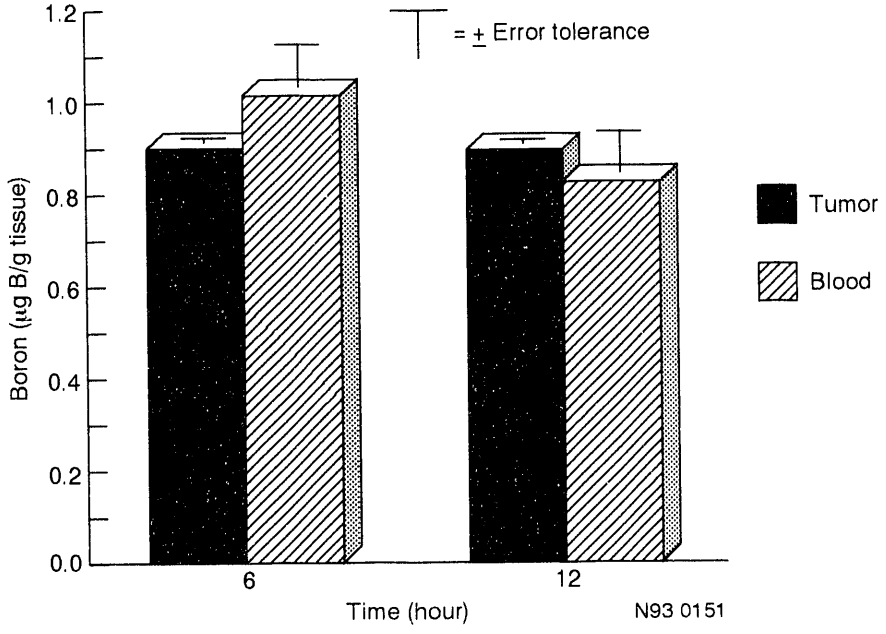

Figure 19. Biodistribution of boron 6 and 12 hours after intravenous injection of 200 µL of BPA into the dilated lateral tail vein of unanesthetized mice.

Table 4. Effect of PAL on tumor levels of boron.

Treatment	Tumor Levels of Boron (μg B/g tumor tissue)
1 mg BPA	
without PAL	1.2 ± 0.42
with PAL	2.9 ± 0.52
4 mg BPA	
without PAL	4.6 ± 0.84
with PAL	6.5 ± 0.56

Radiolabeled Screenings

Research with radiolabeled boron compounds supports observations using ICP-AES analysis that boron does accumulate *in vivo* in tumor tissue. Peak accumulation of an ^{125}I-labelled borovaline compound in subcutaneous BL6 melanoma tumors occurs 2 to 6 hours after intraperitoneal injection of the radiolabeled compound into mice (Figure 20). Tumor:brain and tumor:muscle radioactivity ratios average 10:1 and 2:1, respectively. Since the ^{125}I label/boron relationship on the compound is stable, these ratios of radioactivity in tissues may be extrapolated to ratios of boron in the same tissues. Interestingly, this boron compound is an elastase inhibitor with demonstrated anti-metastatic activity against BL6. Parallel experiments with radioactively labelled and nonradioactive compounds are being planned to correlate radioactive kinetics with boron kinetics.

Experiments of this nature using radiotracer technologies will prove valuable in determining boron pharmacokinetics and will facilitate data collection.

Liposomal and LDL Screenings

The effectiveness of liposomal and LDL delivery of very low doses of boronated compounds to tumors has also been investigated. Delivery of low doses of these compounds minimizes potential cytotoxic effects of these compounds on normal tissues and may facilitate future experiments investigating alternative delivery protocols. These compounds are synthesized by INEL BNCT researchers at UCLA and UCSF and provided to researchers in the College of Pharmacy, for *in vitro* and *in vivo* screening. Following intravenous injection of liposomal-encapsulated boron compounds into tumor-bearing mice, boron accumulation in subcutaneous BL6 tumors typically reaches maximum levels within 24 hours postinjection with concentrations approaching values reported in the scientific literature. A typical *in vivo* assay of a liposomal-encapsulated compound screening with BL6 is represented in Figure 21. Boron levels in the blood are rapidly cleared. Tumor boron levels plateau at approximately 10 μg B/μg tumor. Tumor-to-normal (e.g., muscle, brain) tissue ratios generally range from 5:1 to 11:1 in these assays against BL6. Two liposomal-encapsulated boron compounds have reached subtherapeutic levels *in vivo* in BL6 melanoma: $Na[Co(C_2B_9H_{10}SH)_2]$, 18 μg B/g tumor at 6 hours postinjection, and $Na_2B_{10}H_9NCO$, 22 μg B/g tumor at 24 hours postinjection. Liposomal delivery of low doses of boron has also been investigated with other tumor systems. Boron levels in tumor tissue obtained from mice bearing P1798 lymphosarcoma tumors range from 11-32 μg B/g tumor tissue at 6-12 hours postinjection of liposomal-encapsulated boron compound. Histopathological evidence indicates that the P1798 lymphosarcoma is not a localized tumor when implanted subcutaneously into the dorsal hip of the mouse, but rather spreads to the lymphatic system and other organs. These observations necessitated reevaluation of the P1798 lymphosarcoma tumor system for use in *in vivo* screening assays. Use of the P1798 lymphosarcoma for chemical compound formulation is not excluded. Liposomal-encapsulated boron compounds are presently being screened *in vivo* in murine Lewis lung carcinoma.

Experiments investigating LDL delivery of very low doses (~80 μg B/g) of boronated compound have just recently been undertaken. Preliminary results indicate that maximum levels

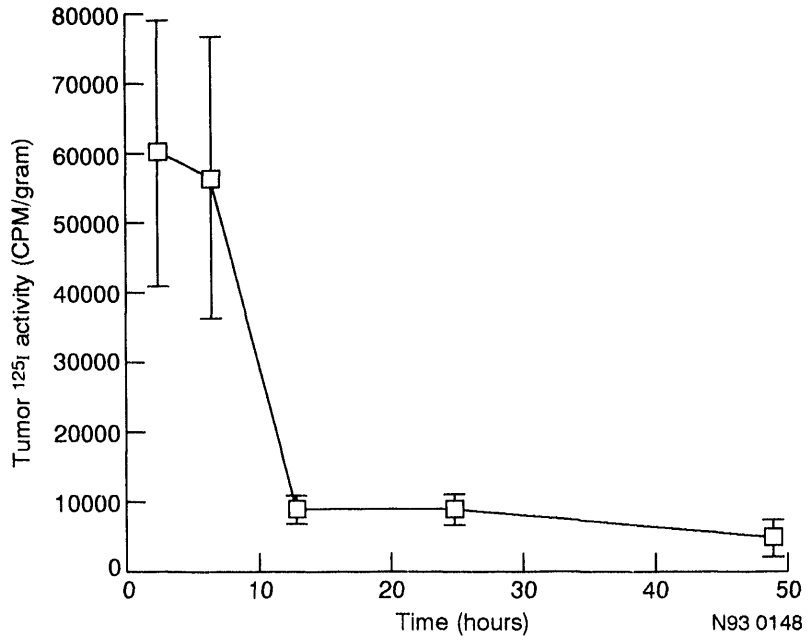

Figure 20. Radioactivity levels in tumor tissue through time after intraperitoneal injection of an ^{125}I-labelled boron compound.

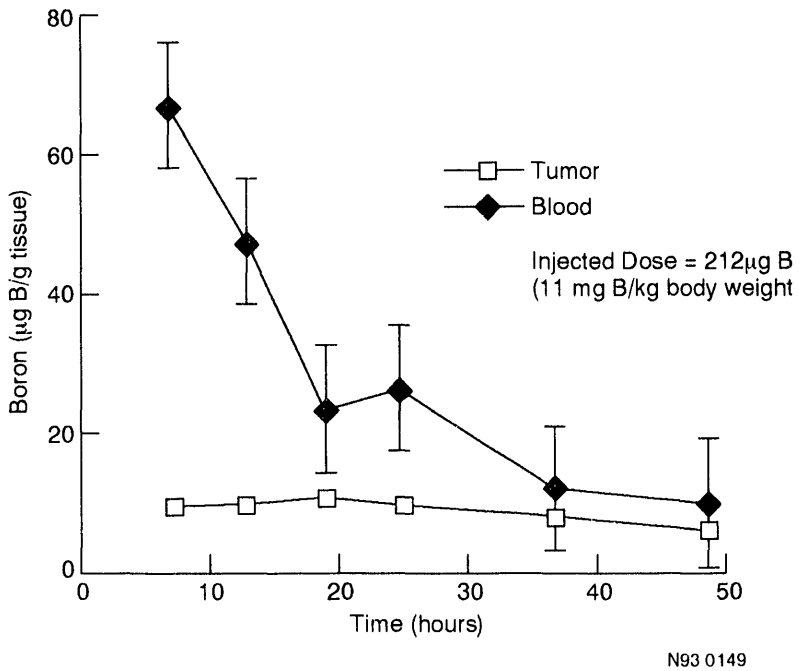

Figure 21. Biodistribution of boron in tumor and blood after intravenous injection of 200 µL of liposomal-encapsulated $Na_2n\text{-}B_{20}H_{18}$.

of boron accumulate in tumor tissue 6 hours post-injection of compound. Tumor levels of boron range from 3-5 μg B/g tumor tissue. These initial results demonstrate *in vivo* LDL delivery of boron to tumor. Present efforts are being directed to optimize the experimental protocols for these LDL-boronated compounds.

Efforts to enhance *in vivo* uptake of these liposomal-encapsulated and LDL-associated boron compounds are in progress. Currently, two approaches are being explored: (a) pretreatment of mice with buffer-containing liposomes to block uptake of boron-containing liposomes by the reticuloendothelial system (i.e., spleen and liver) and (b) multiple administration of boronated compounds. The impact of macrophages and parenchymal cells, primarily in liver and spleen, on liposomal and LDL degradation and kinetics is being investigated. These cells may significantly interfere with boron localization in tumor tissue. Groups of tumor-bearing mice have been pretreated intravenously with buffer-containing liposomes prior to intravenous injection with boron-containing liposomes. These buffer-containing liposomes should be scavenged by the macrophages and parenchymal cells and occupy binding sites in the liver and spleen—thus, allowing the boron-containing liposomes to selectively target the tumor. Current data are inconclusive and experiments are planned to investigate whether liposome composition and size can be manipulated to maximize blocking of binding sites in the liver and spleen. College of Pharmacy researchers have also noted that multiple injections of liposomal-encapsulated boron compound can dramatically increase tumor boron uptake. These observations indicate that an optimum point for a second injection of compound is the 18-hour time point. In one preliminary experiment, P1798 lymphosarcoma-bearing mice receiving intravenous injections of $Na_3B_{20}H_{17}NH_3$ at 0 hours and at 18 hours had tumor boron concentrations averaging 41 μg B/g tumor tissue 72 hours after the initial injection (Figure 22). Similar mice receiving only one injection at 0 hours had tumor boron levels averaging only 10-15 μg B/g tumor tissue at 72 hours. Studies are currently underway to optimize this protocol.

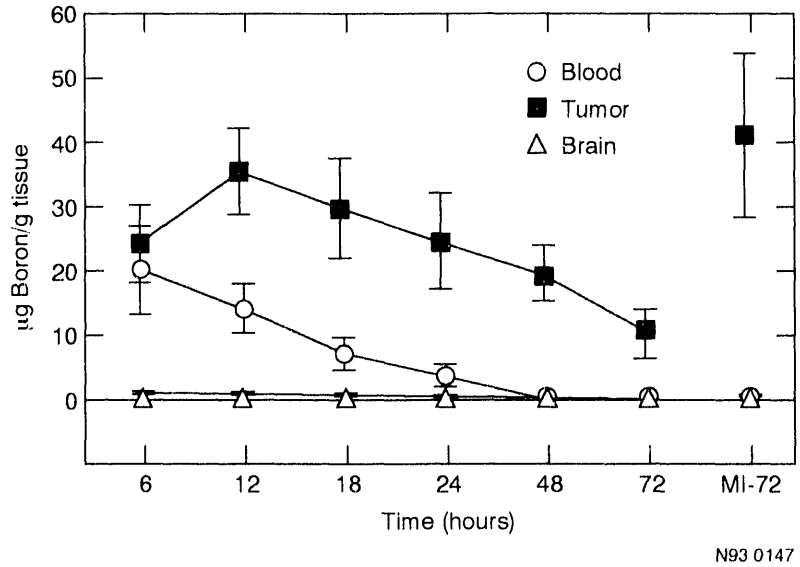

Figure 22. Biodistribution of boron in tumor, blood, and brain after intravenous injection of 200 μL of liposomal-encapsulated $Na_3B_{20}H_{17}NH_3$.

In conclusion, in collaboration with other INEL BNCT researchers, researchers at the WSU College of Pharmacy have developed *in vitro* and *in vivo* assays which utilize current *in vitro* technologies and small animals (mice) to determine the effectiveness of boron compounds for BNCT. These studies are critically evaluated to maximize the potential of these assays, continually improved and perfected, and are necessary before more costly and time-consuming large animal studies and human trials are conducted. Efforts are also targeting alterable factors which may enhance selective uptake of boron into tumor cells to optimize BNCT. Identification of these factors along with the most promising boron compounds will have a significant impact on therapy of cancer using neutron capture.

PHARMACOLOGY AND TOXICOLOGY OF BORON DELIVERY AGENTS

Dr. Tom LaHann, PI, Idaho State University, College of Pharmacy

The Approach to Safety Testing

For BNCT to be a useful cancer treatment, it must be effective and reasonably safe. The need for safety highlights two requirements: (a) to identify all undesirable side effects that can occur with the therapy, and (b) to predict the likelihood that these side effects will occur with a given BNCT treatment protocol. Very little is known about the toxicities associated with boron delivery agents being considered for BNCT. To correct this deficiency, researchers at ISU are developing a tiered, toxicity evaluation program to identify and evaluate the side effects associated with new and existing boron delivery drugs. This program is flexible enough to apply to all new drug candidates for BNCT. It is time and cost effective, and it will be comprehensive, so that there will be a high probability of identifying all clinically important side effects.

Before new boron delivery drugs can be tested in people, the Federal government requires that there be animal data predicting a socially acceptable benefit-to-risk ratio for the intended use. The goal of the toxicity program is to provide such data. Therefore, the program's objectives include:

1. Characterizing the toxicity profile of promising boron delivery compounds in animals to predict which compounds are safe enough to allow clinical evaluation. This characterization includes:

    a. Identifying all major adverse effects that can be elicited by the boron delivery drugs.

    b. Predicting which toxicities are likely to occur under anticipated conditions of clinical use.

2. Identifying the toxicities that preclude the use of otherwise promising boron delivery agents.

To achieve these objectives, the ISU program will use gross and histopathology studies of tissues, clinical chemistry and hematology to gather clues to possible drug-induced functional deficits. The main program emphasis is on evaluation of organ system function and understanding the mechanisms underlying any drug-induced functional defects. Understanding how the toxicities occur will aid in risk assessment and determining the potential for antidote therapy. A knowledge of the chemical's pharmacokinetic profile and metabolism is also necessary to interpret the results of toxicology testing. Pharmacokinetic and metabolic data need to be collected in parallel with toxicity data because a drug's absorption, distribution, metabolism and elimination can vary between species or even within a species as the dose changes. These changes influence the magnitude and even the nature of a drug's toxicities.

The results of animal studies are an accepted means of predicting probable human risk. At least two, and in some cases three, species will be used in toxicity tests: rat, rabbit, and dog. Rats are used for the initial studies because they are relatively cheap and readily available, and because there is a large database of historical information about rats. Drugs are also evaluated in rabbits to reduce the chance of being misled by species specific effects. Drugs which appear to be safe in rats and rabbits may also be tested in dogs. Comparison of rat, rabbit, and dog data indicates how well key findings of the small animal toxicity program apply to the large animal efficacy model (dog).

To frame the significance of any observed toxicities, there must be a standard for comparison. Two boron delivery drugs are currently being used as standards—BSH and BPA. BSH is a boron delivery drug being developed for BNCT for brain cancer, while BPA is a boron delivery drug being developed for BNCT for malignant melanoma. Since a detailed knowledge of the

toxicity profile of the standards is required, these chemicals are currently being evaluated to determine if their intravenous administration causes gross or microscopic tissue alterations or gross alterations of behavior. Because new boron delivery drugs will be tested to determine their ability to alter organ system function, BPA and BSH are also being evaluated for evidence of any alteration of organ system function. Current emphasis is on evaluation of cardiovascular and pulmonary function indicates that both BSH and BPA can impair the functioning of these two systems.

To maximize its cost-effectiveness, the toxicology program uses a tiered testing approach. As each tier is completed, the data is evaluated to determine if the results justify the next tier of testing or if compound development should be terminated. Toxicity data is acquired from a five tiered system that is still under development. The purpose of each of the five tiers is outlined below:

Tier 1: Estimate the maximum tolerated dose (MTD) that can be given to healthy mammals by intravenous injection and identify the limiting toxicities associated with larger doses. The maximum tolerated dose is defined as the largest dose not producing any observed, biologically significant effects in 75% of the treated animals. Testing involves gross and microscopic evaluation of tissues, and an evaluation of function. Which functions are evaluated depends, in part, upon the results of the tissue examination.

Tier 2: Estimate the MTD that can be given repeatedly to healthy mammals over a standard (14 day) period and identify the limiting toxicities associated with larger doses. A limiting toxicity is defined as an undesirable biological effect limiting or preventing therapeutic use.

Tier 3: Evaluate the function of organ systems suspected of being particularly susceptible to damage. Available data indicate a need to evaluate:

- Neurotoxic potential
- Cardiovascular and pulmonary function
- Hepatic and renal function
- Gonadotoxic potential
- Possible cutaneous reactions
- Possible alterations of mineral metabolism

Tier 4: Evaluate organ system function in physiologically impaired animals. Toxic insult that only damages "functional reserve" may not be apparent in young, healthy mammals, yet may be of major concern when expressed in older or sick mammals. The "physiologically impaired" animals will mimic physiological problems commonly observed in cancer patients.

Tier 5: Characterize toxic reactions associated with neutron radiation of mammals administered maximum tolerated doses of boron delivery drug to determine if significant but unanticipated toxicities associated with radiation/boron interactions arise in normal tissue during the post-irradiation period.

The Toxicity of BSH

Clinicians around the world are testing the value of BSH-mediated BNCT as a treatment for glioblastoma multiforme and other high mortality type brain cancers. The value of BSH as a boron delivery agent has already been demonstrated in animal models and promising results have been obtained in clinical studies underway in Japan. Despite the widespread interest in BSH as a boron delivery drug, there is little known about its toxicity.

Clinical experience to date has identified few adverse effects associated with intravenous infusion of BSH, but few patients have received BSH doses greater than 100 mg/kg.[31] Patients receiving higher doses of BSH have experienced undesirable side effects and at least one patient died after receiving BSH, although a causal link between the drug administration and death has not been established. The few animal toxicity

studies available indicate that high doses of BSH cause hepatic and renal necrosis, induce erythrocyte aggregation and cause skeletal muscle paralysis and respiratory arrest.[32,33] Intravenous administration of BSH has been reported to kill rabbits at doses as low as 24 mg/kg, but there are also reports that rabbits and other species tolerate IV infusions of large amounts of BSH (e.g. 600 mg/kg).[34,35]

Over the last year, researchers at ISU have been investigating the toxicity profile of BSH as part of an effort to develop a comprehensive safety evaluation program for testing new boron delivery agents. Toxic effects of BSH (200-750 mg/kg delivered by intravenous infusion to Long-Evans or Sprague-Dawley rats) have been characterized. As a first step toward identification of the MTD, researchers determined the largest dose that could be administered by intravenous infusion without killing the test animal. Lethality following acute intravenous administration of drug can be influenced by dose-rate of administration, physiological state of the animal, vehicle, osmolarity of the infusion solution and volume-rate of administration. Studies now indicate that over the range of parameters examined, the volume-rate of administration failed to dramatically change the dose of BSH that caused death. Interpretation of the effect of dose-rate of administration is more complex. A dose of 200 mg/kg BSH was not toxic by bolus injection or by infusion, while a dose of 625 mg/kg was equally toxic (and lethal) when administered as a bolus injection (200 mg/kg/min) or at different infusion rates (28, 7 or 1.7 mg/kg/min). A dose of 550 mg/kg was equally toxic when infused at rates of 200, 28 or 7 mg/kg/min, but was markedly less toxic when administered at a dose rate of 1.7 mg/kg/min. Whether BSH was dissolved in distilled water or phosphate buffered saline made little difference, and BSH-induced changes in systemic osmolarity did not explain the observed lethality. In fact, animals infused with equal volumes of osmotically equivalent vehicle never died during the 7-day observation period. The physiological state of the animal did seem to dramatically influence BSH toxicity. Conscious animals tolerated BSH better than did anesthetized rats, and anesthetized rats instrumented for measurement of cardiovascular and pulmonary function were much more sensitive to BSH's toxic effects than were anesthetized, non-instrumented rats. Instrumented rats usually died when BSH doses of 275 mg/kg were infused. In anesthetized but non-instrumented rats, intravenous infusion of 550 mg/kg BSH usually resulted in death and infusion of doses greater than 375 mg/kg occasionally resulted in death. In conscious rats, intravenous infusion of 550 mg/kg occasionally resulted in death, while 675 mg/kg usually resulted in the death of the animal. Current clinical protocols call for dosing patients with up to 200 mg/kg BSH. Until the significance of the animal results are better understood, researchers at ISU advise against this.

At the higher BSH doses, death often occurred within six hours of infusion. This rapid onset suggested a drug-induced impairment of either the cardiovascular or pulmonary systems and prompted investigations of cardiovascular and pulmonary function. Pulmonary parameters (rate, flow and tidal volume) were little effected by BSH until just prior to death. Respiratory depression did not appear to be a primary cause of BSH-induced death, since artificial respiration was not an effective antidote. Cardiovascular parameters were rapidly and substantially altered by BSH administration. Blood pressure, heart rate, cardiac contractility and cardiac output initially increased, but then gradually declined until death intervened. Total peripheral resistance began a slow but marked increase shortly after the BSH infusion was initiated. After infusion of 250-300 mg/kg, significant ventricular arrhythmias were noted and continued infusion exacerbated these arrhythmias. The worsening of the arrhythmias correlated with the decline in cardiac output and the precipitous fall in cardiac stroke output seemed to be immediately preceded by ventricular fibrillation. Thus, intravenous infusion of high doses (>550 mg/kg) of BSH caused death secondary to cardiovascular collapse.

Intravenous administration of BSH doses of 375-500 mg/kg were more often associated with delayed death, the animals not succumbing until 1–4 days post-infusion. The delayed time-to-death associated with these lower doses seems to argue against cardiovascular failure or respiratory

arrest as a direct cause of death. Animals appeared to be edematous, had low urine output, and at autopsy, displayed enlarged kidneys. Histopathology confirmed the presence of renal necrosis and indicates a need to evaluate renal function to determine if BSH has a direct toxic effect on the kidneys. Renal failure secondary to cardiogenic shock was suspected, but to date, anti-shock therapy has failed to ameliorate the BSH-induced lethality.

Researchers have noted that the odor of BSH differs from lot to lot and there is concern that this might reflect differences in the amount or nature of contaminants present, which might influence the observed safety profile. Available data is inconclusive regarding possible lot differences in toxicity, but this is felt to be an important area for future investigations.

To summarize:

- Relatively few studies have evaluated the toxicity of BSH and the assumption of human safety seems to be based largely upon the lack of significant toxicities observed in the clinical studies to date. However, clinical experience with the drug is limited and absence of evidence is not the same as evidence of absence, so the impression of clinical safety may be false. Animal studies warn of probable human toxicity at higher BSH doses. The rat data clearly demonstrate that BSH can induce significant, life-threatening toxicities. The key question, that cannot yet be answered, is: How probable is it that clinically efficacious doses of BSH will induce significant toxicities?

- Studies in rats demonstrate that intravenous infusion of BSH can induce sudden death secondary to cardiovascular collapse. Three dogs dosed with BSH at 100 mg B/kg have died suddenly and unexpectedly, apparently due to infusion of BSH. The rat data offers a possible explanation for the death of these dogs, that is, death from BSH-induced cardiovascular collapse.

- The dose-rate of administration seems to be an important determinant of the toxicity of high, but not lethal doses of BSH. The exact relationship between dose-rate of administration and toxicity is complex and requires additional study.

- BSH exerts an initial, positive inotropic effect on the myocardium, followed by myocardial depression. Additional studies are needed to determine if BSH is acting directly on the heart or stimulating neural reflexes.

- The greater sensitivity of instrumented rats to BSH suggests that stress may render rats more susceptible to the toxic effects of BSH. If this is indeed the case, it may mean that cancer victims, who are under more physiological stress than healthy adults, may be more susceptible to the toxic effects of BSH.

The Toxicity of BPA

Because BPA is poorly soluble in most aqueous formulations, it is difficult to deliver enough drug via the intravenous route to precipitate an acute toxic episode. Intravenous infusion of 102 mg/kg BPA (6 mg/mL in pH 7.4 phosphate buffered saline) administered over a one hour period (at a rate of 17 mL/kg/hr) into urethane anesthetized, male, Sprague-Dawley rats did not consistently elicit treatment-related changes in cardiovascular function. However, in open-chest, artificially ventilated rats, this dose of BPA sometimes elevated cardiac output, stroke output and blood pressure. In two instances, after termination of the infusion, BPA elicited cardiovascular lability, with rhythmic oscillations of stroke output, cardiac output and blood pressure (Figure 23). Lability spontaneously dissipated and cardiovascular function returned to normal within an hour. A similar response was observed in two of three beagle dogs infused with BPA/cyclodextrin formulations. These apparently rare instances of BPA-induced lability may indicate the existence of subpopulations of animals particularly sensitive to the effects of BPA.

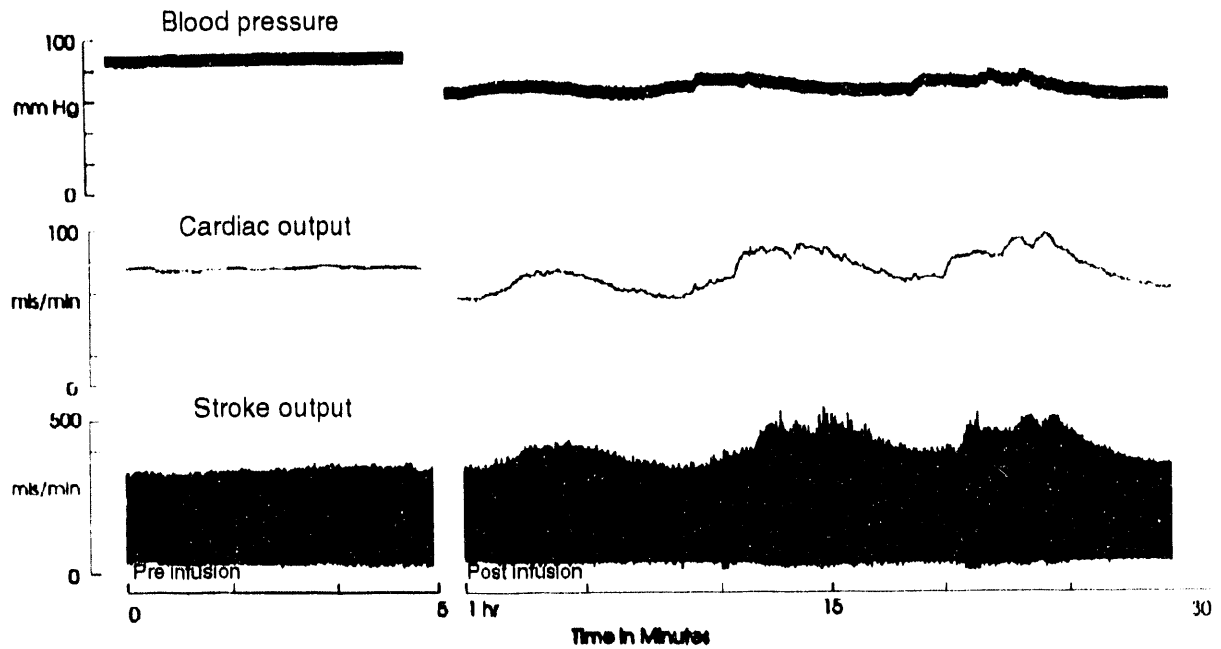

Figure 23. BPA elicited cardiovascular lablity in an open-chest, artificially-ventilated rat.

Expanding the work of Yoshino et al.,[36] ISU researchers found that BPA's aqueous solubility could be dramatically enhanced by complexing it with fructose. Using fructose as a complexing agent and manipulating pH, aqueous solutions of pH 7.4 containing approximately 170 mg BPA/mL have been prepared. This solution has been infused intravenously to anesthetized rats to deliver approximately 2,900 mg/kg BPA over a one-hour infusion period. Rats infused with this dose survived without grossly observable impairment of function if subject to minimal surgical stress, but rats infused with 4,300 mg/kg (over 3 hours) all died. Rats infused with a mannitol/fructose/water solution that mimicked the volume and osmotic load of a 4,800 mg/kg dose of BPA survived without grossly observable impairment of function, suggesting that death associated with the BPA infusion did not result from volume loading or altered systemic osmolarity.

Modeling the rat as a single, well-stirred compartment (an oversimplification), the average tissue distribution of BPA was calculated to be 1.58 mg/g, for an average tissue boron concentration of 76 ppm. For successful BNCT, tumor boron concentrations of at least 20 ppm are thought to be necessary, but higher tumor boron levels are desirable. Calculations (Wheeler et al. 1989) indicate that for a given neutron exposure, each doubling of the tumor boron concentration should increase tumor cell kill by a factor of about 10,000. Thus, even modest increases in the tumor boron concentration can dramatically improve the effectiveness of BNCT as a cancer treatment.

Artificial support of respiration failed to protect against the lethal effect of BPA, suggesting that respiratory failure was not a primary cause of death. Infusion of BPA elevated arterial blood pressure, partially as a result of the volume load infused, but BPA increased blood pressure more than did equal volumes of a control solution. After infusion of large amounts of BPA, the pressor response was followed by a gradual, sustained decline of blood pressure. Only minor changes in central venous pressure were observed. Like blood pressure, cardiac output increased during BPA infusion, but then gradually and continuously declined until the animals died. Total peripheral resistance (a measure of the extent of vascular constriction)

increased over time, possibly to compensate for the fall in cardiac output. Cardiac output and total peripheral resistance were little affected by the mannitol infusion. BPA also altered cardiac strength of contraction (left ventricular dP/dt) and heart rate. In some animals, the cardiac strength of contraction initially increased, but in all animals receiving a lethal dose of BPA, a "second phase" reduction of cardiac strength occurred. Heart rate increased over this same period, perhaps to compensate for the decrease in cardiac strength. However, immediately prior to death, heart rate decreased precipitously. Death was always preceded by ventricular fibrillation.

To summarize, the available data indicate that:

- The BPA/fructose formulation offers an easy and effective means of delivering large amounts of BPA into the systemic circulation. Tissue boron measurements indicate that intravenous administration of the BPA/fructose complex delivers large amounts of boron to tissues. Tumor boron levels achieved after intravenous infusion of BPA/fructose have not yet been quantitated.

- Over 2,000 mg/kg of BPA could usually be administered intravenously without significant cardiovascular or respiratory toxicity and without grossly observable toxicities. For most rats, BPA appeared to be a relatively non-toxic drug and on a mg/kg basis appeared to be safer than BSH.

- A small subpopulation of BPA-sensitive animals may react adversely to administration of relatively small doses of BPA. Cardiovascular lability is a particularly prominent symptom of such sensitivity.

- Infusion of large volumes of BPA/fructose is potentially toxic to the kidneys. Studies are needed to evaluate this possibility.

Future Directions

The development of the tiered toxicity test system needs to be continued. Specific tasks that need to be accomplished include:

- Development and validation of a protocol for determination of the MTD.

- Development and validation of methods to evaluate renal and hepatic function. Current methods for evaluation of cardiovascular and pulmonary function need to be refined.

- Transfer of technology for cardiovascular, pulmonary, renal and hepatic functional measurements to rabbits and dogs.

- Development and validation of pharmacokinetics and metabolism protocols that provide the necessary information for interpreting the results of toxicity testing.

In addition, the results of BSH toxicity tests indicate a need to:

- Gain a better understanding of the significance of:

  - Stress-BSH interactions. The key question is: "Are sick, old or drug-treated animals more sensitive to the toxic effects of BSH?"

  - Infusion dose-rate on toxicity. Preliminary data suggest that toxicity depends upon the total dose of BSH administered, rather than the rate at which the drug is administered. This indicates that blood levels may not predict toxicity. Since the efficacy of BNCT is a function of tumor boron levels, a clear understanding of the effect of dose-rate on toxicity should directly influence the design of clinical protocols.

- Evaluate potential antidotal therapy.

- Identify the physiological mechanisms responsible for BSH-induced delayed death.

- Confirm BSH toxicity observations in at least one additional species to avoid being mislead by possibly species-specific toxicities.

- Determine if BSH contaminants contribute to the toxicity profile ascribed to BSH. As part of this effort BSH used by the European Collaboration will be compared with that used by the U.S. Center.

Finally, the results of ISU BPA toxicity studies indicate a need to further characterize the safety profile of the BPA/fructose formulation, since it shows considerable promise as a new boron delivery system.

TREATMENT PROTOCOL DEVELOPMENT

Dr. Pat Gavin, PI, Washington State University, College of Veterinary Medicine

Research at WSU-College of Veterinary Medicine (CVM) is centered on a large animal model of the effects of BNCT. Our goal is to define treatment parameters that will ensure safe human clinical trials at a future date. The animal model used in these studies is the dog. In order to adequately define safe treatment parameters, it is necessary to establish limits of tolerance of normal tissue to BNCT as well as to determine effectiveness of BNCT in dogs with brain tumors. These studies form the focus of research begun in 1987 at the WSU under the direction of Dr. Pat Gavin, as the PI.

Canine subjects were chosen as the animal model for several reasons. Dogs have a head size closer to that of a human compared to other laboratory animals, for example rats and mice. Also, their head to body size ratio allows for selective irradiation to the head, thus reducing the dose received by other body tissues. Brain tumors occur spontaneously in dogs and occur with a frequency, tumor type distribution, and clinical course comparable to that seen in human patients. Conventional radiation therapy of these tumors in dogs indicates the animals can live for a prolonged period following treatment, making long term monitoring feasible.

One of the first important tasks was to find dogs with spontaneously occurring brain tumors. Through an extensive referral network established throughout the U.S., especially in the Northwest region, researchers at WSU have been able to identify many dogs with brain tumors. Dogs with brain tumors exhibit a variety of symptoms. The most commonly reported include seizures, circling and ataxia (or unsteady gait), and changes in attitude, although many other symptoms are possible. Definitive diagnosis of a brain tumor is made by computed tomography (CT or "CAT scan") and MRI scans. (Figures 24 and 25).

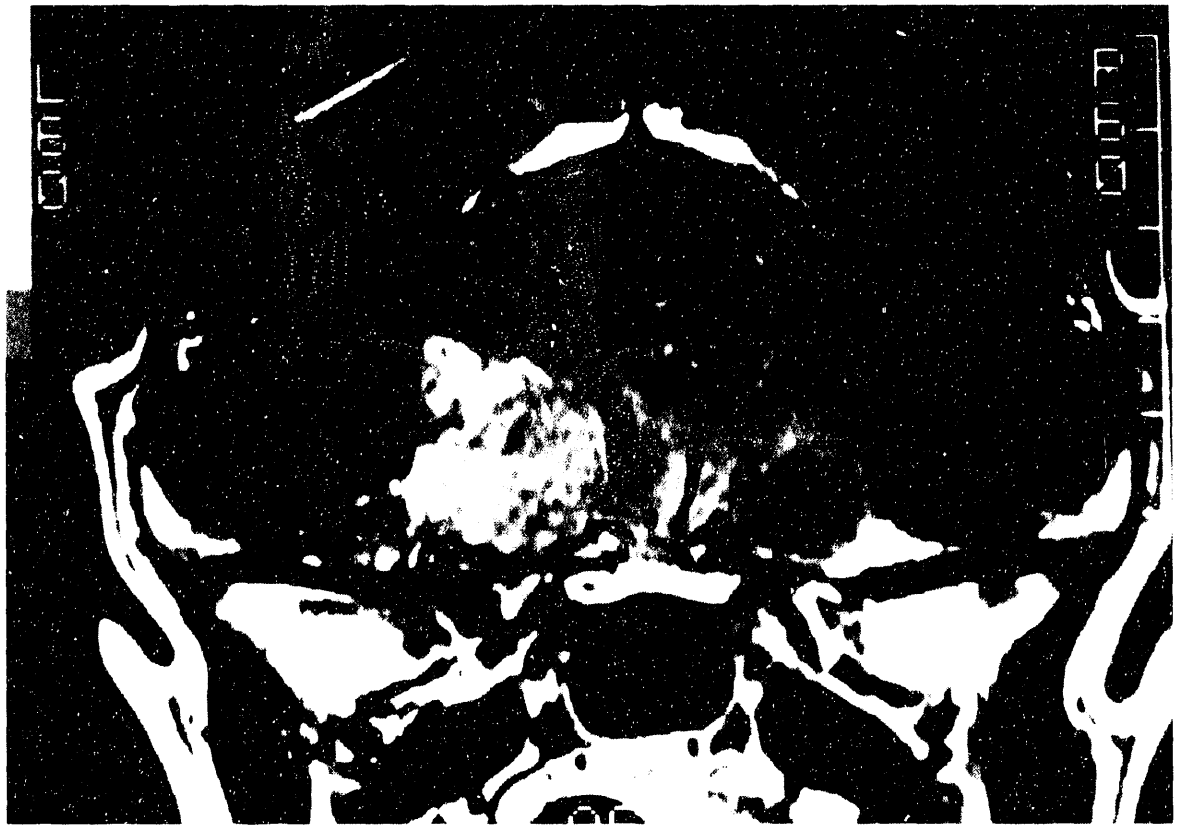

Figure 24. CT image of an intra-axial tumor located in the right temporal lobe with ring enhancement.

Figure 25. MRI of an extra-axial tumor located in the left temporal lobe.

The appearance of the tumors on these scans are characterized by their size, location, extent of uptake of a contrast agent injected intravenously, and degree of displacement of surrounding tissue.

Dogs with suspected brain tumors are referred to the project by practicing veterinarians, primarily from the Northwest, but some have come from as far away as Missouri and New York. These dogs undergo a thorough medical evaluation at the WSU Small Animal Clinic. This evaluation includes complete physical and neurological examinations, laboratory evaluation including blood work, urinalysis, and analysis of the cerebrospinal fluid (CSF) which surrounds the brain and spinal cord. In uncomplicated cases, results of these tests, except for the neurological exam, are often normal. Brain tumors can cause elevations in the protein levels in the CSF. Other laboratory abnormalities are usually due to concurrent disease or medication. CT is then performed to determine the presence of a brain tumor. If a tumor is present, or the CT is equivocal, an MRI is obtained. In WSU's experience, approximately 50% of the patients examined actually have a tumor.

After the first unsuccessful human clinical trials with BNCT in the late 50's and early 60's in the U.S., research efforts were directed toward finding more suitable boron compounds. One reason cited for the early failures was blood vessel damage and hemorrhage caused by inadequate clearing of boron from the bloodstream. In the search for a compound with the necessary characteristics of increased tumor retention and increased clearance from the blood, a potential candidate, BSH, was found. This compound has been used extensively in research at the WSU CVM.

Initial research was designed to study the way in which the body handles BSH. These pharmacokinetics studies focused on determining and comparing boron levels in the blood, tumor, and normal brain tissue. Dogs with spontaneously occurring brain tumors were given an intravenous

infusion of BSH. Several blood samples were takes during and after the infusion. At a set time following the infusion (2, 6, or 12 hours) the dogs were humanely euthanized with an overdose of barbiturate and a full postmortem exam was performed. A variety of tumor types were identified on postmortem exam. (Table 5).

Samples of the tumor, normal brain, and the blood samples were analyzed for boron content. Results of these studies showed that boron concentrations in the blood and tumor were relatively high compared to normal brain tissue and that the concentration declined at approximately the same rate in both tissues. Virtually all of the boron in normal brain can be accounted for by a 4% blood volume in the tissue. (Figure 26). These results showed that BSH provided a favorable tumor to normal brain tissue ratio with more optimal ratios being achieved shortly after the end of the infusion. Thus, there exists the potential for sparing normal brain tissue while significantly affecting the tumor. Although significant tumor retention of the boron was not seen, the recommended boron concentration per cell for effective BNCT was achieved and maintained for several hours after the infusion.

The highest boron concentrations were seen in meningiomas. These are tumors of the meninges, the tissue that covers the brain and spinal cord. They typically lack a blood-brain-barrier, a physiological barrier that excludes most substances carried by the bloodstream from the brain tissue, and have a very good blood supply. Both of these characteristics typically increase boron delivery to the tumor cells. Boron concentrations are lowest in discrete, intra-axial tumors (tumors of the brain tissue itself, such as astrocytomas) due to poor blood flow and a more functional blood-brain-barrier. The lowest concentrations were seen in the diffuse tumors where there is minimal disruption of the blood-brain-barrier.

Before treatment studies could begin, a second potential limitation had to be addressed—normal tissue tolerance to BNCT, especially brain tissue. While radiation therapy, both conventional and BNCT, can produce clinically apparent damage to the brain at high doses, lower doses can produce damage with no accompanying symptoms and which can only be detected with imaging techniques (CT and MRI). (Figure 27). These changes may be unacceptable for human treatment candidates and are the *defined endpoint for the studies*. It was necessary to determine appropriate levels of boron neutron capture radiation that were potentially efficacious without producing the subclinical changes in the brain. Using the results of Phase I and II pharmacokinetics and dose tolerance studies as guidelines, trials on dogs with spontaneously occurring brain tumors were initiated. Dogs were considered suitable candidates if their tumor was confined to the cranial vault, that is, did not involve the pituitary or the nasal cavity, and were otherwise healthy due to the multiple anesthesia episodes involved. Treatments were performed at BNL using BMRR on Long Island, NY. The first treatment was done in June 1989.

To date, 21 dogs have received BNCT and the results have been encouraging. Only a single, dorsal port treatment has been used on all cases regardless of tumor location. BNCT appears to work as well or better than conventional therapies, especially with tumors that are not meningiomas. (Figures 28, 29, 30 and 31). Survival times following BNCT are highly variable depending on the age of the animal, severity of the lesion, and clinical condition of the animal at the time of presentation and treatment. The average time of good to excellent quality of life, usually free of medication, following treatment has been eight months. Several dogs have gone over one year and one dog has been free of symptoms and off medication for over three years after treatment. However, as with more conventional modes of treatment, local recurrence of the tumor is still a problem in some cases. Future studies (Phase III) will maximize neutron delivery to the tumors.

When compared to conventional therapies for brain tumors, BNCT offers some distinct advantages. One is the one-time treatment schedule compared to multiple treatments for conventional radiation therapy. Typical treatment regimens for conventional therapy involve surgical debulking followed by fractionated radiation treatment with

Table 5. Tumor-bearing subjects in BSH biodistribution study.

Dog #	Breed	Age (yr)	Gender[a]	Tumor type
Sampled two hours after end of BSH infusion:				
20	Golden Retriever	10	M	Meningioma
39	Dachshund	13	M	Meningioma
59	Blue Heeler	11	F(s)	Meningioma
62	Schnauzer	9	M	Meningioma
67	Keeshound	6	M	Astrocytoma
70	West Highland	11	M	Fibrillary Astrocytoma
71	Pointer x	10	M(c)	Choroid plexus papilloma
86	German Shepherd	>5	M(c)	Pituitary Adenoma
101	Golden Retriever	5	F(s)	Choroid Plexus Papilloma
104	Airedale	7	M	Choroid Plexus Papilloma
117	Miniature Poodle	7	M(c)	Choroid Plexus Papilloma
121	Dachshund	10	M(c)	Pituitary Adenoma
126	Labrador Retriever	11	M	Pituitary Adenoma
127	Miniature Poodle	6	F(s)	Reticulosis
136	Doberman Pincher	11	F(s)	Choroid Plexus Papilloma
Sampled six hours after end of BSH infusion:				
30	Great Dane x	9	F(s)	Pituitary Carcinoma
32	Boxer	9	F(s)	Meningioma
33	Labrador Retriever	>3	F	Anaplastic Nasal Malignancy
43	Standard Poodle	7	M	Diffuse Astrocytoma
49	Boxer	4	F(s)	Diffuse Astrocytoma
50	Miniature Schnauzer	11	M	Meningioma
55	Golden Retriever	9	M	Diffuse Astrocytoma
76	Collie	4	M	Protoplasmic Astrocytoma
88	Bassett Hound	9	M	Pituitary Adenoma
Sampled twelve hours after end of BSH infusion:				
1	German Shepherd x	5	M(c)	Pituitary Adenoma
14	American Eskimo	13	F(s)	Nasal Adenocarcinoma
15	Labrador Retriever	9	M	Nasal Adenocarcinoma
18	Coon Hound	5	M	Nasal Adenocarcinoma
23	Boxer	>3	M(c)	Pituitary Adenoma
25	Golden Retriever	9	F	Meningioma

a. F(s) designates a spayed (ovariohysterectomized) female, M(c) a castrated male, x a cross breed.

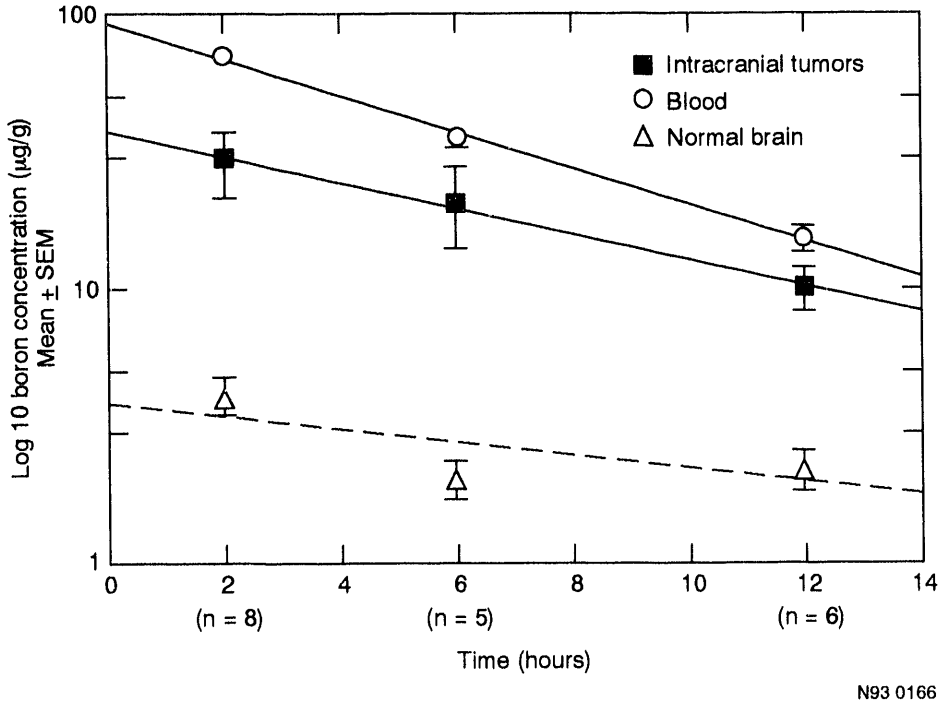

Figure 26. Changes in blood boron levels over time in intracranial tumors, blood, and normal brain. (n = number of subjects sampled at 2, 6 and 12 hours)

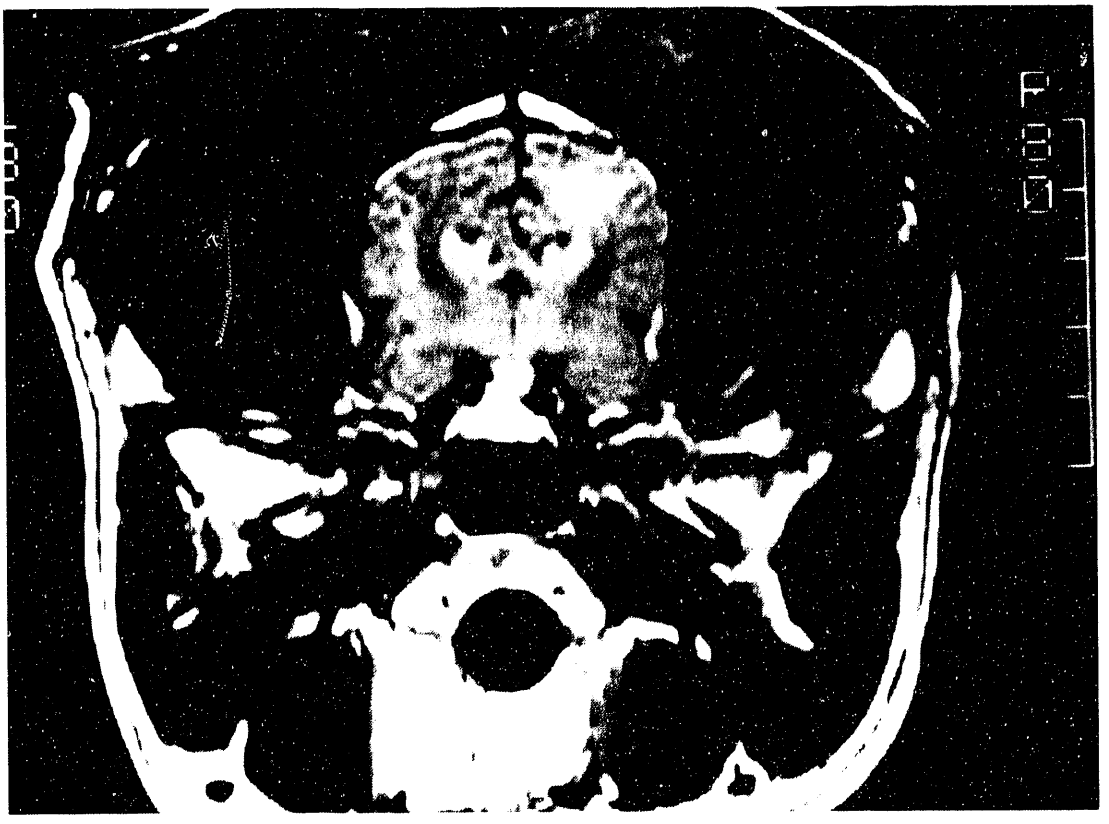

Figure 27. Radiation-induced, subclinical changes in the brain of a dog treated with BNCT.

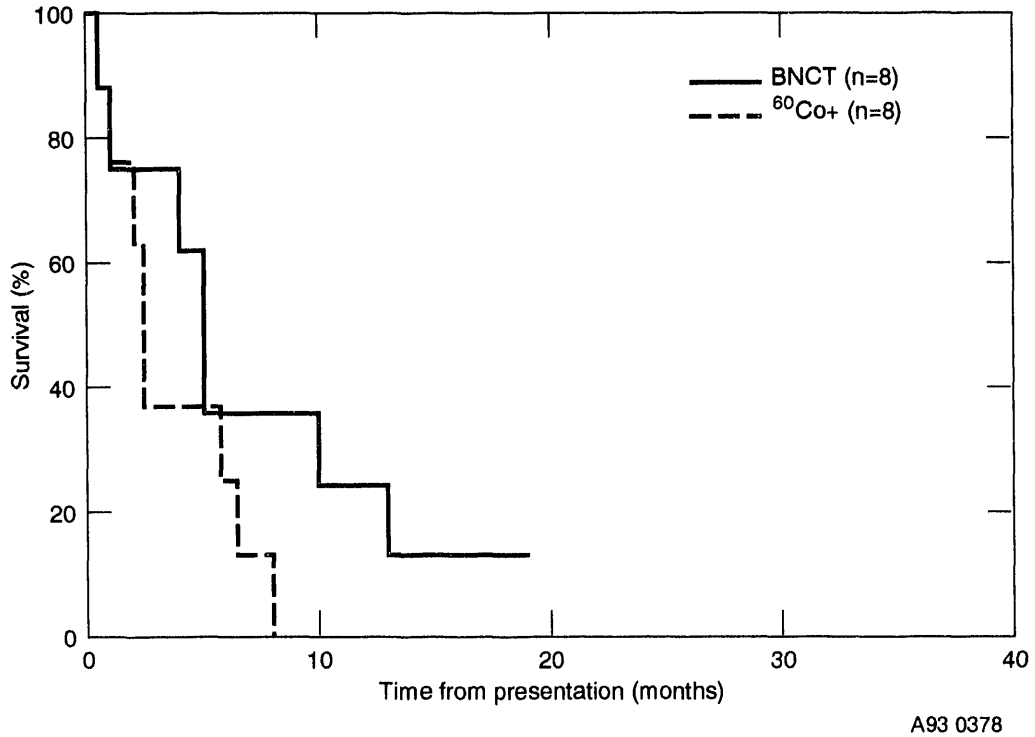

Figure 28. Comparison of survival of dogs with nonmeningioma brain tumors with BNCT and with augmented conventional cobalt (^{60}Co+) radiation therapy. (^{60}Co+ radiation therapy means gamma radiation plus some other form of therapy, i.e., chemo, hyperthermia, etc.)

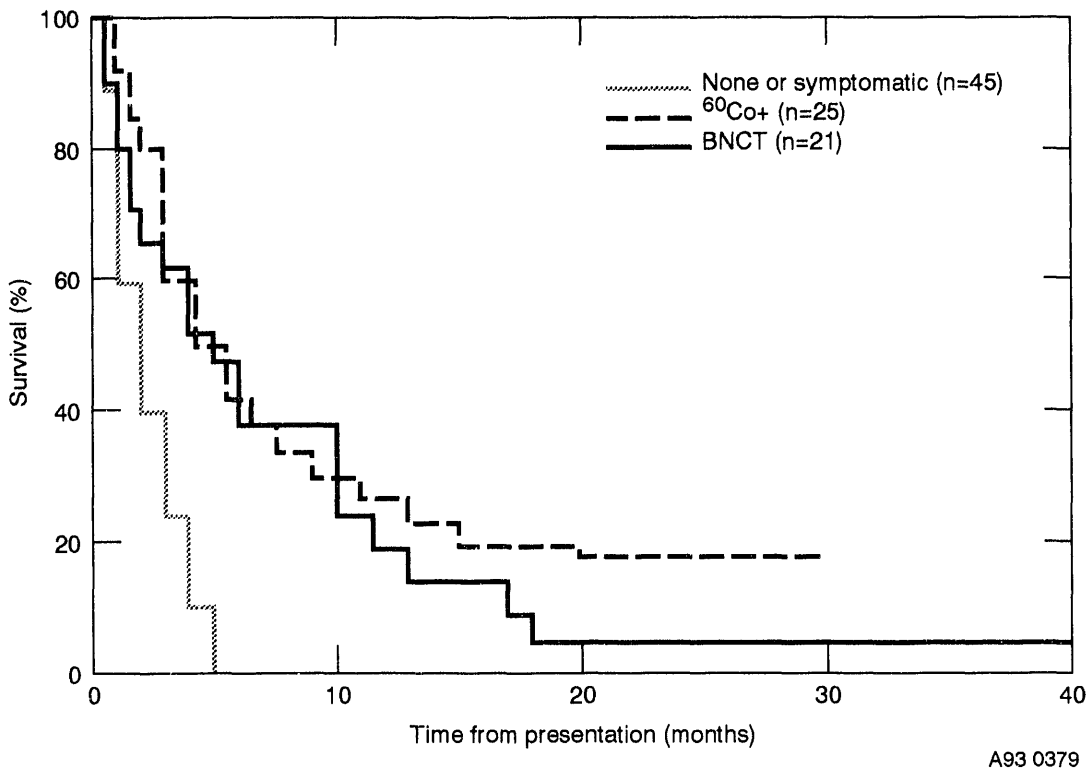

Figure 29. Comparison of survival of dogs with all tumor types with BNCT, augmented conventional cobalt (^{60}Co+) radiation therapy, and symptomatic or no treatment.

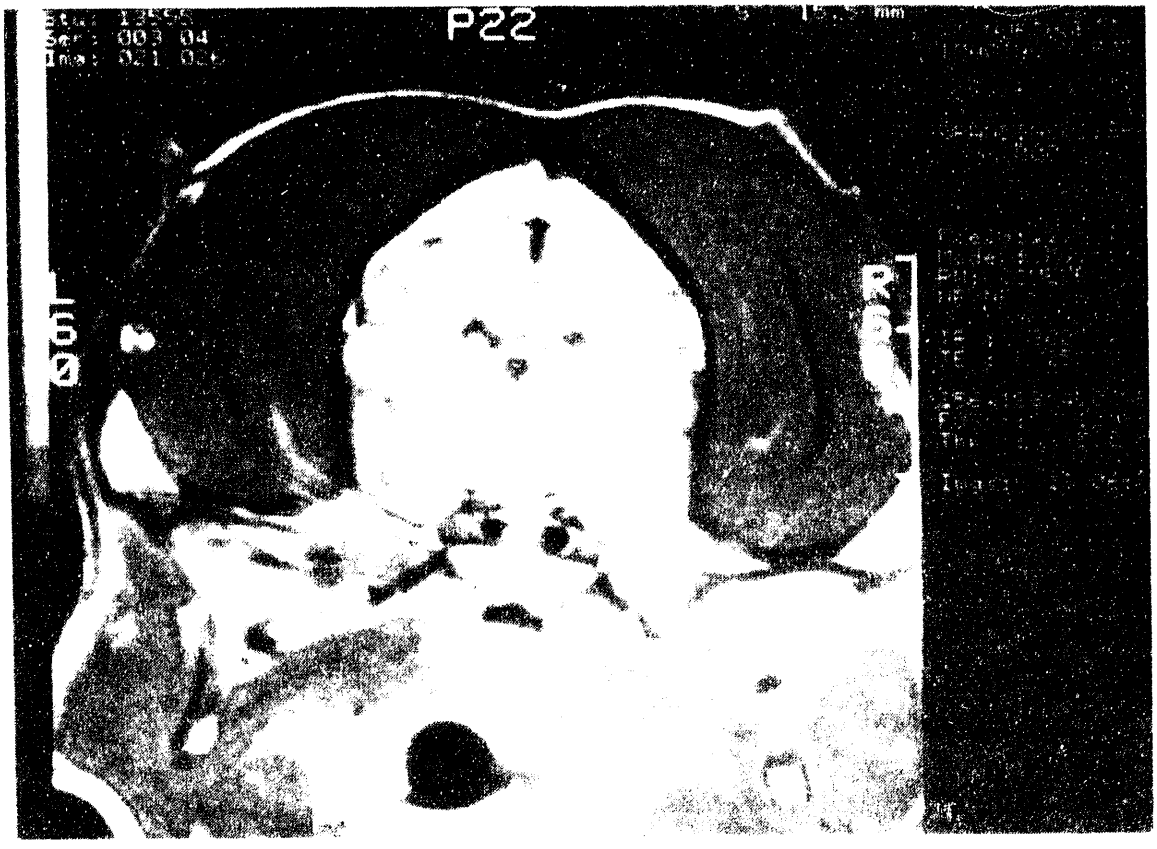

Figure 30. MRI of a dog with a tumor located in the right [illegible]

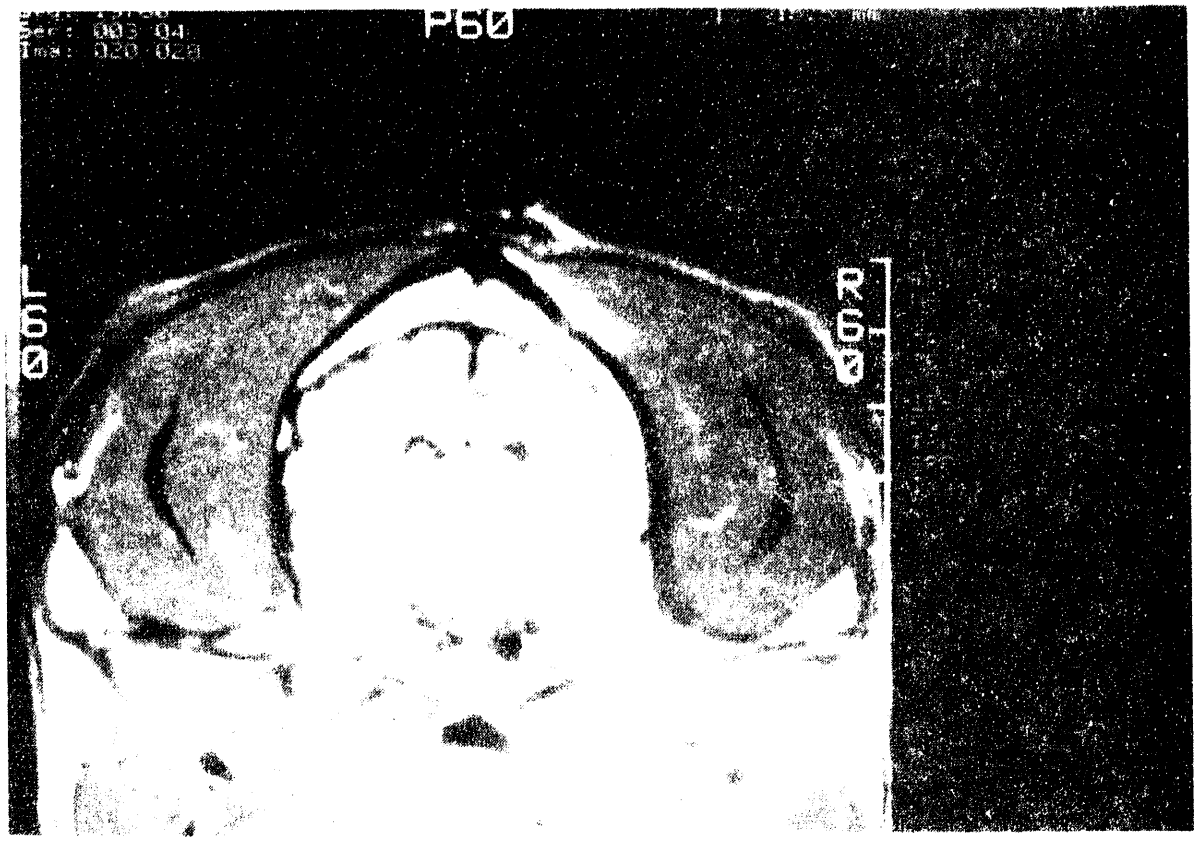

Figure 31. MRI of the same dog [illegible]

10 treatment episodes. Even when combined with surgical debulking and possible coarse fractionation schedules, the number of treatment episodes will be reduced with BNCT. A second advantage is the minimal side affects produced by the treatment. So far, only mild effects have been seen. The intravenous boron infusion can sometimes cause a mild stomach upset and vomiting, but the effect is transient and stops once the infusion is over. Transient drops in lymphocyte and platelet counts are also seen. These are usually back to normal within two to three weeks. One permanent side effect is a change in hair color and potential loss of hair in the area of treatment. (See Figure 32).

Clearly, BNCT has promise as a treatment modality for brain tumors. With further research, investigators at WSU and the INEL hope to define better treatment schedules providing more effective tumor destruction and improved survival times. Future research plans include continuation of the dose tolerance and pharmacokinetics studies using new boron compounds. Surgical debulking of the tumors will be performed prior to the BNCT radiation treatment in an attempt to concentrate the neutron capture events in peripheral, infiltrating tumor cells that cannot be removed surgically and are most often responsible for recurrence of the tumor. Split-dose regimens where the total neutron capture dose is administered over two treatments will also be investigated. The potential of repair of radiation damage by the body for the gamma dose fraction of the treatment will be studied as well. Currently, the theory is the amount of repair necessary will be slight due to the low dose rate of the gamma irradiation.

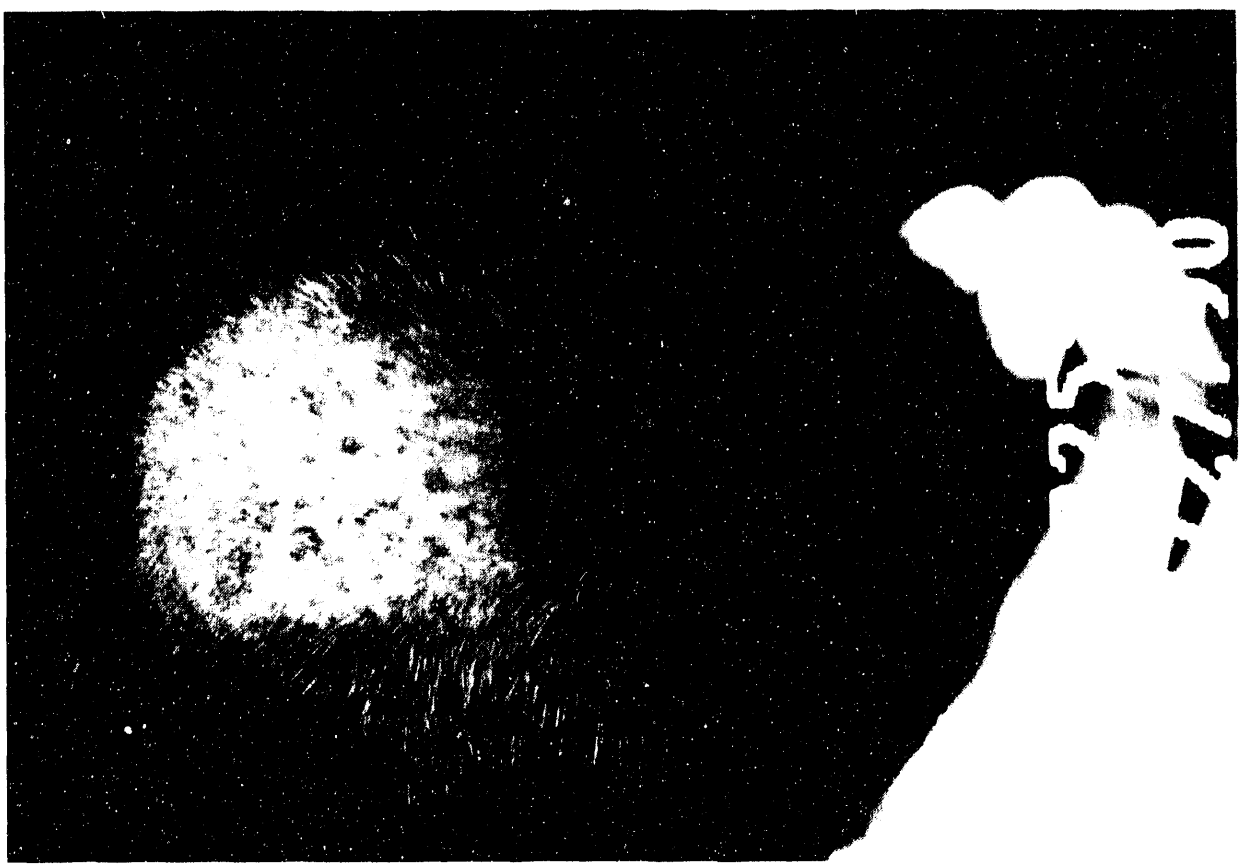

Figure 32. Hair loss and hair color change in a dog following BNCT.

NONINVASIVE BORON QUANTIFICATION

Dr. Marty Schweizer and Ken Bradshaw, University of Utah

A given in the maturation process for BNCT is the establishment of pharmacokinetic profiles for the various candidate boronated agents in large animal models and eventually in humans. Classical *in vivo* methodology in the canine model[37] has produced a wealth of kinetic data at the expense of numerous animals necessary to cover the entire absorption, distribution, and elimination time courses.

With these difficulties in mind as well as the problems with obtaining human biopsy samples, Kabalka et al.[38,39] and Bradshaw and coworkers[40,41] published early attempts to monitor the BNCT agent, BSH noninvasively *in vivo* using boron-11 MRS and MRI using rats and dogs, respectively. Considerable time—60–70 minutes—were required in these early chemical shift imaging experiments to produce boron-11 images with marginal signal-to-noise ratios. Considering the half-life of BSH elimination in most tissues is about four hours,[37] these techniques provided for only a few averaged time points.

Given the ill-defined signal from BSH, with the four chemically different boron species broadened by relaxation and exchange processes *in vivo*, Glover, Pauly, and Bradshaw[42] worked out a rapid three-dimensional projection-reconstruction technique that permitted good image quality to be produced in 8.5 minutes from canine heads. In the next paragraphs, preliminary results obtained with this method in normal dogs and those bearing intracranial tumors will be discussed.

BSH, first synthesized by Soloway et al.,[43] has the structure shown in Figure 33; the boronhydride cage has a net charge of -2. As expected, it does not cross a normal intact capillary endothelial blood-brain-barrier. Also in Figure 33 is the high resolution 160 MHz proton coupled boron correlation spectroscopy (COSY) spectrum illustrating the boron-boron connectivities. Note the four types of boron nuclei span a 10 ppm chemical shift range. This compound is relatively

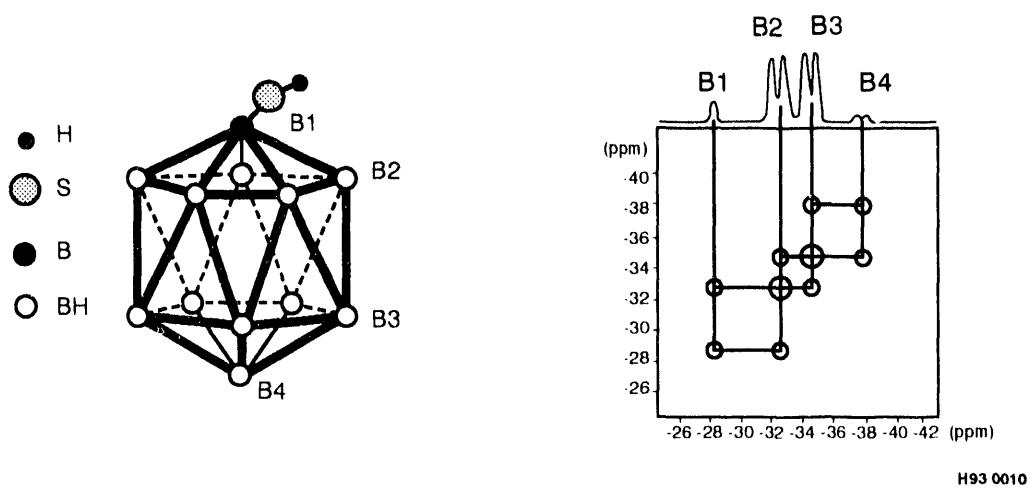

Figure 33. Structure of BSH anion and ^{11}B COSY spectrum. (The connections among the boron nuclei are indicated.)

nontoxic, stable chemically and is in human toxicity and pharmacokinetic trials in several countries, including the U.S. (Investigational New Drug Application for BSH is held by Joseph Goodman, MD, Ohio State University).

Boron-11 MR Imaging and Spectroscopy of BSH in Normal Dogs

(Animal protocols approved by the UofU Institutional Animal Care and Use Committee; protocol U6061, approved March 19, 1991, reapproved March 17, 1992).

Breed characteristic black Labrador Retrievers have been used for these experiments. The data presented below are representative of six normal and four gliosarcoma-bearing animals. All dogs taken for tumor implantation were given complete physicals and any necessary interventions during a 3-4 week period prior to inoculation. All animals were immobilized with Telazol IM® (ca 120 mg/kg combo of 50/50 Tiletamine HCL® and Zolazepam® HCL) prior to transport to the clinical MRI unit (GE SIGNA, 1.5 Tesla); retrofitted for boron-11 observation as per Bradshaw,[44] where they were maintained on isoflurane (1-1.5%) in oxygen. After affixing a boric acid standard onto the forehead, routine T1-weighted sagittal axial plus T2-weighted axial proton images were obtained with the resident head coil. Then a quadrature birdcage coil (Figure 34), tuned to boron-11 at 20.5 MHz, was positioned over the dog's head. Infusion of 170-175 mg BSH (ca 100 mg B) /kg in 11 mL/kg saline was begun with the flow rate adjusted to complete delivery in 60 minutes. Whole head boron-11 signal acquisition and collection of venous blood was performed every 10 minutes during the infusion period and every 20 minutes thereafter. After about two hours into the elimination phase, other clinical uses of the instrument demanded termination of scanning. Termination of scanning was followed by euthanasia and tissue necropsy. Tissue boron content was measured by ICP-AES.

Figure 35 consists of a typical whole head boron-11 spectrum (summation of 100 scans accumulated in 90 seconds with a 90° pulse width of about 100 μsec) late in the infusion period, showing the boric acid standard and the BSH signal, where the reduced resolution plus *in vivo* exchange and relaxation broadening yields a composite of the four chemically different boron nuclei (compare with Figure 33). If the time dependence of this BSH signal, normalized to the highest value at the end of infusion is plotted, throughout the pre- and post-infusion periods, one obtains data as shown in Figure 36. Normalized blood boron levels, determined by ICP-AES are also displayed. Retention of BSH in tissue is noted by the slower elimination kinetics compared with blood.

Boron-11 imaging was instituted at the end of the BSH infusion period. The magnetic resonance properties of the boron-11 nucleus include a gyromagnetic ratio (gamma) only one-third that of protons. Considering the natural abundance of boron-11 (80%, the other 20% is ^{10}B, the neutron capturing nucleus), the sensitivity relative to protons is 0.17. However, both boron-11 and -10 are quadrapolar, yielding very fast longitudinal and transverse relaxation rates. Therefore, one can compensate for the low sensitivity by pulsing rapidly, but excited spin information must be gathered rapidly because of the short T2's (600 μsec).

The pulse sequence used in the three-dimensional projection reconstruction method[42] is shown in Figure 37. Transverse magnetization was produced with a nonselective 90 degree (100 μsec) pulse followed by a 40-50 μsec ring-down delay (TE). Then projection readout gradients (with appropriate combinations of Gx, Gy and Gz values for the various views of k-space) were ramped to about 3 G/cm in 0.6 msec and held there another 0.4 msec for an A/D sampling time of 1 msec. The sequence was repeated 64 times using a 32 x 32 x 32 phase encode matrix. An interpulse delay of 6 msec was used. A field of view (FOV) of 48 cm yields a voxel size of 1.5 cm. During reconstruction of the frequency space (k-space) data, the varying velocity (because of ramp plus plateau periods in the acquisition window) of the trajectories was compensated and the image data transferred to cartesian coordinates with a gridding algorithm permitting usual 256 x 256 imaging displays as shown in Figure 38.

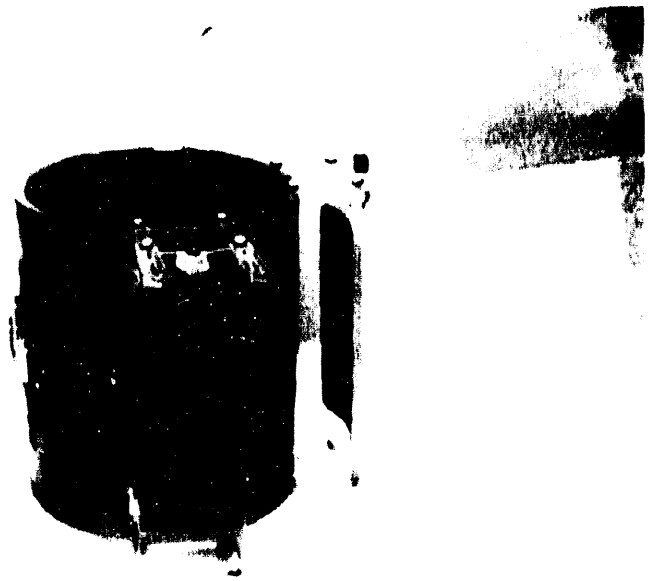

Figure 34. Birdcage coil.

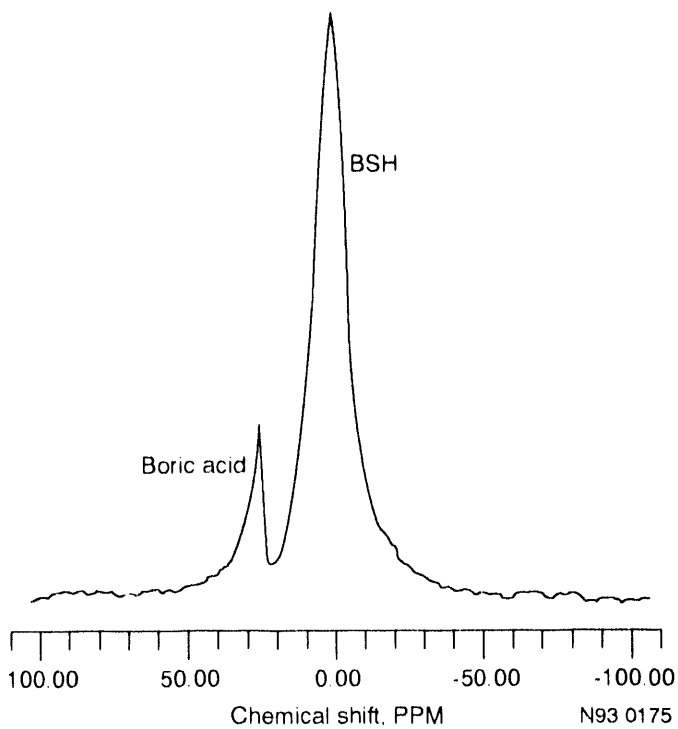

Figure 35. 20.5 MHz boron-11 spectrum of BSH in canine head.

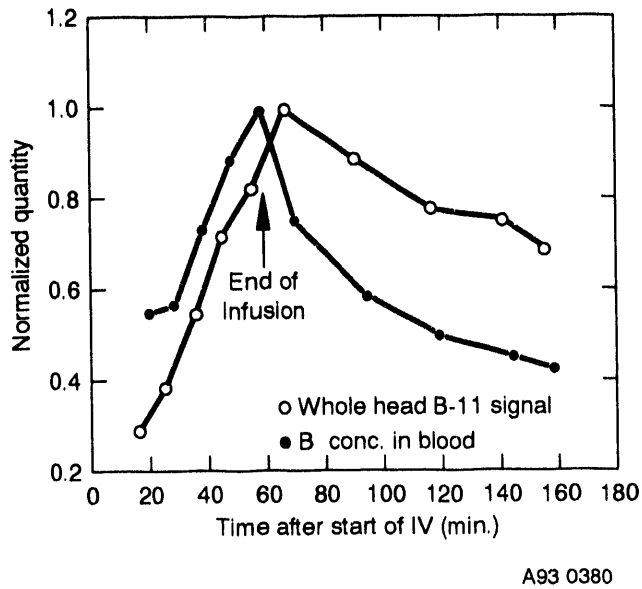

Figure 36. Normalized BSH in dog head and blood.

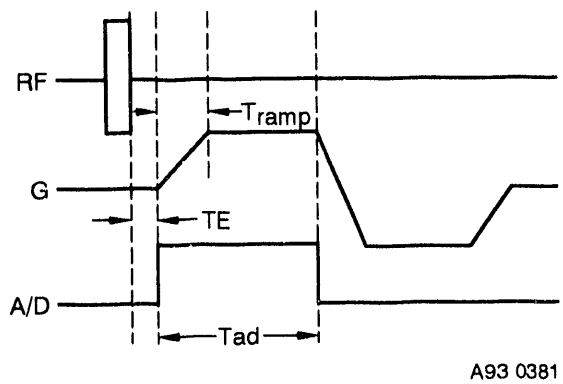

Figure 37. Three-dimensional projection pulse sequence.

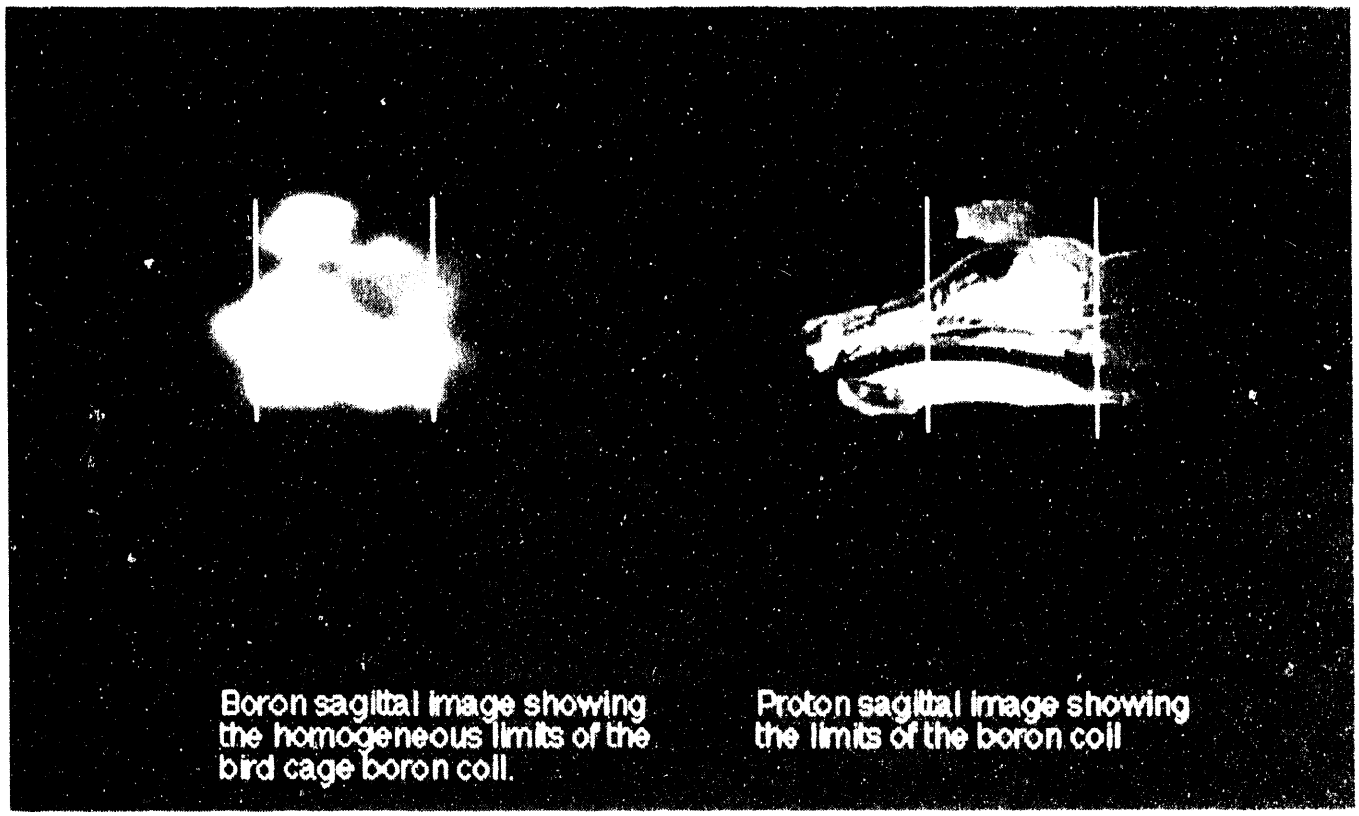

Figure 38. Boron sagittal image showing the homogeneous limits of the bird cage boron coil. Proton sagittal image showing the limits of the boron coil.

The central sagittal slice in Figure 38 shows the expected features of the dog head, with the boric acid bottle attached. Limits of coverage by the boron quadrature coil is shown as two vertical lines. The corresponding boron-11 image on the left (from the central 1.5 cm slice) clearly illustrates high boron content in tongue, oral and nasal mucosa, with less or amounts in muscle and virtually nothing in brain to be expected due to [illegible] of the [illegible] BSH by the blood brain barrier. This image is the [illegible] signal to noise [illegible] exposure of the [illegible] mensional distribution of BSH [illegible]. The [illegible] tion is of course far inferior to the proton image because of the large voxel size of 1.5 cm [illegible]. Images were taken from tumor bearing dogs with 7.5 mm (cubed) voxels which are of higher quality [illegible] shown below. [illegible]

[illegible]

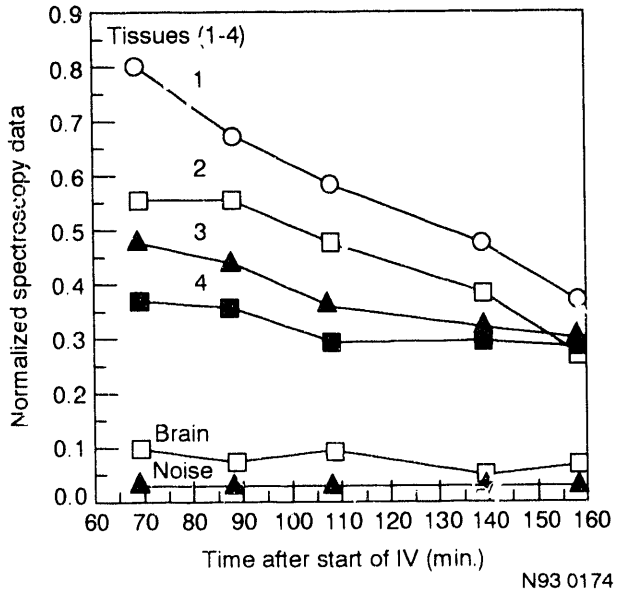

Figure 39. Comparison of boron signal intensity from different tissues of equal volumes after end of infusion. (1 and 2, tongue and mucosa; 3 and 4, muscle.)

Boron-11 Imaging and Spectroscopy in a Canine Tumor Model

In order to test the boron imaging methodology on a relevant tumor model, the canine gliosarcoma system elaborated by Salcman et al.[45] was selected. Frozen cell suspensions have been supplied by Dr. John Hilton, Division of Pharmacology, The Johns Hopkins University Oncology Center. Tumor implantation protocols (performed in the operating suites at the UofU Animal Research Center) were assisted by Richard Tippets, MD, Assistant Professor of Neurosurgery.

Conditioned dogs were immobilized with Telazol IM and subsequently maintained with general isoflurance (1.5–2.0%) in oxygen. After incisions through scalp and mascidor muscle, a 1/4 in. burr hole is prepared through the skull above the parietal lobe. Appropriate location is guided by prior sagittal proton MRI images.

About 10^6 cells of the thawed suspension is injected with a 100 μL Hamilton syringe 1 cm beneath the cortical surface. Bone wax is used to seal the skull; muscle and scalp are closed and the animals closely monitored for post-op complications. Both uni- and bilateral inoculations have been performed.

Serial proton MRI exams, with sagittal and axial T1 weighted, axial T2 weighted and gadolinium enhanced T1 axial views are staged beginning at about day three post implantation. In most cases, tumor presence is noted by day seven.

Proton and boron MR was performed as above for normal dogs, with euthanasia and necropsy following.

Representative serial T2-weighted axial proton images (central slice, 5 mm thickness) are given in Figure 40 showing gliosarcoma development over nine days post inoculation. At day three, some abnormal water accumulation is visible in the left temporal lobe/basal ganglia area. At day seven, this unnatural bright mass is much larger.

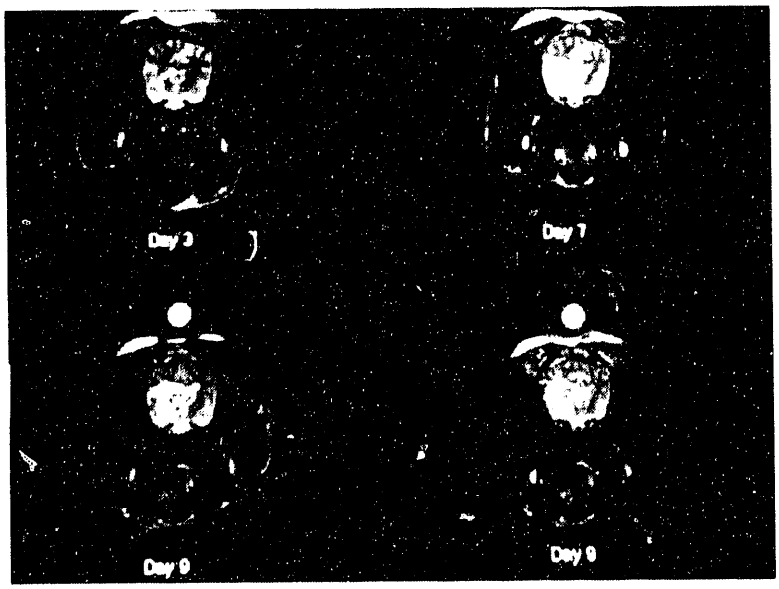

Figure 40. T2 weighted axial proton images show gliosarcoma development over nine days post inoculation.

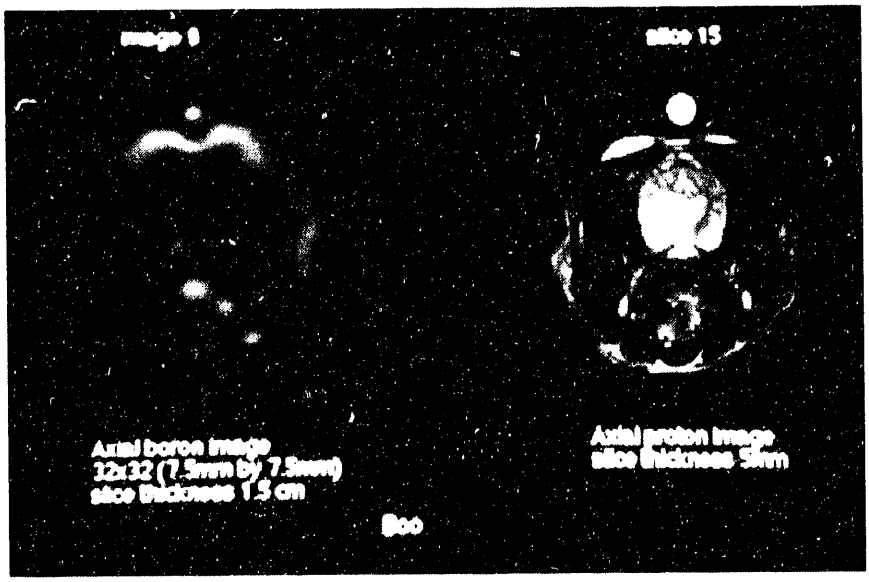

Figure 41. Axial boron image and proton image (same proton image day, Figure 40).

Development of two separate nodules is apparent at day nine; in an adjacent slice (bottom right), the tumorous mass is more elongated. Boron imaging was conducted on this day. Figure 41 contains, on the right, the same proton image (enlarged) shown on the bottom left of Figure 40. On the left is the boron-11 image (pixel dimensions 7.5 mm x 7.5 mm, with an axial slice thickness of 1.5 cm). As expected, boron is found distributed into various tissues, including tumor, but not normal brain.

This dog was also inoculated in the right parietal lobe, but with only one-half the "usual" concentration (10^6) of tumor cells. This lesser amount was evidently below the threshold necessary for tumor formation since no abnormal tissue was seen on proton images, nor was any growth found in necropsy.

In Figure 42, the 16 axial slices (top left, nose through bottom right, ears) show the distribution of BSH seven minutes after the end of infusion (67 minutes after start of injection) (left panel) in the same dog ("Boo") as the Figure 41 data. Drug in tumor is most readily seen in a center slice (#9, counting from upper left and from left to right). BSH content in these slices 120 minutes after the end of infusion is displayed in the right panel, illustrating intensity fall-off as drug eliminates. Although somewhat difficult to visualize, ROI analysis may be used to find that the image intensity representing BSH in tumor falls off only one-half as rapidly as other tissues, illustrating greater retention in tumor.

Another dog ("Sally") was bilaterally inoculated with 1.2 x 10^6 cells into left and right parietal lobes (in that order of implantation). Tumors grew in both lobes near the cortical surface; the lesion on the left, the first site of implantation, grew to about 2 cm diameter, while the right side tumor was one-half this size (measured at necropsy, however, the left tumor size was readily apparent from the proton images while the right side lesion was difficult to discern.)

In Figure 43 is displayed, on the right, a gadolinium enhanced axial T1 weighted image from a central 5 mm slice of "Sally", 10 days post implantation. Enhancing periphery around a necrotic area is typical for this type of tumor. The corresponding boron-11 image of the central 1.5 cm thick slice at day 12 is shown on the left. BSH in tumor is clearly visible.

Histopathology on cell samples taken at necropsy confirm the aggressive profileration of this gliosarcoma seen in the high mitotic index (collaborator; Cheryl Harris, MD, Senior Fellow in Neuropathology, UofU). Numerous capillary fragments are seen, illustrating the vascularity of this type of neoplasm, hence the eventual virtual loss of the blood-brain-barrier.

The foregoing results have been reported at several international meetings[46,47,48] as well as in a manuscript.[49]

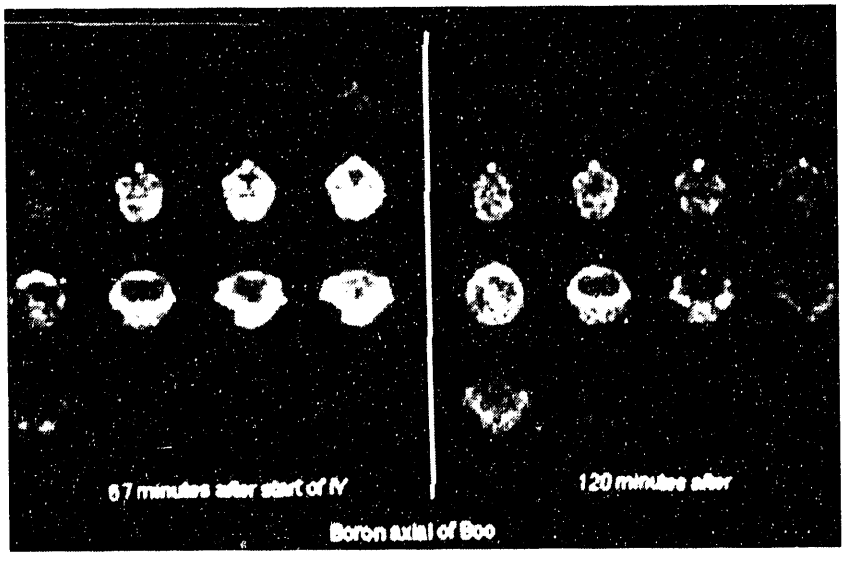

Figure 42. Boron axial of "Boo."

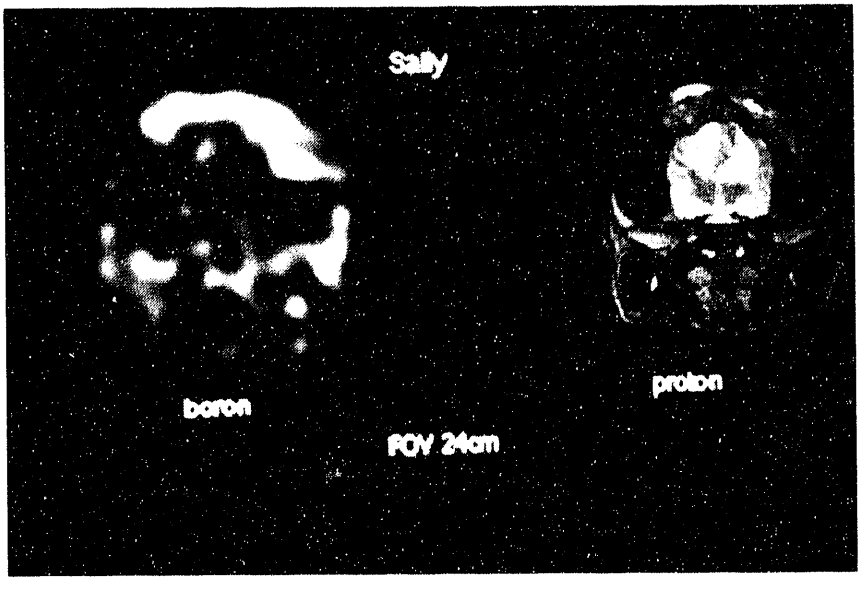

Figure 43. Boron axial of "Sally."

ANALYTICAL DOSIMETRY

Dr. Dave Nigg and Floyd Wheeler, Reactor and Radiation Physics, INEL

Introduction

INEL researchers and selected university collaborators have been engaged for some time in the development of analytical methods and software for performing detailed radiation transport and dosimetry calculations for BNCT. Such calculations are needed for effective planning of experimental BNCT research involving animal irradiations, for interpreting the radiobiological observations resulting from such research and, ultimately, for human treatment planning. Over the past year, the emphasis has been on methods for computation of macroscopic absorbed dose (average energy per unit mass) distributions, although some attention has been devoted to analysis of certain microdosimetric phenomena that contribute decisively to observed radiobiological effects in BNCT.

Development of Analytical Methods for Macroscopic Dosimetry in BNCT

Radiation transport and dose distribution analysis for BNCT is much more complex than is the case for standard photon therapy. There are several different physical radiation dose components associated with BNCT, each of which has its own characteristic spatial distribution and Relative Biological Effectiveness (RBE). Most of these radiation dose components arise from neutron interactions that take place after the incident neutrons from the treatment beam have undergone several scattering interactions. Accordingly, many of the simplifying assumptions that work well for radiation transport calculations associated with treatment planning for standard photon therapy are not appropriate for BNCT. Explicit three-dimensional calculations with a complete treatment of particle scattering are required.

In contrast with photon therapy, where the absorbed dose is deposited by energetic secondary electrons produced via interactions between photons and tissue constituents, most of the major absorbed dose components in BNCT are generated by high-LET heavy charged particles (protons, alpha particles, etc). These particles are produced by a variety of different neutron interactions with the normally-occurring tissue elements as well as with the pharmaceutically-administered ^{10}B. The most important BNCT dose component is, of course, the therapeutic $^{10}B(n,\alpha)$ dose. *All of the other neutron dose components are non-selective and are therefore not desirable.* One of the most significant of these is the proton recoil dose produced by elastic scattering interactions between neutrons and hydrogen. This component is believed to have a particularly high RBE for normal tissue damage. The proton recoil dose component can be suppressed in a properly-designed epithermal-neutron beam but, as a practical matter, it cannot be totally eliminated. Other unavoidable neutron-induced background dose components result from the nitrogen (n,p) interaction and from several other less-important interactions. There is also a photon dose component in BNCT that is produced largely as a result of radiative capture of neutrons by hydrogen within the irradiation volume and, to a much lesser extent, by gamma contamination that is present in any practically attainable neutron beam that is used for treatment.

Figure 44 shows the essential elements that are required in calculational systems used for BNCT analytic dosimetry and treatment planning. At the heart of any such system is a module for calculating the solution of the three-dimensional Boltzman transport equation for neutral particles, given certain descriptive information as input. This descriptive information consists of a geometric model of the irradiation volume (ideally constructed directly from medical image data), a mathematical description of the treatment beam, and a complete set of coupled neutron-photon cross section data for all elements that are present. Three different methods for constructing the

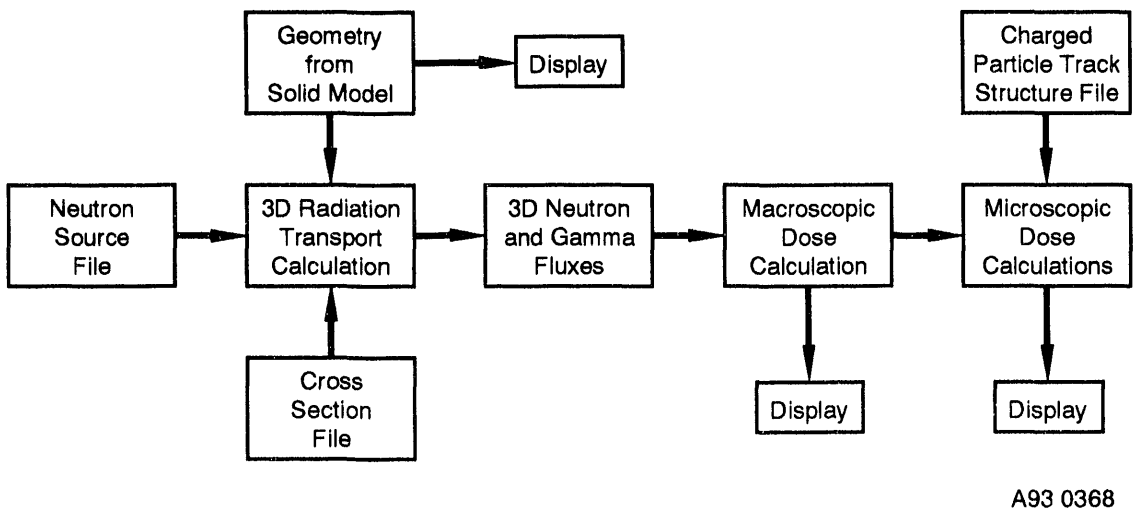

Figure 44. Flow diagram for BNCT neutron particle transport and microdosimetry analysis.

necessary geometric model have been successfully demonstrated by various investigators. The beam description consists of the spectrum, the angular distribution, and the spatial intensity distribution across the plane of incidence, of both the neutron and the photon flux components of the treatment beam. This information is usually constructed from a combination of calculational and experimental data pertinent to the beam of interest. Neutron and photon cross sections are typically taken from standard data collections and preprocessed into an appropriate multigroup or continuous-energy format.

Given the calculated neutron and photon fluxes throughout the treatment volume (that is, the complete space and energy-dependent solution of the Boltzmann equation for the situation of interest), it is a relatively simple matter to construct the resulting macroscopic absorbed dose distribution by convolving the calculated flux data with flux-to-dose conversion factors (which may include RBE multipliers) for each radiation dose component, integrating over the neutron or photon energy range as appropriate, and summing all components. This method is acceptably accurate for all neutron dose components in BNCT since the charged particles that result from these interactions have very short ranges in tissue (on the order of a few micrometers). Thus it is appropriate to assume that, on a macroscopic scale, the spatial distribution for each of these components follows the weighted spatial distribution of the original neutron flux. For the photon dose component this approximation is less-accurate, especially near voids and material interfaces, but it is commonly used in BNCT. Standard void and interface correction methods could be used for this dose component in situations where greater accuracy is desired.

The Monte Carlo stochastic simulation method is the current method of choice for calculations of radiation dose distributions in BNCT since the complex geometries that are characteristic of biological systems can be very accurately represented using this technique, and one can obtain integral information about the radiation dose distribution (for example, integrated dose over

tissue compartments of interest) in quite reasonable (10–30 minute) computing times. This is the method employed in the rtt_MC code, developed over the past few years by INEL researchers specifically for BNCT applications. The rtt_MC module is nearing completion. A beta test version was established during 1992 for use in support of INEL-sponsored *in vivo* research. In addition, this experimental version of rtt_MC was transferred to researchers associated with the European Collaboration on BNCT under a formal cooperative arrangement.

The Monte Carlo method for calculation of radiation transport is conceptually very simple, although the actual mathematical implementations of the method that has been developed by various researchers over the years has reached very high degrees of theoretical sophistication. For BNCT purposes, the basic idea is to solve the fixed-source form of the transport equation by randomly selecting neutrons and photons from a pre-specified boundary source (that is, the incident beam) and following each selected particle through the calculational geometry until it is captured or it leaks out of the irradiation volume of interest. This is accomplished by stochastically simulating particle "histories" as each neutron or photon, as the case may be, travels through the irradiation volume and interacts with the medium. During each history the scalar flux (track length per unit volume) generated by the particle is tallied as it traverses the geometry. If enough particles are followed one can obtain statistically converged estimates of the particle flux in each region of interest.

Three basic methods have been developed for constructing the geometric description of the irradiation volume for use in BNCT dosimetric modeling using the Monte Carlo technique. The first method, which is computationally the simplest and therefore the fastest-running, is to approximate the irradiation volume using logical combinations of a small number of geometric primitives (spheres, cubes, cylinders, etc.) described by simple surface equations. This method has been widely used for a variety of radiation transport calculations over the years. In BNCT, however, use of the geometric primitive method at INEL and elsewhere is now generally limited to calculations of flux and dose distributions in idealized cylindrical or spherical tissue-equivalent phantoms, primarily in connection with neutron beam design and characterization. For actual *in vivo* applications, the geometric primitive method has largely been superseded by two independent methods for constructing the necessary geometric descriptions directly from pertinent medical image data generated either by CT or by MRI.

The first of the direct geometric reconstruction methods employs what may be described as a "voxel reconstruction" technique whereby each plane of medical image data is partitioned into squares (typically 10 mm on a side), each of which is assigned material properties based on average CT density or some other appropriate criterion. Once all of the images are partitioned, the square regions generated in each plane are mathematically stacked to construct a large three-dimensional array of parallelpipeds. The various tissue compartments are thereby represented as combinations of adjacent parallelpipeds. This reconstruction technique can be used with the rtt_MC code, but for a variety of reasons, the primary emphasis at INEL has been on development of software for generation of geometric representations using generalized surface equations instead, as described below.

The second method for direct construction of geometry from medical image data is based on the calculation of non-uniform rational B-spline fits to the various tissue compartment (or any desired subcompartment) surfaces. A B-spline surface reconstruction capability has been provided for the rtt_MC code via the bnct_edit reconstruction module, developed by INEL researchers in collaboration with the Computer Science Departments of the UofU and Montana State University. An initial version of bnct_edit was completed during 1992 and although development is continuing, the initial version is gradually being phased into use in support of the overall BNCT program. With the B-spline reconstruction method, one first electronically outlines the regions of interest (skin, skull, brain, various

tumor regions, etc.) on each medical image plane as illustrated, for example, in Figure 45 for an axial MRI of a Labrador Retriever head. In this figure the brain and the outer surface of the head have been outlined on the image. The region outlines for all image slices are then mathematically combined to produce detailed equations describing the three-dimensional surfaces that enclose each volume of interest. Figure 46 shows a B-spline reconstruction of the outer surface of the canine head while in Figure 47 the outer surface has been stripped away to show interior reconstructions of the brain and eyeballs. This particular canine model was constructed for use in normal tissue tolerance studies, hence there is no tumor region shown. The surface equations generated in the B-spline region reconstructions completely describe the geometry and can subsequently be used in a Monte Carlo radiation transport calculation. The spline surfaces can be combined with geometric primitive surfaces to further specify the calculational geometry if desired. As mentioned previously, the rtt_MC code will also accept parallelpiped arrays constructed using the voxel technique.

The surface equation reconstruction technique is very efficient and accurate. The complex curved surfaces of the various anatomical structures of interest in BNCT dosimetry can be very faithfully represented and particle tracking can be accomplished with the minimum number of boundary crossings that is consistent with the number of tissue compartments modeled. The primary disadvantage is that, unlike the situation with voxel-based reconstructions, one does not automatically obtain spatially-detailed flux and dose distributions. This problem has, however, largely been addressed in the rtt_MC code without unreasonable loss of calculational efficiency and without introducing arrays of time-consuming "flux-at-a-point" estimators by the development by INEL researchers of the so-called "subelement Monte-Carlo" technique.

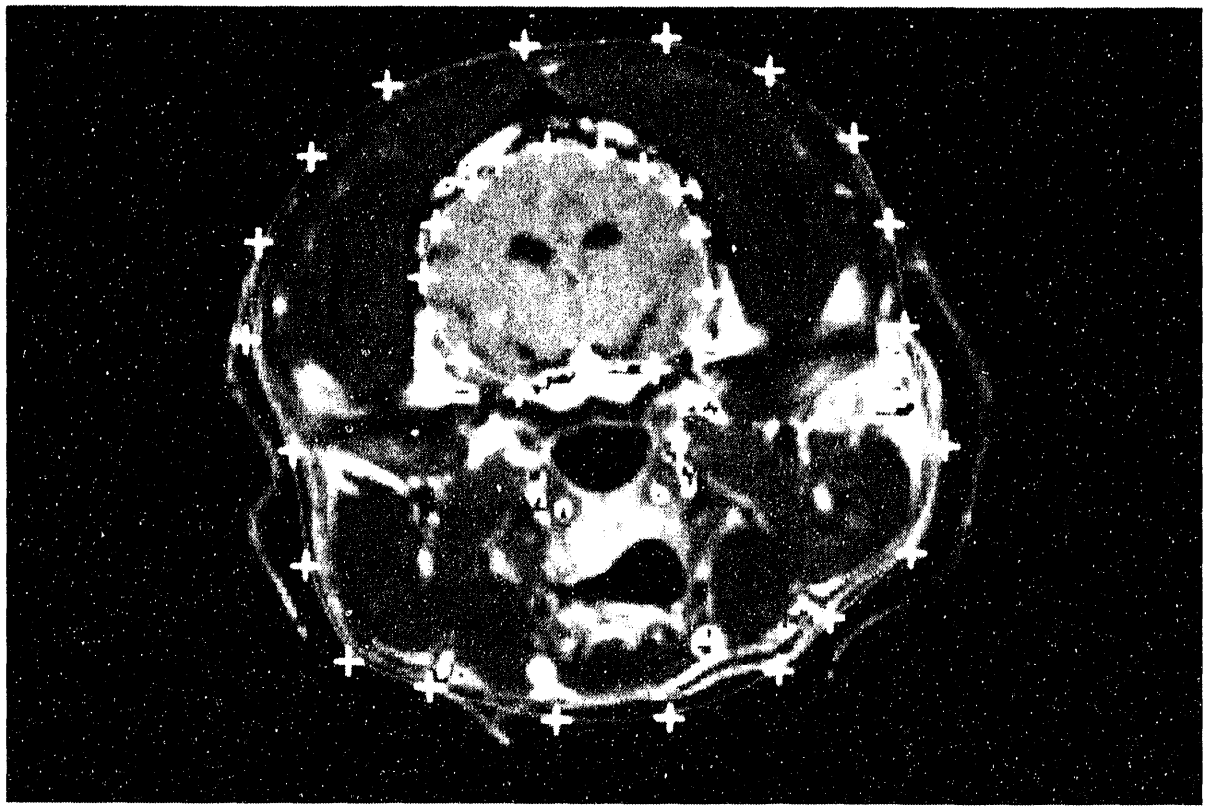

Figure 45. Axial MRI of a Labrador Retriever head showing B-spline outlines of the brain and outer head surface. (The rostral direction is out of the figure.)

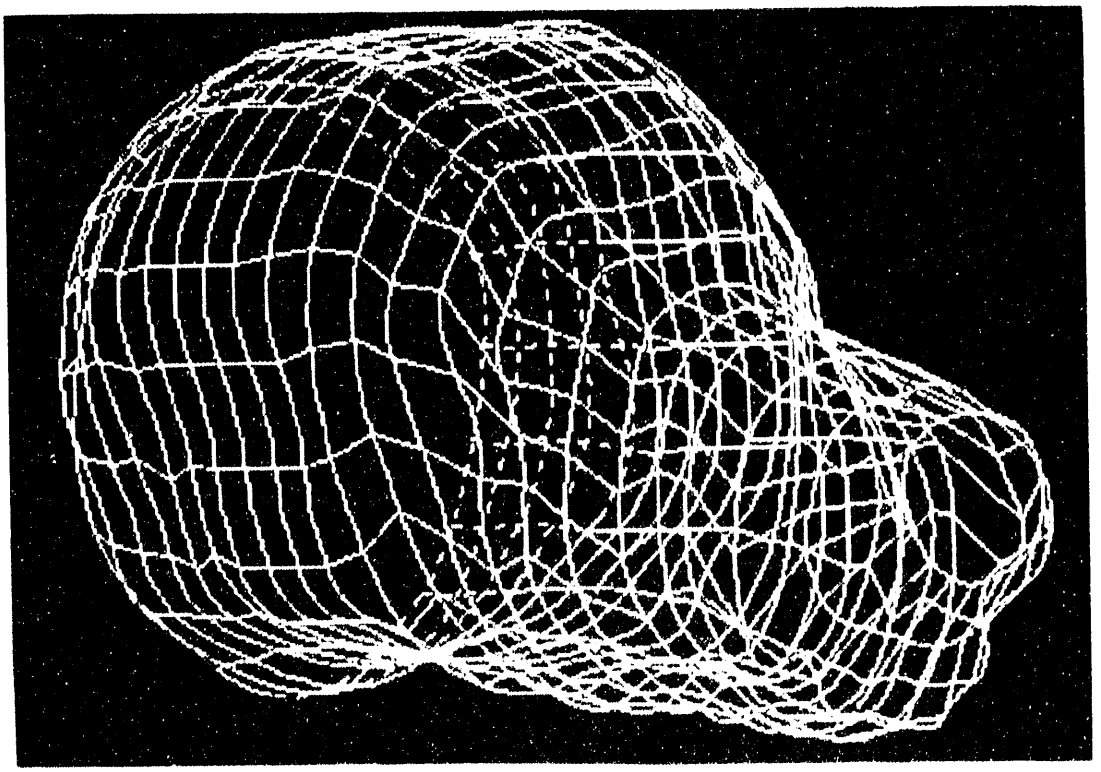

Figure 46

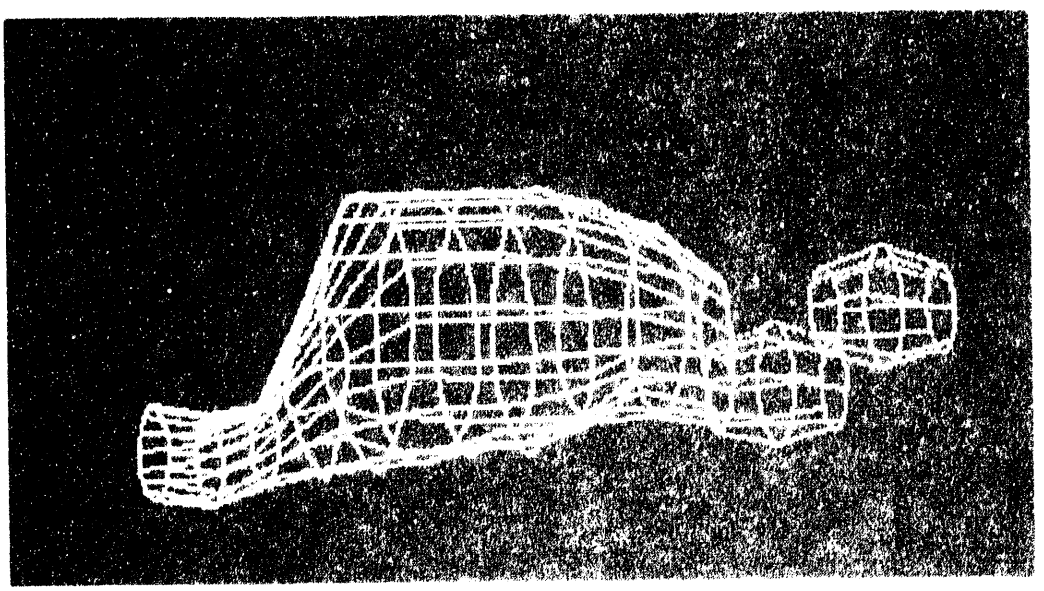

Figure 47

The subelement Monte Carlo technique basically involves superimposing a special three-dimensional subelement mesh structure upon a pre-existing surface reconstruction of the irradiation volume. The subelement mesh is based on three orthogonal sets of parallel planes. It is outwardly similar to the parallelpiped array that would be generated for the irradiation volume by the standard voxel reconstruction method, but it is much more computationally efficient because of the concise manner in which the geometric relationship between a given particle trajectory and the intersecting planes is specified. The subelement mesh is independent of the model geometry and does not affect the particle tracking process, other than to moderately increase the computing time requirements. For typical subelement structures composed of 10 mm cubes the computing time is increased by only about 20%. During particle tracking through the original surface reconstruction, each path is examined to determine the path length to tally for each subelement that is intersected. This is done with a clipping-plane algorithm similar to those used in computer graphics. An additional attractive feature of the algorithm is that flux contributions to subelements that happen to be intersected by a reconstructed surface are rigorously treated, that is the algorithm "knows" that the tissue material properties may change from one side of the intersecting surface to the other. This is illustrated in Figure 48.

Figures 49, 50, and 51 show flux and dose contours calculated for one axial plane of a canine head using the rtt_MC code with a B-spline reconstruction for the overall geometric description and a 10-mm subelement mesh structure for spatial detail. The canine head is assumed to be positioned in the epithermal neutron beam that is available at the BMRR. A rectangular beam delimiter having dimensions of 50 mm by 100 mm was assumed and the beam was oriented such that the angle of incidence was perpendicular to the top of the head, with the long axis of the delimiter perpendicular to the image plane. The beam axis is parallel to and 25 mm to the left of the sagittal midplane of the head. This is the standard arrangement used for hemispherical canine-brain irradiations in the BMRR beam. Calculated thermal neutron flux contours are shown in Figure 49. With the exception of the proton-recoil dose component, which is proportional to the fast (>10 KeV) neutron flux, all of the dose components in BNCT tend to follow the spatial distribution of the thermal neutron flux. Calculated proton-recoil dose contours for this case are shown in Figure 50. This particular dose component is non-selective, as is the photon dose component, shown in Figure 51.

A few dose-depth traverses along a line parallel to the beam axis and passing through the location of the peak thermal flux are shown in Figure 52 for the canine irradiation study. The proton-recoil and photon dose components in Figure 52 are simply traverses through the data given in Figures 50 and 51, respectively. The boron-neutron capture dose component shown in the figure follows the spatial distribution of the thermal neutron flux and is normalized to a clinically-realistic uniform boron concentration of 30 parts per million (ppm) by weight in tissue. The total dose curve includes the boron neutron capture dose, the proton-recoil dose, the photon dose, the nitrogen (n,p) dose and several other smaller components. The total non-boron dose curve is simply the difference between the total dose curve and the boron dose curve. The non-boron dose curve shows the dose that would be seen by normal tissues, from which boron would presumably be excluded. The total dose curve shows the dose that would be seen by tissues containing boron at the assumed concentration. It can be seen that these two curves are separated by factors of 3-4, depending on the spatial location. This provides a simple, but not necessarily radiobiologically-predictive, measure of the attainable therapeutic advantage in BNCT.

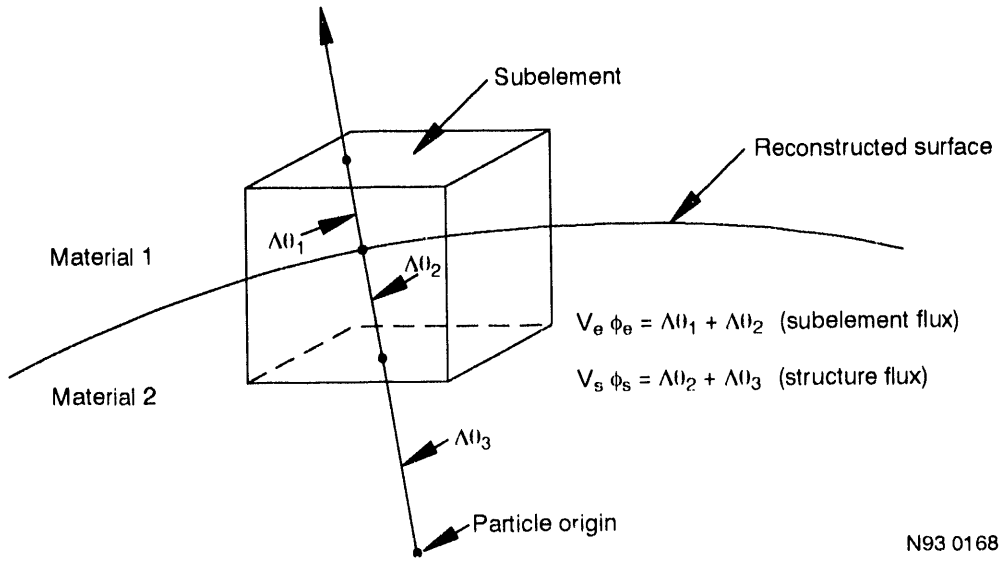

Figure 48. Illustration of the algorithm used for flux tallies in the subelement Monte Carlo method.

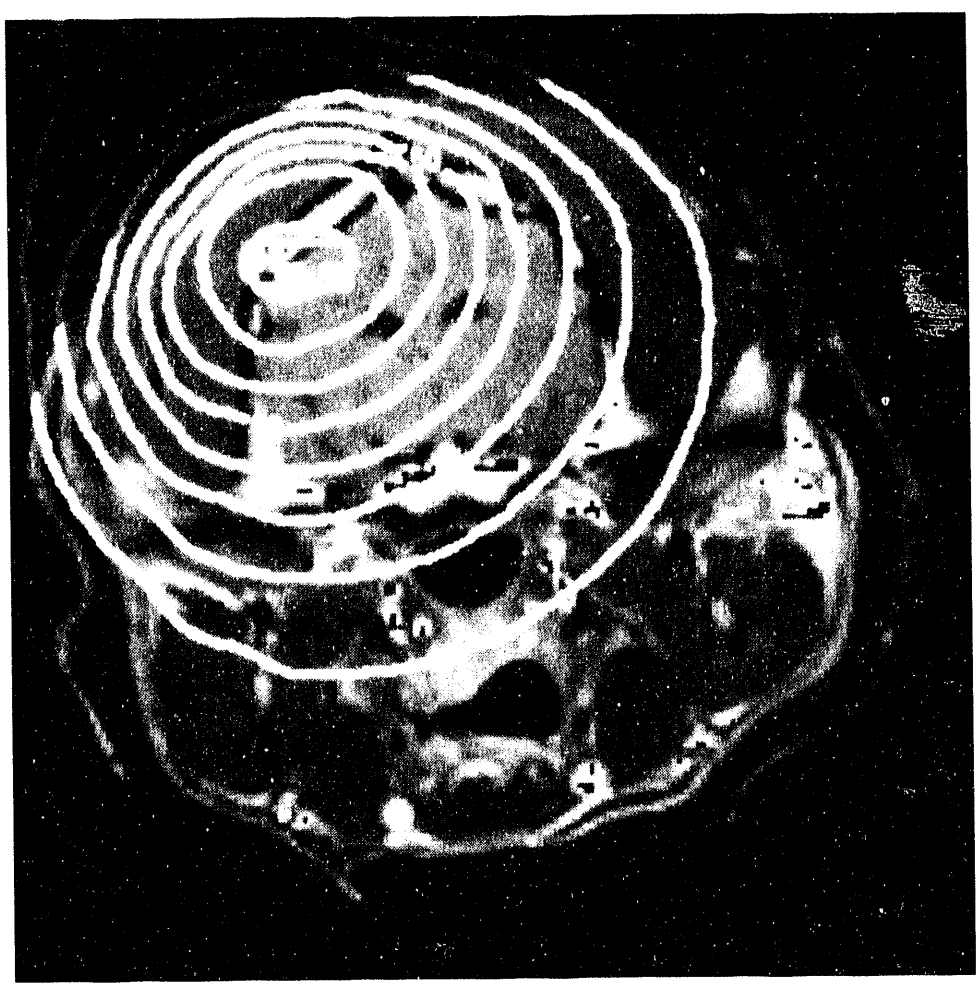

Figure 49. Calculated thermal-neutron flux contours in an axial plane for the B-spline Labrador retriever head model, positioned in the BMRR epithermal-neutron beam.

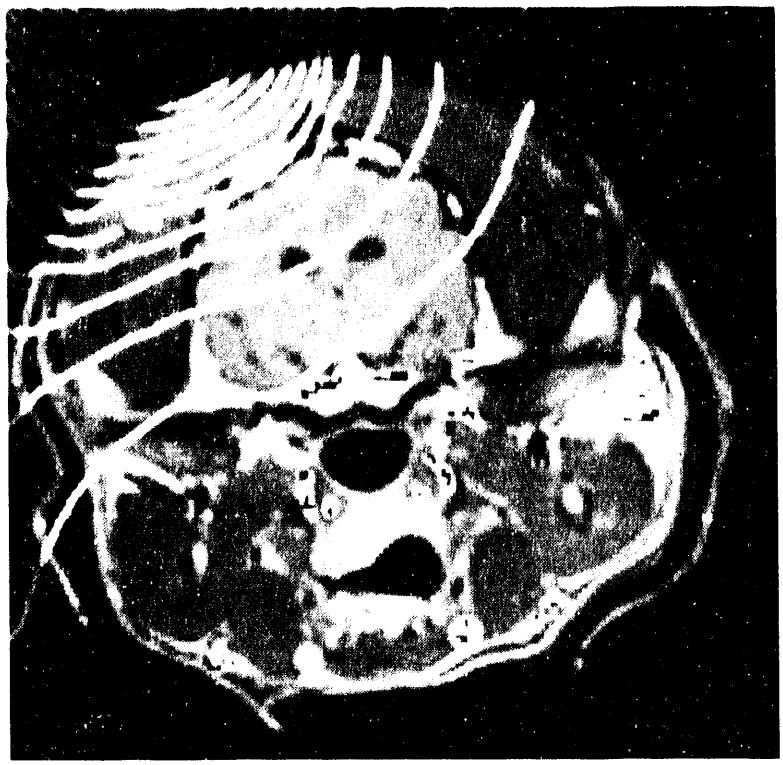

Figure 50. Calculated proton-recoil physical dose contours in an axial plane for the B-spline Labrador Retriever head model, positioned in the BMRR epithermal-neutron beam.

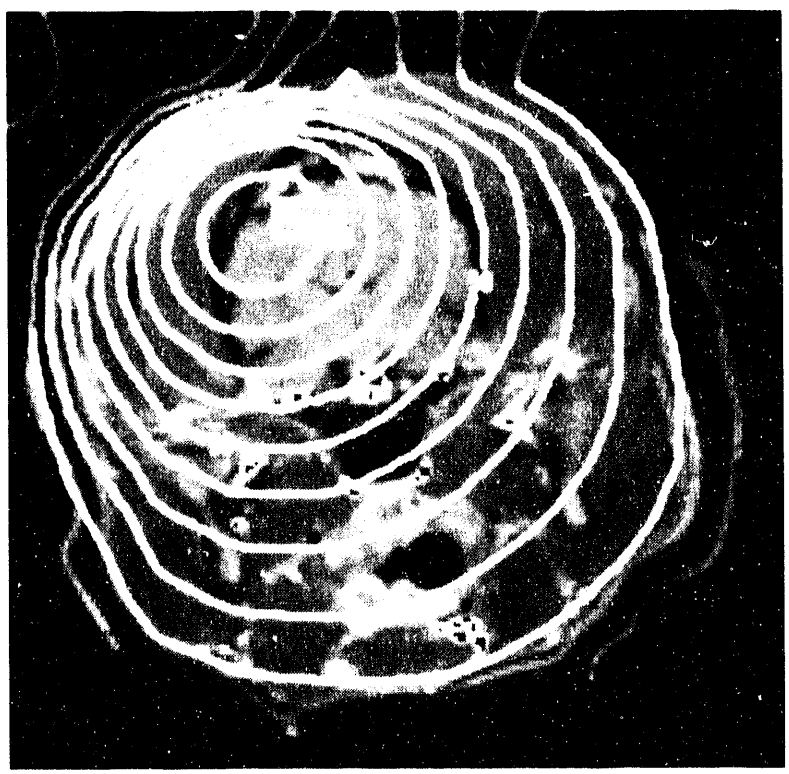

Figure 51. Calculated photon-induced physical dose contours in an axial plane for the B-spline Labrador Retriever head model positioned in the BMRR epithermal neutron beam.

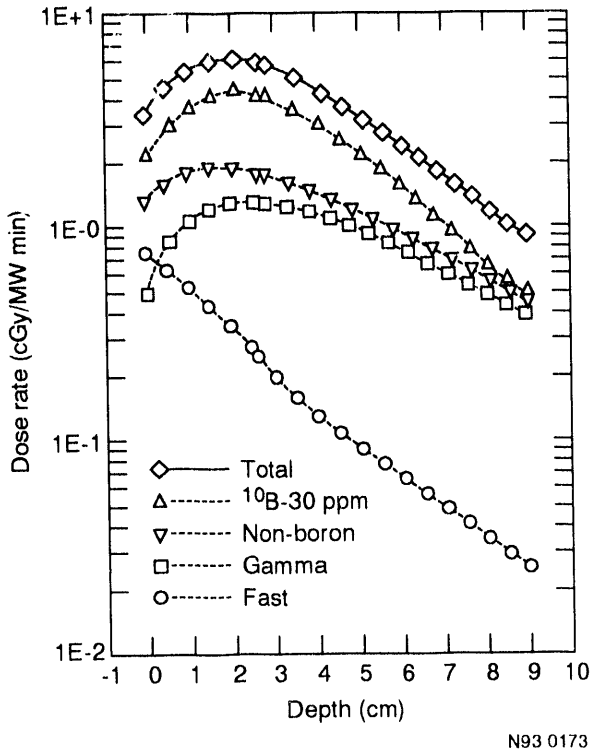

Figure 52. Calculated physical dose-depth profiles along the beam centerline for the B-spline Labrador Retriever head model.

The dose-depth curves and the contour data shown here are all for the physical dose, without RBE factors. The RBE factors for the various dose components are highly-dependent on the specific conditions of the irradiation and the biological endpoint assumed. Although it is difficult to realistically define RBE factors for BNCT purposes, it is a simple matter to include such factors in the displays if desired. The general effect of including RBE factors is to emphasize the boron neutron capture dose component and thereby to increase the calculated therapeutic advantage, provided that the neutron field in the irradiation volume is not unduly contaminated with fast neutrons. This latter stipulation is derived from the fact that the attainable therapeutic ratio in BNCT is highly-dependent on the spectral purity and monodirectionality of the neutron beam that is used. For example, the advanced, low-contaminant, highly-collimated, epithermal neutron beam that has been proposed for installation at GTRR will offer a more favorable therapeutic advantage for BNCT than the BMRR beam assumed for the examples presented here, all other conditions being equal.

Finally, note that the dose distribution data shown in the examples presented here are based on the assumption of an ideal boron distribution, that is, a therapeutic concentration of boron in the tumor and none in normal tissue. In practice, this ideal limit is not fully achieved with currently-available boron carriers (although some carriers come close), and even if boron were to be totally excluded from normal brain tissue one could still reasonably expect to have appreciable concentrations of boron in the blood as well as in the tumor. Fortunately it can be shown that the capillary endothelial cells in the brain are protected to a large extent from the boron interaction products because of microdosimetric considerations and very favorable therapeutic advantages can still be obtained.

Overview of Microdosimetry for BNCT

It is essential to consider microdosimetric phenomena when attempting to correlate absorbed dose with observed radiobiological effect in BNCT. This is particularly important in the case of the boron neutron capture dose component. As noted previously, the track lengths of the charged particles resulting from the boron neutron capture interaction are comparable to typical tissue cell dimensions. In addition, the intercellular and intracellular spatial distributions of boron within the irradiation volume are generally non-uniform and are dependent upon the characteristics of the specific boron carrier that is employed. These factors combine, at any dose level, to create a general lack of spatial equilibrium on a microscopic scale for the secondary charged particles emitted in the boron neutron capture interaction. This situation, in turn, causes the apparent RBE of the boron capture dose component in both normal and malignant tissue to be highly-dependent on both the geometry of the specific cell type of interest as well as on the localization properties of the boron carrier.

The lack of microscopic-scale charged particle equilibrium on the part of the products of the boron neutron capture interaction is further complicated by the fact that, at therapeutic dose levels, there are relatively few (on the order of 20-30, on the average) boron interactions per cell and relatively few charged particle tracks through the critical targets in the cell in BNCT, as opposed to a relatively large number of photon-electron interactions and electron tracks per cell in standard photon therapy. Thus, the statistical nature of the entire neutron interaction and charged particle energy deposition process must be taken into account. Some cells, for example, will experience radiobiologically-significant deviations from the average absorbed dose simply because the number of boron neutron capture interactions in such cells happened to be far from the statistical average.

Transport calculations required to determine the charged-particle track structure data needed for microdosimetric studies in BNCT are performed at INEL using the Monte Carlo method. In the microdosimetric charged particle transport model developed by INEL researchers, particle range-energy relationships rather than nuclear cross sections are employed, and scattering interactions are ordinarily not considered. Each particle deposits energy by electromagnetic interactions as it slows down in accordance with its specified range-energy relationship. Source particles are sampled from a measured or assumed spatial distribution, track lengths are tallied, and the results are typically output in the form of single-event energy-deposition frequency distributions for various critical target regions of interest within the cells being modeled. This information can be used to determine the average absorbed dose rate within the critical target relative to the dose rate that would exist if charged particle equilibrium existed. The geometric correction factor determined in this manner is useful when attempting to estimate RBE factors from *in vivo* and *in vitro* radiobiological response observations. In addition, the calculated energy deposition frequency distributions can be combined with appropriate microscopic radiobiological response functions (assuming that such functions are known) and, using the appropriate statistical formulations, cell response fractions can be estimated directly.

Microdosimetric phenomena can decisively affect the therapeutic advantage that is achievable with BNCT. For example, if the capillary endothelium is taken as the dose-limiting normal tissue for BNCT of brain tumors, and if one assumes the use of a boronated drug that does not cross the blood-brain-barrier and is therefore largely excluded from the capillary endothelium as well as from normal brain tissue (such as is believed to be the case with one of the most commonly-used drugs, BSH), then it has been shown analytically by INEL researchers and others that the nuclei of the capillary endothelial cells will experience significant geometric protection from the boron neutron reaction products simply because local charged particle

equilibrium does not exist. This would, in turn, be expected to cause the apparent RBE, or the so-called "compound factor" (geometric protection factor multiplied by the expected RBE for a spatially-uniform absorbed dose distribution) for damage to the nuclei of the capillary endothelial cells to be significantly less than unity. *In vivo* experimental data developed by INEL researchers (see Treatment Protocol Development section) for canines using BSH strongly support this hypothesis. On the other hand, if the intracellular boron distribution in the *target* (tumor) cells is such that there is a significantly smaller degree of geometric protection (as is thought to be the case with glioblastoma multiforme using BSH as the boron carrier), then one can obtain a very favorable therapeutic ratio even for a tumor/blood boron ratio that is not significantly greater than unity, provided that the absolute boron concentration is sufficient to cause the boron neutron capture dose to be the dominant component of the total absorbed dose at the spatial location of interest. Clearly, one must carefully consider both microscopic-scale boron carrier distribution information as well as microscopic-scale radiation transport and interaction phenomena when attempting to understand and predict radiobiological response in BNCT.

Conclusions and Future Directions

The development of analytical methods and software at INEL for performing radiation dose distribution analysis and treatment planning calculations for BNCT is proceeding rapidly. Initial software modules for reconstructing irradiation volume geometry and performing the necessary three-dimensional calculations have been completed and are being phased into production use at INEL and in Europe. Currently-ongoing efforts are focused on providing detailed, understandable output displays, medical image manipulations, tumor location capabilities and other such "user-friendly" features, similar to those that are available with advanced photon treatment planning systems. Future efforts directed toward the development and application of faster calculational algorithms for radiation transport are planned. The reason is that, even on the most advanced workstations, current execution times are somewhat long for routine clinical use; although they are quite acceptable for research applications. Computational algorithms suitable for execution on parallel machines and distributed workstation clusters as well as advanced high-order algorithms that retain the accuracy of the current methods, but with less computational effort will be investigated as priorities permit. Some examples of the latter methods may include nodal transport methods and possibly high-order diffusion theory techniques. Finally, efforts directed toward a more comprehensive understanding of microdosimetric phenomena associated with the various dose components in BNCT will continue, both in support of the evaluation and testing of proposed new boronated pharmaceuticals and for use in the interpretation of observed dose-response data from ongoing *in vivo* research.

IMPLEMENTATION OF A SINGLE PARTICLE HIGH-LET IRRADIATION SYSTEM

Dr. John M. Nelson and Dr. Leslie A. Braby, PIs, Pacific Northwest Laboratory, Radiation and Chemical Physics, Biology and Chemistry Department

Vascular endothelium is often taken as the dose-limiting normal tissue when irradiating head and neck lesions. Consequently, the response of capillary endothelial cells exposed to moderate doses of high LET particles is essential for establishing exposure limits for neutron-capture therapy. Such doses would be deposited by a relatively small number of randomly occurring charged particle tracks. However, due to the large variance in the number of particles that might pass through individual cells at these doses, it is difficult to define the biological effects of a specific number of tracks. Linear extrapolation from the results of experiments at larger doses, where the variance is more reasonable, may not be suitable for predicting the effects of small numbers of particles.

When low- and high-LET radiations deposit similar amounts of energy in a given volume, the energy deposition on a microscopic scale may still be far from equivalent. Low-LET x and γ rays tend to deposit their energy uniformly throughout a large tissue volume because each interaction deposits only a small amount of energy. Large numbers of interactions occur within cells at moderate doses, and multiple tracks occur in 7 μm diameter volumes (about the size of a cell nucleus) at doses as low as about 0.01 Gy. In contrast, high-LET particles deposit large amounts of energy along their tracks. Even at moderate doses, for example 0.4 Gy, there is an average of only a single charged-particle track per cell. At this level, approximately one third of the cells receive no dose; a third of them received doses ranging between zero and about 0.6 Gy, the maximum produced by a single track; and about a third of them are traversed by two or more tracks, receiving a dose which is usually more than 0.4 Gy. At one tenth this dose, 0.04 Gy, 90% of the cells are not hit at all and the remaining 10% receive doses between zero and 0.6 Gy; essentially no cells receive double tracks.

Beam-segment irradiation experiments with large doses of high-LET particles have yielded radiobiological data with reasonably small variances. However, linear extrapolation from such experiments cannot reliably predict the effects of a small number of particles, because there is no assurance that this dose-effect relationship is linear at low doses. The assumption cannot be made that because the dose effect is linear at high doses, it will continue to be linear all the way to zero. It is also not possible to define biological effects from very low-dose track-segment irradiations, because of the large variances associated with the effects at those low doses. More problems arise from the fact that the morphology of mammalian cells in culture is such that it is difficult to determine the exact cross section of the cell nucleus, creating uncertainty in the estimates of the number of alpha particles necessary for cell inactivation.

In order to predict radiation effects in healthy tissue, the probability of damage production as a function of the number of particles traversing the nucleus, and the stopping power of these particles is needed. Such data can be obtained by irradiating individual cells, one at a time, with predetermined numbers of accelerator-produced high-LET particles, which pass through or stop within individual cell nuclei. This requires precision beam collimation to limit exposure to the portion of the cell being irradiated, a detector to count each particle as it interacts with the cell, and a beam line shutter to stop the irradiation at the desired number of particles.

PNL researchers have designed and built such a system, and are presently using it to irradiate SVEC4-10 endothelial cells with 1 to 5 MeV α particles. This single-cell irradiation apparatus allows researchers to expose single cells to known numbers of high-LET particles, to follow these cells for extended periods, and to assess the effects of individual particles on cell growth

kinetics. Cells are irradiated as a sparse monolayer on 1.5 μm thick Mylar® film that forms the bottom of specially fabricated Petri dishes. Following irradiation, the growth of individual cells is followed using an automated video time-lapse microscope system. Clonogenic-cell survival and growth characteristics, for example, time between divisions and reproductive competence of both daughter cells, are monitored for several generations.

Preliminary cell irradiation experiments revealed several complications that are currently being resolved. Those problems of most concern are related to the smooth and efficient operation of the equipment. Consequently, much effort during the past year has been directed toward the requirements for single-cell irradiation, improvements in the apparatus, and testing of the experimental procedures.

The single-cell irradiation apparatus is shown schematically in Figure 53. The particle beam, produced by a 2 MeV National Electrostatics, Corp. tandem accelerator, is bent vertically below the exposure port. In its present configuration, the beam is collimated to a square beam ~0.5μm on a side by two sets of knife edges set 6 and 22.5 cm below the exit window. It exits vertically upward through the center of a 5.0 μm aperture covered by a 1.5 μm Mylar® film. Immediately above this window is a small piece of scintillation film that

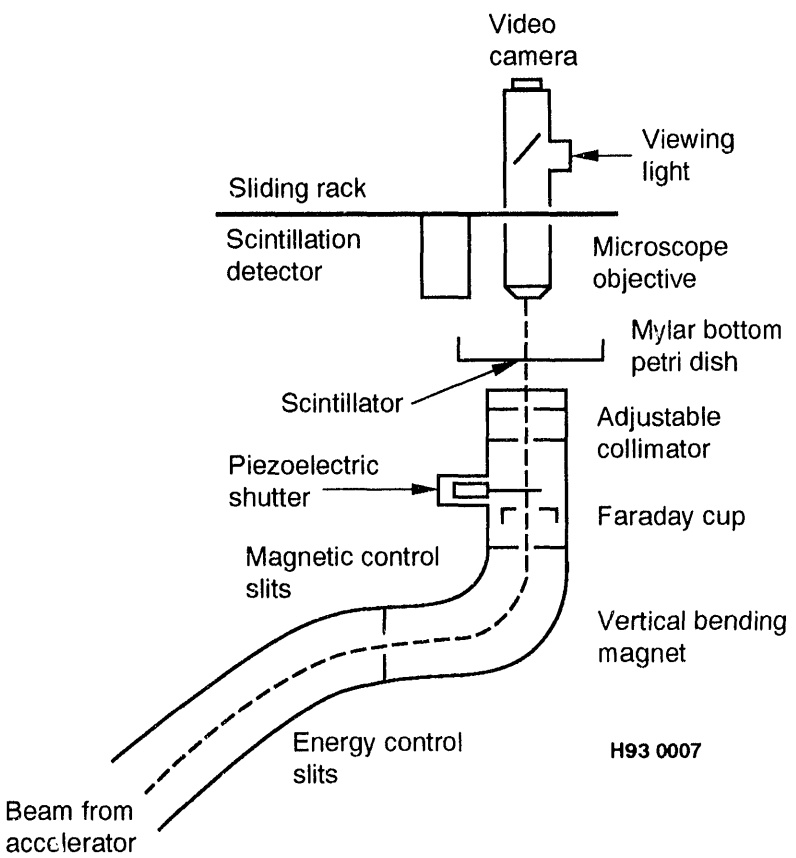

Figure 53. Schematic diagram of the single particle irradiator. (The beam is bent vertically upward; single particles pass through the nuclei of cells growing on the Mylar® film.)

produces light signals as each particle passes. This scintillator is used to count the individual particles. Cells to be irradiated are allowed to attach to the Mylar ® bottom of a specially fabricated Petri dish; this dish sits immediately above, and in contact with, the scintillator. The proximity of the Mylar® film to the scintillator reduces scatter. The whole assembly is surrounded by a Zeiss Axiomat ® microscope equipped with phase optics. When in use, the dish containing cells attached to the Mylar® film is positioned on the microscope stage within a light-tight box. The entire apparatus, except for the accelerator itself, is remotely operated from a console with a computer terminal and oscilloscope.

A reflected-light (epi-illumination) rather than a transmitted-light optical system is used because there is no room beneath the stage for condensing optics. Because the light intensity cannot be significantly increased without distorting the scintillator or even the Mylar® window itself, an image intensifier is needed to amplify the very small fraction of light reflected by the cells with this optical system. Output from a video camera mounted on the microscope headpiece is digitized by an image processor and displayed on a monitor for cell recognition. During each cell irradiation, the objective lens is replaced by a photomultiplier tube (PMT). Once the PMT is in place, a very fast-acting piezoelectric shutter opens and allows particles to pass through the aperture, beginning the irradiation.

Scintillation pulses are counted by a subroutine in the control computer. After a predetermined number of particles have passed through the scintillating film, a piezoelectric shutter is closed. Since this shutter closes in about 200 μsec, irradiations with only single particles can be made with beams of around 500 particles per second. Figure 54 shows an image of the beam, made by exposing a piece of the radiachromic film which turns blue with exposure to ionizing radiations. The film was positioned at the location of the film to which cells would be growing.

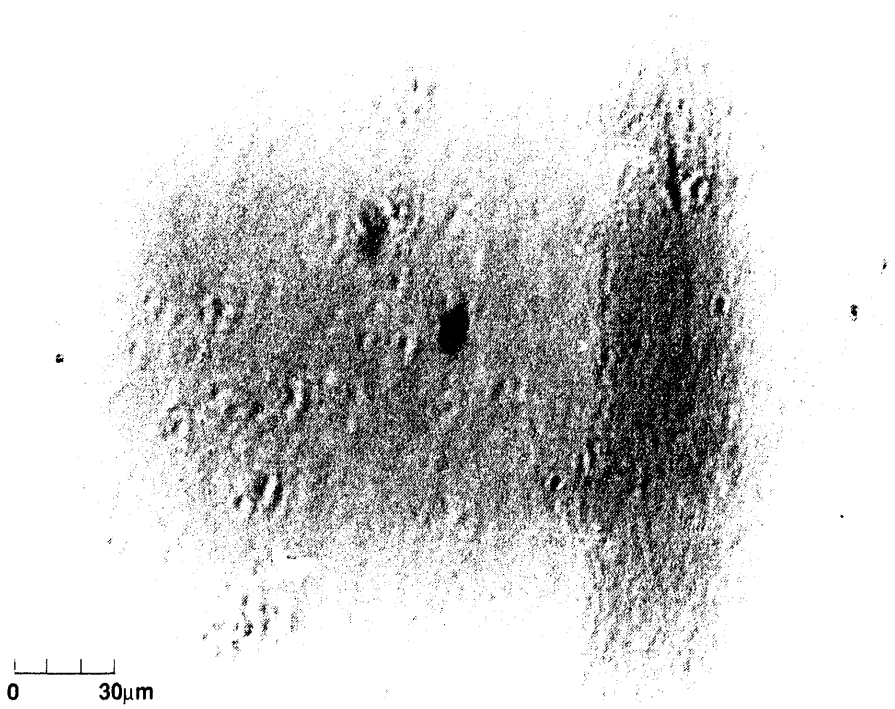

Figure 54. Image of a 7-8 μm beam made by placing a piece of radiachromic film on the Mylar® surface of the culture dish, opening the shutter, and exposing it to a large number of particles.

A variety of particle beams are available with this apparatus, as can be seen in Table 6. Note that a significant amount of energy is lost as the beam passes through the exit window, the plastic scintillator, and the film to which the cells are attached. This energy loss is sufficient to cause lithium ions to stop within the nucleus of attached and even relatively flattened cells.

After investigating several cultured endothelial cell lines, including a bovine adrenal medulla endothelial line (EJG) and a bovine pulmonary artery endothelial line (CPAE), both from the American Type Culture Collection, a transformed murine endothelial cell line (SVEC4-10), and a bovine endothelial cell line from WSU, we chose the SVEC4-10 of O'Connell and Edidin (1990) for our studies.[50] This is a mouse leukocyte endothelial cell line, derived from lymph-node stroma and transformed by infection with SV40. The SVEC4-10 cells, which retain many of the morphological characteristics of *in situ* capillary endothelium, seemed most promising for studies of cell survival and function, and PNL researchers have concentrated on characterizing these cells, determining their growth requirements, and establishing culture conditions suitable for their use in the single-particle experiments.

In the laboratory, monolayer cultures of SVEC4-10 cells are carried by twice-weekly serial passage in polystyrene culture flasks (Falcon 3024 or Corning 25110). Since their acquisition, cells from the 3rd to 5th passages were preserved by storage under liquid nitrogen. Because of the interesting growth characteristics of the SVEC4-10 cell line, only cells from cultures between the 6th and 15th passage (at PNL) have been used for these experiments. They are maintained in Dulbecco's modification of Eagle's Minimum Essential Medium (DME), modified according to the GIBCO (Grand Island, NY) dry-powder formulation (Cat. No. 430-1600EP), supplemented with 10% fetal calf serum, 100 i.u./mL K-penicillin, and 100 μg/mL streptomycin-SO_4. After preparation, medium osmolarity was adjusted to 285-295 mOsM. Cell cultures are grown in an incubator held at 37°C, under a water-vapor-saturated atmosphere of 5% CO_2 in air. Figure 55 shows the characteristic growth pattern of SVEC4-10 cells in DME medium. For reference purposes and to determine that the radiation sensitivity of SVEC4-10 cells was not dissimilar from that of most other cultured mammalian cells, researchers measured survival of these cells to 250 kV x rays. As shown in Figure 56, although they appear somewhat more sensitive than Chinese hamster ovary cells, the difference in sensitivity is probably not significant.

Cells to be irradiated are plated into specially designed and manufactured Petri dishes constructed with a 1.5 μm (0.06 mil) Mylar® bottom, Figure 57. They attach to the Mylar® and grow equally well as on the polystyrene substrate of standard commercial plastic culture dishes. After 60-90 minutes, the cells are firmly attached and the culture dish can then be placed into the holding assembly on the end of the micropositioner arm. Held in this manner, each cell can then be positioned in the X-Y plane directly over the exit window, with a resolution of about 0.2 μm. The culture medium remains over the cells throughout the entire irradiation procedure. As

Table 6. Particle beams available for single-cell irradiation studies.

Particle	Initial energy (MeV)	Energy in cell (MeV)	Stopping power (KeV/μm)
Proton	2-4	1.8-3.9	9.8-17.6
Deuteron	2-4	1.7-3.8	17-32
Alpha	3-6	1.7-5.2	83-230
Lithium	3-6	0-3	Stop in nucleus

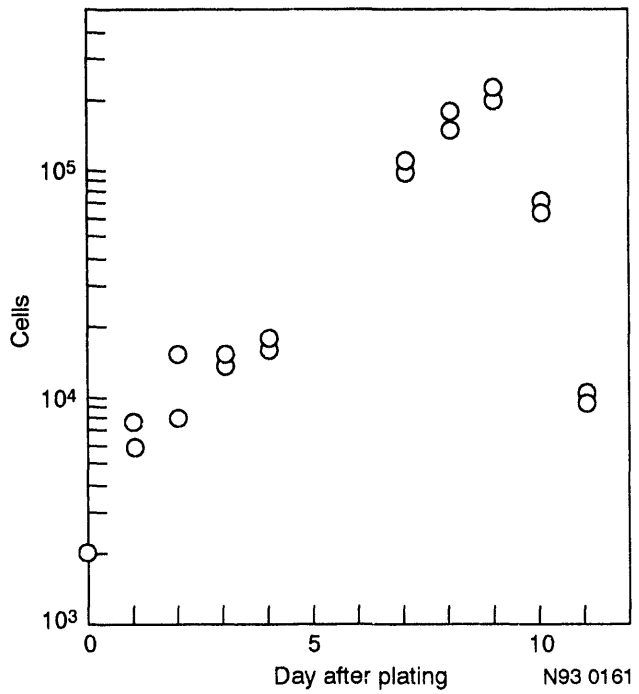

Figure 55. Although SVEC4-10 cells appear quite similar to many other cell lines, their growth appears to be poorly regulated and the cultures become overgrown at relatively low densities.

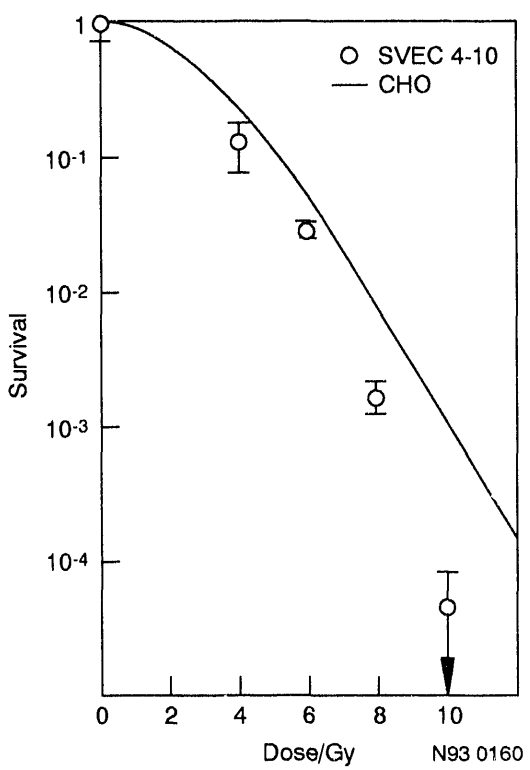

Figure 56. X-ray survival data for SVEC-10 cells relative to CHO cells. (Although the SVEC4-10 cells appear somewhat more sensitive, this difference is probably not significant.)

Figure 57. Cells are typsinized, plated at low density (~5 cells/mm^2), and allowed to attach firmly to the Mylar® bottom of the dish. (Surviving cells will grow into visible clones in 5-7 days.)

described, these cells are viewed using the video microscope optics. The resolution of our video system is set by the image processor at about 1 μm, that is each pixel represents 1 μm on the Mylar® film.

After the accelerator has been finely tuned to provide the desired beam through the small exit window of the apparatus, the Mylar® bottom culture dish is installed onto the X-Y positioning arm as described, and the light-tight box enclosing the microscope is sealed to minimize background in the PMT. Identifying, positioning, and irradiating individual cells is then done completely from the console. The procedure is summarized as follows:

- Mark each cell in the microscope viewing frame
- Move to the first cell
- Position the cell nucleus over the exit window
- Replace the microscope objective lens with the PMT
- Open the beam shutter
- Count the particles that pass through the scintillator
- When the desired number of particles has passed, close the beam shutter
- Move to the second cell selected in the field
- Replace the PMT with the microscope objective lens
- Position this cell over the exit window and repeat until all marked cells have been irradiated
- Move to next video frame and start the repeat procedure.

This procedure is repeated from one frame to the next within the chosen area of the culture dish. Presently, it takes about 30 seconds to find and

irradiate a single cell. For split-dose irradiations, it generally takes about nine seconds to return to any cell and deliver the second dose.

Following the irradiation of all cells within a given area of the Petri dish, the dish is removed from the irradiation apparatus and placed into a miniature incubator built onto the stage of a Zeiss ® inverted microscope. This small but sophisticated incubator maintains the cultures at 37°C under a water-vapor saturated atmosphere consisting of 5% CO_2 in air. As with the irradiation apparatus, movement of the microscope stage is also controlled by stepping motors which are used to position individual fields containing cells to be followed to within 1 μm accuracy. Its movement is controlled by a computer that records all stage motions and uses this information to return to each of several hundred selected positions, and record additional images at specified intervals over several days. The computer also coordinates the assembling of these video images to form time-lapse sequences of each cell. Figure 58 illustrates such a sequence of images. In this figure, only selected images have been included to illustrate the growth progression of each individual endothelial cell.

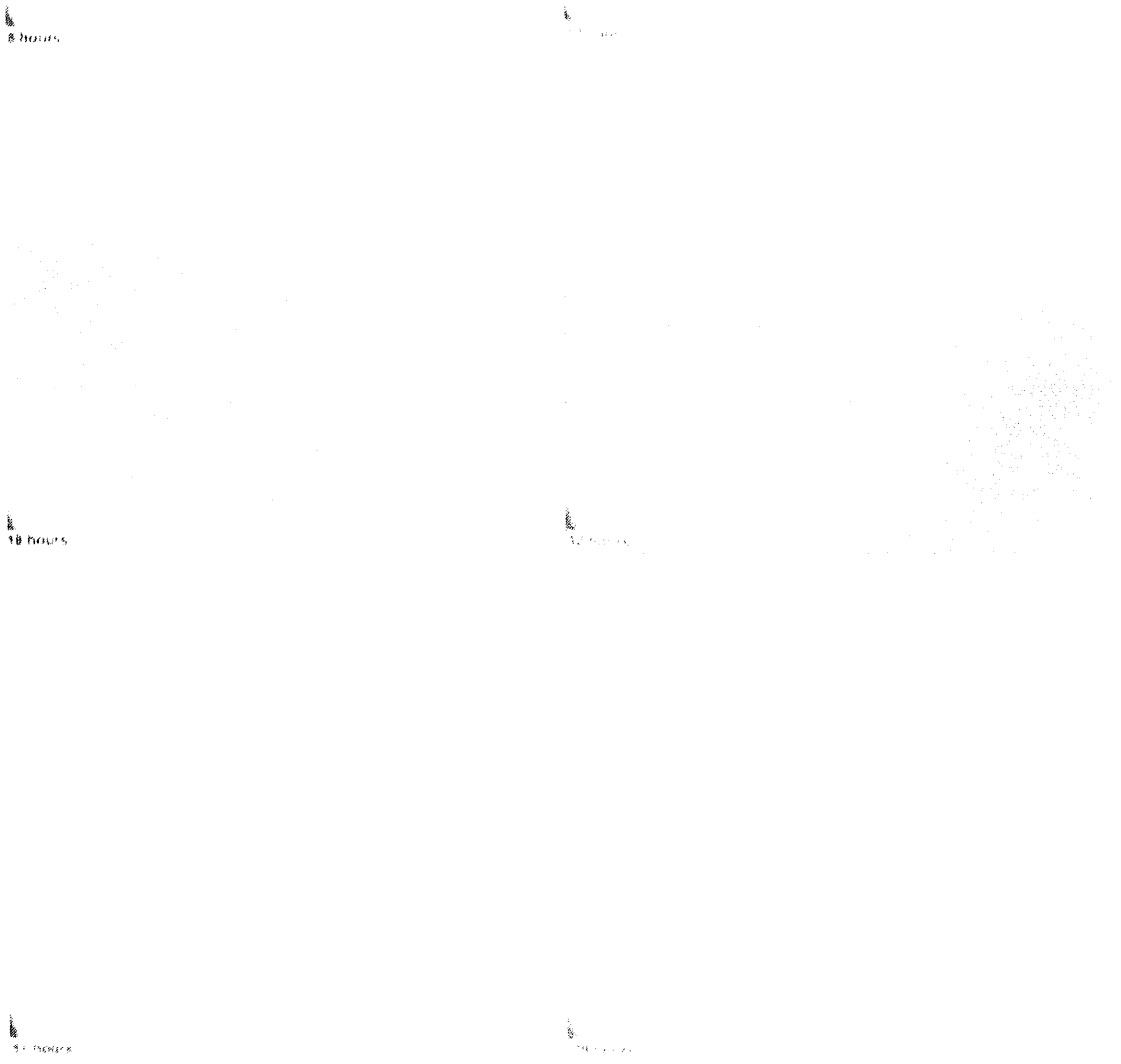

Figure 58. Set of images, assembled from one of the time lapse sequences, demonstrating both the precision movement of the motor controlled stage and the quality of the growth environment within the incubator.

ANALYSES OF BORON IN BIOLOGICAL SAMPLES

Dr. Bill Bauer, Analytical Chemistry, INEL

Introduction

A recent resurgence of interest has developed concerning the use of BNCT[51,52,53] for a variety of tumor types that are not treatable using established therapies. In BNCT, a patient is administered a boronated molecular species (enriched in ^{10}B) that localizes in the tumor through various mechanisms that are dependant upon the tumor type and location. A very important aspect of the continuing research being performed on BNCT is the need to accurately and precisely determine boron concentrations at relatively low levels of boron in biological samples. This need arises from the fact that while the boronated species do localize in the tumor tissue, they also localize, in varying degrees, in other tissue and in organs such as the kidney and the liver. Thus, prior to utilization of a specific boronated species in BNCT, it is necessary to determine the biodistribution of this compound in a statistically significant population. This requires a large number of samples to be processed in a timely fashion. Thus, the preferred method used for total boron analysis in tissues must possess the following characteristics. The method should not be dependant upon the chemical form of the boron, should be relatively fast and easy, and should be capable of accurately determining boron concentrations over a relatively wide range.

Atomic absorption (AA) spectroscopy (AAS) would initially seem to be an ideal method for this analysis, but the usefulness of flame AA is limited by the relatively high detection limits and short linear dynamic range, while flameless (graphite furnace) AA is plagued by the memory effects caused by the formation of a stable carbide species[54]. Colorimetric methods[55,56,57] are also hindered by relatively short linear dynamic ranges, lengthy procedures that require much sample handling, the need to convert all of the boron to the same chemical form, and often involve the use of potentially hazardous chemicals. Prompt gamma analysis[54,58,59] would be an ideal technique since it has a relatively large linear dynamic range and does not require any pretreatment of the samples. However, prompt gamma analysis requires a nuclear reactor, thus making it expensive or inaccessible to many BNCT researchers. An additional problem is that only ^{10}B is actually measured, thus counting statistics limit its effective use with very small sample sizes (0.1g) with low boron concentrations.[59,60]

The technique that currently demonstrates the most promise for meeting all of the analytical criteria is ICP-AES, which has been shown to be a very versatile technique for the determination of boron in many different matrices.[61-66] This method combines relative ease with a long linear dynamic range and detection limits of less than 10 parts-per-billion in solution. An additional advantage of an ICP-AES procedure is that it can easily be modified to include other elements, such as tracer elements, in the analysis. The major problem with this technique stems from the requirement that all solid samples be converted to a liquid form prior to the analysis.

Dry ashing prior to dissolution has been used effectively for the preparation of dried plant samples[56,57] prior to colorimetric analysis for boron, but no reliable data has been obtained for animal tissues with this method.[55] Alkali fusions were also successful in the preparation of biological samples for colorimetric analysis,[55] but this procedure appears to be relatively labor intensive as it requires very careful technique, and is thus unsuitable for the large scale preparation of samples (> 40 samples/analyst/day).

More recently, sample preparation procedures for the ICP-AES determination of boron in animal tissues have been reported.[64,65] One involves the use of perchloric acid and hydrogen peroxide,[64] the other nitric acid and hydrogen peroxide.[65] The major drawback to the perchloric acid method is the specialized equipment and training required for the safe handling of perchloric acid. In addition, preliminary experiments at the INEL suggested that this test tube digestion

method was incapable of completely dissolving certain biological samples and thus might be incapable of completely extracting the tissue incorporated boron. The direct combination of perchloric acid and hydrogen peroxide also causes some concern since perchloric acid is not normally considered to be a strong oxidizing agent at concentrations less than 50% and temperatures less than approximately 60°C and, even though hydrogen peroxide is a strong oxidizing agent, its action is slowed considerably in acidic solutions.[67] The procedure employing nitric acid and hydrogen peroxide is hampered by the time consuming and potentially labor intensive steps of evaporating the sample to near dryness, cooling, redissolving, and reheating the sample.

Since 1987, the EG&G Idaho, Inc. Analytical Chemistry Unit, with laboratories located in the Idaho Research Center (IRC) at INEL, has been involved in developing methods for total boron analysis in biological samples to meet the various needs of the INEL BNCT program. The techniques and analytical methods described in this section are the result of those six years of involvement with BNCT. All methods described involve the use of AES for the reasons described previously. The initial method development will be described as well as modifications to those methods, including a study comparing several methods for digesting tissue samples. Methods for rapid boron analysis using flow injection analysis and slurry nebulization of whole blood will also be described. A method for quantitation of nanogram quantities of boron in milligram-sized tissues will also be described.

ICP-AES Method Development

Initial work for the analysis of total boron in biological samples was performed utilizing the AAS as an analysis tool. It quickly became apparent that the limited linear dynamic range of flame AAS and the relatively poor detection limits were inadequate to determine B at low µg/g in biological samples. Attempts at using graphite furnace atomic absorption spectroscopy (GFAAS) were also unsuccessful due to the formation of boron carbides that caused unacceptable sample-to-sample carryover. The problems with the limited linear dynamic range, detection limits and carry over observed with AAS were readily overcome with ICP-AES.

This section of this report describes the development of methods for the analysis of boron in various biological samples including urine, blood plasma and serum, blood, and tissues with ICP-AES. As a method of verification of the developed methods, a comparison was made between results obtained by the ICP-AES method and by the standard prompt-gamma technique using the same samples.

Experimental Methods

Preparation of Urine and Plasma Samples. Urine and blood plasma samples are simply prepared by dissolving a weighed 0.1 g sample in deionized water and diluting to 10 mL in a volumetric flask. The samples are then transferred to polypropylene bottles for storage until the ICP-AES analysis is performed.

Preparation of Tissue Samples. Tissue samples are prepared by adding 10 mL of concentrated, ultrapure nitric acid (J. T. Baker Ultrex) to a weighed 0.5 to 1.0 g tissue sample in a Teflon-lined acid digestion bomb (Parr model #4748). Prior to sealing, the bombs are spiked with 50 µg of a 1000 µg/mL scandium standard (to make 2 ppm in the final solution) for use as a recovery standard. The bombs are then sealed and heated to 150°C for three hours in an oven. The completely digested samples are then transferred to a 25 mL volumetric flask, spiked with 50 µg of a 1000 ppm yttrium standard (to make 2 ppm in the final solution) for use as an internal standard and diluted to the volume. The digested sample solutions are then transferred to polypropylene bottles for storage until analysis.

ICP-AES Analysis of Prepared Samples. Calibration curves are prepared for each matrix using five standards, one of which is a blank. The standards for the urine and plasma determinations are prepared in deionized water and standards for the tissue digests are prepared in 35% v/v nitric acid, as this most closely resembles the matrix of

the sample digests based upon a comparison of the intensities of known concentrations of a reference element in standard solutions and sample digests. Actual ICP-AES determinations of boron are done using both the B I 208.959 nm emission line, since it is essentially free from spectral interferences, and the B I 249.678 nm emission line. The latter line was selected as it is less likely to be interfered with by iron than the more sensitive 249.778 nm B I emission line. Two lines were selected to assure the quality of the results by identifying situations where a potential interference or background problems occur. Spikes and duplicates are prepared for both matrices to further assess the accuracy and precision. Alternately, the B I 182.59 nm emission line can be used if unexpected interferences are noted with either of the other 2 emission lines; however, very high concentrations of sulfur may interfere with analysis at this line.

Internal standards are used for analysis of the tissue digests to correct for errors caused by the differing aspiration rates of the samples into the ICP. Varying aspiration rates are potentially due to differences in the viscosity, salt content or amount of suspended particulate matter in the samples. Internal standardization and quantitation is done by ratioing the net intensities of the analyte signals (boron and Sc II at 361.384 nm) to the net intensity of Y II 371.030 nm. These ratios are then plotted versus concentration to obtain the standard curves for the analytes. The concentrations of the unknown samples are taken from these curves using the appropriate ratio. Typical recoveries of scandium (the recovery standard) from the digest solutions are 100 ± 1%.

Prompt-γ Analyses. Prompt-γ analyses were performed at the BMRR by the method described in reference 59 by R. Fairchild, P. Micca and J. Coderre. Generally, this procedure consisted of weighing 1 g of the biological sample into a quartz test tube, irradiating with thermal neutrons and counting for 200-300 seconds. Peak counts from the 478 keV prompt-γ-ray peak of boron are background corrected and ratioed to the 2.23 MeV capture γ ray peak of hydrogen.

Results and Discussion

Initial Analyses and Matrix Spike Recovery Problems. Initially, digested samples were prepared and the analyses performed without the addition or use of internal or recovery standards. Standards were prepared to match the sample matrix as closely as possible, that is, 20% HNO_3 (v/v) assuming that some HNO_3 was used up in the oxidation of the samples. The viscosity of these standards appeared similar to the digested samples. Quality of the analyses was monitored via matrix duplicates and spikes with boron in the form of boric acid and occasionally as $Na_2B_{12}H_{11}SH$. After compiling and examining the representative boron spike recovery data shown in Table 7, it became obvious that there was a problem with the analysis procedure used to quantitate boron in biological tissues. The problem did not appear to be with the tissue sampling for the digestion procedure or the digestion procedure itself since in many cases, duplicate samples were usually reasonable even though the recovery of the 10 to 20 microgram boron spikes was consistently low. The spike recoveries were low even with tissue samples that had been ground and homogenized (see results for Dog 1 in Table 7) and spiked bomb blanks.

Since there seemed to be no reasonable way that the boron could escape from the bomb, it was concluded that the inaccuracies were probably due the uptake rate and nebulization of the of the solutions into the ICP itself. To this point, the samples were being freely aspirated by the nebulizer into the spray chamber and the 20% acid content of the standards produced a similar aspiration rate as that of the samples, however the aspiration rate of the samples was not consistent. Addition of a peristaltic pump to the sample introduction system succeeded in delivering all solutions to the nebulizer/spray chamber at a constant rate, but the mean recoveries of the spiked samples still did not improve. The problem was then thought to be related to a difference in the matrices between the 20% HNO_3 standards and the digested sample solutions containing an undetermined concentration of acid. Molecular and spectral interferences are

Table 7. Spike recovery data for 10 to 20 microgram spikes to tissue samples prior to acid bomb digestion.

Dog	Tissue	Percent recovery
Ch	Heart spike with BSH compound	113
Ma	Temporal muscle	90
Am	Liver	76
Am	Spleen	81
Am	Tumor Site #1	70
Sl	Cerebral grey	73
Sl	Tongue	101
	Spiked bomb Blank-1	84
Sl	Calvarium	90
Mi	Heart	75
Dog 1	Kidney (homogenized)-sl	82
Dog 1	Kidney (homogenized)-s2	66
Dog 1	Kidney (homogenized)-s3	73
	Spiked blank Spiked-2	88
Mean recovery		83
Standard deviation		13

rare in ICP-AES, however, matrix effects related to both nebulization and the ICP itself are known. In this particular analysis, plasma effects were not considered significant since maximum elemental concentrations in a 25 mL sample resulting from a 1 g (wet) sample would usually be less than ~400 µg/mL. Plasma effects are most often noted for ionic emission lines when elements with reasonably high ionization potentials are present in relatively high concentrations.[68] Nebulizer-related matrix effects are due to such physical properties as density, viscosity and surface tension.[68] These parameters affect the size of the droplets formed by the nebulizer which in turn affects the analyte transport to the plasma. Mineral acids have been shown to have dramatic negative effects on the sensitivity of both ionic and atomic emission lines.[68,69] Variation of the acid content of the standards used for calibration and subsequent analysis of the tissue sample digests produced the boron spike recovery results shown in Table 8.

As seen in Table 8, increasing the acid content of the standards improved the spike recoveries and resulted in a general increase in the concentrations determined for the samples as predicted from the trends shown in reference 69. The data in Table 8 indicated that the problem causing the low boron spike recoveries was due primarily to a physical effect resulting from solution differences causing changes in the nebulization and transport of the sample and analyte to the ICP. Since researchers felt reasonably confident that plasma effects due to high salt concentrations and large variations in acid content were limited, it was decided that a better way to deal with the matrix problem would be to use an internal standard to compensate for any instrument drift and the physical differences from standard to sample

Table 8. Effect of varying the acid content of the standards.

Dog	Tissue	Percent acid in standard	Original µg B/g	Spike[a] or duplicate µg/g	Duplicate RPD[b]	Spike percent recovery[c]
Ro	Cerebral white	0	1.35	8.51	—	62
		20	1.32	9.33	—	69
		30	1.32	9.95	—	74
		40	1.62	13.25	—	100
Ro	Brainstem	20	2.52	2.34	7.4	—
		40	2.78	2.54	9.1	—
Ma	Cerebral grey	20	0.93	9.27	—	72
		40	0.87	10.62	—	84
Ma	Liver	20	20.54	19.67	4.4	—
		40	25.27	22.42	12.0	—

a. Samples were spiked with ~ 10 µg B.

b. RPD = Relative Percent Difference = | difference * 100 | ÷ mean.

c. Spike recoveries have been corrected for the mass of the sample.

and sample to sample.[70,71] The method of standard additions is generally recommended for compensating for physical matrix effects when matrix matching is not possible.[68] However, the method of standard additions increases the time per analysis by at least a factor of 2, and was therefore determined to be unacceptable, since the ultimate goal was to develop a method for the routine analysis of total boron in thousands of tissue samples. Selection of an appropriate internal standard element for atomic emission spectrometry is difficult. It has been suggested that for general emission spectrometry, consideration be given to the excitation energies, ionization energies, and atomic weights of the analyte and the internal standard elements.[72] For ICP-AES, these general rules do not apply often and it has been shown that the "hardness" or "softness" of the emission lines and the response to various plasma parameters are more important considerations for internal standard element and line selections.[70,71,73] Many atomic and ionic emission lines with similar "hardness" appear to behave similarly given a set of compromise plasma conditions.[70]

Selection of an internal standard element that mimics boron is difficult since boron has a relatively high ionization potential; it is only about 58% ionized in an ICP with an ion temperature of 7500°K.[74] Also, very few elements with reasonable emission characteristics behave chemically like boron, and would not normally be found in tissue samples or are nontoxic. For these reasons, elements such as As, Si, Zn or Te were determined to be unsuitable choices for internal standards. The elements Sc and Y were selected as potential substitutes, primarily since they are unlikely to be present in a normal tissue sample and since overcoming a nebulization and transport problem was still the only real consideration.

Association for Information and Image Management
1100 Wayne Avenue, Suite 1100
Silver Spring, Maryland 20910
301/587-8202

Centimeter

Inches

MANUFACTURED TO AIIM STANDARDS
BY APPLIED IMAGE, INC.

2 of 2

Table 9. Analysis results with Sc spiked to previously digested samples for use as an internal standard to quantitate B.

Dog	Tissue	Scandium intensity mV	Boron concentration µg/g	Duplicate RPD[a]	Spike percent recovery
Calibration Standards		2270 ± 12	—	—	—
Sl	Tongue	2064	4.17	—	—
Sl	Tongue spike	2185	14.34	—	97
Sl	Peritumor #3	2183	5.33	—	—
Sl	Peritumor #3 dup	2068	2.71	65.2[b]	—
Sl	Cerebral grey	2161	1.61	—	—
Sl	Cerebral grey spike	2010	9.89	—	—
Ro	Brainstem	2108	3.19	—	—
Ro	Brainstem dup	2118	3.09	3.2	—
Ma	Cerebral grey	1954	1.39	—	—
Ma	Cerebral grey spike	1874	12.51	—	96
Ma	Liver	2145	23.60	—	—
Ma	Liver dup	2062	24.04	1.9	—

a. RPD = Relative Percent Difference = | difference * 100 | ÷ mean.

b. Edematous peritumor tissue from the area of the brain in very inhomogeneous.

For an initial test, scandium was selected as the internal standard and 20 µg of Sc was spiked to 10 mL (2 µg Sc/mL) of some previously digested and analyzed sample solutions. The boron standards were prepared in 20% HNO_3 and spiked with an appropriate amount of Sc to make them 2 µg/mL. Boron emission intensities were ratioed to the Sc II 361.384 nm emission line. The results from these analyses are shown in Table 9. Comparing the spike recovery for the same dog (Ma) cerebral grey digest quantitated with (Table 9) and without (Table 8) an internal standard was quite encouraging as the recoveries improved from 72–84% to 96%. The relative percent difference (RPD) between solutions of the same replicate digestions of Ro brainstem and Ma liver also improved dramatically with the addition of the internal standard to the analysis. Also note in Table 9 is that the net peak intensity of Sc for the solutions of the various sample digests was lower and varied quite dramatically when compared to the consistency found in the calibration standard solutions.

Since the addition of Sc to the digests for use as an internal standard seemed to improve the spike recovery and duplicate sample results, the digestion procedure was changed and new digestions were performed in which 50 µg of Sc was spiked directly onto the tissue in the digestion bombs prior to sealing and putting them in the oven. Prior to the final dilution to 25 mL, the samples, now in volumetric flasks, were also spiked with 50 µg yttrium. The resulting solutions contained 2 µg/mL each of Sc and Y. The analysis results using Sc as the internal standard are shown in Table 10. Once again, note that the Sc peak intensities are lower and vary widely compared to the Sc intensity of the standards. The boron spike recoveries, are on the whole, much better than those obtained without the use of an internal standard (Table 7). The over recovery of the spike to

Mi lung is not a great concern since the tissue concentration was ~5 times the spike level and a 5–10% sampling error or tissue inhomogeneity would easily cause a 20–40% error in the spike recovery.

There was also some concern over the ability to transfer the B containing sample quantitatively from the bomb to the volumetric flask for the final dilution. To investigate the possibility of any procedural losses of analytes, Y was used as the internal standard to quantitate Sc and B after the digestion. The emission intensities of both Sc and B were ratioed to the Y II 371.030 nm emission line. The results of these analyses are also shown in Table 10. When Y is used as the internal standard, the B concentrations, replicate RPDs and spike recoveries are approximately the same as when Sc is used as an internal standard. The Sc was recovered with an error of no more than 1.5% indicating a quantitative transfer of the sample from the bomb to the volumetric flask. A conclusion is that as internal standards, Y and Sc behave nearly the same and that the use of an internal standard is imperative for accurate and precise measurement of boron in acid digested tissue samples. Using Y as an internal standard, Sc can be used as a recovery standard to verify sample transfers and overall integrity of the analysis.

Validation of Procedure for the Quantitative Analysis of Total B Using Acid Bomb Digestions and ICP-AES with Internal Standardization. Initially most of the samples quantitated by ICP-AES in the INEL laboratory were from dogs that had been administered boron in the form of disodium-mercapto-undodecahydro-closo-dodecaborate ($Na_2B_{12}H_{11}SH$ or BSH). Some typical results for one such case are shown in Table 11. The relative accuracy and precision of the analyses are indicated by the good recoveries of the spiked samples, the low RPD of the duplicate samples and the low relative standard deviation (RSD) of the replicate analyses of a single sample solution. This agreement is particularly good for the serum samples, which is expected since these can be

Table 10. Results for tissue digestions with Sc and Y as internal standards. (Sc was spiked into the digestion bomb prior to digestion and Y was added just prior to the final dilution.)

				Scandium as IS		Yttrium as IS	
Dog	Tissue	Scandium intensity mV	Yttrium intensity mV	Boron duplicate RPD[a]	Boron spike % recovery	Boron spike % recovery	Scandium % recovery
Calibration standards		1550 ± 7	1016 ± 14	—	—	—	—
Mi	Lung	1129	852	—	—	—	100.5
Mi	Lung spike	1148	858	—	142	137	100.5
M	Spiked bomb blank	1435	934	—	104	103	99.5
Am	Spleen	1150	785	—	—	—	101.5
Am	Spleen spike	1398	908	—	99	99	101.5
A	Spiked bomb blank	1424	928	—	99	99	101.5
Sl	Spleen	1383	—	—	—	—	—
Sl	Spleen duplicate	1418	—	9.0	—	—	—
Sl	Spleen spike	1419	—	—	94	—	—

a. RPD = Relative Percent Difference = | difference * 100 | ÷ mean.

Table 11. Typical ICP-AES boron analysis results of tissue samples from a dog that had been administered B in the form of $Na_2B_{12}H_{11}SH$.

INEL No.	Tissue	N	Tissue concentration µg B/g	Standard deviation	%RSD	Duplicate RPD[a]	Spike percent recovery
716	CSF post-mortem	4	3.1	1.0	31.2	—	—
717	Serum 50 minutes	4	14.0	0.9	6.3	—	—
718	Serum 65 minutes	4	74	2	2.9	—	—
719	Serum 80 minutes	4	116	3	2.6	—	—
	Duplicate	4	113	3	3.0	1.9	—
720	Serum 100 minutes	4	146	3	1.8	—	—
721	Serum 110 minutes	4	168	4	2.3	—	—
722	Serum 170 minutes	4	121	3	2.7	—	—
	Spike	4	219	2	1.1	—	99.6
723	Serum 290 minutes	4	82	2	2.6	—	—
724	Serum 410 minutes	4	71	2	3.1	—	—
715	Boron infusion solution	4	3167	28	0.9	—	—
	Mean % RSD for samples prepared by simple dilution				5.1	—	—
681	Right retina	4	22.7	0.5	2.2	—	—
682	Brainstem	4	3.3	0.3	7.6	—	—
683	Cerebral white	4	1.1	0.2	22.2	—	—
685	Left inguinal mass	4	40.7	0.4	1.1	—	—
686	Anterior Tumor I	4	22.6	0.3	1.3	—	—
687	Caudal Tumor I	4	33.0	0.4	1.1	—	—
689	Cerebral grey	6	1.5	0.2	13.3	—	—
	duplicate	6	1.6	0.2	11.8	5.4	—
	Spike	6	14.4	0.6	4.4	—	104.8
691	Left retina	4	17.6	0.1	0.8	—	—
693	Basal nuclei	4	1.8	0.1	6.8	—	—
694	Oral mucosa	4	34.5	0.6	1.8	—	—
695	Tongue	4	30.3	0.6	1.8	—	—
	Spike	4	37.0	0.4	1.0	—	48.6
697	Caudal Tumor II	4	29.4	0.6	1.9	—	—
699	Cerebellum grey	4	3.2	0.1	3.5	—	—
700	Hippocampus	4	2.2	0.3	15.0	—	—
	Spiked bomb blank[b]	4	10.1	0.2	2.1	—	104.1
702	Midbrain	2	1.5	NA[c]	NA[c]	—	—
703	Cerebellum white	2	0.9	NA[c]	NA[c]	—	—
704	Mass invading thalamus	4	21.0	0.3	1.6	—	—
705	Anterior Tumor II	4	23.7	0.9	3.8	—	—
706	Left adrenal	2	20.9	NA[c]	NA[c]	—	—
707	Scalp	2	35.4	NA[c]	NA[c]	—	—
	Bomb blank[b]	4	0.017	0.005	31.1	—	—
	Mean % RSD for digestion and quantitation with an internal standard				6.7	—	—

a. RPD = Relative Percent Difference = | difference * 100 | ÷ mean

b. Bomb blank spike concentration is actually µg B.

c. Not applicable.

considered to be relatively homogeneous solutions and reproducible sampling is easily achievable. It was, however, noted that for both serum and urine samples, it is necessary to thoroughly mix the sample with a vortex mixer since the samples tend to separate into layers after freezing, thawing and standing.

Table 11 also points to the problems associated with sampling and subsampling a heterogenous tissue such as the tongue for analysis. The percent recovery of the spike for the tongue in Table 11 is reported as only 48.6%. Table 12 shows the results of two more replicate digestions on pieces of the same tongue and a second spike on fifth piece of the tongue. Using the average boron concentration of these three digested samples as the "true" value, the percent recovery of the original spike can be recalculated at 70 percent. The second spiked and digested sample gave a recovery of 102 percent. The spikes for these samples were relatively small considering that the variability (%RSD) of the sample was at least ± 10% and the spike was at a level of only ~1/3 of the total boron in the sample. At this spike level, a 10% sampling variability can easily produce spike recoveries in the range of 100 ± 30%. These results emphasize the necessity to acquire the most representative sample of the tissue for any boron analysis requiring small samples, which is a difficult task with many biological sample types. Spike levels should also be high enough to allow a realistic determination of the analytical accuracy in the form of the matrix spike recovery.

Prompt-γ analysis for boron in biological samples[58,60,75] is a proven technique and is a widely accepted method for boron analysis in the BNCT scientific community. To verify the acid bomb digestion procedure and the quantitative analysis of boron by ICP-AES, samples were analyzed by both prompt-γ and ICP-AES. The ICP-AES data compares quite favorably with the prompt-γ technique as can be seen in Figure 59 and Figure 60. Figure 59 shows the results from sets of urine and blood serum samples that were assayed by both prompt-γ and ICP-AES. Serum and urine had never presented a problem, and samples were simply diluted for ICP-AES and no internal standards were used. For the urine samples, one set of the samples was submitted directly for ICP-AES and one set was assayed by the prompt-γ method and then reassayed by ICP-AES. A slight sampling error can be seen between the two sets of urine samples, however the sample set that was analyzed by both methods produced nearly identical results. Good agreement between the methods is also demonstrated by results for the blood serum samples. It is also notable that the ICP-AES procedure used < 0.1 g of sample for each analysis and the prompt-γ method required 1 g to achieve similar detectabilities.

Figure 60 is a comparison boron analysis results from the prompt-γ analysis and the

Table 12. Replicate acid bomb digestions of the same tongue sample, including matrix spiked digestions, demonstrating the effects of sample inhomogeneity on the accuracy and precision of the B analysis.

Sample	Tongue μg B/g	Spike[a] μg B/g	μg B added	Percent recovery[b]
Digest 1	30.3	37.0	9.8	70
Digest 2	23.9	43.2	9.9	102
Digest 3	27.9			
Mean	27.4			86
Standard deviation	2.6			
Percent RSD	9.6			

a. Spiked to separately digested aliquots.

b. Calculated using the mean tongue concentration.

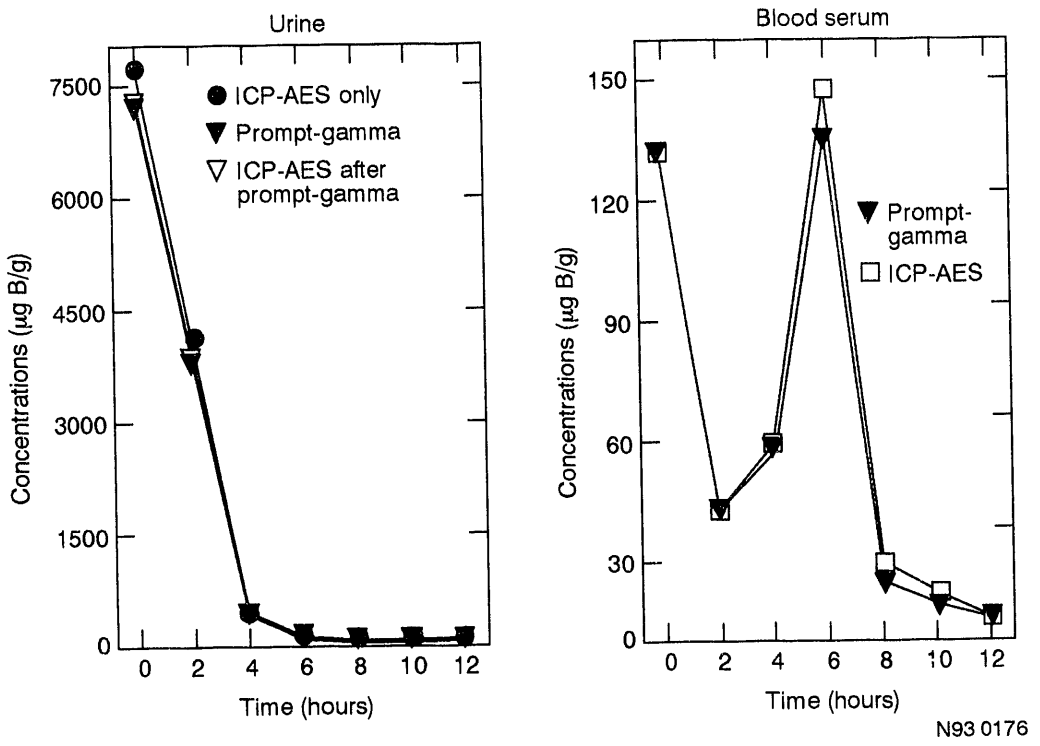

Figure 59. Comparison of boron analysis results in blood serum and plasma using prompt-γ analysis and ICP-AES.

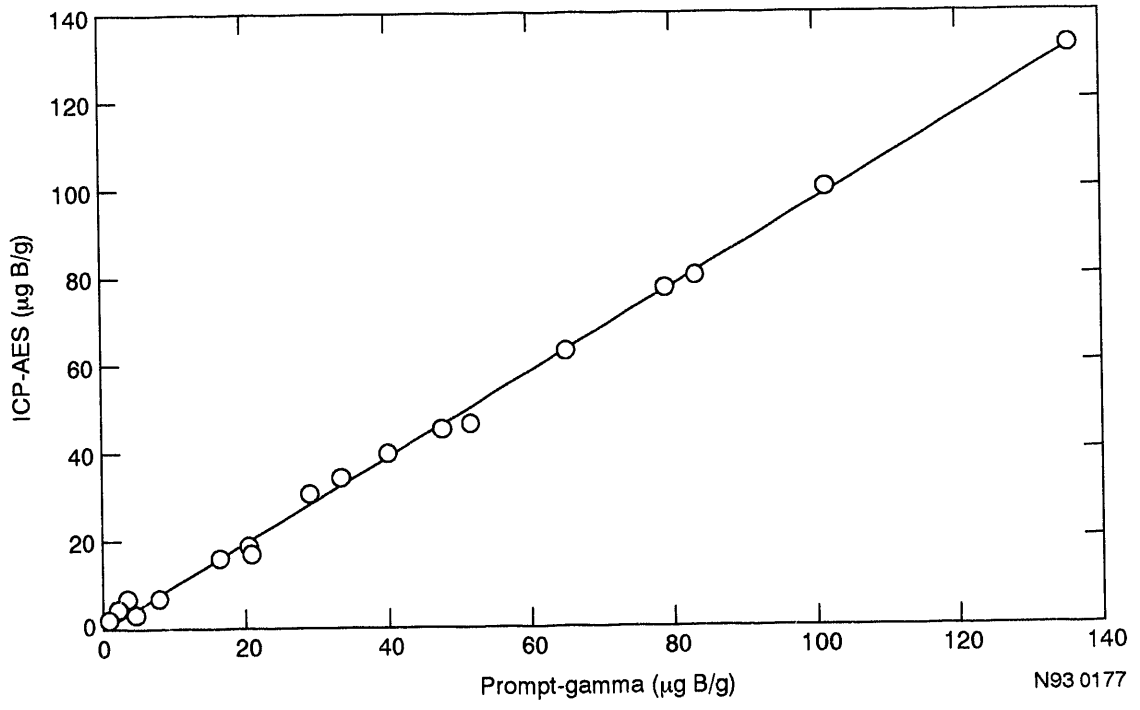

Figure 60. Comparison of boron concentrations in tissue samples determined by prompt-γ analysis and acid digestion, and ICP-AES with internal standardization.

ICP-AES methods. The samples for ICP-AES were digested with HNO_3 in the acid bomb and quantitation utilized the internal standardization method. Exactly the same tissue samples and masses were used for both methods of analysis. The two techniques compare quite favorably as is indicated by the regression line for this particular set of data, which has a regression coefficient of 0.997, and the best fit line can be expressed as ICP-AES=0.97($\pm$0.01)*prompt-γ+0.3. The mean differences for the points on the line was -1.1 $\pm$2.2 (n = 18). Using this information, at the P=0.05 confidence interval, $t_{calculated}$ = 2.12 and $t_{tabulated}$ = 2.11, indicating that there may be a very small probability of a slight bias in the analysis of this particular set of samples. The mean difference and the minor statistical difference are not that great considering that the concentrations in the sample set ranged from ~1 μg/g to greater than 135 μg B/g. When considering the errors, the largest relative differences between the two techniques occur at the lower concentrations where the prompt-γ method is hindered by the conflict between the low natural relative abundance of the ^{10}B isotope (20%) and the 1 μg ^{10}B detection limit for a 200 second count.[59,60] The ICP-AES method also nears the limits of ~0.4 μg B/g, and the reliable quantitation is in the range of 1-2 μg B/g as evidenced by the increasing relative standard deviations of the measurements for low concentration samples as seen in Table 11.

In summary, an ICP-AES method has been described that can be used for reliable quantitative analysis of boron in biological fluid and tissue samples. This method is relatively quick, with the only time limiting factor being the acid digestion of tissue samples. The acid bomb digestion procedure has the advantage of providing a more complete digestion of tissue samples and thus does not require filtration of the digestion solution, a step that can add an additional source of error into the analysis. The primary problems of the analysis stem from sampling errors and the relatively large dilutions currently in use. The ICP-AES procedure as described in the experimental section was published (see references 76 and 77) and later altered to be used for μg B/g analysis in 0.1-0.2 g samples. This modification is described in more detail in the following section.

Comparison of Digestion Methods for Boron Determinations in Biological Samples by ICP-AES

This study was undertaken to compare boron analytical results obtained with ICP-AES on biological samples that had been prepared with a slightly modified version of the bomb digestion procedure described previously in this report and in references 76 and 77 with the $HClO_4/H_2O_2$ test tube digestion procedure of reference 64. Additional test tube digestions using nitric acid with hydrogen peroxide and nitric acid alone were included as alternate procedures to the perchloric acid digestion method. The nitric acid/hydrogen peroxide procedure was chosen to determine if the same degree of digestion could be accomplished without using perchloric acid. The nitric acid only test tube procedure was chosen as an extension of the bomb digestion procedure. These procedures were performed in a manner analogous to the perchloric acid digestions. This study was necessary because a) the reported digestion procedures lacked data on the digestion of brain tissues, a tissue of primary importance in the INEL research, b) the work described in the literature dealt with samples to which boron had been added to the surface of the tissues and did not address possible differences in boron analytical results arising from surface spiking or contamination, and results from samples in which the boron was biologically incorporated, and c) safety concerns over the use of perchloric acid. In addition to the comparison of analytical results, the various procedures were examined for ease of use and the amount of time needed to prepare samples for analysis to determine if one procedure was preferable to another.

Experimental Procedure

Reagents. Boron, scandium, and yttrium standards were prepared from appropriate AA standards (Fisher Scientific). An additional 0.5 μg B/mL standard was prepared from a

certified 5000 μg B/mL NIST standard (SRM 3107) for use as a calibration check standard. Concentrated, ultrapure nitric acid (J. T. Baker Ultrex) was used for all digestions involving nitric acid and in the preparation of all associated standards. The 30% hydrogen peroxide and 70% perchloric acid were of reagent grade (Fisher Scientific). All solutions and digests were stored in polyethylene bottles.

Biological tissues were obtained from dogs that had been administered a solution containing the compound $Na_2B_{12}H_{11}SH$ (Callery Chemical) as part of a biodistribution study in dogs having brain tumors.[78] All tissue samples were frozen until use. A beef liver sample was also obtained for use as a blank, or control, sample. The tissue samples were defrosted, cut into small pieces and ground with a mortar and pestle to assure the most homogeneous sample possible, even though some connective tissues could not be completely ground with this method.

Acid Bomb Digestions. Samples were prepared by adding 3 mL of concentrated, ultrapure nitric acid to a weighed 0.1 to 0.2 g (wet weight) sample of homogenized tissue in a Teflon-lined acid digestion bomb (Parr Instrument Company, Bomb No. 4749). The bombs were spiked with 100 μL of a 200 μg Sc/mL standard prior to sealing. The sealed bombs were placed in a 150°C oven for two hours and then were removed from the oven and allowed to cool to room temperature prior to opening. The resulting solutions were clear and contained no visible particulate matter. The completely digested samples were then transferred to a 10 mL volumetric flask, spiked with 100 μL of a 200 μg Y/mL standard and diluted to the mark with boron-free water.

Perchloric Acid/Hydrogen Peroxide Digestions. Perchloric acid digestions of tissues were done following the method described by Tamat et al.[64] To a weighed 0.1 to 0.2 g (wet weight) of sample in polypropylene test tube, 0.3 mL of 70% perchloric acid and 100 μL of a 200 μg Sc/mL standard were added and the contents were allowed to mix. Then 0.6 mL of 28% hydrogen peroxide was added and the test tubes were placed in a hot water bath and heated to 75°C for one hour. After one hour, the solution in the tubes was a very light yellow color and contained a white coagulant, the amount of which varied with tissue type. The samples were then filtered through a 0.45 μm filter (Gelman Acrodisc CR), spiked with 100 μL of 200 μg Y/mL standard and diluted to the mark of a 10 mL volumetric flask with boron free water.

Nitric Acid/Hydrogen Peroxide and Nitric Acid Digestions. These digestion procedures were done in a manner analogous to the $HClO_4/H_2O_2$ procedure described above. The exceptions are that 0.5 mL of concentrated nitric acid and 0.5 mL of 28% hydrogen peroxide were used for the nitric acid/hydrogen peroxide procedure and 1 mL of concentrated nitric acid was used for the nitric acid digestion. The HNO_3/H_2O_2 digestions yielded solutions that were light yellow and contained some white coagulant and thus required filtering. The HNO_3 digestions yielded dark yellow solutions with considerable particulate matter.

ICP-AES Analysis. All analytical measurements were made on an Applied Research Laboratories Model 3520 ICP-AES. Samples were pumped into the spray chamber through a Meinhart type nebulizer via a peristaltic pump operating at 2.5 mL/min.

Calibration curves were prepared for each matrix using five standards, one of which was a blank, prepared from a 1000 μg B/mL stock solution. The ICP-AES determinations were made using yttrium at 2 μg/mL as an internal standard in order to compensate for any physical interferences arising from differences in viscosity, salt content, and suspended particulate matter in the sample. Scandium was spiked to all samples prior to all digestions and was used to identify any losses due to analytical technique.

The baseline corrected intensities of the 208.959 nm and 249.678 nm lines of boron and the 361.384 nm line of scandium were ratioed to the 371.030 nm line of yttrium that was similarly baseline corrected. Background correction points

for yttrium, scandium, boron at 208.959 nm, and boron at 249.678 nm were selected at +0.040, +0.040, -0.026 and -0.038 nm, respectively. Two lines were selected for boron in order to verify that the instrument was still in calibration and to help identify possible spectral interferences such as that arising from iron in blood, a potential high concentration interference of the 249.678 nm line of boron.

Results and Discussion

Upon visual inspection, it was clear that none of the test tube digestion procedures resulted in complete dissolution of the tissue samples. The best success from the test tube procedures was obtained using the $HClO_4/H_2O_2$ procedure, while nitric acid alone proved to be a far inferior oxidizing agent as evidenced by the high degree of particulate matter and the deep yellow color of the digest. Prolonged heating in the hot water bath did not improve the appearance of any of the digests from the test tube procedures. The particulate matter appeared to be directly related to the amount of lipid material in the tissue. Brain tissue, which is high in lipid content, left a considerably larger quantity of the coagulated, white precipitate. This precipitate could be filtered out of the digested samples. The $HClO_4/H_2O_2$ brain digestates were an exception as a considerable amount of this precipitate passed through the filter causing the final solution to have a milky appearance. A filter of smaller pore size would probably eliminate the precipitate completely, but the time for the filtration step would increase.

The acid bomb digestion procedure, a much more rigorous method because of the higher temperatures and pressures employed, completely digested all of the tissue samples. With this procedure, there was little, if any, evidence of remaining color and no visible particulate matter.

For the four tissue types involved in this study, a minimum of four to a maximum of six replicate samples were digested using each of the four digestion procedures previously defined. The analytical results for these samples are given in Table 13. Initial examination of these results indicate that all four methods may be suitable to a limited degree for the digestion of tissues for boron analysis by ICP-AES. The acid bomb and $HClO_4/H_2O_2$ procedures do not show any significant differences. The HNO_3/H_2O_2 and HNO_3 procedures show significantly lower boron concentrations for the liver sample and the HNO_3/H_2O_2 procedure has a significantly higher result for the cerebral grey tissue.

Table 13. Results from the ICP-AES determination of B in tissues digests with different digestions methods. Values in μg B/g ± standard deviation determined from replicate digestions and analyses.

	Boron concentration (μg B/g)			
Tissue	Method 1	Method 2	Method 3	Method 4
Cerebral white	1.09 ± 0.12	1.01 ± 0.19	1.20 ± 0.24	1.145 ± 0.079
Cerebral grey	1.13 ± 0.14	1.02 ± 0.22	1.53 ± 0.17	1.36 ± 0.23
Liver	53.2 ± 1.7	53.06 ± 0.90	48.7 ± 2.7	45.74 ± 0.55
Tongue	13.39 ± 0.65	12.4 ± 1.0	13.8 ± 1.0	12.47 ± 0.81

Method 1: Acid bomb digestion with nitric acid.
Method 2: $HClO_4/H_2O_2$ digestion procedure.
Method 3: HNO_3/H_2O_2 digestion procedure.
Method 4: HNO_3 digestion procedure.

A comparison of several means, calculated by applying a one-way analysis of variance scheme[79] at the P = 0.05 significance level to the analytical results from the four digestion procedures for each of the tissues, confirmed that not all of the methods gave statistically the same result for the cerebral grey tissue or for the dog liver samples. Further analysis, using the least significant difference statistic, identified the HNO_3/H_2O_2 test tube procedure as giving a significantly different result for the cerebral grey tissue. Both the HNO_3/H_2O_2 and the HNO_3 test tube digestions were statistically different from the acid bomb and the $HClO_4/H_2O_2$ digestion procedures for the dog liver sample, but were not judged to be significantly different from each other for this sample. The acid bomb and the $HClO_4/H_2O_2$ digestion procedures did not exhibit any significant difference for any of the tissue samples.

Method blank and beef liver blank boron spikes were all recovered within the range of 92 to 108 percent for all four methods with an overall average boron recovery of 102 ± 4 percent. Only the $HClO_4/H_2O_2$ digestion procedure, with an average boron recovery of 103 ± 2 percent, was different from 100 percent recovery at the P = 0.05 significance level.

An interesting aspect of this study surfaced during the examination of the recovery data for scandium. As previously mentioned, scandium was added to all of the samples prior to the actual digestion in order to assess the possibility of analyte losses and the technique of the analyst. This procedure was originally adopted for use with the acid bomb digestion procedure and has proven to be quite useful.[76] For the work reported in this experiment, it was decided to incorporate a scandium recovery standard in the test tube digestions for consistency, even though it was realized that scandium may not be the most appropriate element for these digestions.

The average Sc recovery data for all of the digestion procedures and samples are listed in Table 14. Excellent recovery data was obtained for all samples prepared with the acid bomb digestion procedure and the method blanks of the test tube digestion procedures, but the recovery of scandium spikes from the tissue samples prepared via the test tube digestions show a dramatic loss of scandium with nearly all of the tissue samples. This loss of scandium is related, although not linearly, to the sample mass being digested. As the mass of the sample increased, the percent recovery of the scandium standard spiked onto the sample decreased. Some correlation can also be made between low scandium recovery and the lipid content of the sample. This is most apparent in Table 14 for the $HClO_4/H_2O_2$ digestion procedure that shows much lower scandium recoveries for the brain tissue. Since scandium is cationic in nature and forms highly charged cationic species in perchlorate solutions,[67] it is possible that these species are complexed by the anionic nature of the water soluble fatty acid portions of the lipid material and removed in the filtration step. Boron is expected to be oxidized to boric acid which would appear as an anion in aqueous media and is thus not influenced by the presence of the lipid material. It can be hypothesized from this data that the test tube digestion procedures may be unsuitable if other elements that form cationic species are desired as part of the analysis scheme. Possible examples would include Ga and In which are being investigated as imaging agents[80] and Gd which is being investigated as both an imaging agent and as a neutron capture therapy agent.[81] Based upon this data, the acid bomb procedure is the preferred method for tissue digestions.

When the four procedures were examined for ease of use and sample preparation time, it was determined that of the two methods (acid bomb and $HClO_4/H_2O_2$ digestions) that yielded comparable analytical results, the acid bomb digestion procedure was the easiest to perform in the INEL laboratory. During the test tube digestions it was necessary to constantly monitor the progress of the digestion to minimize the frothing that was observed with many of the samples. In contrast, the acid bomb digestion procedure requires no monitoring after the bombs are placed in the oven, thus allowing the person doing the sample

Table 14. Percent recoveries of scandium spiked to each sample as a recovery standard. Values represent the average recovery ± standard deviation of replicate digestions.

	Scandium spike recovery percent			
Tissue	Method 1	Method 2	Method 3	Method 4
Cerebral white	98.9 ± 3.3	43.8 ± 4.7	71.6 ± 7.4	82.6 ± 5.8
Cerebral grey	97.8 ± 1.1	53.8 ± 5.0	87.5 ± 8.2	83.5 ± 2.5
Liver	99.9 ± 0.4	68.8 ± 5.0	75.5 ± 9.8	82.0 ± 5.0
Tongue	101.3 ± 1.4	64.0 ± 8.3	86.9 ± 1.6	96.5 ± 0.8
Beef liver[a]	101.6 ± 1.5	69.4 ± 4.2	83.2 ± 2.9	81.2 ± 3.1
Blanks[b]	100.1 ± 1.1	99.4 ± 0.7	93.6 ± 3.0	99.3 ± 1.8
Overall	99.7 ± 1.8	68 ± 18	81 ± 10	86.7 ± 8.1

Method 1: Acid bomb digestion with nitric acid.
Method 2: $HClO_4/H_2O_2$ digestion procedure.
Method 3: HNO_3/H_2O_2 digestion procedure.
Method 4: HNO_3 digestion procedure.
a. Includes beef liver blanks and spikes.
b. Includes reagent blanks and reagent blank spikes.

preparation to perform other laboratory tasks. The main drawback to the acid bomb digestion is the time necessary to clean the reusable Teflon bomb liners. Even though it is possible to use disposable polypropylene test tubes with the $HClO_4/H_2O_2$ digestion procedure, the overall sample preparation time is approximately equal to the acid bomb technique due to the time required to filter the samples to remove undigested material.

It must be stressed that this work consists of a limited set of tissue types. As mentioned earlier, the $HClO_4/H_2O_2$ digestion procedure leaves more residue behind for brain tissues than it does for tissues such as the liver and the tongue. With appropriate modification to the digestion procedure (and/or to the other test tube procedures) it may be possible to reduce or eliminate the amount of undigested material and to assure good recoveries of other elements of potential interest. This would make the test tube digestion procedure a more attractive method. However, at present, the acid bomb technique gives the highest level of confidence at no additional loss in time or effort.

Boron Determination in Biological Fluids with Flow Injection for Sample Introduction to the ICP-AES

An important aspect of any BNCT program is the ability to rapidly and quantitatively determine boron in a variety of biological sample types. ICP-AES has shown to be quite well suited for boron analysis in biological samples.[64,76] Detection limits for boron by ICP-AES are typically less than 0.010 μg B/mL in the analytical solution (that is, biological samples at 1 μg B/g can be quantitated with dilution factors as large as 100) and the linear dynamic range is in the range of 5-6 orders of magnitude. The major limitation of boron determinations by ICP-AES is due to problems with carryover.[61] INEL researchers have found that a rinse cycle utilizing both basic and acidic conditions helps to limit this problem. Unfortunately, the rinse procedure is time consuming and drives the total analysis time to 5-7 minutes per sample, depending upon the B concentration of the previous sample. In order to limit the required rinse time, samples that are

expected to have very high boron concentrations are diluted so that the resulting analytical solution concentrations are less than 5 μg B/mL.

In order to combat the carryover problems mentioned above and to simultaneously allow a much greater instrumental sample throughput, flow injection analysis (FIA) with ICP-AES detection (FIA-ICP-AES) was investigated. Flow injection analysis[82] is a type of continuous flow analysis in which a small volume of sample is very reproducibly injected into a continuously flowing, nonsegmented stream. In the simplest case, the primary function of the stream is to carry a minimal amount of sample to a detector. In more elaborate systems, the sample can diluted or modified online by the addition of reagents required for analysis. The only major disadvantage to FIA is that in some cases where extensive sample preparation is carried out online, detection limits can be adversely affected. A list of advantages of FIA would include very high reproducibility and accuracy, speed of analysis, the need for only small sample volumes, very short residence times thus limiting carryover, and the potential for doing some sample preparation procedures online.

Experimental Procedure

All experiments and analyses were performed on an ARL Model 3520 ICP-AES instrument. Liquid argon provided the plasma torch gas supply under standard operating conditions. The instrument was used for both conventional, continuous aspiration ICP-AES B analysis and for FIA-ICP-AES. In conventional ICP-AES, sample uptake was maintained at 2.6 mL/min with a peristaltic pump. Quantitation was the result of three five second integrations at both the 208.959 and 249.678 nm B lines. In the FIA-ICP-AES analysis mode, no modifications of the ICP sample introduction system were made other than to place a Rheodyne Model 5020 injection valve with a 200 μL sample loop into the carrier stream between the peristaltic pump and the nebulizer. The carrier stream consisted only of deionized water flowing at 3 mL/min. Only 30 cm of 0.5 mm id Teflon™ tubing were used between the injection valve and the nebulizer, thus the sample plug reached the ICP almost immediately after injection. Quantitation for an FIA-ICP-AES analysis was the result of a single 40 second integration which began immediately after injection. Emission intensity values were manual input to the calibration routines so that replicate information was included in the calibration curve. Transient signals were recorded with a Perkin-Elmer LCI-100 recording integrator connected to the PMT output in the ICP-AES electronics with the instrument software operating in the "test" mode.[83]

Blood serum and urine samples were prepared by dilution of 20-200 μL of sample to 10 mL with deionized water. Calibration standards were prepared from a commercial 1000 μg B/mL solution (Fisher). Calibrations were checked with either a 0.5 or 2.5 μg B/mL solution prepared from a 5 mg B/mL NIST standard (SRM 3107).

Results and Discussion

The utility of FIA-ICP-AES in boron analysis is demonstrated by the traces in Figure 61. The upper trace is representative of the time required for conventional, continuous aspiration ICP-AES analysis where two boron channels are monitored. This trace includes the aspiration time required to reach a steady state signal, to measure the two channels in triplicate, and to clear all of the connecting tubing of sample once the measurements have been made. The lower trace is of four 200 μL injections of the same 1 μg B/mL solution made within the same time frame as the upper trace. Reproducibility of these four injections is quite good (RSD = 2.3%) and the signal returns to the baseline much more quickly than for the continuous aspiration technique. Carryover problems with the continuous aspiration technique are enhanced at higher concentrations and when long (5 sec) integrations times are used to average the noise seen in Figure 61. Generally, no carryover is noted at sampling frequencies up to and greater than 1 sample/minute with the FIA method. The calibration data (r^2=0.998) shown in Figure 62, and the subsequent sample analyses were acquired at an overall sampling rate of 1.17 samples/min (51 manual injections in 43.5 minutes).

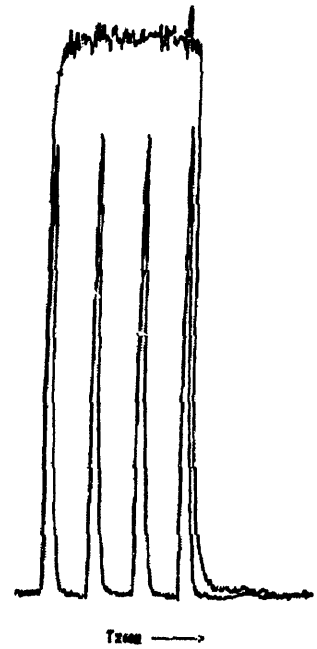

Figure 61. Comparison of a conventional continuous aspiration ICP-AES and FIA-ICP-AES for 1 μg B/mL solution.

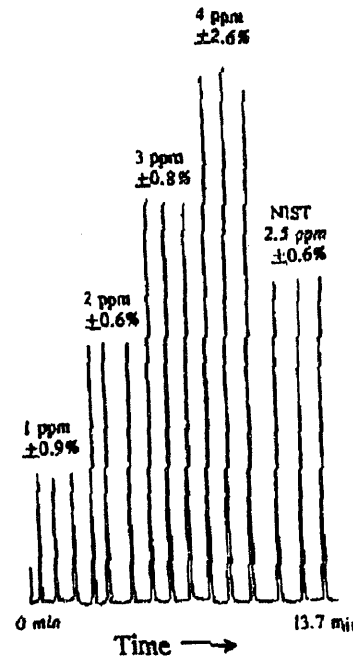

Figure 62. Typical calibration by FIA-ICP-AES from 0-4 μg B/mL (ppm) standards with an NIST calibration check. Values indicate the % RSD for the replicate injections.

While the recording integrator is a very useful tool and can be used to determine the heights and areas of the FIA peaks, it is subject to integration errors caused by the periodic sampling of the natural flicker in the torch. Additionally, the integrator is unable to provide convenient feedback of concentration information to the analyst. A much better method of integration is performed by the ICP-AES instrument electronics when the entire signal is in effect collected and "integrated" for a period of 40 seconds. This latter method of sampling the torch output is more effective at averaging noise and thus provides more stable and precise instrumental output for quantitation.

Using the 40 second integration method, the instrument was calibrated and used to quantitate several prepared serum and urine samples by FIA-ICP-AES. Over a period of 3.6 hours, 120 manual injections were made including triplicate injections of calibration and calibration check standards and 15 samples. An NIST boron standard used as a calibration check had a mean % error of 0 ± 2% (n=21). A blind standard and a matrix spike had recoveries of 101% and 95%, respectively. The mean relative standard deviation (% RSD) for all injections made in triplicate was 1 ± 1%, and the diluted sample concentrations ranged from 0.08-5.0 μg B/mL. The detection limit determined as 3 times the standard deviation of the blank analyses was 0.012 μg B/mL. In a separate experiment, a set of samples were run with both conventional ICP-AES and by FIA-ICP-AES with quite good agreement. The linear regression of the two techniques plotted against each other resulted in a line with slope of 1.00 ± 0.01, y-intercept of 0 ± 4 and r^2 of 0.994.

Blood serum samples have concentrations running as high 100 μg/g or more. Serums are quite viscous and are normally diluted by a factor of 100 or more to thin the matrix because these high boron concentrations cause significant carryover during normal aspiration into the ICP. Using FIA to dilute the samples prior to reaching the sample introduction system of the ICP would allow serum samples to be quantitated directly without prior sample preparation. To test the concept of direct introduction of blood serum samples for FIA-ICP-AES analysis, solutions of 30, 60, and 90 μg B/mL with boron as boric acid and $Na_2B_{12}H_{11}SH$ were prepared in an artificial serum consisting of 4% bovine serum albumin and 8 mM phosphate buffer. Calibration standards were prepared at 25, 50, 75, and 100 μg B/mL in deionized water. The 200 μL sample loop on the FIA injection valve was shortened to ~100 μL. Using peak areas from the peaks recorded on the integrator, the recovery of boron as boric acid and $Na_2B_{12}H_{11}SH$ from the artificial serums were 101.1 ± 1.3 % and 99.6 ± 0.5%, respectively. Based on this data, it appears that by using FIA-ICP-AES, the boron content blood serum and plasma samples can be performed directly.

The data presented above indicate that FIA as a sample introduction method for ICP-AES analysis of B is accurate, very precise, and potentially very time efficient. The reproducibility is such that samples need not always be injected and run in triplicate and the throughput of samples can potentially be doubled or tripled over that of conventional ICP-AES. Total analysis time can be reduced even further by directly injecting serum samples into the FIA manifold and diluted on their way to the spray chamber and ICP. Much of the work described in this section was presented in reference 84.

Direct Analysis of Boron in Whole Blood with AES

The INEL BNCT program has been involved in normal tissue dose tolerance studies using dogs as the large animal model.[84] In order to accurately predict when to begin an irradiation and then determine the length of the radiation required to achieve the desired radiological dose at a specified mean boron concentration, a rapid technique for the determination of blood-boron is required. It has previously been shown that after administration and distribution of BSH, the elimination phase has a $T_{\frac{1}{2}}$ of ~300 minutes[78] and blood B concentrations should be roughly predictable at specified times during the elimination. However, the physiology can be expected to vary somewhat from animal to animal

and the blood B concentrations are expected to vary as well. These variations mean that target B concentrations can easily be missed.

There are numerous methods available for B analysis in biological samples, however, most require some form of time-consuming digestion procedure (20 minutes minimum) to eliminate the matrix and, in many cases, to convert the B to a single form. Rapid analysis of animal tissues by atomic emission spectroscopy has been performed by suspending homogenized tissue in a deionized water slurry.[85] This analysis procedure, including tissue homogenization, could be performed in ~10 minutes. Since a heparinized blood sample would not require homogenization, it should readily be suspendable in solution.

This section describes the analysis of heparinized whole blood using slurry sample introduction into both an ICP-AES and a direct current plasma-atomic emission spectrometer (DCP-AES). A non-ionic surfactant (Triton X-100 ™) is used to form a stable slurry of suspended blood cells. The non-ionic surfactant was selected to minimize cell destruction and ICP or DCP problems caused by excess alkali metal content.

Experimental

Samples were prepared as slurries simply by weighing a 300 mg aliquot into a 10 mL volumetric flask, adding 0.2 mL of a 2.5% solution of Triton X-100 ™, and diluting to the mark with deionized, boron-free water. Standards were prepared in a similar 0.05% solution of Triton X-100 ™ from commercial standard solutions (SPEX Industries and NIST). Salts of BSH were obtained from Callery Chemical and Centronics Limited, and BPA was obtained from Callery Chemical. The $Na_4B_{24}H_{22}S_2$ (BSSB) was prepared from BSH by the method described in reference 86. Standard solutions containing ^{10}B were prepared from dried 95% ^{10}B enriched $B(OH)_3$ obtained from NIST. Boron analysis was performed by ICP-AES at both the 208.959 and 249.678 nm emission lines, while the DCP-AES analysis used the 208.959 and 249.778 nm emission lines of boron.

Results and Discussion

Initial experimentation was performed using blood obtained from a healthy Labrador retriever. Aliquots (1 mL) of the heparinized whole blood were spiked with differing quantities of a BSH stock solution (691 μg B/mL) and a commercial standard containing B (1000 μg/mL) as ammonium tetraborate. The resulting solutions were analyzed by standard ICP-AES procedures after digestion of 200 mg with nitric acid.[76] Slurries for ICP-AES consisted of 200 mg aliquots of the spiked blood that had been suspended in 0.05% Triton X-100 ™. The results of this experiment are shown in Table 15. Plotting the ICP-AES analysis results for slurry nebulization versus the standard digestion procedure results in the regression line $C_{slurry}=(1.03_8 \pm 0.01_4)C_{digest}-(0.09 \pm 0.43)$. The results from the two sample preparation techniques agree very well, however, a slight (~3%) positive bias may be present in the slurry results. This slight bias was not a great concern because it most likely was the result of having mismatched standard and sample matrices. This initial study utilized calibration standards that were prepared in only a deionized water matrix. To avoid this potential problem, all subsequent standards were prepared in 0.05% Triton X-100 ™.

Since the aspiration and nebulization of the blood slurries for boron analysis by ICP-AES worked well for both BSH and a simple borate, the technique was taken to BNL to be used with the DCP-AES in direct support of the large animal irradiations. Because the detection limits for the 208.959 nm B emission on the DCP-AES were only ~0.023 μg/mL, it was decided to use 300 mg of heparinized whole blood instead of the 200 mg used in the ICP-AES experiments. To be sure that there were no significant physical or spectral interferences associated with this change, increasing quantities of B-free whole dog blood were spiked with B from a commercial standard. The results of this experiment are shown in Table 16 and indicate that no significant interferences exist with as much as 5% blood in the slurry when using DCP-AES.

Table 15. Results of an initial study comparing slurry nebulization and acid digestion of whole blood spiked with either BSH or tetraborate. Analysis was by ICP-AES.

	Slurry µg B/g	Digestion µg B/g	Difference[a]	RPD[b]
Blood	<0.42	<0.40	—	—
15 µL BSH	9.50	9.57	-0.08	-0.8
30 µL BSH	18.43	17.96	0.47	2.6
45 µL BSH	30.16	29.76	0.40	1.3
60 µL BSH	39.16	38.02	1.14	2.9
75 µL BSH	49.20	48.38	0.82	1.7
60 µL $B_4O_7^{2-}$	53.02	50.68	2.34	4.5
40 µL $B_4O_7^{2-}$	36.27	34.24	2.02	5.7
30 µL $B_4O_7^{2-}$	27.70	26.31	1.40	5.2
20 µL $B_4O_7^{2-}$	19.39	18.25	1.14	6.1
10 µL $B_4O_7^{2-}$	9.69	9.60	0.09	1.0
Mean	—	—	0.97	3.0
Standard Deviation	—	—	0.79	2.3

a. Difference = slurry - digestion

b. Relative % difference = difference x 100/mean

Table 16. Effect of blood volume on the recovery of B by DCP-AES with slurry sample introduction.

mg blood	0	109	219	300	400	500
% recovery	100	97	101	103	101	101

Some typical analysis results for the same blood samples by prompt γ^{59} and slurry nebulization with DCP-AES and ICP-AES are shown in Table 17. The ICP-AES analyses were performed at the INEL on the same slurry preparations that were used for DCP-AES at BNL. Prompt γ was in some cases done twice—once the day the sample was taken using only a blank and a single standard for calibration and a second time when a multipoint calibration curve could be obtained. Examination of Table 17 indicates that the DCP-AES results are always lower for blood and the BSSB compound and near normal for BPA and boric acid. Assuming that the multipoint prompt γ results are near the true values, the % errors were calculated and averaged as presented in Table 18. The precision for the methods and B compounds are quite comparable; however the first DCP-AES analysis shows a mean -11% error for boron cage compounds. This discrepancy was not noted in other DCP-AES analyses where the samples were digested.[87] Viewing a cooler region of the DCP appeared to give an enhanced recovery for B as BSSB, so some blood slurry samples were rerun viewing this region. The results of this run are presented in the last column of Table 18. Even though the recovery of the cage compounds was somewhat better, the mean error was still ~-6% for B in the cage compounds. All subsequent B analyses by DCP-AES were corrected for this negative bias after the analysis of a reference standard or sample.

Figure 63 indicates the utility of the rapid analytical technique in treatment planning. In this dog, the B elimination was quite normal until ~560 minutes. At this point the dog was taken to the reactor and anesthetized. This, in some way, disrupted the normal elimination and during the course of the irradiation there was no net change in the blood B level. By using the rapid DCP-AES analysis of the blood slurries, adjustments could be made in the irradiation schedule knowing that the elimination had ceased.

Table 17. Table 17. Comparison of typical results for B analysis by prompt γ, DCP-AES and ICP-AES.

Sample	Concentrations in μg $^{10}B/g$			
	Prompt γ[a]	Prompt γ[b]	DCP-AES	ICP-AES[c]
BPA solution	26.9	—	27.1	—
9.5 μg ^{10}B/mL standard	9.6	9.5	9.7	—
Blank blood spike (borate)	12.5	—	12.2	—
bSSB solution	122	125	114	—
A 300 min blood	48.5	47.3	43.2	50.5
A 360 min blood	43.6	41.8	37.7	42.2
A 420 min blood	37.5	38.9	33.3	38.0
A 489 min blood	32.3	32.2	28.8	32.5
A 558 min blood	29.0	29.5	26.3	26.6
A 627 min blood	24.3	—	22.6	26.4
B 360 min blood	44.2	—	40.0	45.7
B 420 min blood	40.3	—	34.8	40.5
B 496 min blood	36.0	—	31.7	37.1
B 562 min blood	33.3	—	29.1	33.6
B 622 min blood	30.2	—	26.5	30.8
C 240 min blood	60.7	—	54.0	62.7
C 300 min blood	54.1	—	47.2	56.0
C 360 min blood	45.9	—	42.0	48.4
C 420 min blood	39.3	—	34.7	39.4
C 506 min blood	33.2	—	28.1	32.3
C 571 min blood	29.9	—	26.3	30.7
C 639 min blood	26.8	—	24.4	27.6

a. Using multipoint calibration at a later date

b. Using only a 2 point calibration on the day of the infusion

c. Same slurries as for DCP but analysis was several days later

Table 18. Mean % errors for whole blood B analysis by prompt γ, ICP-AES and DCP-AES.

	Mean percent errors[a]			
Sample type	Prompt γ[b]	ICP-AES	DCP-1[c]	DCP-2[c]
Overall error	0.1 ± 2.8	1.6 ± 3.7	-9.5 ± 4.4	-3.9 ± 6.4
Cage compounds	0.2 ± 3.0	1.6 ± 3.7	-11.0 ± 2.3	-5.8 ± 4.1
Borate compounds	-.08	—	0.0 ± 1.9	—

a. Assumes prompt γ with multipoint calibration is true value
b. Prompt γ with 2 point calibration
c. DCP-AES analysis prior to (-1) and after (-2) viewing area adjustments

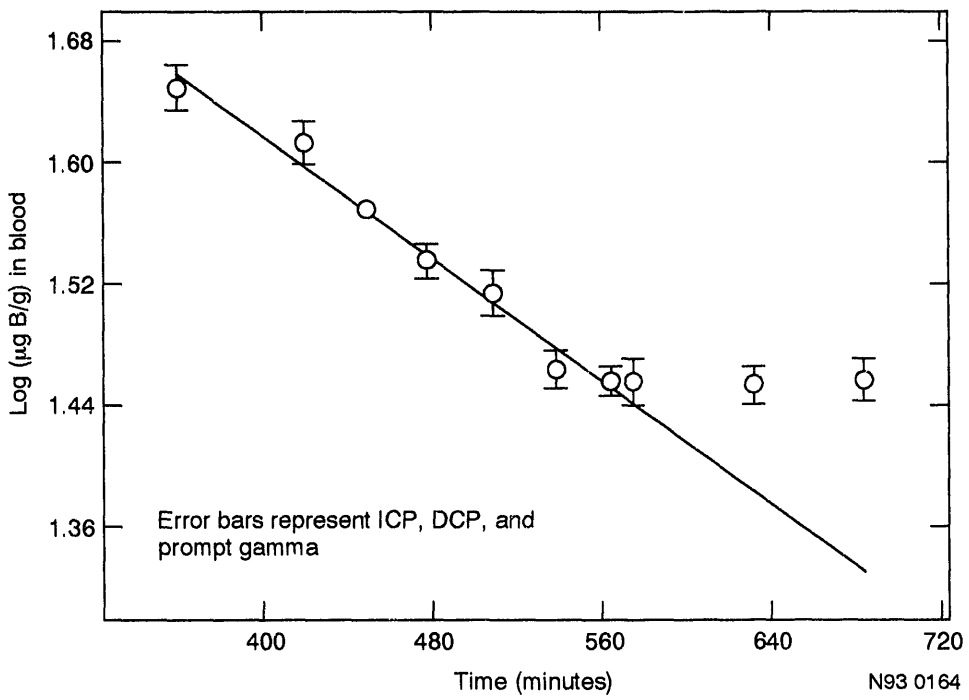

Figure 63. Elimination of B in an atypical dog following administration of BSH. Each point represents the mean of the DCP-AES analysis and ICP-AES and prompt γ performed at a later date.

Conclusions

Blood samples can be prepared and analyzed for B as slurries within 5-15 minutes of receipt. The analysis does not appear to be affected by blood slurry concentrations of up to 5% and the slurries are stable for several days. When B is present as a cage type compound, DCP-AES results are typically 5-15% low. This negative error can easily be corrected for if a suitable reference standard or a reference analysis of a sample is available. Boron analysis in the slurries by ICP-AES is unaffected by the compound type, however, caution should be used in order to assure that positive errors do not result from volatile B compounds. The work in this section will appear in reference 88.

Determination of Boron in Milligram-Sized Tissue Samples with ICP-AES

The ability to accurately determine boron in biological tissue samples of all sizes is important in evaluating the tumor specificity of the boron compounds being studied in BNCT research. The analytical literature having to do with determining boron in biological specimens includes techniques based on prompt-gamma ray spectroscopy,[59,60] colorimetric procedures,[89,90] atomic spectroscopy,[64,76,88] and, most recently, ICP-mass spectrometry (ICP-MS).[91] Unfortunately, all of these papers describe bulk sample analysis techniques that lack the absolute sensitivity needed to determine low μg/g levels of boron in milligram-sized samples. The capability to analyze very small samples is important because researchers find it desirable to be able to do boron concentration-mapping within and around specific structures, and physicians would like to be able to use needle-biopsy sampling techniques to determine if the drugs are actually localizing before they expose the patient to neutron sources. While it is possible to roughly quantitate boron in small samples with ion microscopy[92] or track-etch autoradiography,[93] both of these techniques suffer from poor precision and require expensive and rather specialized instrumentation.

AES has supplanted other methods of determining boron in many applications.[64,76,88] The primary reasons for this are that techniques such as ICP-AES have excellent solution-concentration sensitivity, are reasonably free from matrix effects, and the equipment has become widely available at a reasonable cost. Unfortunately, the absolute sensitivity of conventional ICP-AES is marginal for small sample applications. For example, a typical traditional approach to analyzing a five-milligram tissue sample would first involve dissolving it into a minimum of 5 mL of solution (1000:1 dilution). This degree of dilution is required because 5 mL is about the minimum volume needed to do an analysis and possibly reserve sufficient sample for a duplicate measurement. A typical ICP-AES instrument has detection limits for boron of about 5 μg/L for the 249.68 and 208.96 nm lines in the absence of matrix effects. The detection limit for the 249.77 line is about 3 μg/L; however, this line is significantly overlapped by an iron emission line and often cannot be used to quantify boron in most samples. The practical detection limit for tissue sample analysis is about 8 μg/L and practical quantitation limits are about 20-30 μg/L. The practical detection limit for boron in the 5-mg sample would therefore be ~8 μg/g and practical quantitation limit would be about 20-30 μg/g. Since the tissue boron concentrations used in BNCT therapy are typically only 15-30 μg/g, conventional ICP-AES is quite marginal for such small sample work.

Accurate quantitation of low ppm levels of boron in small tissue samples requires an efficient way of getting the analyte into the plasma. The method described in this report accomplishes this with a cold-vapor generation approach that is roughly analogous to those applied for determining both the hydride-forming elements and mercury. The reaction used to volatilize the boron is acid-catalyzed formation of volatile methoxyborate. This approach is not only more efficient at transporting analyte to the plasma, it also eliminates the iron emission line interference that often contraindicates use of boron's most sensitive emission line (249.779 nm) in traditional analyses.

The basic idea of interfacing a borate ester volatilization system directly to an atomic spectrometer was first reported by Siemer in 1982.[94] A commercial AAS spectrometer was used in its "emission" mode to integrate the transient green BO_2 band responses generated when the methoxyborate was introduced into an air-acetylene flame. A few years later, Castillo, et.al.,[95] performed basically the same experiment, but recorded the atomic absorption signal instead. Unfortunately, flames are not hot enough to efficiently atomize boron, which means that flame-based atomic spectrometric methods lack the sensitivity needed for BNCT research.

Methods that combine some type of borate ester volatilization step with ICP-AES detection have already been reported. The technique of Novozamsky et al.[96] generates a continuous, steady-state signal by pumping aqueous sample, sulfuric acid, and methanol streams into a gas-liquid separator and then introducing a portion of the gas phase into the torch. Unfortunately, the volume of carrier gas used is too small to carry more than a small fraction of the boron ester into the plasma—so little, in fact, that the method's detection limit (50 ng/mL) is considerably worse than that normally associated with strictly conventional pneumatic-nebulization. The approach of Hosoya et al.[97] simply combines collection of the methoxyborate volatilized from a sample in water with a conventional ICP-AES analysis of the collecting solution. Since the actual determination is strictly conventional, the only thing gained by the esterification/distillation steps is freedom from line overlap problems.

Another paper[98] describes a technique involving two separate volatilizations of the ester: the first separates the methoxyborate and the bulk of the methanol from the sample matrix and condenses the two out together. The second step involves a gradual heating of the condensate to volatilize a portion of the ester into the argon stream going to the torch. Since methanol and methoxyborate form an azeotrope with a boiling point of ~53°C, the azeotrope reaches the torch before the bulk of the methanol, even though the methoxyborate and methanol have boiling points within one degree of each other. Introducing all of the ester would have simultaneously put enough methanol into the plasma to extinguish the discharge. The detection limit was equally unimpressive—approximately 40 ng/mL.

The technique described here uses a carefully miniaturized version of the simple apparatus that Siemer originally developed for boron detection by flame emission. In common with the earlier approach, it combines convenient "one-step" operational simplicity with quantitative transfer of analyte from the sample aliquot to the excitation source. Even though most of the methanol accompanies the boron into the plasma, the amount of methanol used per analysis is so small that the plasma is not seriously perturbed. Consequently, the method features the best absolute detection limits reported by ICP-AES for boron.

Experimental Procedure

Instrumentation. An Applied Research Laboratories, model ARL-3520, ICP-AES was used for the development of this method. The sample introduction system was modified as shown in Figure 64. Argon plasma flow, coolant flow, and other ICP instrument settings are listed in Table 19 and are quite similar to those used by the same instrument for conventional analyses. The sample pickup tube (0.5 mm ID PTFE) of a standard pneumatic nebulizer (Meinhard TR-30-A3) was inserted through the rubber stopper-tube adaptor used to seal the top of the polypropylene test-tube reaction vessel. Two other small PTFE tubes were also inserted through this stopper. One of these was connected to a syringe pump (Sage Instruments model 341A) used to deliver methanol, and the other (0.8 mm ID) to vent the bottom of the stoppered reaction vessel to an atmospheric-pressure argon reservoir. A "Y" inserted into the nebulizer's argon line directed a small fraction of this argon first through a flow restrictor and then into this reservoir. The reaction vessels were 9.5 x 74 mm polypropylene test tubes cut to a length of 32 mm. The nebulizer was connected directly to the bottom of the torch with a short piece of surgical rubber tubing. The reaction test tubes were kept as short a possible and the spray chamber was removed to minimize severe "tailing" of the signals that would otherwise occur as the methoxyborate would absorb/desorb from the excess surface area on its way to the torch.

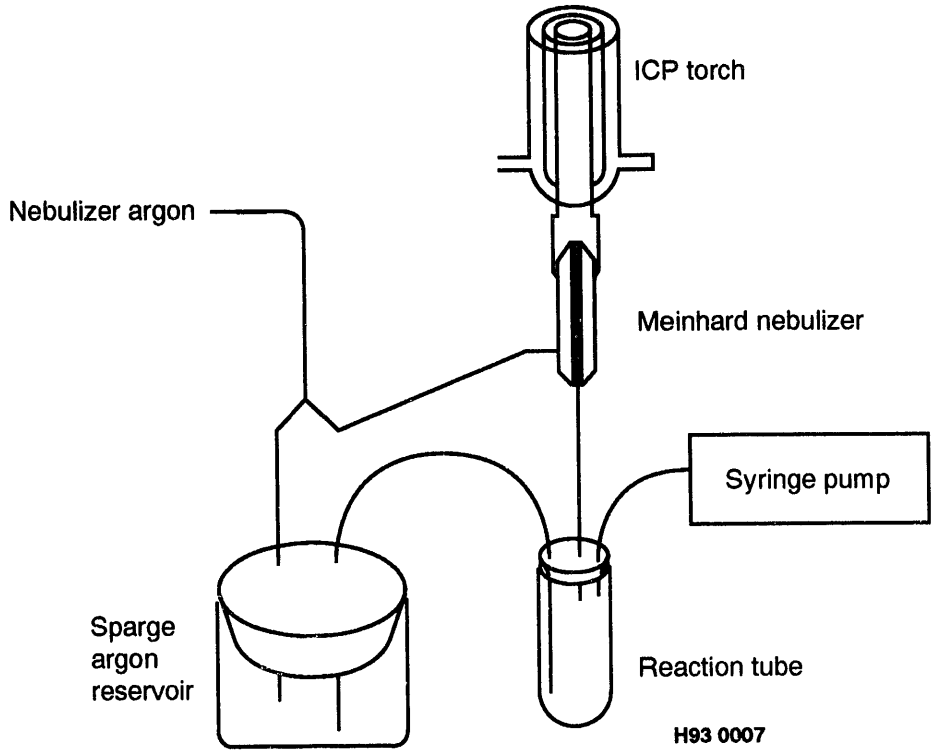

Figure 64. Schematic of modification to ICP-AES sample introduction system for the *in-situ* generation of methoxyborate.

Table 19. ICP-AES parameters for the determination of boron as methoxyborate.

Coolant flow (L/min)	11
Plasma flow (L/min)	1
Carrier flow (L/min)	1.1
Incident power (Kw)	1.2
Viewing height (mm)	15
Boron wavelength (nm)	249.776
Meinhard nebulizer	TR-30-A3
Radio frequency (MHz)	27

The nebulizer's natural suction was used to provide the force necessary to sparge the argon carrier flow though the solution in the reaction vessel, and then aspirate the resulting gas mix into the torch. The aspiration rate of the selected nebulizer was ~40 mL/min of gas. Using the standard nebulizer to do this is not only convenient, but a negative-pressure sample introduction system also prevents any inadvertent leaks from causing loss of analyte.

Plastics are used wherever possible because they are both readily available and chemically compatible with the reagents. Glass is to be avoided wherever possible because most types of glass seem to have sufficient "acid-leachable" boron in them that "background signal" is overwhelming.

The instrument's tuning system was adjusted so the plasma would not be extinguished, since

the gas being aspirated into the torch's sample introduction tube changes during the various stages of an individual analysis. The three different gases introduced during an analysis include argon only, argon with a combination of methanol and methoxyborate vapors, and air only. In the case of the ARL-3520, adjusting the tunable air-capacitor to give minimum reflected power when the nebulizer was freely aspirating air meets this requirement. With this adjustment, the reflected power ranges between 0 and 15 Watts as the gas composition varies during analyses.

For developmental/diagnostic work, a standard laboratory integrator-recorder (Perkin-Elmer LCI-100) was used to record/display the "raw" photomultiplier tube signal. The ARL-3520 with "A-type" electronics already has test jacks suitable for this. These jacks are not normally active, but can be activated using software commands in the "TEST" mode of operation.

A previous report[83] describing use of the ARL-3520 as a chromatographic detector made similar use of those jacks. For routine analytical work, the spectrometer's standard readout system was used to integrate the peak response for 60 seconds.

Calibration. Calibration was performed using standards prepared from 1000 μg/mL commercial boron standards for atomic spectroscopy (Fisher Scientific) that contain the boron as boric acid. At each boron concentration, 5 μL of the standard was placed into the bottom of the reaction vessel, 25 μL of concentrated sulfuric acid (approximately 0.04 g) was added, and the reaction vessel was stoppered with the modified stopper. Methanol was added via the syringe pump for five seconds (70 μL). The signal integration period was initiated at the beginning of the methanol addition. The boron response was integrated for 60 seconds—enough time for the signal to essentially return to baseline. Calibration was generally done, in triplicate, with standards containing 0, 5, 15, and 50 ng of boron (i.e. 5 μL of 0, 1, 3, and 10 μg B/mL aqueous standards). Linearity is excellent. A typical calibration curve would give a line slope of 31.9 ± 0.3 mV/ng, y-intercept of 159 ± 8 mV, standard error of the y estimate of 16 mV, and regression coefficients (r^2) greater than 0.998. Typical detection limits, expressed as three times the standard deviation of a blank, are about 0.2 ng.

Tissue Sample Preparation. Tissues samples were acquired from a dog that had been administered BSH intravenously at a rate of 1 mg boron/kg body weight/min, with a total dose equal to 55 mg B/kg body weight. The 1-2 g samples were homogenized to a paste with a mortar and pestle prior to the subsampling for analysis. To create a more homogenous sample that would provide more reliable subsampling, a separate "reference" tissue was prepared by adding BSH to raw beef liver. The beef liver was then homogenized in a blender, lyophilized, and ground to a powder.

Samples were prepared for methoxyborate ICP-AES analysis by a "caustic ashing" technique. This technique involved weighing the sample (1-30 mg) into a tared 5-mL platinum crucible and wetting it with two drops of a dilute sodium hydroxide solution (~0.2 M). The crucibles were then placed onto a cold hotplate, gently heated to dry the samples, and the hot plate was turned to its maximum setting to char the samples. Final decomposition was performed by heating the crucibles to a bright orange color over an open air-propane flame. When a crucible had cooled, it was placed onto an electronic balance, tared, and 100 μL (0.18 g) of concentrated sulfuric acid was weighed into it. An Eppendorf pipette was then used to rinse this acid repeatedly down the sides of the crucible to assure both complete dissolution and thorough mixing. The crucibles were then stored in a desiccator until the actual analysis was to be performed.

Sample Analysis. One of the reaction vessels was tared onto a top-loading electronic balance and a 25-μL aliquot of the sulfuric acid solution from a sample crucible was weighed into it. The vessel was capped with the stopper-adaptor and the remainder of the analysis was performed

exactly as described previously with the calibration standards.

Results and Discussion. The argon carrier gas flow rate affects the rate at which the generated methoxyborate is sparged from the reaction mixture and carried to the torch, the height of maximum boron emission intensity above the torch's load coil, and the residence time of individual boron atoms within the viewing area of the plasma. Low sparge and total carrier gas flow rates generally give larger responses, peak and area, but the time necessary to integrate them becomes inconveniently long. For this work, the total carrier flow was kept at 1.1 L/min (~20 psi), which kept the nebulizer uptake rate at about 40 mL/min. These values represent an acceptable tradeoff of sensitivity and analysis time. Figure 65 shows both peak widths (at 20% of peak maximum) and cut and weigh integrals of signals generated by 5 ng of boron at various argon carrier flow rates/pressures. For routine analytical work, carrier gas flow rate is usually adjusted to force practically all of the boron through the torch within a convenient 60-second integration period. The previously quoted detection limit of 0.2 ng absolute was generated with this sensitivity-compromised flow rate.

The amounts, both relative and absolute, of water, sulfuric acid, and methanol also affect the peak shape and/or sensitivity of the response. Table 20 shows the effect of varying the amount of sulfuric acid while keeping the amounts of boron (5 ng), water (5 μL), and methanol (70 μL) constant. If insufficient acid is used, the responses are both small and drawn out. Presumably, this is because of water's inhibitory effect on the esterification process; sufficiently concentrated sulfuric acid can absorb this water and keep its activity low. As more acid is added, the response passes through a rather broad maximum and then starts decreasing. Presumably, the reason for this is that if there is too much sulfuric acid, its own reactions with the alcohol does not leave enough

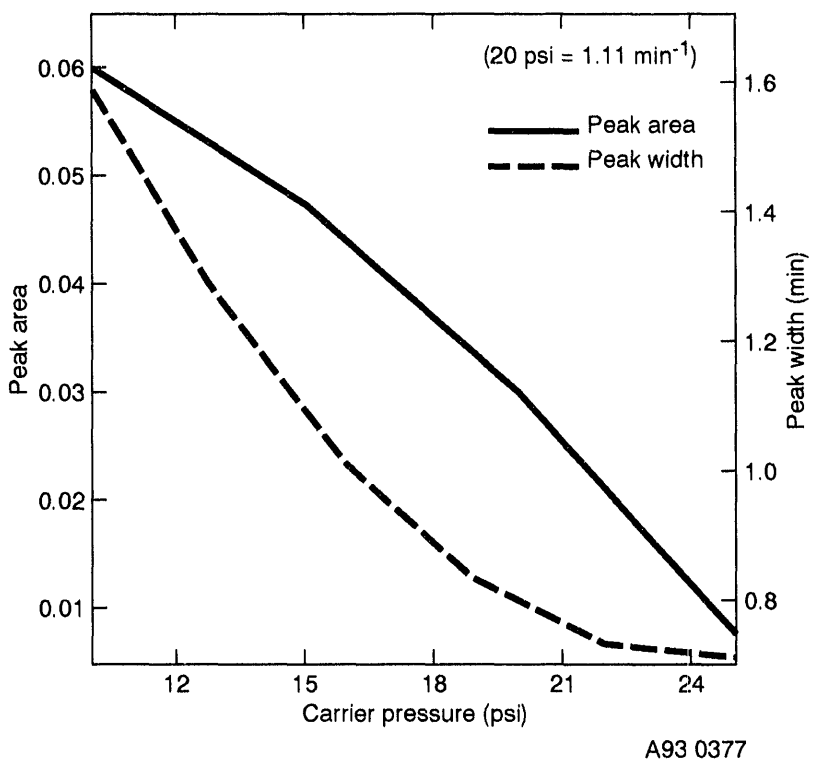

Figure 65. Effect of the carrier flow rate (represented as psi of back pressure) on the peak area and peak width at 20% of the maximum height.

Table 20. The dependance of the quantity of water and sulfuric acid on the measurable boron from the *in-situ* formation of methoxyborate.

Sulfuric acid[a]		Water[b]	
µL	Area	µL	Area
20	17.5	5	24.7
40	15.3	10	23.3
60	8.3	15	15.8
80	3.0	20	4.6

a. Methanol, boron, and water are constant
b. Methanol, boron and H_2SO_4 are constant

"free" alcohol left over to esterify the boron. As less boron is transported to the torch per unit of time, it becomes difficult to distinguish the boron signal from the baseline and the peak areas drop significantly. The ratio of sulfuric acid to methanol appears to be the important feature in this case, since the addition of more methanol will restore the signal.

As can be seen from Table 20, excess water added to the reaction mixture in the test tube also affects the peak shape and should be kept constant and to a minimum. Less than 5-10 µL of water does not have a significant effect on the peak shape or area, but as the amount of water increases, the peaks again become shorter and broader and generally less well defined.

In the INEL laboratory, boron carryover has been noted during standard ICP-AES boron analysis. To limit the carryover, a rather lengthy between sample rinse procedure has been implemented for routine boron analysis. This rinse procedure reduces boron carryover, but does not completely eliminate boron accumulation in the torch. Boron accumulation in the torch can be easily demonstrated when the same torch used for standard analyses is also used for the methoxyborate technique. With each succeeding blank analysis a significant, but decreasing, boron background signal can be observed. Therefore, torches previously used to analyze solutions containing any significant boron concentrations should be avoided. A clean, boron-free torch must be used with the methoxyborate technique to achieve good background stability and to prevent drift during sample analysis.

The recorder tracing in Figure 66 demonstrates a typical peak shape and gives an idea of the reproducibility of the method. The reproducibility of 60-second electronically integrated responses are somewhat better than those of peak height measurements of the same signals. The reproducibility of signal integrals seen with triplicate analyses of either standards *or* blanks is typically less than 2.5% RSD, and often less than 1.5% RSD. A representative mean integral response value for series of blanks would be 135 mV (s = 2.5), and the corresponding integrals for a series of 50-ng standards would be 1700 mV (s = 22.3). Linearity extends from the detection limits to well beyond 250 ng boron. When the boron level exceeds the latter level, this technique would offer no advantage over conventional ICP-AES, unless there was a significant matrix interference. Many different sample decomposition methods were investigated. These methods include nitric acid digestions in Parr bombs, test tube digestions using sulfuric acid/potassium permanganate or nitric acid/hydrogen peroxide, and caustic ashing with both flames and furnaces. Apparent boron recoveries from BSH after Parr bomb acid digestions were typically twice as high when the determination was done by standard ICP-AES than when the same solution was analyzed with the esterification process. The problem was not tissue decomposition, but conversion of the very stable $Na_2B_{12}H_{11}SH$ to borate. None of the previously mentioned wet digestion techniques reproducibly

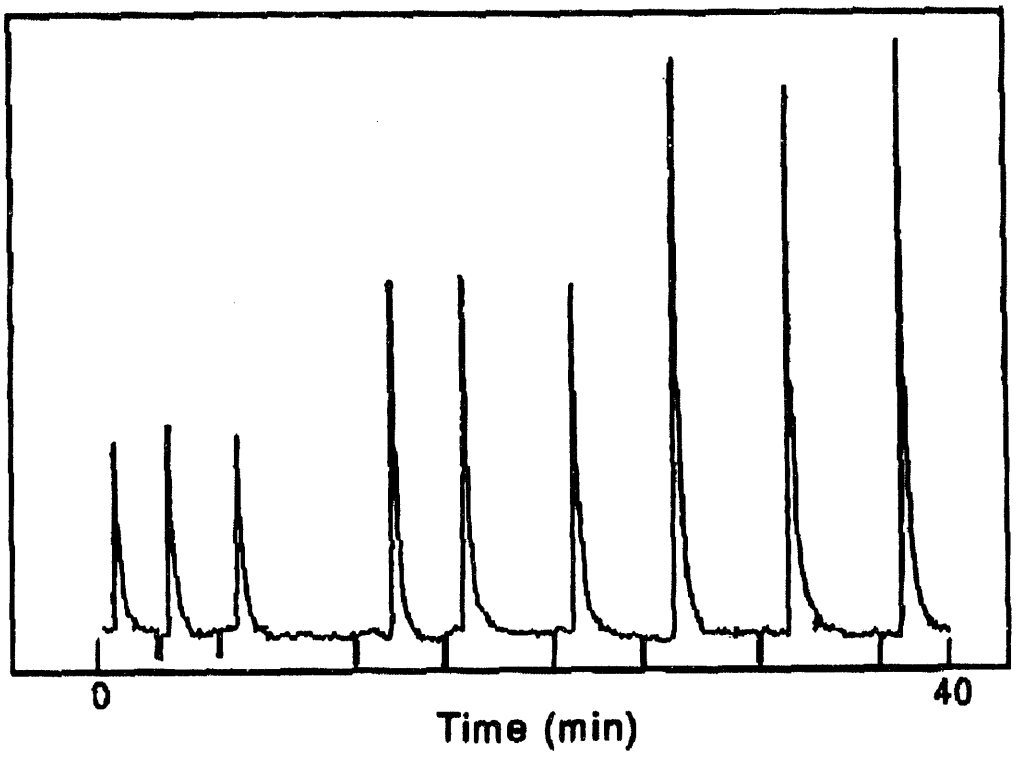

Figure 66. Representative peak shapes obtained from repeated analysis of 5, 10, and 15-ng boron standards.

and quantitatively decomposed this compound. Dry ashing methods with sodium hydroxide in high temperature furnaces (~500°C) were unsuccessful because all of the available furnaces had previously been used for borate fusions, and boron recoveries were much greater than 100%. To prevent the external boron from entering, the crucibles were covered, but after 1.5 hr, only ~36% of BSH boron could be recovered. The quickest and most satisfactory sample preparation technique for dealing with samples containing boron as BSH has been caustic ashing at high temperatures over a burner.

Comparison of samples analyzed with the caustic ashing/methoxyborate technique and acid digestion/standard ICP-AES demonstrates reasonable agreement. Five individual tissue samples of different organs acquired from a dog that had been treated with the BSH compound were analyzed by the methoxyborate technique and by a standard ICP-AES method. In both methods all analyses were done in duplicate. The results of this comparison are presented in Table 21. A paired t-test indicates that there is no significant difference between methods at $P = 0.05$. An F-test shows no difference in the precision of the method. The precision of the two analysis methods is similar as reflected by the relative percent differences between two measurements of the same sample digest, which ranged from 0-5% for the standard ICP-AES analysis technique, and from 0-6% for the methoxyborate technique.

Table 21. Comparison of tissue sample analysis results from standard ICP-AES and DCP-AES with methoxyborate generation.

Tissue	Direct aspiration ICP-AES (μg B/g)	Methoxyborate generation ICP-AES (μg B/g)	Difference
Spinal cord	5.6	4.1	1.5
Liver	81.9	87.8	-6.1
Spleen	20.4	22.9	-2.5
Adrenal gland	44.3	49.0	-4.7
Thyroid	22.0	22.7	-0.7
Lyophilized beef liver[a]	7.8	7.4	0.4
Mean difference			-2.0
Standard deviation			3.0
t_{calc}			1.63
t_{tab} at P = 0.05			2.57

a. Spiked with boron as $Na_2B_{12}H_{11}SH$

Also included in Table 21 is the lyophilized beef liver sample. The boron concentration in the beef liver was again determined by both the standard ICP-AES and the methoxyborate techniques. The standard ICP-AES analysis determined the concentration to be 7.8 ± 0.3 μg B/g (n = 6). The determination by the methoxyborate technique found the tissue concentration to be 7.4 ± 0.2 μg B/g (n = 5). Boron in an aqueous BSH standard was recovered at ~90%.

Overall, good agreement exists between standard ICP-AES and ICP-AES with methoxyborate sample introduction for tissue samples. Absolute detection limits on the order of 0.2 ng boron with the methoxyborate sample introduction will allow this technique to easily quantitate boron at ng/mg levels in samples as small as 1-10 mg. With this technique, detectability of boron in a 5-mg sample is now approximately 0.2 ng B/mg with practical quantitation limits near 0.6 ng B/mg. This represents a minimum of a tenfold decrease in the detection limit of boron in small tissue samples over the best conventional ICP-AES procedures.

Summary

This work has described a relatively simple modification of the sample introduction system of a standard ICP-AES instrument so it can be used to reliably quantitate boron in small samples. The introduction of boron into the ICP torch as methoxyborate in the vapor phase allows the most sensitive boron emission line to be used for quantitation, since the boron is removed effectively from the sample matrix. The primary limitation of this technique is that all boron in the sample must be converted to boric acid to acquire quantitative generation of the methoxyborate. The conversion of boron containing compounds, including BSH, in tissues to boric acid can be done effectively with a caustic ashing procedure followed by dissolution in concentrated sulfuric acid. The methodology described here may potentially be used to determine both therapeutic and dietary boron at part-per-million levels in a variety of small biological sample types. This work has also appeared as reference 99.

SECONDARY ION MASS SPECTROMETRY (SIMS)

Dr. Victor Chia, PI, Charles Evans & Associates

Localization studies of boron in tissues were performed at CE&A under the direction of Dr. Robert Odom. The research group comprised of Drs. Victor Chia, Roger Bleiler, David Sams, Clive Jones, Jack Sheng and Connie John with Dr. Chia as the CE&A coordinator with researchers from INEL, WSU, and Duke University Medical Center (DUMC). The goal of the research was to establish experimental (sample and instrumental) protocols for quantitative imaging of boron atoms in brain tumor tissue cells. If successful, this technique could be used to evaluate the effectiveness of carrier drugs to deliver boron to malignant tissue cells.

Instrumentation

All SIMS analyses were performed using either a Cameca IMS-3f or 4f mass analyzer. These instruments are double-focussing (electrostatic and magnetic sectors) mass spectrometers with mass resolution greater than 3500, and imaging with a spatial resolution of 1-2 μm. A schematic diagram of a Cameca IMS-4f is shown in Figure 67. High mass resolution was necessary to resolve $^{10}B^{1}H$ from ^{11}B and $^{11}B^{1}H$ from ^{12}C (carbon is a major constituent of all tissue samples.) A state-of-the-art time-of-flight SIMS (TOF-SIMS) instrument manufactured at CE&A was also utilized in this research. The system, shown in Figure 68, was equipped with a Cs^{+} ion source for ion microscope analysis and a liquid metal ion gun Ga^{+} microbeam source for ion microprobe analysis. Ion microscope analysis employs a large diameter (>300 μm) primary ion beam and forms mass-resolved ion images by projecting the lateral distribution of secondary ions formed at the surface onto a two dimensional image detector. Ion microscope image resolution is typically 1 to 5 μm. Ion microprobe TOF-SIMS utilizes a finely focussed primary beam that is rastered about the sample surface. Ion microprobe image resolution is determined by the primary beam diameter which is typically 0.2 μm. Fundamental research of ion and molecular imaging of biological tissues by TOF-SIMS probably represents the future in instrumentation for intracellular localization studies.

Quantification

Preliminary experiments to certify SIMS for boron quantification in tissues were performed using boron doped agarose and gelatin samples. Boron doped mixtures of 0.7% w/v of agarose and 5% w/v of gelatin were prepared and their concentrations determined using ICP-AES by INEL researchers. These solutions were deposited using a micropipette onto high purity semiconductor silicon wafers forming a relatively smooth, untextured film after air drying overnight. Spin coating techniques were also used to improve surface homogeneity with little or no improvements. All samples were gold-coated prior to SIMS analysis using a Cameca IMS to improve charge compensation. The SIMS analyses of boron doped agarose and gelatin samples were performed in a dynamic mode using a high primary beam current. Secondary ions of boron (^{10}B and ^{11}B) and carbon were monitored as a function of sputter depth and these in-depth profiles were continued until they were constant. Table 22 shows typical instrument parameters used for these experiments. Boron/carbon ratios were calculated by normalizing the ^{11}B ion counts by its isotopic abundance. The results of this experiment are presented in Figures 69 and 70 which show boron concentrations in agarose and gelatin versus SIMS boron/carbon ratios. Although these calibration plots showed good linearity, it is

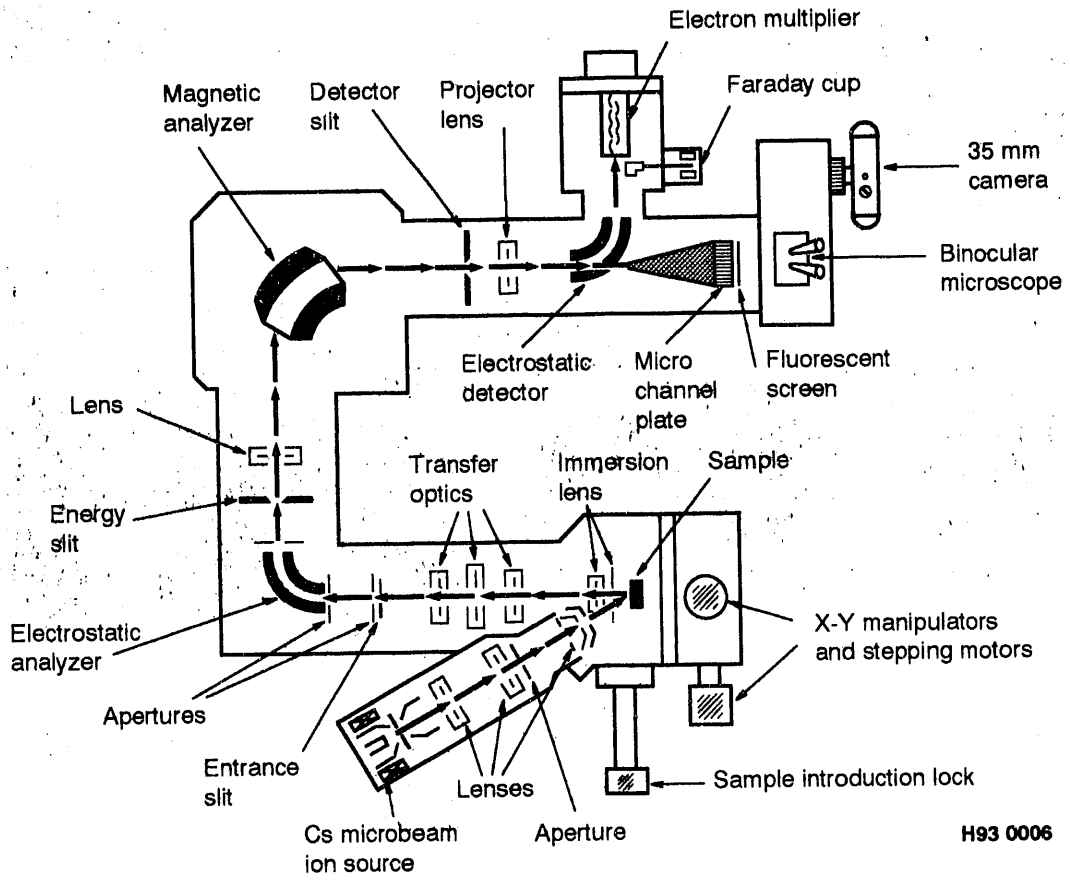

Figure 67. A schematic diagram of a Cameca IMS-4f.

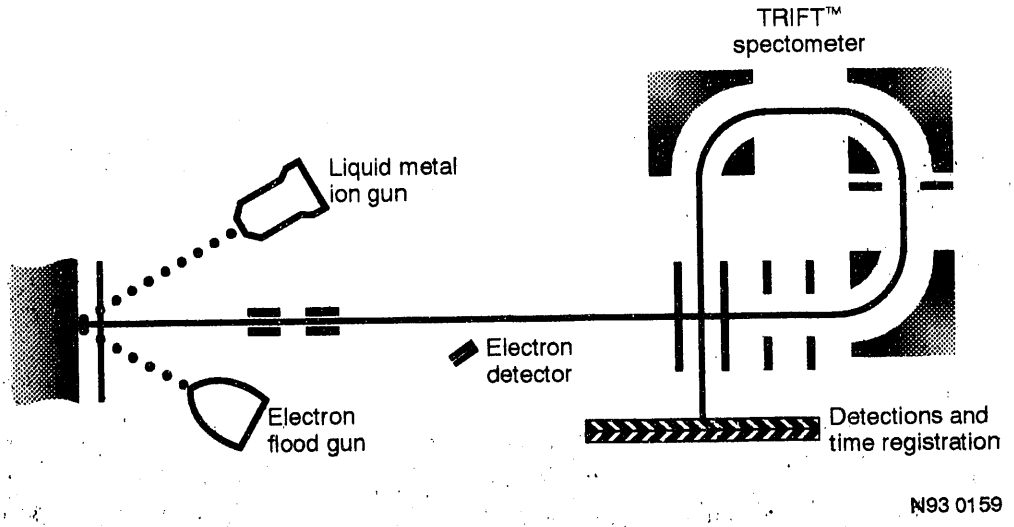

Figure 68. A schematic diagram of a TFS™ TOF-SIMS Surface Analyzer.

Table 22. Cameca instrument conditions used for Gelatin and Agarose analyses.

Parameters	Gelatin	Agarose
Primary beam		
Ion source	O_2+	O_2+
Accelerating voltage	8 keV	8 keV
Intensity	300 nA	30 nA
Beam diameter	250 μm	50 μm
Raster size	0 μm	250 μm
Secondary beam		
Polarity	Positive	Positive
Contrast aperture	150 μm	150 μm
Field aperture	85 μm	85 μm
Resolving power	1000	1000

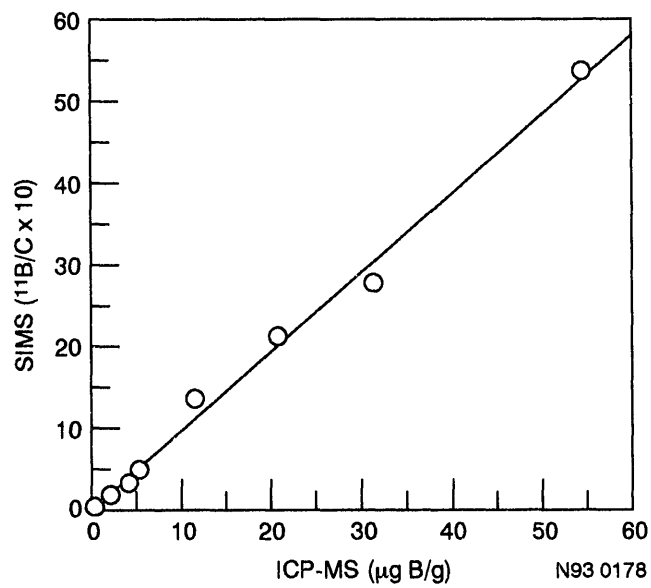

Figure 69. Boron calibration curve in agarose.

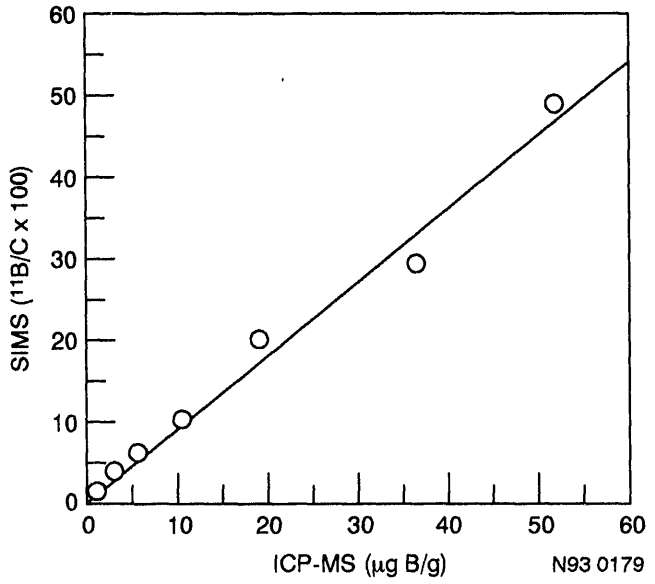

Figure 70. Boron calibration curve in gelatin.

generally accepted within the SIMS community, that accurate calibration standards for quantification is matrix specific. We therefore also performed boron calibration experiments using rat brain stripped (#56005-2, Pel Freez) (50% w/w) and dog brain homogenates spiked with ^{10}B and ^{11}B prepared from $Na_2B_{12}H_{11}SH$ and H_3BO_3 to evaluate their suitability as calibration standards. The SIMS depth profiles and the calibration plot from the rat brain calibration experiment are shown in Figure 71 and 72. All calibration experiments displayed linearity with a correlation coefficient greater than 0.98.

Sample Preparation

The first few tissue samples supplied to CE&A for SIMS analyses were inappropriate due to poor sample preparation. For instance, boron was observed at significant concentrations in regions surrounding the tissue specimen suggesting leaching of boron from the tissue. We suspect that these samples were prepared by freezing tissue at 0°C, sectioning at this temperature and air drying with minimal consideration to the tissue integrity during the sample preparation procedure. For successful SIMS imaging, *viable* tissues with a flat surface is a prerequisite requirement.

In the later part of 1992, attention was focussed on developing tissue sample preparation procedures in collaboration with WSU and DUMC researchers. The methodology developed was based on cryotechniques to stabilize and "fix" ultrastructures of the specimen cells *as it existed under physiological conditions*. Under ideal experimental conditions, cryofixation will preserve the constituents of the biological system in their viable position and minimize ice crystal formation to within a size range that is smaller than the spatial resolution of the observation technique.

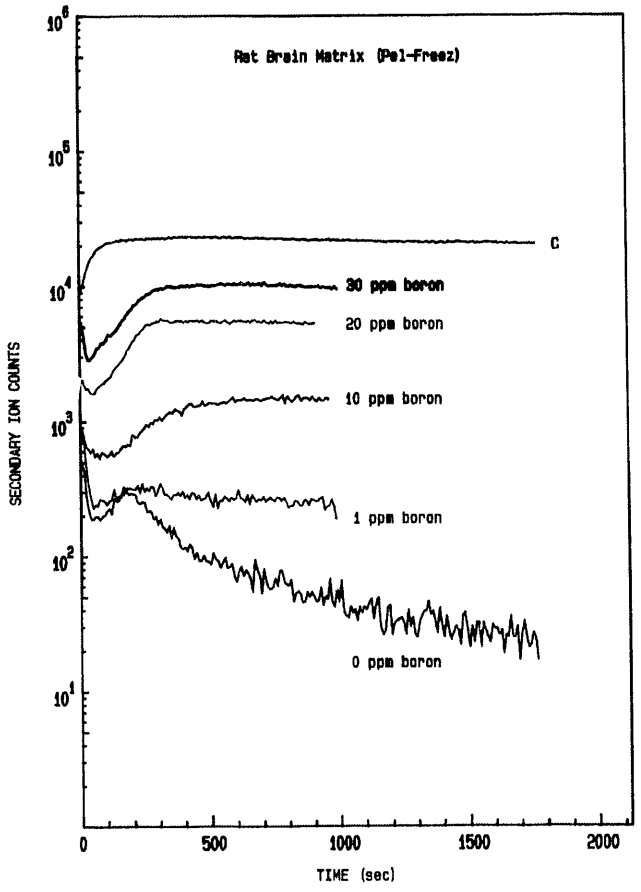

Figure 71. SIMS depth profiles of boron in rat brain matrix.

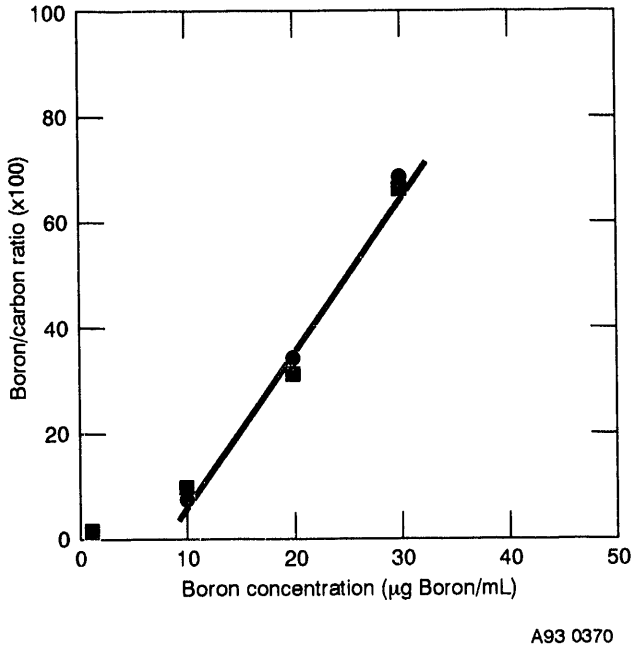

Figure 72. Boron calibration curve in rat brain matrix.

The general procedure adopted was to cryofix a viable tissue using a Reichert-Jung MM 80E Metal Mirror Cryofixation System for ultrarapid freezing. This method provided cooling rates in the vicinity of 50,000 K/s and good freezing (vitrification) to a depth of about 10-15 μm. Cryoultramicrotoming of the frozen tissue (if necessary) was then followed by freeze-drying. An outline of a sample preparation flowchart is shown in Figure 73. Sample preparation by cryofixation is more difficult to perform than chemical fixation. However, the advantages of cryofixation were very significant. For example, leaching of endogenous diffusible elements and loss of organic compounds during dehydration and embedding steps were eliminated in this procedure. Concentration buildup of diffusible elements in artifactual locations due to concentration gradients in the tissue and preferentially bound sites were also eliminated. It is true that cryofixation, as opposed to chemical fixation, is the *only* method that preserves intracellular elemental distributions without adding potential contaminants. As Figure 73 indicates, conventional transmission electron microscopy must be performed in parallel to the SIMS analysis to evaluate the quality of the cryosections with respect to induced structural artifacts from the cryopreparation procedures.

TOF-SIMS Imaging

Several examples of TOF-SIMS images are presented to demonstrate the utility of TOF-SIMS for localization studies. Figure 74 shows the positive secondary ion image of a model membrane surface, composed of phosphatidylcholine covalently attached to silica particles with the polar end groups exposed. This image was acquired in the ion microprobe mode. The beads are 7-12 μm in diameter (cell dimensions) and were randomly distributed onto a carbon substrate. Pseudo three-dimensional images of the spheres are clearly observed in this figure. It was important to realize

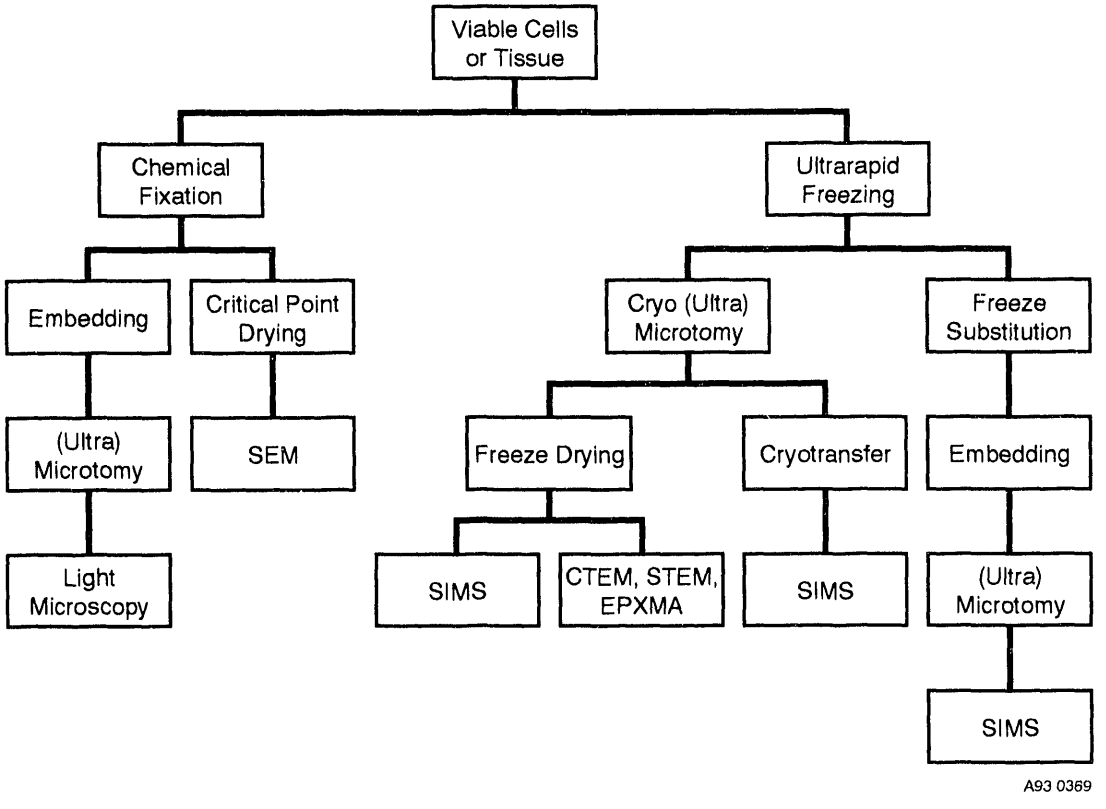

Figure 73. Biological tissue preparation.

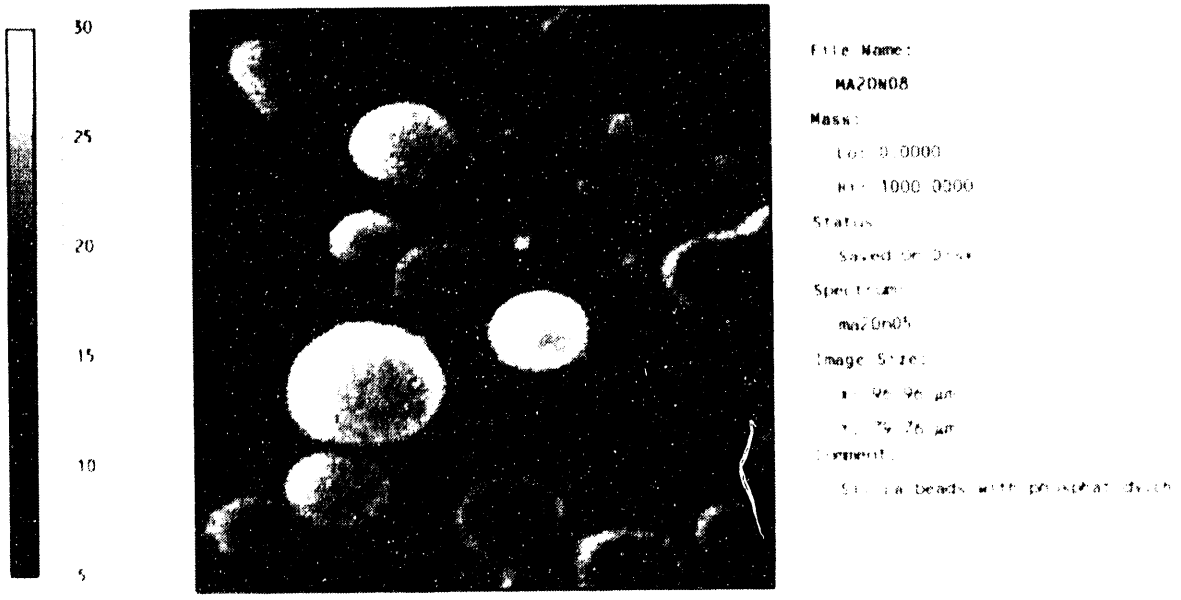

Figure 74. Total secondary ion image of silica beads.

during this analysis that sample surface inhomogeneities can produce artifact features in a SIMS image. Matrix ion intensity normalization was therefore routinely performed to determine if features were intrinsic to the sample surface.

A second example is presented in Figures 75 and 76. These show how the total secondary ion and boron images were acquired from a selected region of skin #3 of dog #2714. Boron was observed homogeneously across the tissue sample, even in the tissue voids (top center of figure), confirming previous observations of leaching occurring during sample preparation. These examples illustrate that the TFS™ TOF-SIMS Surface Analyzer is a capable tool for inter- and intracellular localization studies. Instrumental research is continually improving the detection efficiency of organics and boron using post-ionization and post-acceleration techniques and spatial resolution with new and improved primary sources.

SIMS Imaging of Boron Infused Rat Liver

During the first half of 1992, several tissue samples were imaged from Beagle #2174 as an exercise to determine optimal instrument conditions for the Cameca IMS. By September 1992, researchers felt reasonably confident in attempting a SIMS image analysis of tissue from a boron infused rat. This experiment involved WSU, INEL and DUMC. The boron infusion of the rat and sample preparation were performed at WSU. Ultracryomicrotoming and freeze drying of these tissue sections were done at DUMC. ICP-AES analyses for boron were performed at INEL and the SIMS imaging was performed at CE&A. This experiment was coordinated by Dr. Chia (CE&A), who also supervised the sample preparation procedures at WSU.

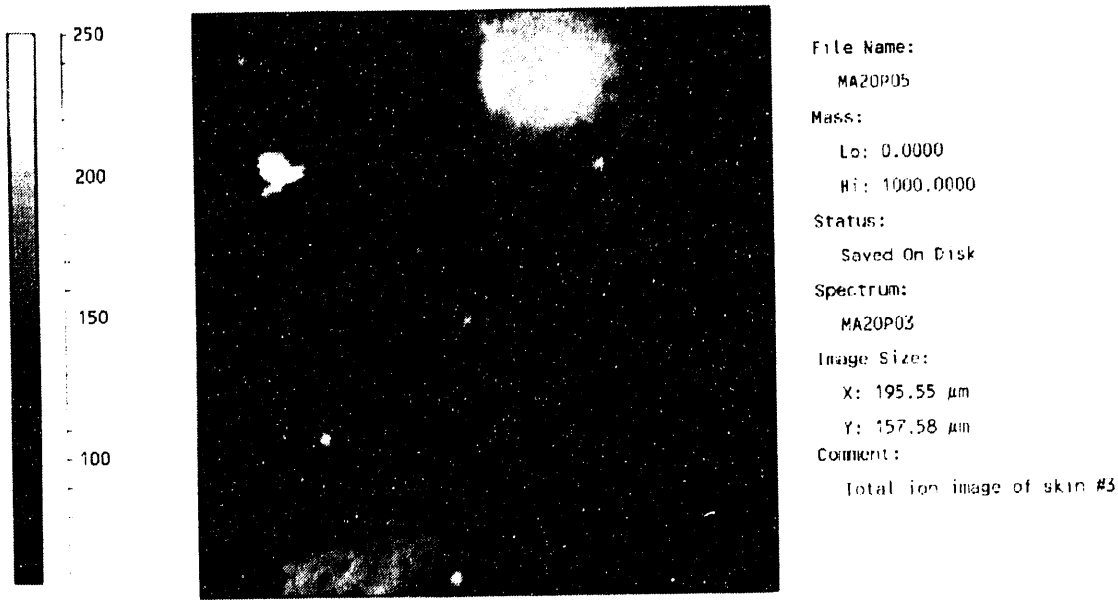

Figure 75. Total secondary ion image of dog skin.

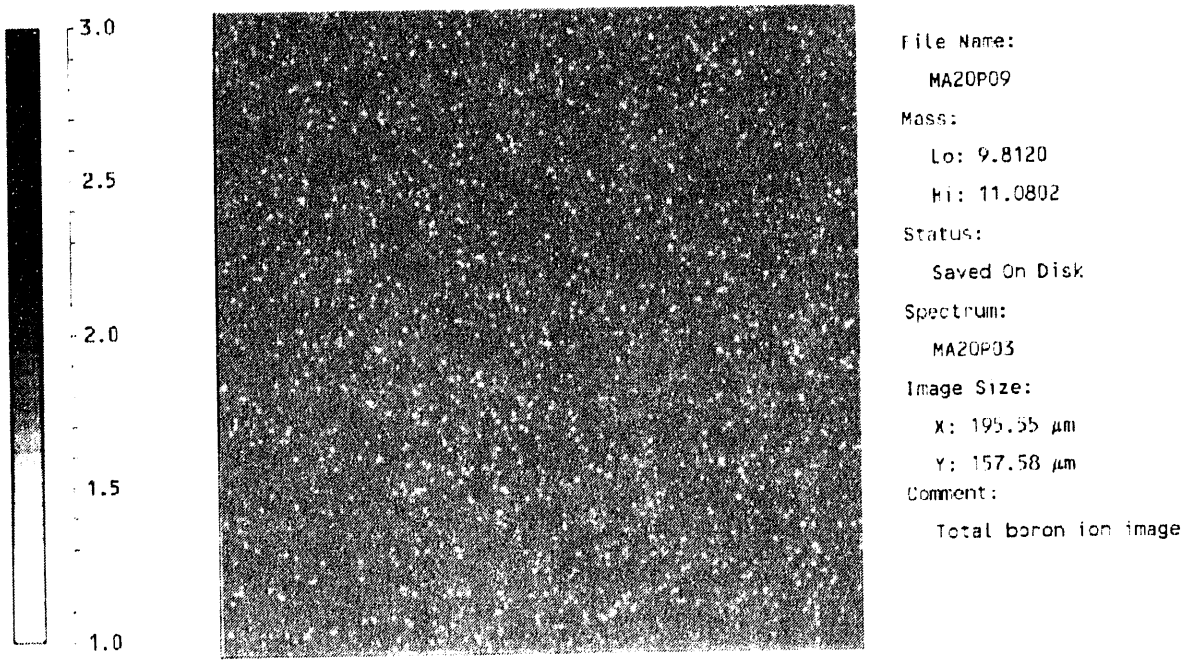

Figure 76. Total boron ion image of dog skin.

A laboratory rat was intravenously infused with BSH (100 mg B/kg body weight, natural abundance boron) and the boron was allowed to distribute to the tissues for about one hour. This rat and a control rat (not administered with boron) were then euthanized and the liver and three regions of the brain (cerebral hemispheres and brainstem) removed and immediately cryopreserved using a liquid nitrogen metal mirror fixation unit. Tissue samples designated for SIMS analysis were stored in a liquid nitrogen dry-shipper dewar and mailed to DUMC. After ultracryomicrotoming and freeze-drying at DUMC the tissue samples were returned to CE&A under vacuum for SIMS analysis. The remaining portions were shipped to INEL for ICP-AES analyses.

Presently, only the liver tissue samples have been imaged and depth profiled by SIMS. Boron quantification was performed using brain homogenate as the matrix standard. Figure 77 shows boron calibration curves of boric acid and BSH in brain homogenate and BSH in gelatin in which the absolute boron concentrations were quantified by ICP-AES. Note that the slope of the calibration plot for BSH in brain homogenate was lower than the corresponding boric acid plot, and that similar slopes were observed for the plots of boric acid in brain homogenate and BSH in gelatin, suggesting that the sampled aliquots from BSH in brain homogenate contained the aqueous unbound boron.

For the purpose of this study, an average value of the brain homogenate and gelatin calibration results was used for boron quantification in the liver tissue. Dynamic SIMS profiles acquired from the liver of the diffused and control rat are shown in Figure 78. Boron concentrations of about 53 μg B/g in the infused rat and about 13 μg B/g in the control rat were observed. An optical micrograph of the freeze-dried section and a boron secondary ion image of the infused rat's liver are shown in Figure 79. Boron appears homogeneously distributed and was not observed in the tissue voids indicating that no diffusible boron was lost during sample preparation. The potassium secondary ion image in Figure 80 shows clusters of high intensity spots probably corresponding to cells. The observed potassium/sodium ratio of about eight suggests that the tissue was viable at the time of cryopreservation.

These preliminary results illustrate that quantitative imaging is possible by SIMS with appropriate cryopreservation of tissue. Quantification using brain homogenate gave reasonable boron concentration values in the liver; a comparison with ICP-AES results will confirm the accuracy. Boron was homogeneously distributed in the freeze-dried liver section of the infused rat. The viability of the tissue at the time of cryopreservation was confirmed by the high potassium to sodium ratio. The high intensity potassium spots observed probably correspond to individual cells. Further improvements in the cryopreservation methodology is required to obtain higher resolution images which will provide even better localization of boron in tissue.

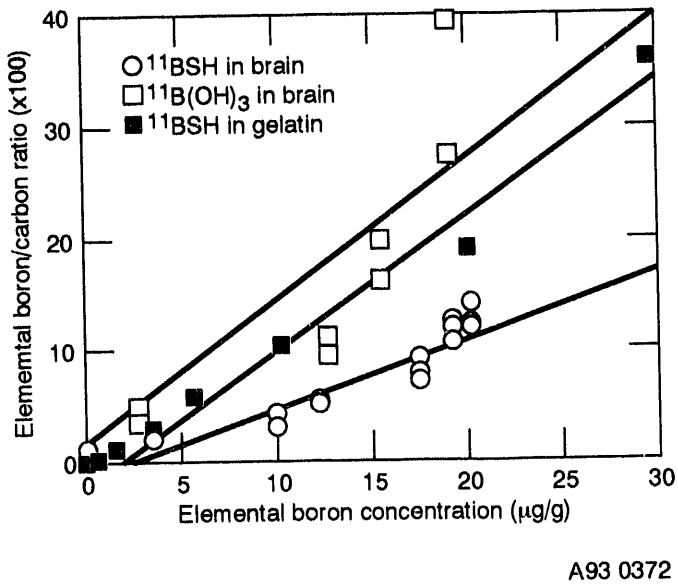

Figure 77. Boron calibration curves of BSH and boric acid in brain homogenate and gelatin.

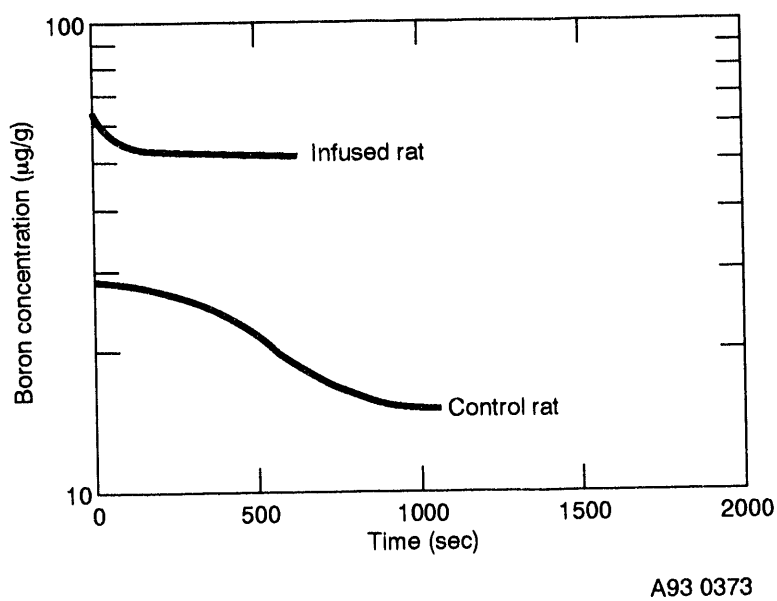

Figure 78. SIMS depth profiles of boron in the liver of an infused BSH rat and control rat

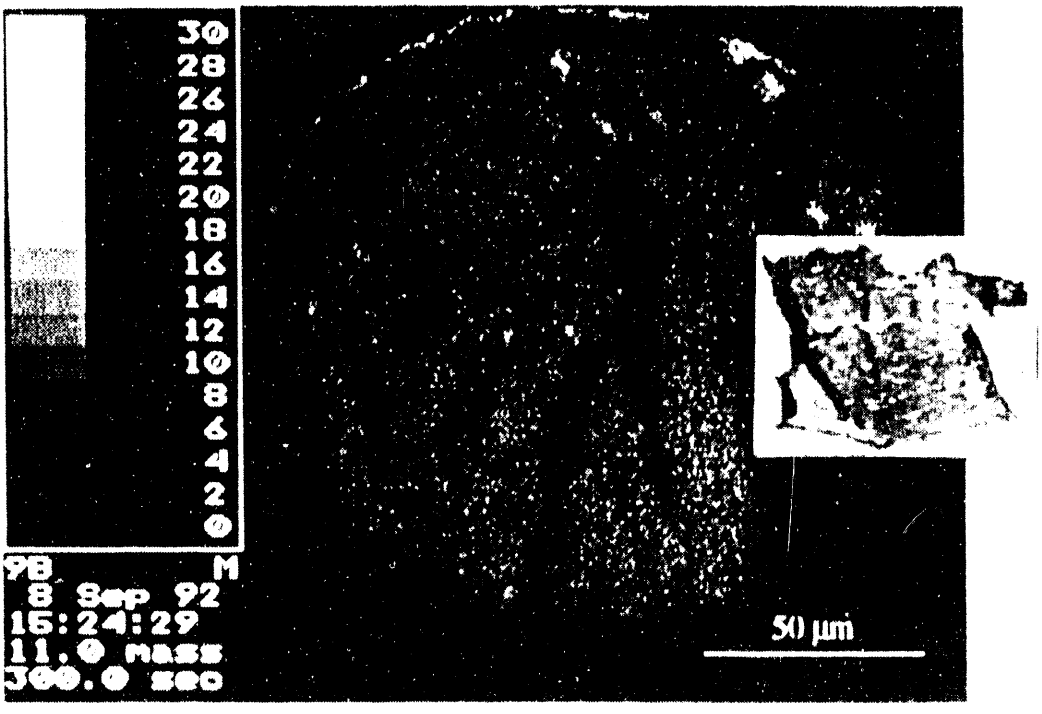

Figure 79. Boron secondary ion image of liver tissue from the injected rat. Insert shows an optical micrograph of the freeze dried liver section prepared at DUMC

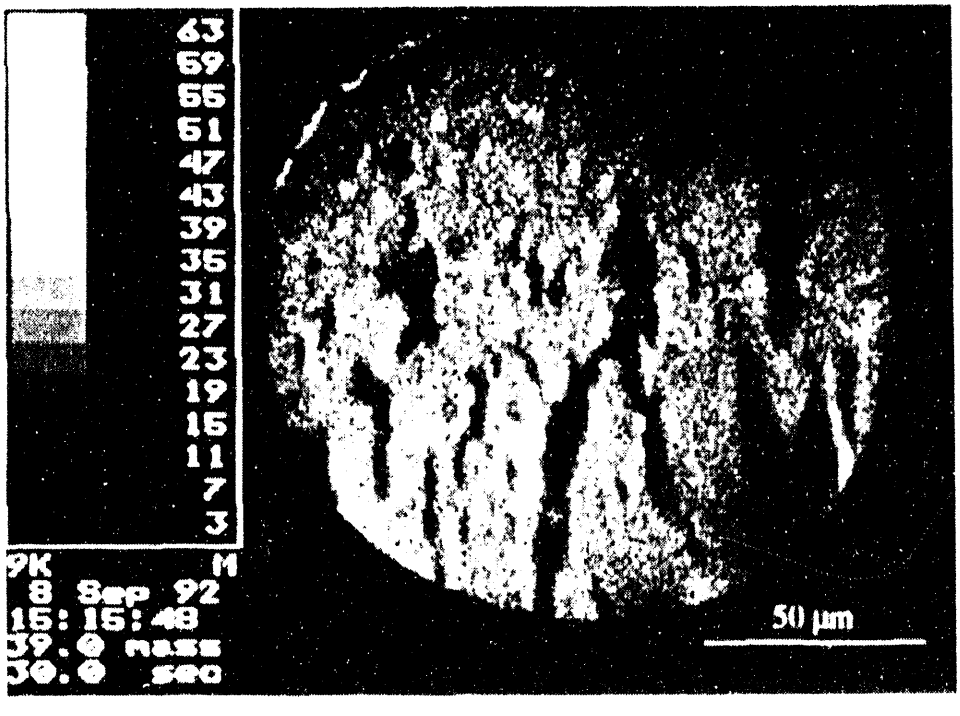

Figure 80. Potassium secondary ion image of liver tissue from the injected rat

ALPHA TRACK-ETCH

Dr. Clive Nelson, PI, Idaho State University, College of Pharmacy

Researchers at ISU have demonstrated the use of track-etch techniques for measuring boron in tumors and brain tissue.

There are various brain imaging techniques (for example, CT, positron emission tomography and nuclear magnetic resonance) that have become available during the past decade. These techniques have made it possible to map the structure and function in both normal and chemically altered human brain.

Such techniques have proven extremely helpful in certain types of analyses; yet their demonstrated use in the measurements of brain boron is limited, and the sensitivity in fine structure analysis (for example, boron in nuclear masses) generally ranges from poor to unachievable. The boron images are often poorly defined in comparison to the resolution and sensitivity of boron determinations by track-etch methods. On the other hand, track-etch methods cannot be used under *in vivo* condition.

Conventional autoradiographic techniques are still generally used to obtain the distribution of selected chemical substances in biological tissues. The substance under consideration is tagged or labelled with a radioactive element; often carbon-14 or tritium that naturally emits beta particles for long periods of time. The beta particles are registered as density changes in silver impregnated film. Conventional autoradiography, however, cannot be used to adequately measure boron. Boron has no isotope that emits beta particles over long periods of time, and exposure of the film to a reactor environment essentially ruins the sensitivity of the film. Other methods are available to determine boron in tissue but they have traditionally been based on either pooled samples (that is, in the case of small animals or brain areas) or the excision of enough tissue to enable the measurement of boron content by various techniques. Although these methods of measuring boron in liquid or ashed samples are sufficiently adequate for most clinical purposes, it prevents a detailed correlative anatomical investigation of boron distributions within intact tissue.

A method for obtaining the concentration and distribution of boron in intact whole brain sections in small animals or in intact tissue from larger animals is possible by track-etch methods. The method essentially involves freeze-drying sections of tissue, overlaying them with specially prepared films sensitive to nuclear particles, bombarding the tissue and film with thermal neutrons, etching out the $^{10}B(n,\alpha)^{7}Li$ particle tracks in the film, superimposing the film on the tissue, and analyzing the distribution of tracks with the aid of a light microscope. Atoms of boron are evidenced by those areas wherein particle tracks occur. The method is sensitive and suitable for any tissue where boron-induced tracks are significantly above background.

Materials and Methods

Liver and brain tissues from dogs that had been given substances containing ^{10}B were made available for this work by WSU researchers. The tissues were received in a frozen condition and were immediately stored in a low temperature freezer. In preparing the tissues for sectioning, small amounts (~1 cm^3) were cut from the frozen specimens and quickly mounted on tissue holders. Normal saline, made with distilled water, was used to freeze the tissue to the holders. Twenty micron-thick sections were cut in a cryostat microtome and the sections were systematically mounted and affixed to a cold plastic slide by slightly warming the plastic under the section with a finger. The procedure was carried out in the atmosphere of the cryostat microtome with a controlled minimum thawing of the tissue. The plexiglass slides with mounted tissue sections were placed in open slide boxes (containing a few small pieces of dry ice) and freeze-dried.

In a series of experiments, three types of nuclear track detector films were analyzed for

their effectiveness in measuring tracks from $^{10}B(n,\alpha)^7Li$ reactions in dog brain and liver tissues. The films included allyl diglycol carbonate (CR-39), from American Acrylics, Stratford, CT; colorless cellulose nitrate (LR115-3) from Kodak-Pathe, Paris, France; and cellulose nitrate (CN-1) fabricated in our laboratory from Hercules Incorporated nitrocellulose. The films were placed over unstained freeze-dried sections of tissue and securely attached at both ends of the slide with plastic tape. The slides and the overlaying films were stacked 10 to 15 per packet, tightly pressed and taped together. To measure the neutron flux that the packets were exposed to during neutron irradiation, four gold disks (30mg/disk) were dispersed throughout each packet. The packets were placed in polyethylene bags, sealed and irradiated with about 10^{11} neutrons/cm^2 in the ISU nuclear reactor. After irradiations, the gold disks were removed from the packets and counted for gamma radiation activities with a multi-channel analyzer that allowed neutron flux determinations.

The perimeters of several tissue sections on each slide were carefully traced on the film with a fine-pointed tungsten carbide scribe and two small holes were drilled through the film and into the plexiglass slide with a high speed twist drill. The tracings were done with the aid of a zoom microscope at about 10X to 15X magnification. Unlike the conventional bright field microscope, the zoom scope allows up to 10 centimeters working distance and greatly increases the ease and accuracy of the tracing procedure. The tracings and later realignment of the holes (drilled diagonally apart near the ends of the slides) made it possible to accurately count and analyze the alpha tracks in the etched films.

The films were detached from the slides and etched in a series of different concentrations and temperatures of sodium hydroxide to determine the best etching conditions for track production. A thermoregulator kept the temperatures within ±1°C. After etching the procedure of repositioning and realigning the high speed twist drill holes was undertaken. The realignment of holes by this technique can be within 5 to 7 μ.

The nuclear tracks in the film originating from tissue sections were counted by use of a net reticle in the eyepiece of the microscope. The track counts were obtained in two ways throughout the film. One was to count tracks in random fields of view over the film (random counting). The other was to count tracks in a series of adjacent field views across or up and down the film (deliberate counting).

Boron concentrations in liver and brain were obtained by comparing the number of tracks originating from $^{10}B(n,\alpha)^7Li$ reactions in these tissues with $^{10}B(n,\alpha)^7Li$ tracks produced from a set of standards. The standards were made by mixing ^{10}B (as boric acid, $H_3{}^{10}BO_3$ 99% enrichment; Eagle Picher) in solution with 1 gm amounts of homogenized chicken liver in 20 mL plastic beakers. A small amount (100 μl) of a warm 5% gelatin solution was added to each beaker, the mixture was gently stirred for 10 minutes and then placed on a Vortex-Genie test tube mixer for two minutes to expel air pockets. Several series of 10^{-3}, 10^{-4}, 10^{-5}, 10^{-6}, 10^{-7}, and 10^{-8} grams of ^{10}B per gram of homogenized liver were made-up. The standards were allowed to set up over night at 35°C and were then kept frozen at -60°C until sectioned, affixed to plexiglass slides, and freeze-dried. The various types of films (CR-39, LR115-3 and CN-1) were positioned against slides containing the unstained standards, exposed to about 10^{11} neutrons/cm^2 and processed like the tissue specimens. The nuclear tracks from the liver standards were counted, corrected for background tracks, and normalized to an exposure of 10^{11} neutrons/cm^2. The track counts were used to construct a set of standards.

Results

Allyl diglycol carbonate (CR-39) film

The first film to be analyzed for possible use in determining the distribution and concentration of ^{10}B in tissues was CR-39. This polymer was introduced as a possible track detector about 12 years ago and has been described by some as having remarkable track-recording properties. It was observed some years ago in CR-39 plastic, like various other plastics used for nuclear track

detection, that the ratio of tracks to bulk (surface) etch rate increases with increasing temperatures in the caustic etch solution. Also it was observed that CR-39 obtained from different manufacturers has different etch characteristics. Therefore, it was necessary to check the response of the CR-39 film for alpha track production under various etching conditions. Thus, a series of these films was exposed to radioactive lead-(^{210}Pb, an alpha particle source) and etched over a period of 60 to 90 minutes at 70°C and 75°C in various concentrations of sodium hydroxide (NaOH). Every three minutes during the etching period, the film was removed from the etching bath and analyzed for track formation and optimum etching conditions were determined. Alpha tracks in CR-39 film from a ^{210}Pb alpha source are shown in Figure 81c. It is evident that pits rather than tracks occur in the film.

A series of experiments using liver standards (containing from 10^{-3} to 10^{-8} g B/g standard) with CR-39 films was also carried out. The films exposed to 10^{-7} and 10^{-8} g boron liver standards and irradiated with 10^{11} neutron/cm^2 were especially difficult to quantitate because of background tracks. Due to the low energy of the $^{10}B(n,\alpha)^7Li$ nuclear particles, the originally formed needle-like ghost tracks in the CR-39 film rapidly change to pits during etching. If the etching process is stopped when the first needle-like tracks appear, the number of tracks are significantly reduced. Alternatively, optimum track production requires a longer time interval of etching that results in pit-like tracks.

Dog brain and liver tissues were included in the analysis of ^{10}B concentrations by use of CR-39 films. The background tracks in the films caused difficulties in the track analysis of both liver tissue and liver standards. When CR-39 films were exposed to neutrons, it was nearly impossible to differentiate background from $^{10}B(n,\alpha)^7Li$ tracks. Apparently many of these background tracks originate from recoil protons within the film.

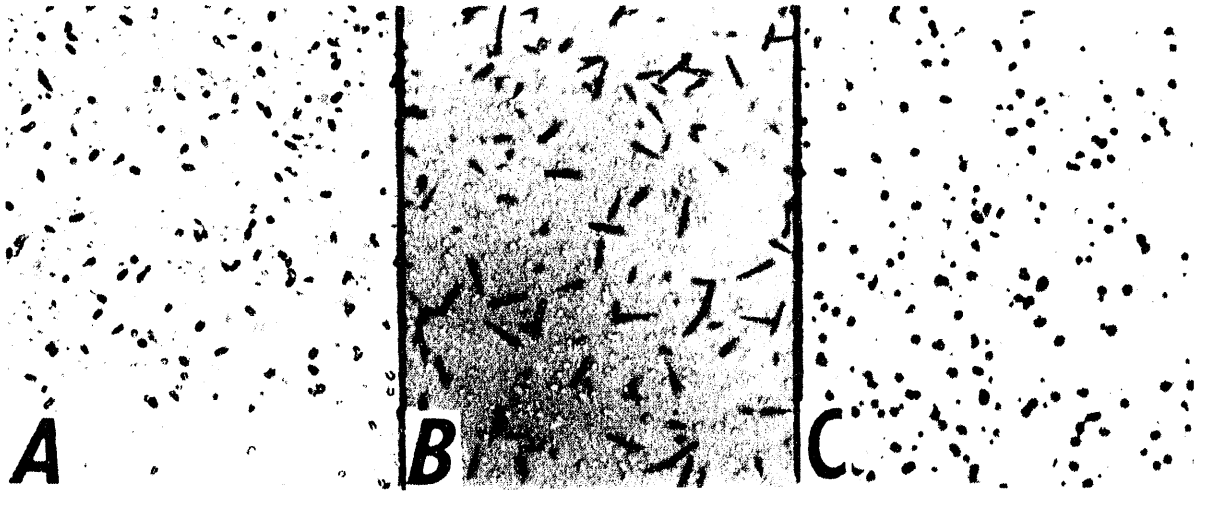

Figure 81. Alpha tracks from the radioactive isotope of Lead-210 (^{210}Pb) in three types of nuclear track detecting film: A - LR115-3, B - CN-1 and C - CR-39; ~ 400X.

Kodak-Pathe Colorless LR115-3 Film

The LR115-3 film was next analyzed for its potential use in determining the concentration and distribution of ^{10}B in tissues. Kodak originally made cellulose nitrate film in Rochester, NY as a part of their products for special biomedical imaging applications. Later the manufacturing of cellulose nitrate films was moved to the Kodak facilities in France. The colorless LR115-3 film allows the alignment of tracks in the film with their origin in the tissue. Like the CR-39 film, it was necessary to check the response of LR115-3 film for $^{10}B(n,\alpha)^7Li$ track production. A succession of films was exposed to ^{210}Pb alpha particles and etched over a period of 25 to 75 minutes at 60°C in a 2.5 normal sodium hydroxide solution. Films were analyzed for track formation every five minutes. A photomicrograph typifying track formation in LR115-3 film from a ^{210}Pb source is shown in Figure 81a. The film is slightly overetched and the tracks are beginning to take on a pit-like form.

A series of track analyses using liver standards (from 10^{-3} to 10^{-8} g^{10}B/g standard), and dog liver and brain tissue was also done with LR115-3 films. As expected from the higher energy of the ^{210}Pb alpha, the length of tracks from standards and tissues were shorter than those in ^{210}Pb exposed film. Longer etching periods are required to obtain an optimum track number and length. However, tight control of etching time is necessary, otherwise many of the tracks become pit-like and ^{10}B origins in tissue become difficult to locate.

Cellulose Nitrate (CN-1) Film

This film has been used before by the PI of this project and the optimum etching conditions for the CN film were known. Nevertheless, since new batches of the cellulose nitrate solution were made up at the beginning of the project it seemed prudent to check out the response of films made from the new solutions. Alpha tracks in CN-1 films from a ^{210}Pb source are shown in Figure 81b. The higher energy alpha particles from the ^{210}Pb source produce a desirable needle-like track that allows a better means of determining boron origins.

Dog brain, liver, and liver standards 10^{-3} through 10^{-8} g B/g standard were analyzed for boron by CN-1 films. The $^{10}B(n,\alpha)^7Li$ reactions in brain tissue produced the best tracks. Photomicrographs of the processed CN-1 films are shown in Figures 82 and 83. It is evident from Figure 82a that $^{10}B(n,\alpha)^7Li$ boron tracks in cerebral gray matter were unevenly distributed. Some areas indicted considerably more boron (track) deposition than other areas.

The boron (tracks) in the cerebral white matter (Figure 82b) were much less concentrated and more evenly distributed than tracks in cerebral gray matter. The boron (tracks) in the granular layer of the cerebellum (Figure 83a) were less than those found in cerebral gray matter and it did not appear to be as unevenly distributed. The boron (tracks) in cerebellum white matter (Figure 83b) had a distribution similar to cerebral while matter. Figure 83b shows (at a lower magnification) the edge of some cerebral gray tissue where boron (tracks) were more evenly distributed than the boron (tracks) in the cerebral gray tissue shown in Figure 82a. The number of boron (tracks) in the gray matter areas of the cerebellum and cerebrum were consistently greater than boron (tracks) located in the gray-white transitional and white matter areas.

Brain boron concentrations obtained by $^{10}B(n,\alpha)^7Li$ track analysis in CN-1 film were compared with INEL brain boron determinations by ICP-AES techniques. The $^{10}B(n,\alpha)^7Li$ track analysis results were generally within plus or minus 10 percent of the ICP-AES results. This was encouraging when considering that one method (Track-etch) relies on track counts from rather small areas of uneven distributions of boron atoms in intact tissues and the other method (ICP-AES) requires liquefying the tissue before measurements are made.

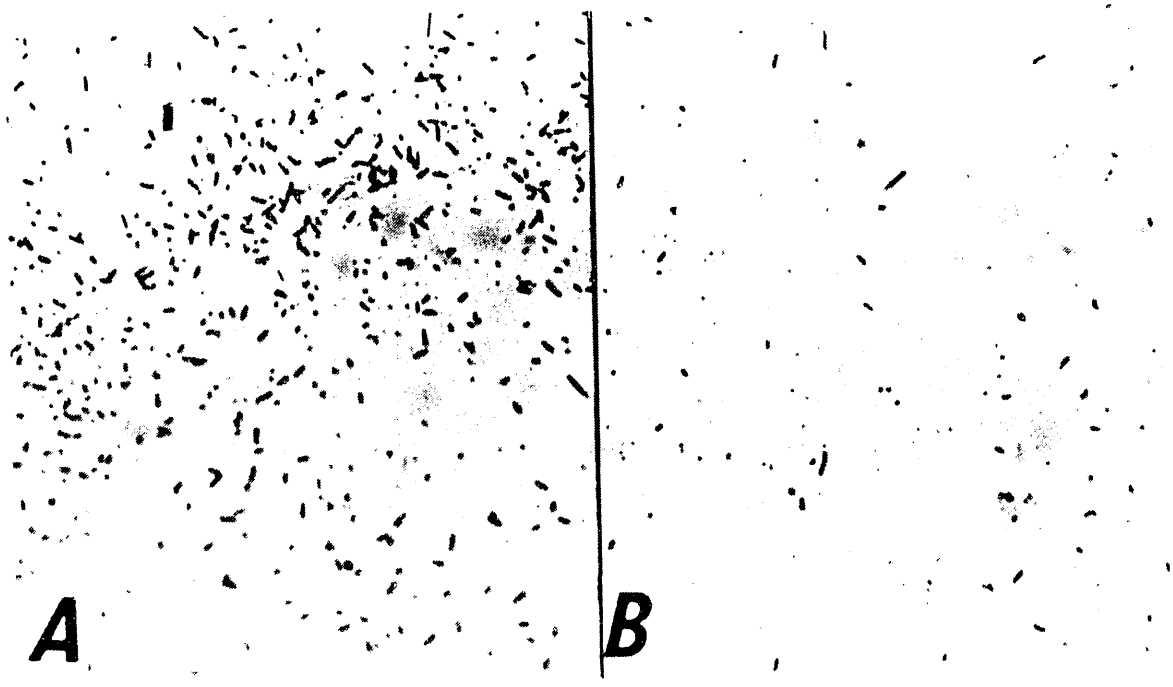

Figure 82. Distribution of tracks in CN-1 films from $^{10}B(n,\alpha)^{7}Li$ reactions in A, cerebral gray matter and B, cerebral white matter; ~ 400X.

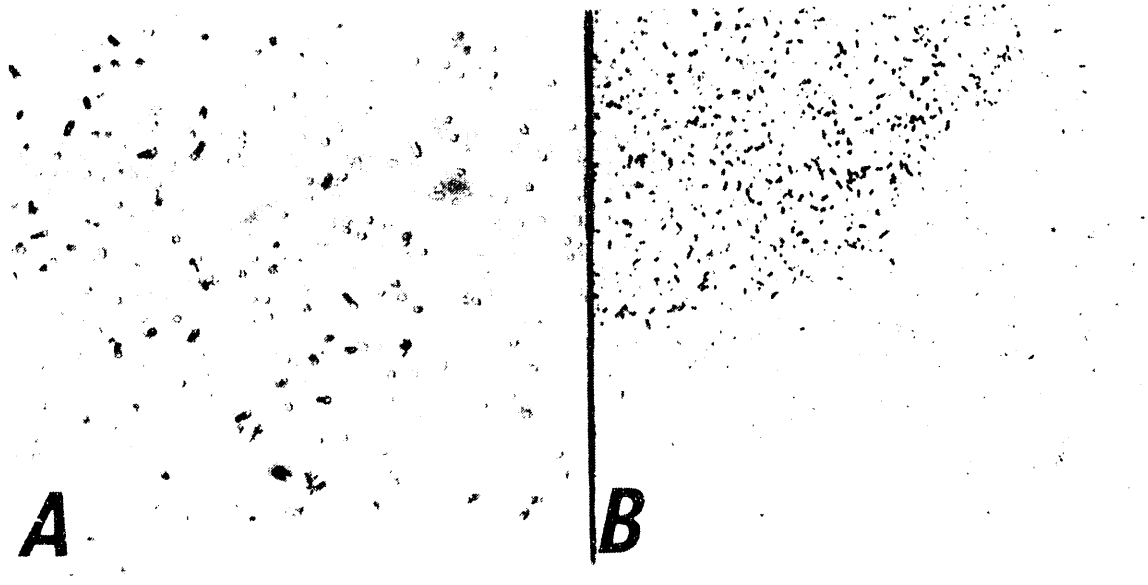

Figure 83. Distribution of tracks in CN-1 films from $^{10}B(n,\alpha)^{7}Li$ reactions in dog brain.

The sensitivity of boron measurements by use of the CN-1 films used in this projects was limited by the background tracks. A series of statistical testing of means from track count populations (i.e., tracks from 10^{-8} g^{10}B/g standard and background tracks with neutron exposures at 10^{11} neutrons/cm^2) indicated the limit of analysis to be close to 10^{-8} g of ^{10}B/g.

Discussion and Conclusion

The results of this project indicate that CN-1 film can be used to determine the distribution and concentration of ^{10}B in brain tumors and surrounding tissue. CN-1 films can be fabricated to a desired thickness, are sensitive to low energy alpha particles, and form slender tracks rather than pits. Their colorless transparent characteristics permit the simultaneous viewing of $^{10}B(n,\alpha)^7Li$ tracks and tissue.

The difficulties with uniformity and reproducibility of low alpha particle energies in track formation in CR-39 film were clearly apparent in various experiments with this polymer. However, both CR-39 and LR115-3 films may be useful for certain types of ^{10}B determinations.

ISU researchers hope to utilize track-etch techniques in the future to analyze ^{10}B distributions in animal tumors. The analysis would be used to examine the application of processes that may alter the microenvironment of the tumor and optimize ^{10}B distributions.

RESONANCE IONIZATION SPECTROSCOPY, SIRIS AND LARIS

Dr. Heinrich Arlinghaus, PI, Atom Sciences, Inc.

Introduction

BNCT relies on the capture of thermal neutrons by boron deposited biochemically in the tumor, and subsequent fissioning of the boron into energetic lithium ions and alpha particles. As the range of the fission fragments is relatively small (a few μm), the clinical efficacy of the therapy is only guaranteed if the boron is positioned in a sensitive area of the tumor cell, such as the cell nucleus. An important requirement for improved BNCT is the development of a more selective boron delivery mechanism. This will enable targeting only malignant cells, while maintaining a sufficiently long biological half-life of the boronated compound for delivery of a therapeutic neutron dose. The ability to image the boron concentration in tissue sections and even inside individual cells would be an important aid in the development of these delivery mechanisms. However, to date, this has not been possible because of limitations in analytical capabilities. Recently, workers at Atom Sciences, Inc., in Oak Ridge, TN, under the direction of the PI, Dr. Arlinghaus, have been developing two methods to address this problem. These techniques both use resonance ionization spectroscopy (RIS) to detect boron and differ only in the method of atomizing the sample for RIS analysis. Using these two techniques, called SIRIS and LARIS, Atom Sciences has recorded images of boron concentrations as a function of position in biological tissues. Concentrations at the low parts per million (ppm) have been demonstrated for SIRIS, and sub-ppm levels for LARIS. Spatial resolutions of about 3x6 μm^2 for SIRIS and 10x20 μm^2 for LARIS have been shown, but can be improved to sub-μm levels with instrumental improvements.

Several techniques such as alpha track-etch[100] and SIMS[101] have been used to identify boron in cells. The alpha track-etch methodology lacks the required resolution and may suffer from loss of boron not bound to protein as a result of procedures required by the process. SIMS, in combination with an ion microscope, or the ion microprobe, is capable of achieving micron to near sub-micron lateral resolution. Despite its relative high sensitivity (down to low ppm for some elements), SIMS has not yet been successful in locating and quantitating boron accurately in intracellular areas of tissue sections at concentrations of interest in BNCT.

In the SIMS technique the sample is bombarded with a focused, energetic ion beam which sputters particles off the sample surface. Some fraction of the sputtered particles are ejected as ions. These ions are extracted, mass analyzed, and detected. The ion beam can be focused to a few microns in diameter enabling analysis with high lateral resolution. There are, however, several limitations to the SIMS technique, some inherent in the secondary ion formation, some due to the physics of ion beams, and some due to the nature of sputtering. Sputtering produces predominantly neutral atoms; the ion yield for B is typical 10^{-4} - 10^{-6} or smaller, and can vary by many orders of magnitude as a function of surface contamination and matrix composition. These factors have several consequences. First, sensitivity is inherently limited due to the low ion yield. This is a particularly serious limitation when high lateral and depth resolution analyses are required, since relatively few atoms are available. For example, a square micrometer of a solid surface has 10^7 atoms on its surface. If the ion yield is 10%, removal of one monolayer would yield a single count at the ppm level; but, with ion yields of 0.01%, the same measurement would require 1000 ppm to detect a single count. Secondly, the orders-of-magnitude variability in ion yield as a function of surface and bulk composition makes quantitation difficult. Quantitation can also be jeopardized by interferences from molecules and isobars having the same mass as the analyte. In addition, charge effects often complicate analysis.

SIRIS and LARIS do not suffer from many of the limitations of SIMS but also do not benefit from the maturity of a well-established procedure such as SIMS. However, the recent progress at Atom Sciences in developing SIRIS and LARIS for boron imaging in biological tissues is quite encouraging and is described in this report.

Experiment

RIS is a laser-based ionization technique common to both SIRIS and LARIS. It uses tunable lasers to resonantly ionize neutral (usually ground state) atoms of a selected element sputtered from a sample surface. Typically, the resulting ions are detected in a mass spectrometer. The transitions between discrete excited states are unique to each element; therefore resonance ionization is extremely selective (see Figure 84). This makes RIS especially valuable for trace element analysis in biological materials where molecular ions or isobars are a serious source of interferences. The ionization efficiency for the selected element can be as much as 10^9 times higher than for the other elements in the sample.[102] The high selectivity of the RIS process also helps maintain linearity in the mass spectrometer ion extraction region by reducing space charge effects that would otherwise be present due to ionization of the major constituents of the sample. Since the isotope shifts of most elements are small in comparison to the bandwidth of the RIS lasers used in the experiments (7 - 12 GHz), all isotopes of a chosen element will be ionized with essentially equal sensitivity. Isotopic selectivity is achieved with the mass spectrometer. If a TOF mass spectrometer is used, all isotopes of an element can be detected simultaneously. The mass spectrometer requirements are therefore reduced to the resolution of neighboring isotopes of a single element; the high ionization selectivity of RIS and the suppression of the secondary ions virtually eliminate interferences from molecular ions, isobars or scattered ions from the major constituents of the sample.

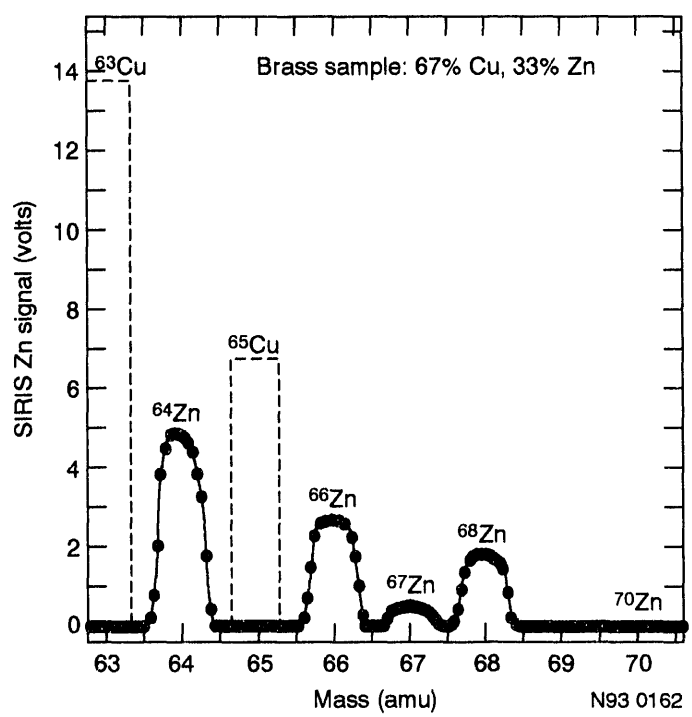

Figure 84. Demonstration of the SIRIS element selectivity. [SIRIS signal for Zn (solid line) in a brass ample containing Cu (67%) and Zn (~33%).]

The RIS process is also extremely sensitive and efficient. The intensity of modern pulsed dye lasers is sufficient to saturate both the bound-bound transitions and the ionization step, thereby assuring near-unit probability of ionizing all atoms of the selected element that are in the volume intersected by the RIS laser beams. The efficiency of the process of ionizing and detecting a selected element in a sputtered cloud depends on the temporal and spatial overlap of the resonance laser beam with the atomized cloud (20-50%), the ionization efficiency (~100%), the total transmission of the mass spectrometer (50-80%), and the detector efficiency (50-80%). For most elements, useful yields (atoms detected/ atoms sputtered) between 2-10% can be achieved and sub-parts-per billion detection limits are possible.[103,104,105] So far, the highest reported useful yield is ~26% for indium in silicon.[104]

Laser RIS schemes have been proposed from the ground state of all elements except He and Ne. Simple RIS schemes, such as ultraviolet (UV) + visible (VIS) + infrared (IR) (Figure 85a), UV+UV+IR, VIS+VIS+IR, and UV+IR, yield near-uniform sensitivity down to the few-atom level for 80% of the elements in the periodic system.[103,106] Ionization via autoionizing states (Figure 85b) requires lower laser intensity in the photoionization step, thereby reducing interference from nonresonant processes. Selective ionization in elements of the upper right-hand corner of the periodic system requires more complex laser arrangements to generate vacuum ultraviolet radiation (Figure 85c). These elements can also be ionized with simple laser schemes by the absorption of two photons to reach a two-photon resonance, with consequent ionization from the absorption of a third photon (Figure 85d). Although this process is less selective and sensitive than the previous ones, shown in Figure 85a,b,c, it still has a significant advantage over conventional ionization and non-resonant photoionization methods.

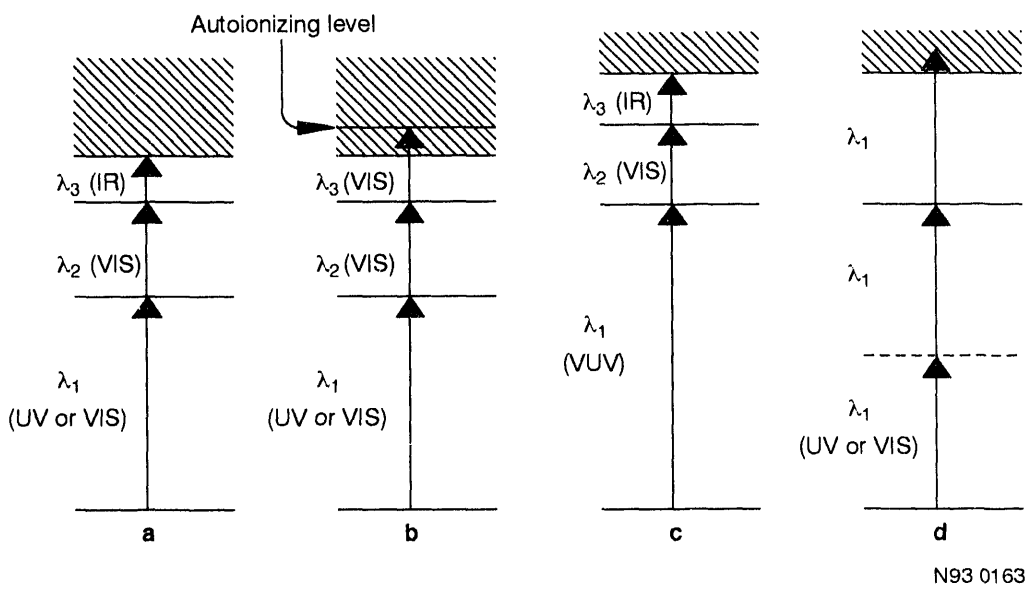

Figure 85. Simplified energy level diagrams illustrating the photoionization of neutral atoms.

SIRIS

RIS requires free atoms in the gas phase. One atomization method, ion sputtering - SIRIS[104,107] - provides an analytical technique that avoids many of the disadvantages of nonresonant and electron impact secondary neutral mass spectrometry while maintaining most of the advantages of SIMS, and offers significant improvements over SIMS in efficiency, matrix dependence, isobaric and molecular interferences, sensitivity, dynamic range, and quantitation accuracy.

In the SIRIS experiments, the sample is bombarded with a pulsed Ar^+ ion beam (up to 10^7 ions/500 ns pulse). The expanding cloud of sputtered material consists of excited state and ground state neutral atoms, molecular fragments, and ions; the ions are removed by timed extraction voltage switching (positive ions are retarded, negative ions are accelerated) and electrostatic energy analysis. The remaining neutral particles are then selectively ionized by the RIS laser beams. Efficient overlap of the laser beams with the cloud of desorbed material is achieved by choosing the appropriate delay time between firing the ion gun and firing the RIS laser, and carefully positioning the RIS laser beams with regard to the ion beam/sample surface intersection. The ionized atoms are extracted into a mass spectrometer consisting of an electrostatic energy analyzer and magnetic sector. Imaging is achieved by either scanning the ion beam over the sample or by changing the x and z target positions while the ion beam position remains fixed.

Charging of insulating samples such as biological tissues can lead to quantitation difficulties in SIMS measurements by altering electrostatic potentials in the ion extraction region and thereby significantly changing ion detection efficiency. With SIRIS, charge compensation is possible using pulsed low energy (down to 10 eV) electrons, which are introduced during the time interval between sputtering pulses. In addition, the time separation between ion bombardment and the extraction process reduces the effects of charge build up and leads to much better quantitation during analysis of insulating samples. For example, in some insulating or semi-insulating samples, the delay between ion sputtering and the RIS laser pulse is sufficient to dissipate any charge without additional compensation.

SIRIS can be employed to measure element concentration as a function of depth. SIRIS depth profile measurements involve two steps: (a) scanning the sample with a continuous ion beam to etch a crater to a specific depth, and (b) taking data with a pulsed ion beam in the center of the crater after a specific number of raster frames. The crater is typically made much larger then the analysis area to avoid crater-edge effect. Trace element concentrations can be monitored at frequent (less than 0.1 nm) depth intervals because the high efficiency of the SIRIS technique enables detection at the ppb level while consuming less than one monolayer of material in an area of $\sim 1 \times 10^{-4}$ cm^2.

LARIS

Much lower detection limits in the same analysis time can be achieved by replacing the ion beam with a laser beam, i.e., LARIS.[108,109] Use of a laser pulse instead of an ion pulse for the atomization process results in three or more orders of magnitude more material being released from the sample. Thus, with LARIS, tens of monolayers can be removed with a single atomizing laser pulse while with SIRIS many bombarding ion pulses are required to remove one monolayer of atoms from a sample. The practical lateral resolution limit of LARIS is 1-2 μm, thus inter/intracellular mapping is possible. Imaging is achieved by changing the x and z target positions while the atomization laser beam and the RIS laser beam positions remain fixed.

Electron Imaging

Visual images of the sample surface can be obtained by rastering the ion beam over a fairly large area (~ 1 mm^2) and synchronously (with the raster signal) use the detected ion-induced electrons from the sample to modulate a high

brightness x-y CRT display. As the raster generator is digital, it is possible to position the ion beam anywhere within its raster field at a resolution of 1024 pixels per axis. Absolute calibration between the atomization laser position and the ion beam position can be readily achieved by imaging a laser-made burn spot with the ion-induced electron microscope. Secondary electron images can be obtained from the tissue samples and compared with photographs to identify the position of characteristic features (specific cell structures, etc.) as well as to absolutely calibrate the ion beam position with the photomicrograph.

Experimental Setup

A schematic of the SIRIS/LARIS instrument used for the experiments is shown in Figure 86. The system consists of an excimer laser for laser atomization, a duoplasmatron microbeam ion gun, a pulsed flood electron gun, an RIS laser system (repetition rate 30 Hz) pumping two pulsed dye lasers, a secondary electron imaging system, a computer-controlled (x, y, z, ϕ) sample holder, two HeNe lasers for exact target positioning, a video imaging system for sample observation, a computer-controlled sample insertion system, and a double focussing mass spectrometer detection system (for more details see references 108 and 110). The excimer laser system is very versatile and can run at 158 nm (F_2), 193 nm (ArF), 222 nm (KrCl), 248 nm (KrF), 308 nm (XeCl), and 351 nm (XeF) wavelengths. The high-precision manipulator provides ± 25 mm motion in x and y with a resolution of 0.25 µm and a repeatability of 1 µm, 200 mm motion in z with resolution of 1 µm and a repeatability of 1 µm, 360° motion in Θ and a linear drive to actuate a fifth axis. The manipulator provides stepper motors driven under computer control that can change positions at a speed of up to 10,000 steps per second. A sample carousel can hold up to eight regular sized 20 mm x 20 mm samples, or four regular sized samples and four 20 mm x 170 mm long samples. All the important SIRIS/LARIS system functions are controlled by an IBM compatible computer.

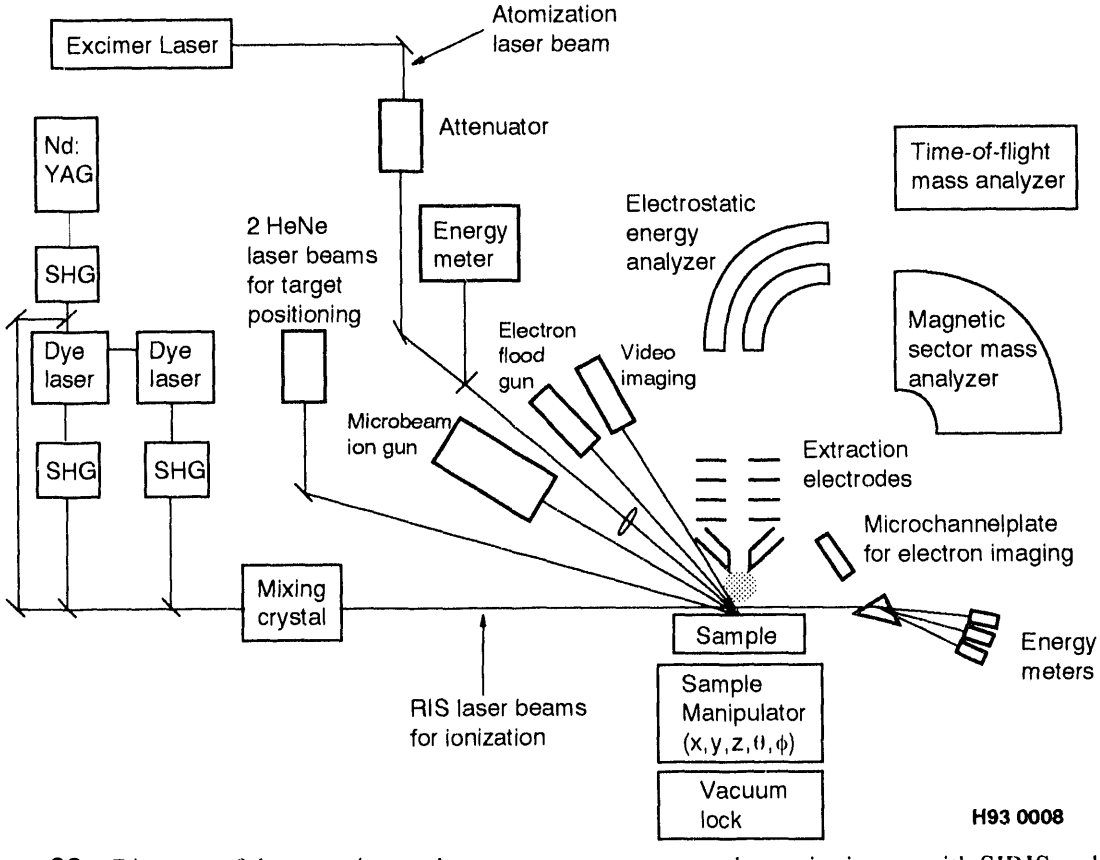

Figure 86. Diagram of the experimental arrangement to measure boron in tissues with SIRIS and LARIS.

Result and Discussion

Spatial Resolution

To determine the spatial resolution of the ion beam, ion-induced electron images were obtained on various test specimens (grids, line gratings, and tissue materials). A typical ion-induced electron image obtained from a 600 mesh, ~65% transparent Cu grid (42 μm grid spacing) is shown in Figure 87. The hexagonal grid structure can be readily resolved, and the grid dimensions (grid transparency) are in agreement with the actual ones. From these and other images, the spatial resolution was determined to be better than 3 μm x 6 μm. The typical ion beam current for this beam diameter was 0.6 nA (~1900 ions/500 ns pulse).

To determine the spatial resolution of the atomization laser beam, LARIS images were obtained on 300 mesh, 60% transparent Al grids (84.7 μm grid spacing) and 400 mesh, 50% transparent Cu grids (63.5 μm grid spacing). In these experiments, the RIS lasers were tuned respectively to Al or Cu. Figure 88 shows a LARIS image obtained from the 400 mesh Cu grid. This image was taken with 3 μm steps over a 160 μm x160 μm area. The grid structure can be readily resolved, and the grid dimensions (grid transparency) are in agreement with the actual ones. From the images, and additional linescans over the grids, the spatial resolution was determined to be better than 10 μm x 20 μm. This resolution can be improved with special optics.

The following standard set of operating parameters were selected for use in imaging the tissue samples. Ion beam current = ~0.6 nA (7500 ions/2 μs pulse), ion beam spot size = 3 μm x 6 μm, number of shots = 3000-7500, atomization laser wavelength = 248 nm, atomization laser spot size = 10 μm x 20 μm, atomization laser fluence = 1-2 J/cm^2, laser shots per point = 30, sampling interval = 20 μm. These parameters enabled us to acquire SIRIS data to low ppm, and LARIS data to low-ppb sensitivity limits without ablating through the full thickness of the sample. Typical SIRIS scans and images required several hours of run time while LARIS scans could be obtained in several minutes, with images in less than one hour. The reproducibility and signal level of the LARIS data is sufficient for good images to be acquired with only five laser shots per point.

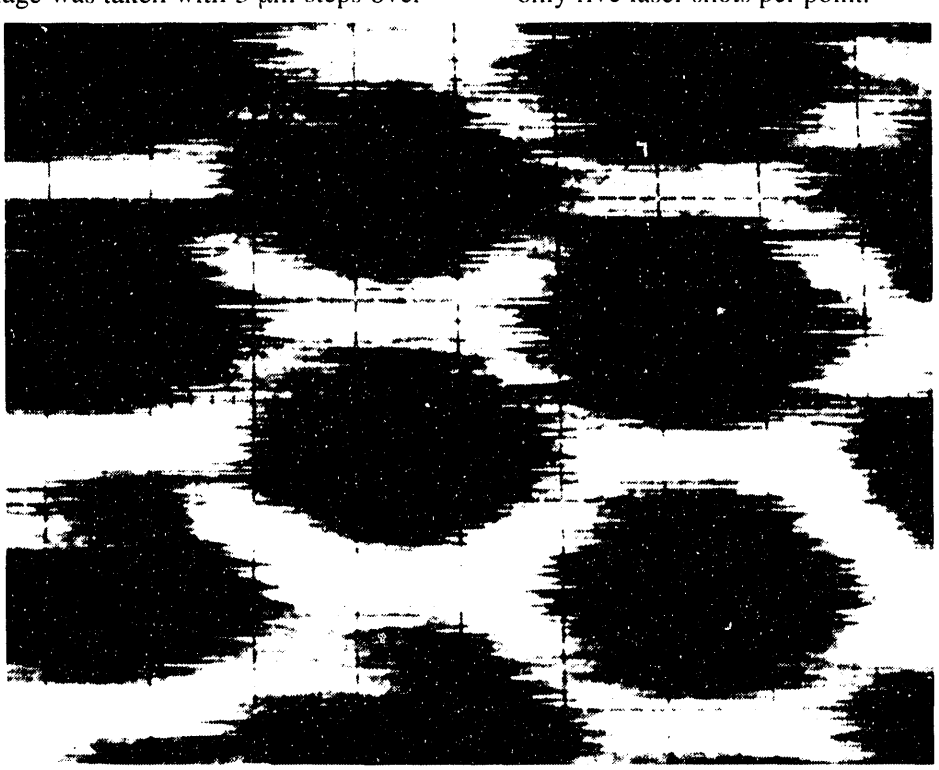

Figure 87. Ion-induced electron image of a 600 mesh (42 μm grid spacing) hexagonal Cu grid.

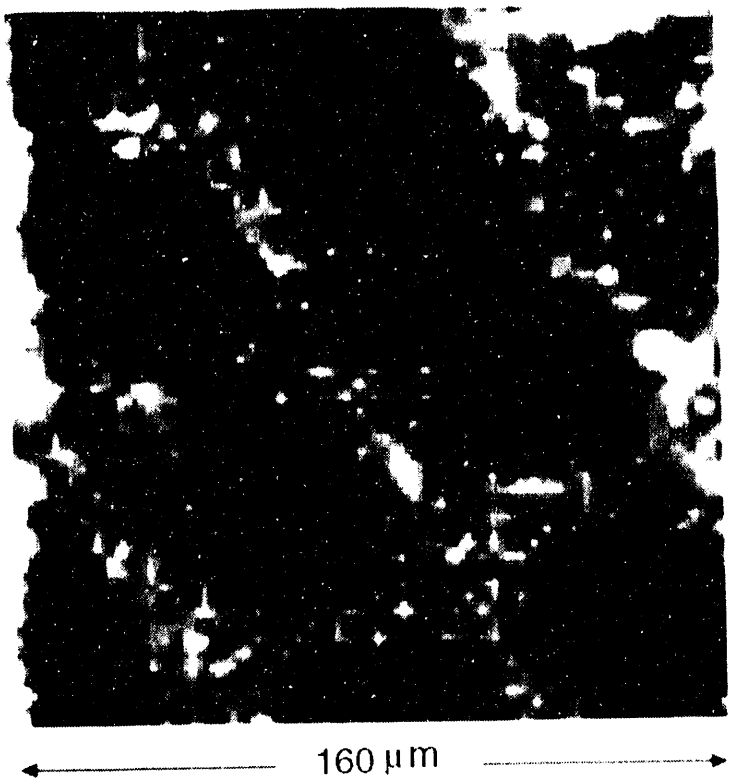

Figure 88. LARIS image of a 400 mesh, 50% transparency (63.5 µm spacing) Cu grid.

Quantitation

To test the quantitation accuracy and the detection limits of SIRIS, microfuge tubes containing blank and BSH (sodium salt of the closododecaboranyl mercaptide anion $B_{12}H_{11}SH^{-2}$) doped gelatin samples with concentrations between 2 µg B/g and 100 µg B/g, were prepared at INEL in the Chemical Sciences Group under the direction of Dr. Bauer. Gelatin was chosen as it is believed to be a good match to the density and chemical composition of tissue. The boron concentration was determined by ICP-AES measurements at INEL. Samples were pushed out of the microfuge tubes with a polyethylene rod after cutting off the tapered end. As the material extruded out of the large end, slices of approximately 0.5 to 1.0 mm thickness were sliced off with a cleaned double edged razor blade. The slices were mounted on a clean silicon surface with a few µL of >18 Megohm-cm ultrapure water to provide adhesion, and dried in an oven at ~45°C overnight. The correlation of boron concentration in BSH doped gelatin samples with the B SIRIS signal is shown in Figure 89. The calibration curve obtained with SIRIS is linear down to the 1 ppm level. The lowest concentration point was quoted as an upper limit by the INEL, and therefore was not used to fit the data. The real value can be extrapolated from the correlation plot and was determined to be ~80 ppb. The detection limit for SIRIS was much lower than 100 ppb because the signal virtually disappeared when the RIS laser was detuned off resonance. The same samples were also analyzed with LARIS. Good correlation was also obtained with LARIS, but the signal is much higher than the SIRIS signal (Figure 89). The SIRIS signal for the blank sample deviated to higher boron concentrations, which could be due to surface contamination. SIRIS is much more sensitive to surface contamination than LARIS because SIRIS typically analyzes only the top few monolayers.

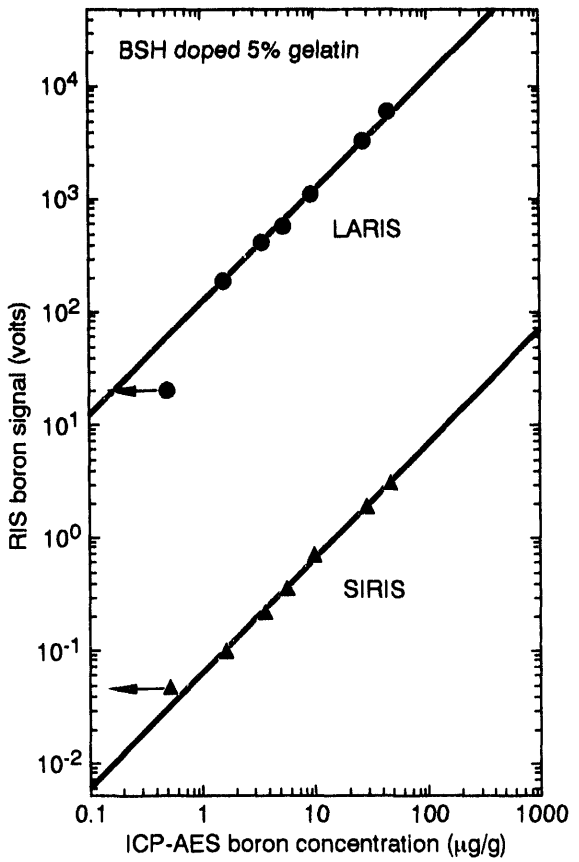

A93 0374

Figure 89. Correlation of boron signals from identical BSH doped gelatin samples using SIRIS and LARIS.

The results demonstrate that identical quantitative results can be achieved with either SIRIS or LARIS, but with a factor of ~1000 more signal in the LARIS mode. LARIS also integrates over hundreds of monolayers while SIRIS analyzes only the first few monolayers. In the 1 to 50 μg B/g concentration range tested in these measurements, excellent correlation between boron concentration and the measured signal was obtained. The standard deviation of the measurements was between less than 1% to at most 3%. It was anticipated that the sputtering/atomization process in gelatin materials is similar to that of biological tissues. This allows the use of doped gelatin standards to calibrate the BSH concentration in tissues.

Tissue Sections of Uninfused and BSH Infused Dogs

SIRIS scans were initiated to optimize the mounting process of tissue samples. Several samples such as skin and retina tissue from uninfused and BSH infused dogs were prepared by Dr. Gavin's group at WSU. Skin biopsies from two dogs that had been infused with BSH were embedded in O.C.T. embedding compound, frozen to -20°C, microtomed to 3 μm thickness sections, and mounted on clean silicon wafers that had been supplied by Atom Sciences. Controls and blanks were provided by using skin tissue from an untreated dog, and by using frozen O.C.T. material. These samples were scanned over several millimeter long tracks with the

SIRIS system to determine the boron concentration as a function of position. Boron was ionized by using ultraviolet (249.7 nm) and visible (563.3 nm) photons for the resonance steps, and infrared photons (1064 nm) for the ionization step. For all of these samples, the highest boron concentration was found on the silicon wafer, and at the junction with the mounting substance. No significant differences were seen between control samples and BSH infused samples. A possible explanation for these strange results is that the long time period between sample microtoming, mounting on the Si wafer, and drying, allowed diffusion of surface boron contamination on the silicon to accumulate at interfaces. A typical SIRIS scan is shown in Figure 90.

Tissue Section of BSSB Infused Rat

Another opportunity for obtaining test samples came from Dr. George Kabalka at the University of Tennessee (UofT) as a byproduct of his ^{11}B MRI experiments on BSSB (BSH dimer = $B_{24}H_{22}S_2^{4-}$) infused rats from BNL. The samples were prepared by Dr. Robert Switzer, also from UofT. Brain, kidney, liver and tumor samples were excised approximately one hour after euthanasia of a rat that had been infused for one week with a total dose of ~250 μg B/g body weight with an interperitoneal osmotic pump. After removal of the organs, they were sliced into 0.5 mm slabs and frozen on dry ice. The frozen slabs were mounted on cryostat chunks and 20 μm thick sections taken in the cryostat. These were picked up on gold-coated Si wafers, thawed briefly to flatten the section and immediately refrozen and maintained at 70°C for several days until dry. These were then transferred to a sealed polyethylene box in the presence of desiccant until final transference into the vacuum of the SIRIS/LARIS system.

Kidney

Photomicrographs of the mounted tissue sections were taken with an AO dissection microscope and a 35 mm camera adaptor. Low magnification images were taken so that the position of the sample on the sample holder could be measured. Additional images were taken at higher magnification to highlight various interesting regions of the sample. From the photomicrographs, the position of interesting features relative to the sample holder was determined by measuring with a vernier caliper and recorded for future reference.

After introduction of the sample into the SIRIS/LARIS system, ion-induced electron images were taken to absolutely calibrate the ion beam position. Then several traverses, both in the x and the z direction, were taken to gain an overall understanding of boron concentration, and its variability as a function of position and visible sample morphology. The sample was then removed from the SIRIS/LARIS system vacuum chamber and rephotographed. The location of where the atomization laser sampled the tissue section was usually visible as a lightening of the sample, allowing us to make an accurate measurement of atomization laser position on the sample in relationship with the manipulator position. The ion beam track was not visible because the ion beam current density was so low that only a fraction of a monolayer of material was consumed for each data point. Figure 91 shows a photomicrograph, an ion-induced electron image, and the boron SIRIS and LARIS signal as a function of position in BSSB infused rat kidney. The first SIRIS scan (top left figure) was obtained with a sampling interval of 200 μm over a distance of 7 mm. For the second SIRIS scan, (top right figure) the track length and the sampling interval were reduced to 2 mm by 20 μm. The intensity variation in the high-resolution SIRIS scan is similar to the low-resolution SIRIS scan, demonstrating the high reproducibility achievable with SIRIS. The data show a significantly higher boron concentration in the outer, lighter colored region of the kidney as compared to the inner regions. The outer part of the kidney is the region in which filtration is taking place, with a very large mass of blood vessels and a barrier through which numerous electrolytes and metabolites diffuse and exchange. The inner part of the kidney is just a mass of collection tubes that transports the substances extracted from the blood to the bladder. Therefore, it is not unreasonable to have a high boron (presumably BSSB) concentration at this barrier as the kidneys work overtime to remove this foreign substance from the blood.

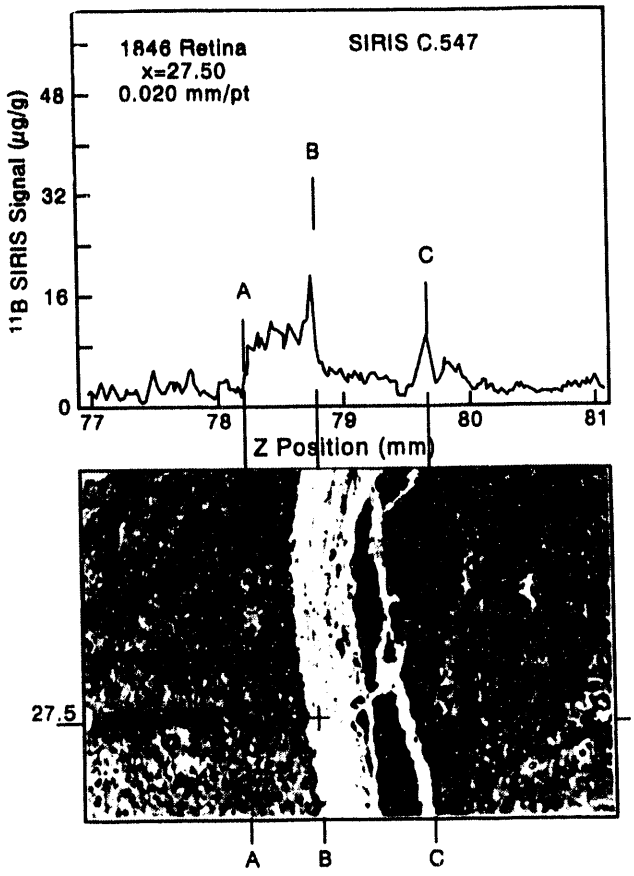

Figure 90. Position/concentration measurements using SIRIS in retina tissue section of control animal in which no BSH infusion was performed.

The SIRIS/LARIS system performance and sensitivity was checked frequently by taking SIRIS data on the same 49.1 µg B/g BSH doped 5% gelatin sample and LARIS data on the 5.6 µg B/g BSH doped 5% gelatin sample. These measurements were always made at the beginning and the end of each day, plus several times throughout the day. The average sensitivity for boron in the 5% gelatin was approximately 2 µg B/1 cts/1000 shots for SIRIS, and 1 µg B/Volt (= 1 µg B/10,000 cts/1000 shots) for LARIS.

If one assumes that the SIRIS response to boron in BSSB in tissues is the same as to boron in BSH in 5% gelatin, then the ~8 cts/1,000 shots average signal seen in the outer regions (z=83.2 to z=84.0) corresponds to ~16 µg B/g, and the 1 cts/1,000 shots average signal in the inner region to ~2.0 µg B/g. The LARIS response for the same regions corresponds to 19 µg B/g and 1.8 µg B/g. The good correlation between the SIRIS and LARIS results indicates that both techniques are feasible for measuring the boron concentration in tissues. The LARIS signal was ~20,000 times higher than the SIRIS signal. This implies that within its operating range, LARIS can reduce the analysis time for imaging of boron concentration in tissues significantly.

Even though we do not have direct comparison measurements from these tissues, Kabalka, et al.,[110] reported 240 µg B/g average concentration in the entire kidney of a similarly infused rat. This factor of 10 discrepancy could have several possible causes—such as analyzing only an area of low boron concentration or underestimating the dry to total weight ratio of the tissues. The LARIS scan shows that the signal between z = 84.8 and z = 85.5 is approximately a factor of 4 to 5 times higher than between z = 83.2 and z = 84.0. If one would take this number as an average boron

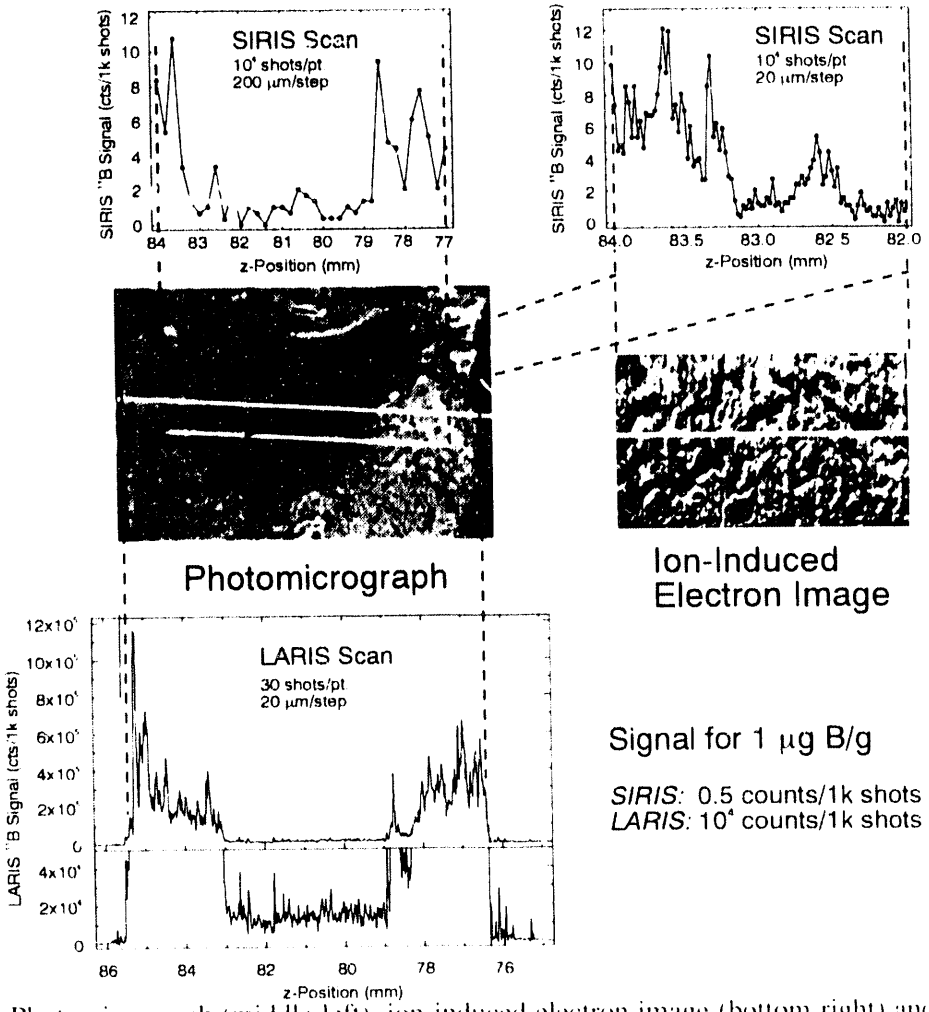

Figure 91. Photomicrograph (middle left), ion-induced electron image (bottom right) and boron SIRIS (top left and right) and LARIS (bottom left) signal in BSSB infused rat kidney.

concentration value, the discrepancy would already be reduced to a factor of 2. More detailed studies of means to calibrate the boron concentration from SIRIS/LARIS measurements has to be done in future experiments.

Figure 92 shows a photomicrograph of the kidney section with both the x (vertical white line) and z position (horizontal white lines) atomization laser traverses, and two boron concentration images of two different areas (both at the junction between the outer and inner regions) in the rat kidney. Bright areas correspond to high boron concentration, dark areas to low boron concentration. The upper image was sampled at 10 μm intervals and covers a 500 μm x 500 μm area. The lower image was sampled at 20 μm inter-vals over a 1.2 mm x 1.2 mm area. Notice the detailed structure in both images, with several "hot spots" in boron concentration. Also notice that there is structure in the inner (low B concentration) region, with infrequent, but occasional "hot spots." Unfortunately, the present image display capabilities are limited and show only a very small part of the detail available in the data. Also displayed in Figure 92 are the boron concentration profiles along two adjacent x-scans that make up the image. The strong correlation of peaks and valleys in concentration for the adjacent scans indicates that the rapid signal variations as a function of position seen in Figure 91 (and also the other figures to be discussed below) are real changes in boron concentrations in the tissues, and not an artifact of the measurement.

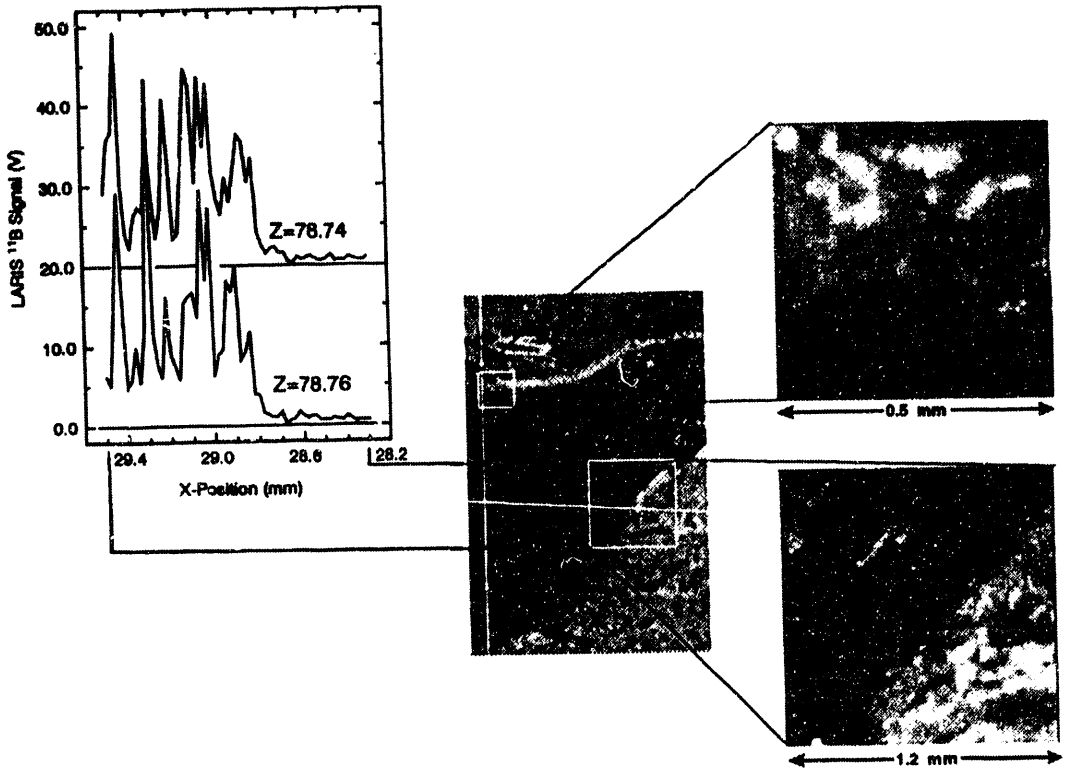

Figure 92. Photomicrograph (middle) and LARIS images (right) of BSSB infused rat kidney.

Brain

Figure 93 shows two orthogonal position-concentration LARIS boron measurements through a section of rat brain. The most immediate impression is the factor of more than 100 reduction in boron concentration as compared to kidney tissue. This is quite reasonable, considering that the blood-brain-barrier was intact in this animal, as the artificially induced tumor was confined to one of the rat's legs. Even though the signal is very low (average of 0.02 V in the lower regions, corresponding to 20 ng B/g relative to the gelatin calibration), we are confident in its authenticity. We note that the x-scan was completed before the z-scan; careful inspection of the data at the intersection (x = 26.5, z = 76.7; Figure 93b) shows that the signals from the x and z scans are within 10% of each other and the x scan measurement is the higher one, as expected. In addition, the boron signal seen is in the tissue, as no detectable boron signal is seen at the ends of the scans where the atomizing laser beam has moved off the tissue and onto the gold coated silicon wafer (Figure 93a, at x = 34 and z = 73). A SIRIS scan was not obtained from the brain tissue as it would have taken too long for the B concentrations in the brain tissue samples with the present ion gun adjusted to produce a 5 μm ion beam spot.

An expanded view of the central region of the LARIS scans through the brain tissue section is shown in Figure 93b. The photomicrograph in the lower corner of the figure was taken under different lighting conditions to enhance the structural contrast; the black marks on the laser tracks indicate the range of the expanded view. The intersection of the two position concentration traverses is in the hippocampus region of the brain. Both the x and z scans traverse the choroid plexus, which produces CSF by an active "ultra-filtration" process from blood. The CSF contains very little protein and no cells. In some sense, this is similar to the kidney (but at a much lower level), where the boron is concentrated in the region in which an

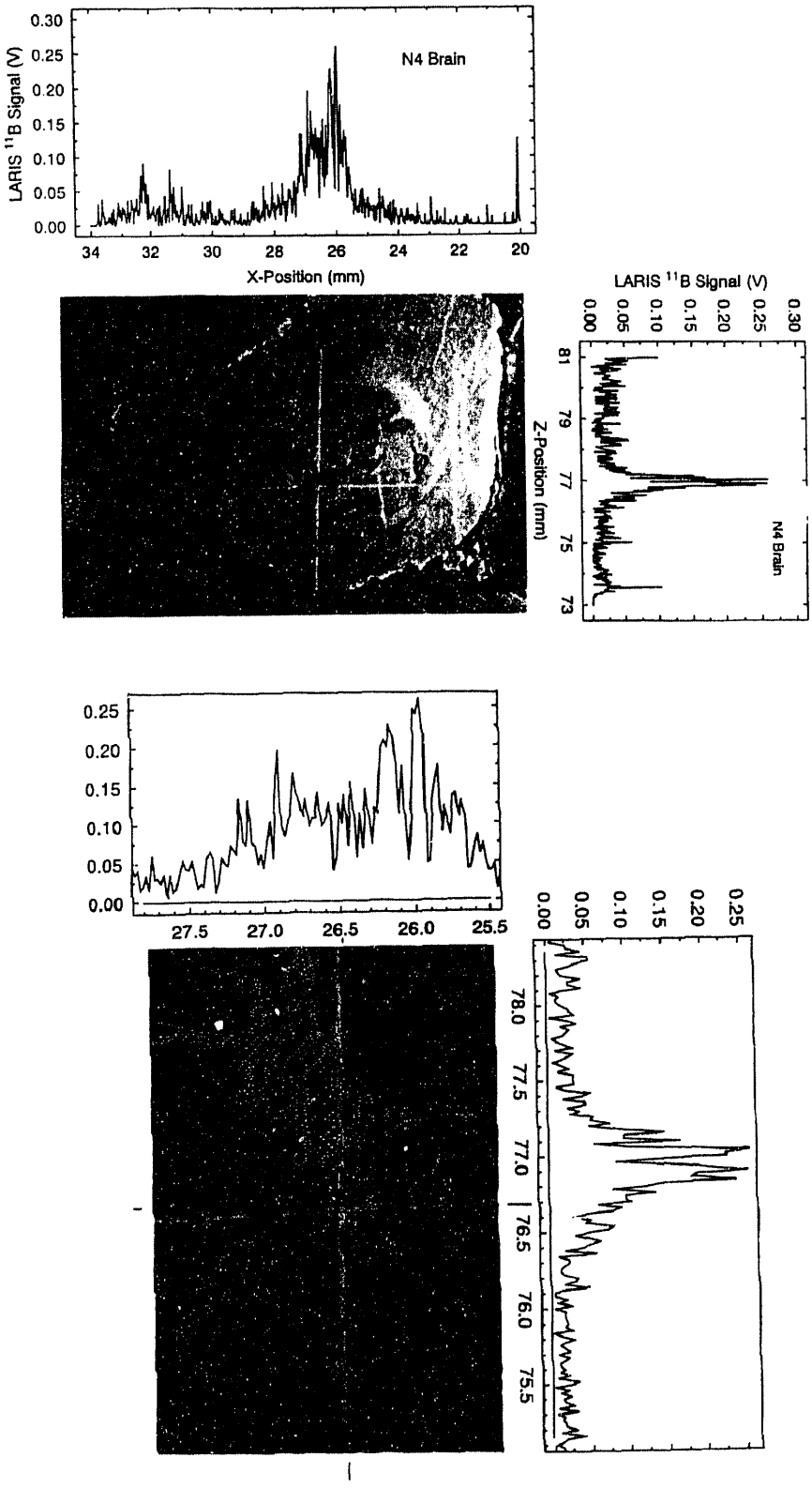

Figure 93. Boron concentration along two orthogonal tracks in BSSB rat brain (left). (Data was collected at 20 μm sampling intervals.)

"ultra-filtration" process is occurring. Note that the boron peak is much broader in the x-scan than in the z-scan, which correlates with the fact that the beam traverses a much longer region of the choroid plexus in the x-scan than in the z-scan. Even the "saddle" in the x-scan data corresponds to the region in which the atomizing beam traverses tissue of the hippocampus.

Referring back to Figure 93a, the minor peaks at x = 31.2 correspond to the location of the external capsule (a band of axons) that separates the cortex from the striatum. This is also a watershed zone for two sources of the vascular supply for this area. The somewhat higher boron concentration may be explained by the fact that this is a fine capillary bed, similar to that found in the kidney filtration zone and in the choroid plexus.

Liver and Tumor

Two tumors were in this rat, one labeled "left," one "right." LARIS position-concentration scans of both tumors, and also a section from the liver, yielded similar results, and were intermediate between the kidney and the brain concentrations. The boron LARIS signal from the liver showed very fine-scale concentration variations that averaged to a fairly constant 2 V (2 μg B/g) throughout the liver, except when the beam crossed a blood vessel lumen or other sinus, in which case it dropped to essentially zero, indicating that we were not having contamination problems. The rat tumors did show somewhat more systematic variations in boron concentration, in that regions that looked dark in the photomicrograph tended to have lower boron concentrations than the light regions, as shown in Figure 94a.

Figure 94b shows a SIRIS scan from the "right" tumor. The SIRIS scan was obtained with a sampling interval of 20 μm over a distance of 2 mm. The white line represents the SIRIS line scan while the dark line shows a previous LARIS line scan. The dark area at the bottom left corner of the photomicrograph shows a region imaged with LARIS. The data shows a higher boron concentration in the regions that looked lighter on the photomicrograph as compared to the darker regions. This was also observed with LARIS. The signal between 30.25 and 30.65 is slightly reduced because the SIRIS line scan intersects the LARIS image region.

Figure 95 shows a photomicrograph, an ion-induced electron image, and a SIRIS boron image of the tumor section. The image was blended to improve visualization. Bright areas correspond to high boron concentration, dark areas to low boron concentration. The image was sampled at 5 μm intervals and covers a 50 μm x 50 μm area. Notice the detailed structure in the image, with "hot spots" in boron concentrations. Also notice that features of the electron image can be easily correlated to the photomicrograph. The LARIS boron image of a 2.44 mm x 1.22 mm tumor region and the corresponding photomicrograph is shown in Figure 96. This large rat tumor image shows somewhat more systematic variations in boron concentration, in that regions that looked dark in the photomicrograph tended to have lower boron concentrations than the light regions. The low signal in the dark regions is mainly caused by freeze drying effects exposing the probing laser beam to the substrate material. This can be improved by better mounting techniques. Also, the mobility can be reduced by cooling the samples with liquid nitrogen during analysis. It should be even possible to transfer frozen samples into the cold stage sample carousel position.

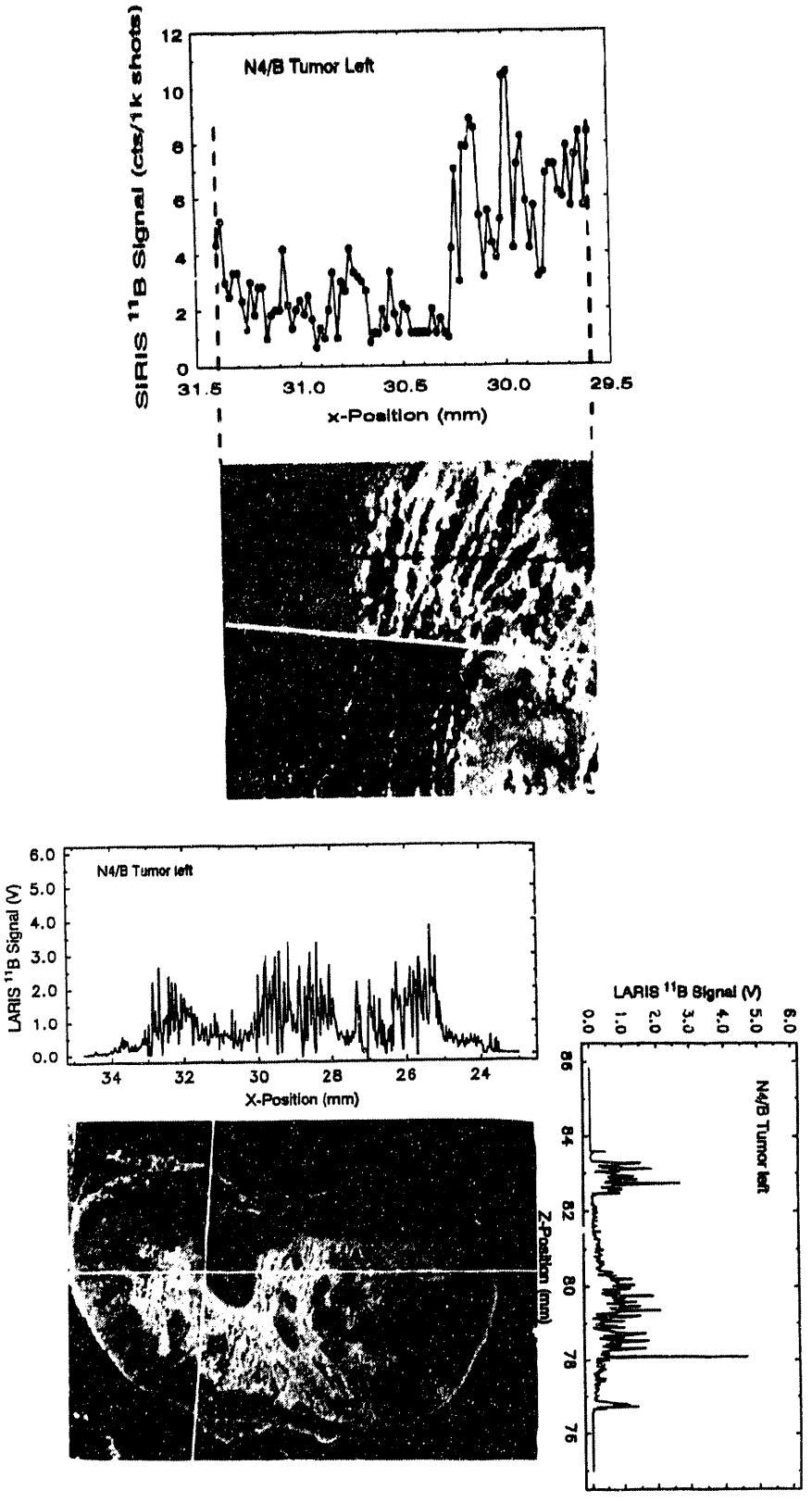

Figure 94. Boron LARIS concentration along two orthogonal tracks in BSSB infused rat tumor (left).

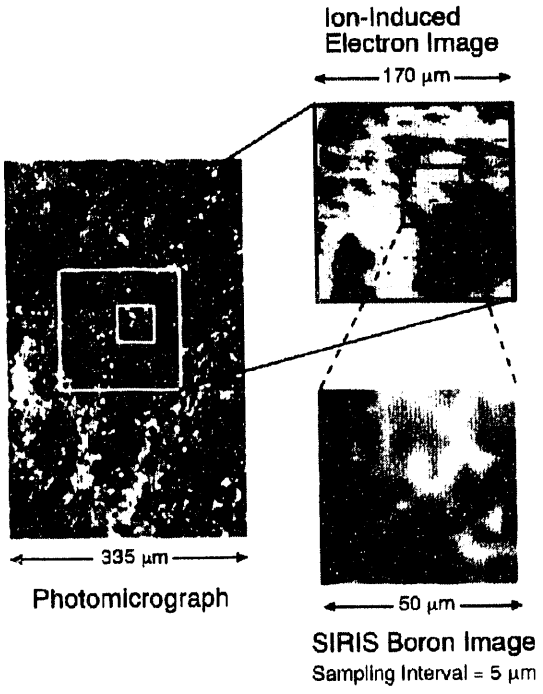

Figure 95. Photomicrograph (left), ion-induced electron image (top right), and SIRIS boron image (bottom right) of a tumor section.

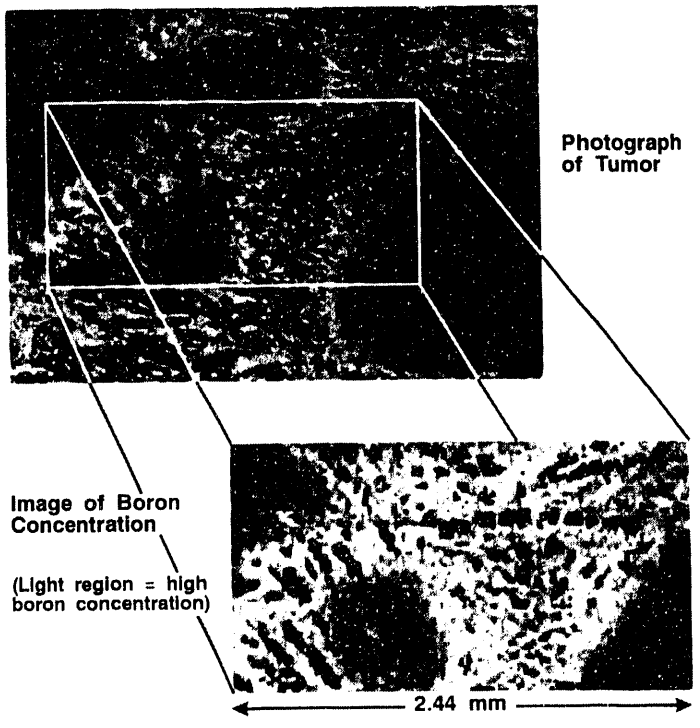

Figure 96. Photomicrograph (upper) and LARIS image (lower) of BSSB infused rat tumor. (The sampling interval was 20 μm. Light region correspond to high boron concentration.)

Conclusion

From the data presented above, it is quite clear that the SIRIS/LARIS technique is well suited for quantitative and sensitive imaging of trace element concentrations in biological tissue sections. Even though the measurements made on tissue sections were only intended to demonstrate the feasibility of the technique, the quality of the data is sufficient to make useful biological observations. Future enhancements of the SIRIS/LARIS instrumentation can significantly improve the analytical performance. A liquid metal ion gun could increase SIRIS spatial resolution to 0.1 μm with sensitivities in the low ppm level. Similarly, better focussing optics could improve LARIS spatial resolution to 1.0 μm or better with sensitivities in the low ppm level. A high repetition rate excimer laser system, used for both atomization (LARIS) and to pump dye lasers (SIRIS and LARIS) could reduce the time required to record an image over a 500 μm x 500 μm area with a few μm resolution to less than five minutes. The LARIS mode could be used to quickly determine the spatial boron concentration down to the low ng/g level in intercellular areas while the SIRIS mode could be used to determine the spatial boron concentration and its variability in intracellular areas. If a TOF mass spectrometer is used in future experiments (currently under construction), all the B isotopes could be detected simultaneously. Thus, infused BSH could be separated from natural boron background in tumor cells by isotope ratio measurements if isotope-enriched BSH were used.

NEUTRON BEAM MEASUREMENT DOSIMETRY

Dr. Yale Harker, Dr. Pete Randolph, and Cecilia Amaro, Radiation Measurement Physics, INEL

In 1992, the BMRR core was modified primarily to increase the intensity of the epithermal- neutron beam. As a result of this modification, it was necessary to perform a series of beam characterization measurements to confirm the changes to the neutron spectrum, the beam penetrability, and the resulting dose components preparatory to resuming irradiations in the large animal model studies. The characterization measurements were, as much as possible, repeats of previous measurements performed before the BMRR modification and were performed in November 1992 and January 1993. They consisted of neutron spectrum measurements in the free beam and neutron flux and gamma dose distribution measurements in plastic phantoms. The latter measurements were performed in the free beam and using beam defining apertures. This report briefly describes the measurements performed, presents the results and compares these results against the before modification measurement data and with data derived from neutron transport calculations for the new BMRR configuration.

Neutron Spectrum Measurements

Neutron spectrum measurements were performed using a set of neutron activation foil stacks. The activity on each foil is analyzed using a high resolution gamma spectrometer that is able to identify the specific activity of the activation product. From the specific activity data, the neutron reaction rate can be calculated for each foil analyzed. The material used in each foil stack is selected on the basis of its response with respect to the neutron energy; i.e., neutron cross section as a function of neutron energy. In the epithermal-neutron energy range (0.5eV–10keV), the material selection is based on the energy of the neutron cross section primary resonance. A foil stack rather than a single foil is used to modify the energy response of the different foils in the stack by progressively reducing the neutron flux at the primary resonance energy. In the fast neutron energy range (>10 keV), the material selection is based on the threshold energy of the specific response neutron cross section.

Neutron reaction rate data from epithermal neutron response foils and the fast neutron response foils are analyzed to determine the neutron spectrum using the least squares analysis adjustment code FERRET.[11]

The specific details of the spectrum measurement process are given in reference 112 which presents the methods and results of spectrum measurements performed on the BMRR epithermal neutron in 1988 and 1989 prior to the core modifications discussed above.

Shown in Figure 97 is the neutron spectrum from reference 112 as measured by the foil activation method before the BMRR core modification. In this figure, the measured spectrum is compared to the neutron spectrum calculated from a Monte Carlo neutron transport code for the core configuration prior to modification. Shown in Figure 98 is the current neutron spectrum measured by the same method and compared with the calculated neutron spectrum using the same transport code for the current core configuration. From these two figures, it is apparent that there are no major changes to the shape of the spectrum resulting from the core modification. The major change is the magnitude of the spectrum. Listed in Table 23 are the integral flux and dose values before and after the core modification. From the data presented in this table, the increase in epithermal flux for the epithermal beam without beam defining apertures is 49%. The increase in fast neutron dose is indicated to be 26%. As a result, the core modification may have improved the beam quality (fast neutron Kerma) by 15%. However, the improvement in beam quality is considered at this time as a possible effect because there were limitations on the after-modification fast-neutron measurements. Those measurements were limited to one fast neutron

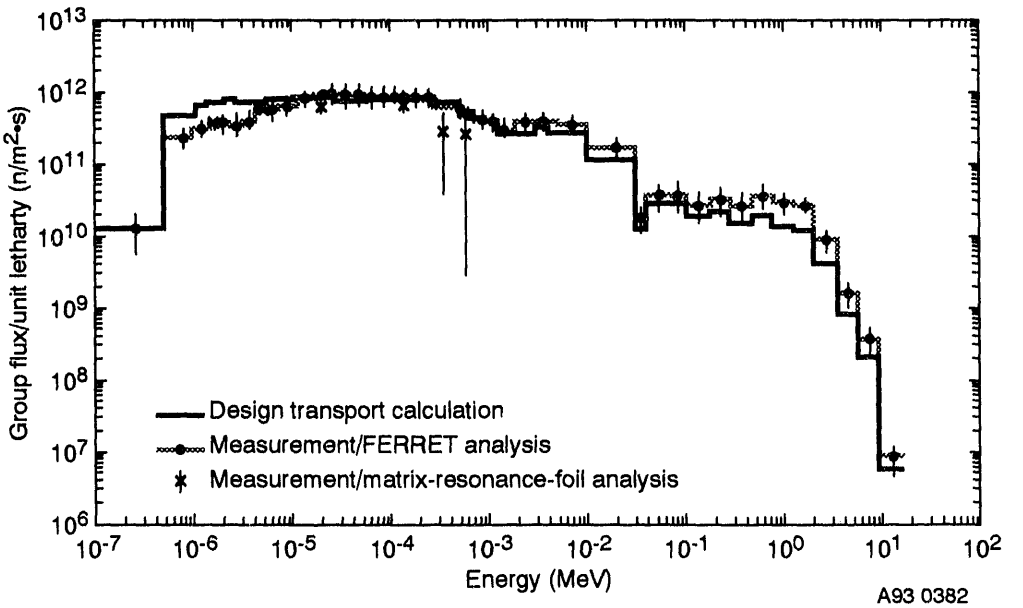

Figure 97. BMRR epithermal-beam neutron spectrum before core modification.

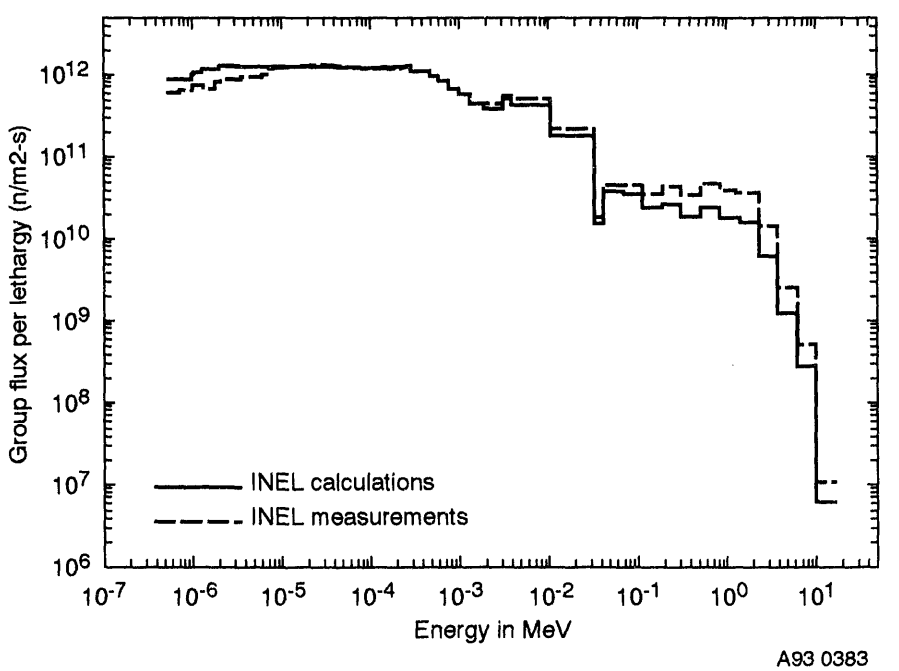

Figure 98. BMRR epithermal-beam neutron spectrum after core modification.

Table 23. BMRR epithermal beam parameters - integral flux and dose values.

	Before modification	After modification	Ratio after/before
Total neutron flux (n/cm^2-s per MW)	6.54E+08	9.64E+08	1.47
Fast neutron flux (n/cm^2-s per MW)	3.44E+07	4.29E+07	1.25
Epithermal flux (n/cm^2-s per MW)	6.20E+08	9.21E+08	1.49
Fast neutron dose (cGy/min per MW)	1.67	2.10	1.26
Neutron kerma (cGy per n/cm^2)	4.49E-11	3.80E-11	0.85

response activation reaction, $^{115}In(n,n')^{115m}In$; whereas the before-modification measurements included both the $^{115}In(n,n')^{115m}In$ reaction and the ^{10}B shielded $^{235}U(n,f)$fission product reaction, the combination of which gave a broader energy range of response. The measurement of the latter reaction was not performed for the after-modification series.

Table 24 shows a comparison of the after-modification measured epithermal-beam parameters and the corresponding parameters derived from a Monte-Carlo neutron transport calculation. The calculation is based on a detailed model of modified core. From the data presented in this table, measured and calculated epithermal flux are in good agreement. The differences in the fast neutron flux and dose are much the same as in a similar comparison for the before modification fast parameters and are due to a deficiency in the calculation model to accurately handle neutron streaming at high neutron energies. In the before-modification case, the fast-neutron range of the BMRR calculated spectrum was adjusted to be consistent with the measured data. This same procedure will be applied to the after-modification calculated spectrum.

Phantom Measurements

In these measurements the thermal-neutron flux, epithermal-neutron flux, and gamma dose are measured as a function of position inside the phantom. Three phantoms were used in the after-modification characterization of the BMRR epithermal-neutron beam. These consisted of a cylindrical phantom, a Labrador dog head phantom, and an ellipsoid phantom. All phantoms were constructed of clear acrylic plastic. The cylindrical and Labrador head phantoms were used in the before-modification characterization measurements and one-to-one comparisons of the current data with previous data are possible. In the case of the cylindrical phantom measurements, a 7.62-cm (3-in) diameter beam defining aperture was used in both the before- and after-modification measurements. In the case of the Labrador head phantom, 10-cm x 10-cm and a 5-cm x 10-cm apertures were used. The ellipsoid phantom was only used in the after-modification measurements. This phantom measurement was performed so that INEL dosimeter data and BNL dosimeter data can be compared directly. For the ellipsoid phantom measurement set, no beam defining aperture was used.

In the INEL phantom measurements, copper/gold alloy wire segments were used to measure the thermal-neutron and epithermal-neutron flux distributions. The gamma dose distributions were measured using CaF_2:Mn thermoluminescence dosimeters (TLD 400). The BNL phantom measurements used bare and cadmium-covered gold foils for measuring the thermal- and epithermal-neutron flux distributions and ^7LiF thermoluminescence dosimeters (TLD 700) for measuring the gamma dose distributions.

Table 24. BMRR epithermal beam measurements and calculations, after modification.

	Measurement	Calculation	Ratio
Total neutron flux (n/cm^2-s per MW)	9.64E+08	1.01E+09	0.95
Fast neutron flux (n/cm^2-s per MW)	4.29E+07	3.18E+07	1.35
Epithermal flux (n/cm^2-s per MW)	9.21E+08	9.78E+08	0.94
Fast neutron dose (cGy/min per MW)	2.10	1.31	1.61
Neutron kerma (cGy per n/cm^2)	3.80E-11	2.23E-11	1.70

Shown in Figure 99 are the thermal-neutron flux distributions versus the distance along beam (z) axis inside the cylindrical phantom.

Both the before-modification (4/91) and after-modification (11/92) measurements are shown. In both cases, the peak thermal-neutron flux occurs at a depth of between 2 and 3 cm inside the phantom. Beyond that point, the after-modification flux drops off faster than the before-modification flux. The epithermal neutron flux distributions are shown for the same phantom in Figure 100. Once again the after-modification flux falls off faster with depth than does the before modification flux. This type of behavior can be explained by a difference in the angular flux distribution between the before- and after-modification neutron beams. Listed in Table 25 are the peak thermal-neutron flux values for cylindrical and labrador phantoms. In both phantoms, the core modification amounted to a 28% increase in the peak thermal-neutron flux. This increase is below that observed for the free beam flux measurements (49%) reported above. It is felt that the difference in angular flux distribution combined with the collimating effect of the beam limiting apertures used in the phantoms measurements is the reason behind this difference. The calculated neutron fluxes for the free beam and the phantoms also indicated the same differences in the increase in neutron flux; that is,~50% for the free beam fluxes and ~30% for the phantom fluxes.

The thermal- and epithermal-neutron flux distributions for the ellipsoid phantom are shown in Figures 101 and 102. In Figure 101, the INEL measurements are compared with the BNL measurements and calculations. In Figure 102, the INEL measurements are compared with the INEL calculations (rtt_MC). From these two figures, it can be seen that there is excellent consistency between the INEL and BNL measurements and calculations. The gamma dose distribution in the ellipsoid phantom is shown in Figure 103. In this figure, only the results from the BNL measurements and calculations are shown. The INEL dose measurements are about a factor of 2 below these results and the difference is thought to be due to a difficulty in processing the TLD400s used in the INEL measurements. However, the INEL calculations are in agreement with the BNL results.

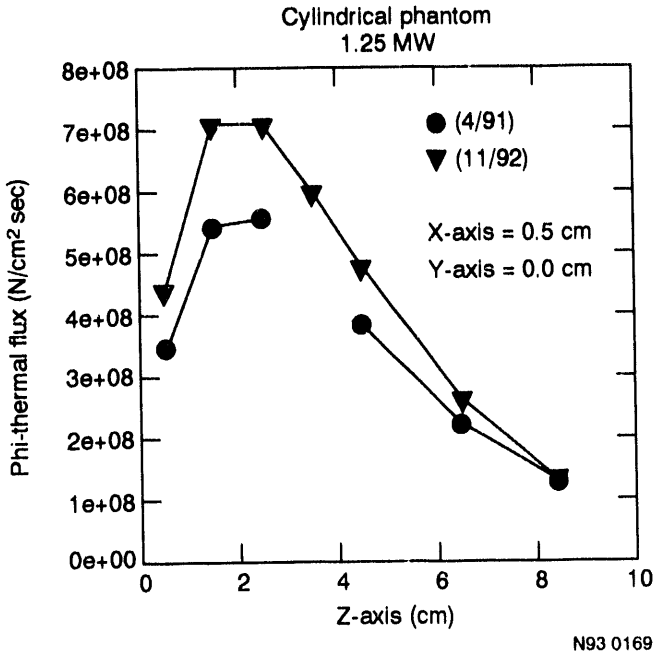

Figure 99. Thermal neutron flux distribution as a function of depth in the cylindrical phantom.

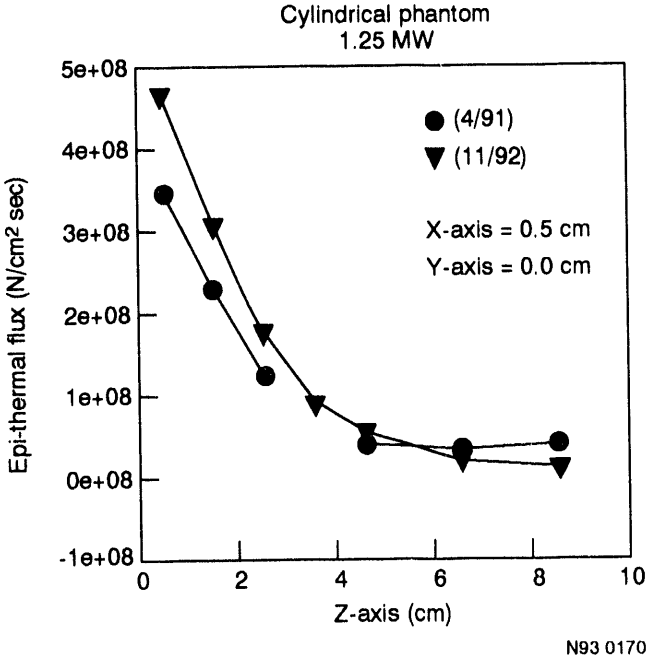

Figure 100. Epithermal-neutron flux distribution as a function of depth in the cylindrical phantom.

Table 25. Peak thermal neutron flux data.

	Before modification peak flux (n/cm^2-s per MW)	After modification peak flux (n/cm^2-s per MW)	Ratio (after/before)
Cylindrical phantom 7.62cm dia. aperture	4.44E+08	5.66E+08	1.28
Labrador phantom 10cm x 10cm aperture	6.55E+08	8.41E+08	1.28

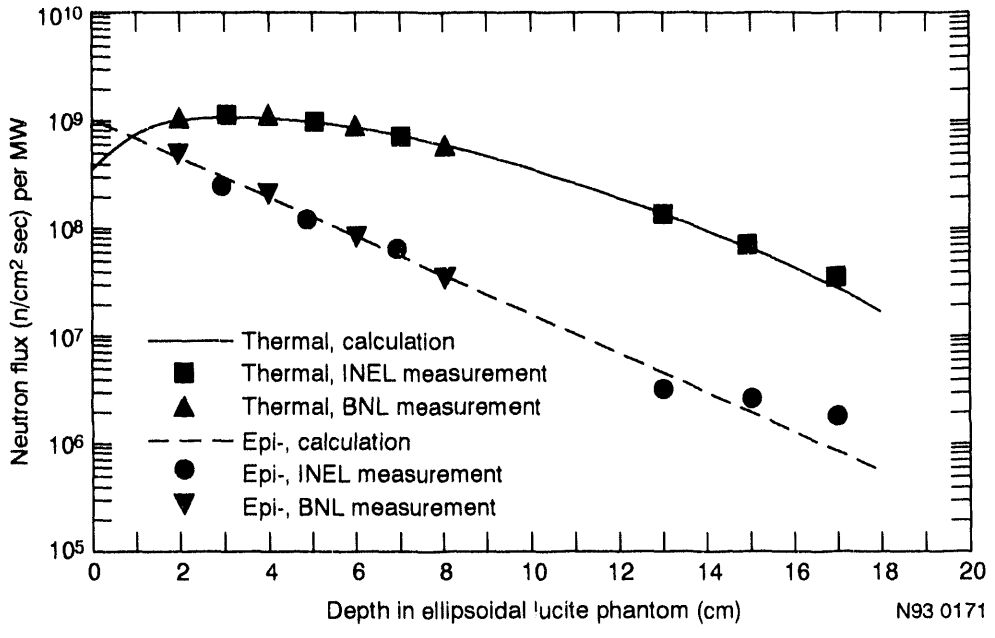

Figure 101. Thermal and epithermal-neutron flux distributions as a function of depth in the ellipsoid phantom (INEL measurements compared with BNL measurements and calculations).

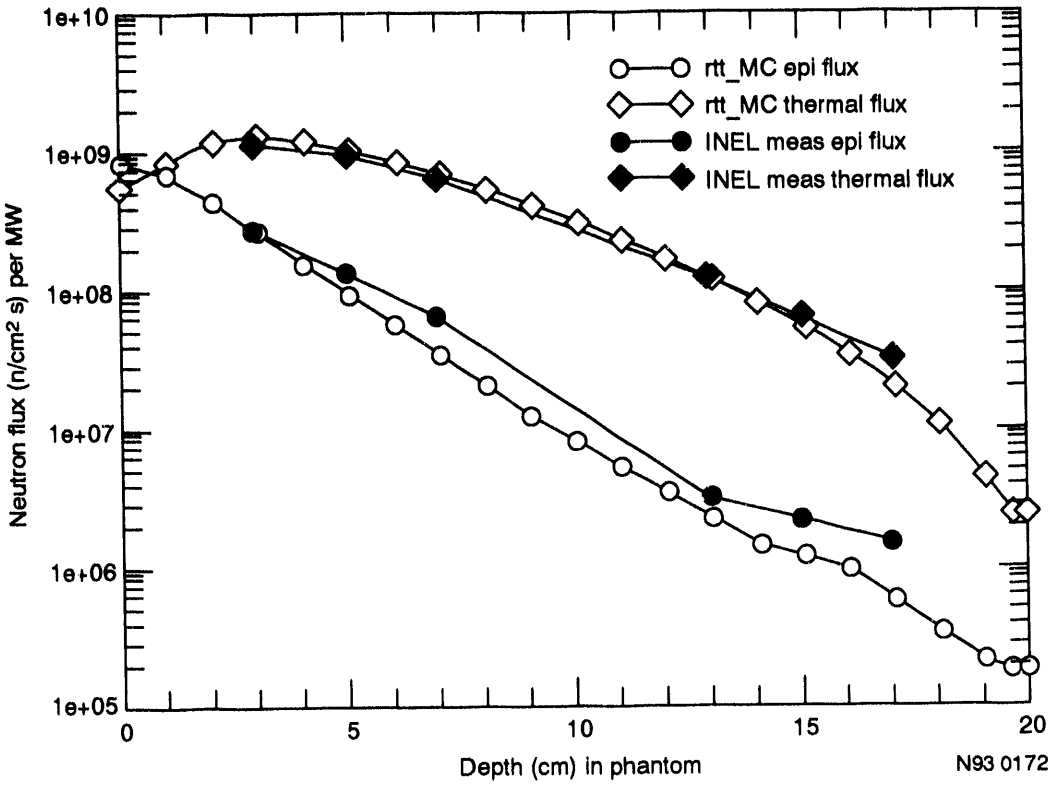

Figure 102. Thermal and epithermal-neutron flux distributions as a function of depth in the ellipsoid phantom (INEL measurements compared with INEL calculations).

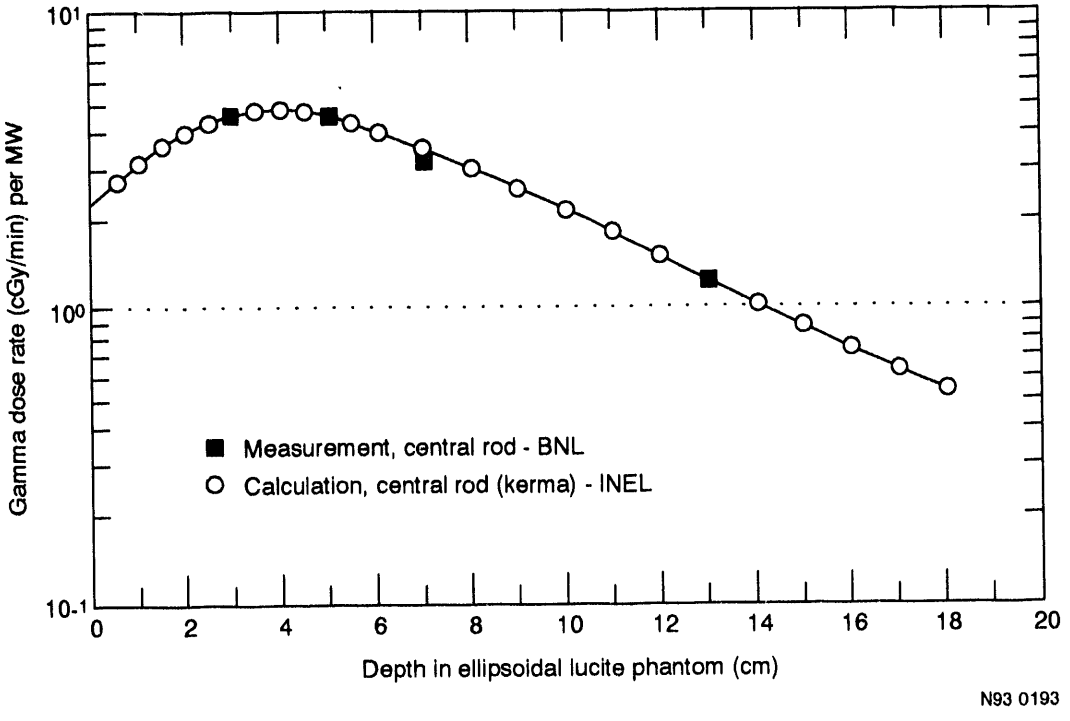

Figure 103. Gamma dose distribution in ellipsoid phantom.

Conclusions

From the data presented in this report, the BMRR core modification completed in 1992 resulted in an increase in free beam intensity of 49% and there are no significant alterations in the shape of the epithermal neutron spectrum. Evidence exists to suggest that the fast-neutron dose to epithermal neutron flux has been reduced by the core modification. However, more measurements will be needed to confirm this observation. When beam defining apertures such as those used in the INEL large animal model studies are used, the net increase in beam intensity is 28%. The difference between the increase in free beam intensity (49%) and the increase in the collimated beam intensity (28%) is due to a change in the beam angular flux distribution at large angles. The differences in neutron flux distributions in the phantoms (before and after modification) also support this conclusion. There is excellent agreement between INEL measurements and INEL calculations and between INEL results (measurements and calculations) and the BNL results (measurements and calculations) in cases where direct comparisons can be made. The one exception is the gamma dose data and in this case it is felt that the problem lies with the INEL gamma measurements.

In summary, it is felt that the BMRR epithermal-neutron beam is now sufficiently characterized to proceed with the INEL large animal model studies and that the INEL model developed for patient treatment planning is capable of accurately predicting dose contributions for future irradiations using the new BMRR epithermal-neutron beam.

GTRR PHYSICS SUPPORT

Dr. Dave Nigg and Floyd Wheeler, Reactor and Radiation Physics, INEL

Introduction

BNCT research in the U.S. has focused on the use of an epithermal (0.5 eV to 10 KeV) neutron beam. An epithermal-neutron beam offers much better tissue penetration than the thermal-neutron beams currently used for BNCT of human tumors in Japan. Various types of epithermal-neutron sources for BNCT have been proposed over the years. Reactor-based sources, accelerator-based sources, and radioactive neutron sources have all been extensively examined. The first practical, large-scale, epithermal-neutron beam for BNCT was installed at the BMRR approximately four years ago. This beam was designed and constructed in a cooperative effort between BNL and INEL. It has been used extensively for BNCT research activities conducted by INEL, BNL, and others.

Although the BMRR beam has served the BNCT research community well, and will continue to be a valuable research tool for the forseeable future, there are also reasons to seriously consider the construction of an advanced epithermal-neutron beam facility that would offer certain significant improvements in performance relative to the BMRR beam. Conceptual design calculations conducted during the year by INEL researchers, in collaboration with the Georgia Institute of Technology, have shown that a beam having higher intensity significantly lowers fast neutron contamination and offers much better collimation than the BMRR beam. This proposed beam would allow certain types of large animal irradiations to be done without surgically reflecting the scalp and other tissue overlying the treatment volume of interest. Also, extrapolation of animal BNCT irradiation data for the purpose of deciding whether to proceed to human clinical trials (the ultimate objective of all BNCT research) would be facilitated by the availability of the proposed GTRR beam. This is because this beam has spectral qualities that are more typical of that required for routine human treatment should BNCT become a widespread modality. In addition, the GTRR beam, if eventually employed for human clinical trials, would offer patients a significantly better probability of local tumor control, and would allow treatment of a much larger fraction of those patients who could potentially benefit from BNCT than with the BMRR beam. Finally, it may be noted that there are ongoing efforts directed toward development of drugs that are more effective (that is, that have a greater preferential accumulation in malignant tissue relative to normal tissue) than the most widely-employed, currently-available drug (BSH). It can be demonstrated that neutron beam quality and boron drug quality tend to have a synergetic relationship. *The increased effectiveness of any improved boron drug will be significantly magnified by an improved beam, that is, the system is not linear.* Beam quality and drug quality do not combine linearly. Overall treatment efficacy depends upon a complex interaction of both.

The basic, generally-accepted criteria for a therapeutically-useful epithermal-neutron beam for BNCT are as follows:

- The intensity should be sufficient to allow reasonably short treatment times (perhaps one hour or less) without surgical removal of overlying tissue. This reduces the stress on the patient and allows treatment to be completed before significant bioelimination of boron from the irradiation volume has occurred.

- There should not be an excessive level of fast (that is, greater than 10-20 KeV) neutron contamination. Fast neutrons are disproportionately damaging to normal tissue.

- There should not be an excessive level of gamma contamination.

- The beam should be well-collimated in order to provide the maximum level of

thermal neutron flux generated at depth per unit flux at the surface. Collimation also serves to reduce uncertainties in the delivered radiation dose that arise from positioning of the target irradiation volume.

Knowledgeable individuals can (and do) argue ad-infinitum with regard to the relative importance of each of the above criteria. Informed opinions also vary considerably as to exactly what specific numerical requirements should be associated with each criterion. As a practical matter, an ideal beam (neutrons only in the desired energy range, monodirectional, with sufficient intensity and no gamma contamination) cannot be generated using any currently-known technology. Hence the arguments center around the issue of "how good is good enough". The currently-operational BMRR epithermal-neutron beam is generally considered to have physical properties that are acceptable for a variety of animal research applications and possibly for treatment of a small fraction of human brain tumors (those near the surface). As will be discussed, the proposed GTRR beam offers certain significant performance improvements over the BMRR beam.

The discussion presented here will include a brief technical description of the proposed GTRR epithermal beam facility. Following this, the results of some representative dosimetry calculations that compare the radiobiological efficacy of the BMRR and GTRR beams will be presented. Finally, some observations and conclusions will be offered.

Description of the Proposed GTRR Epithermal Beam Facility

The GTRR is a heavy-water moderated and cooled plate-fuel-type reactor with a graphite neutron reflector. The proposed GTRR epithermal-neutron beam facility would be installed in the existing large biomedical irradiation port as shown in Figure 104. In this conceptual design, an in-vessel filter/moderator structure, composed of 90% aluminum and 10% D_2O by volume, occupies the space between the core and the reactor vessel on the side of the reactor adjacent to the biomedical beam port. Outside the vessel, the existing large reflector and shield penetration is lined with a laminated bismuth-lead-cadmium filter housing. Within this housing is a region of dry aluminum plates occupying a volume fraction of 90%. This region is approximately 0.7 m thick. It is followed by a 0.076 m region of lithiated-aluminum plates and a 0.01 m titanium plate for spectral shaping in the 0-1 eV and the 10-100 KeV ranges, respectively. Finally, there is a 0.076 m bismuth-lead gamma shield. The movable concrete shield block is also lined with laminated bismuth, lead, and cadmium to help provide collimation of the neutron beam and to suppress contamination from concrete capture gamma radiation. A bismuth and lithiated-polyethylene thermal neutron and gamma shield is positioned on the exit port wall of the currently-existing treatment room. Provision can be made for a variety of beam delimiter inserts to control the size and shape of the beam exit port.

Calculations to estimate the neutronic performance of the proposed epithermal beam at the GTRR were performed by the same basic combination of two- and three-dimensional radiation transport techniques that was successfully employed for physics design of the BMRR epithermal-neutron beam.

The calculated exit port neutron flux spectra for the BMRR and the GTRR neutron beams are compared in Figure 105. It can be seen that intensity of the GTRR beam is somewhat greater than that of the BMRR beam and the fast neutron component is significantly smaller. The RBE of the fast neutron component of the BMRR beam has been measured as high as 5 ± 1, emphasizing the need to suppress this component as much as possible in order to avoid unnecessary healthy tissue damage during therapy. The proposed GTRR beam is also well-collimated. This is shown in Figure 106, where the angular distribution of this beam is compared to that of the BMRR beam. A well-collimated epithermal-neutron beam generates approximately twice as much desirable thermal neutron flux at depth per unit entrance flux than an isotropic beam.

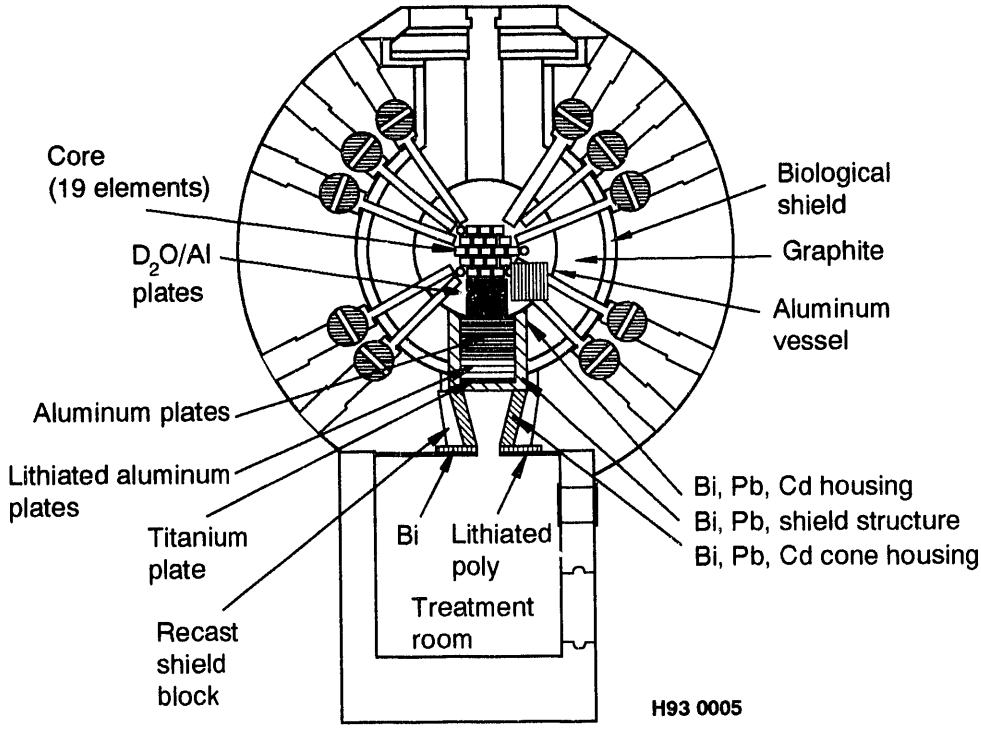

Figure 104. Conceptual epithermal-neutron facility at the GTRR.

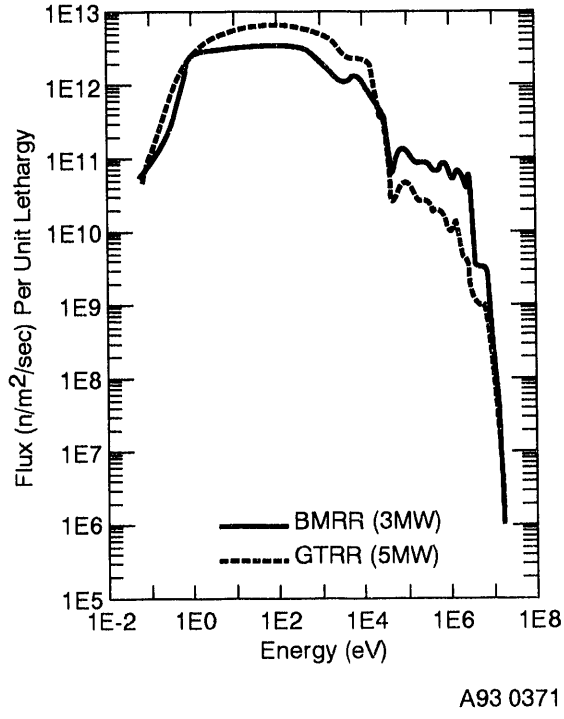

Figure 105. Comparison of BMRR and GTRR neutron beam spectrum.

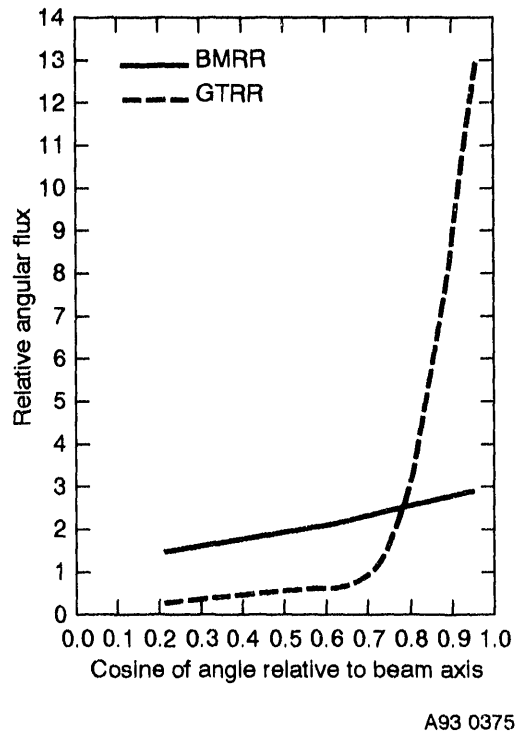

Figure 106. Comparison of BMRR and GTRR neutron beam angular distributions.

This reduces the undesirable healthy-tissue dose near the surface relative to the desirable boron capture dose (which is proportional to thermal neutron flux) at depth. Some integral parameters of interest for the two beams are shown in Table 26. Again it can be seen that the GTRR intensity is somewhat greater, with a reduced fast neutron component and greater collimation (ratio of exit port current to flux). The significance of the Advantage Depth data given in Table 26 is discussed in the following section.

Therapeutic Comparison of the BMRR and GTRR Epithermal Beams

The differences between the actual clinical performance of the BMRR beam (prior to the September, 1992 reactor BMRR core modifications) and the proposed GTRR beam can be illustrated by analytic dosimetry calculations for a tissue-equivalent phantom. The comparison presented here will be for a lucite canine-head phantom that has been used extensively for experimental characterization of the BMRR beam. This phantom is shown in Figure 107. It has dimensions that are typical of a Labrador Retriever head. (This is the breed used for tissue tolerance studies in the INEL Large Animal Project). A variety of flux wires and gamma dosimeters can be placed in the vertical and horizontal holes that are drilled at evenly-spaced intervals throughout the phantom. This phantom has been extensively modeled using a variety of independent three-dimensional radiation transport techniques. Excellent agreement between calculated and measured thermal neutron fluxes that are developed in the phantom when it is placed in the BMRR epithermal-neutron beam has been demonstrated. Because the canine phantom is almost as large as a human head, the calculated results presented here are also qualitatively similar to what would be expected for human applications.

Table 26. Integral parameters—GTRR conceptual design.

Parameter	Design requirement	GTRR (5MW)	BMRR (3MW)
Epithermal neutron flux ($n/cm^2/sec$)	$>2 \times 10^9$	$(4 \pm 1) \times 10^9$	$(2 \pm 0.5) \times 10^9$
Fast neutron dose per unit epithermal flux ($cGy/n\text{-}cm^2$)	$<2 \times 10^{-11}$	$(1.5 \pm 0.5) \times 10^{-11}$	4.7×10^{-11}
Current to flux ratio	Maximize	0.86	0.6
RBE advantage depth (cm)	Maximize	7(@ 30 ppm ^{10}B)	6(@ 30 ppm ^{10}B)

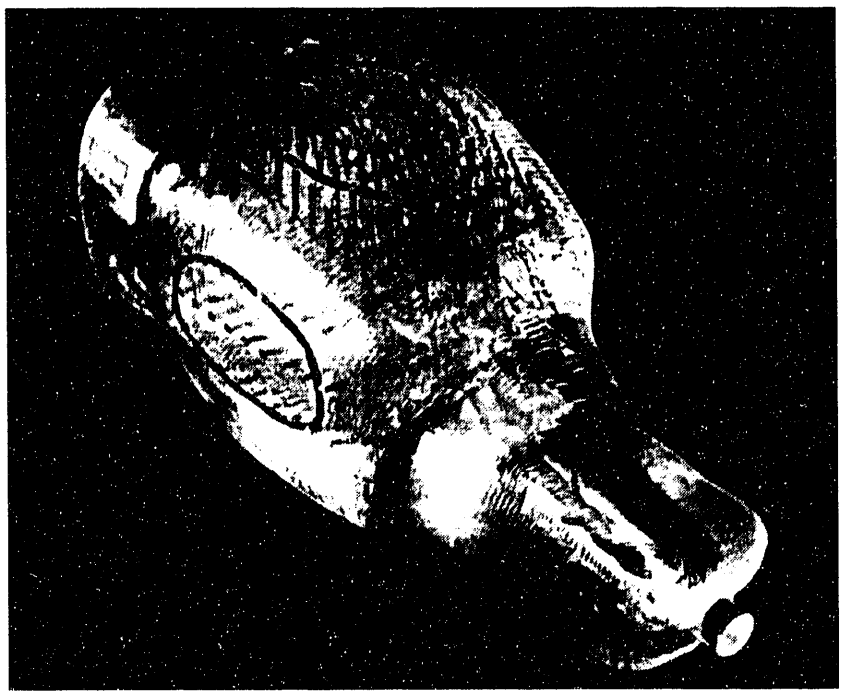

Figure 107. Lucite canine-head phantom.

For the demonstration presented here, the canine phantom was assumed to be positioned in the BMRR and the GTRR beams with the beam axis perpendicular to, and the beam impinging upon, the top of the head in both cases. The standard 10 cm by 10 cm external BMRR beam delimiter was assumed. The same size and shape was assumed for the internal GTRR beam delimiter port in order to provide a consistent comparison. Figure 108 shows selected dose-depth profiles generated in the canine phantom for each of the two beams. The dose from boron capture (at 50 ppm), the total non-boron dose (the fast neutron dose, the incident and capture gamma dose, the nitrogen (n,p) dose, etc.) are shown, along with the fast neutron dose component plotted separately. The geometry of the phantom model was exactly the same for both beams. The neutron spectrum, intensity, and angular distribution of the beam source for each model was represented by an angular flux boundary condition, constructed from the results of the transport calculations used for design of each respective beam facility.

It can be seen from Figure 108 that the desirable boron dose at depth is generally about a factor of three times larger per MW of reactor power for GTRR. For a given total therapeutic dose, the treatment time for GTRR is therefore about a factor of 5 shorter at the rated reactor power of 5 MW than is the case for BMRR at its rated power of 3 MW. In addition, the significant suppression of the fast neutron (or hydrogen recoil) dose component for the GTRR beam relative to that of the BMRR beam is readily apparent. Although not immediately obvious from the plots, the GTRR beam also offers a slightly more favorable boron dose-depth profile than the BMRR beam. These latter two characteristics of the GTRR beam are radiobiologically very significant.

It should be noted that the data presented here are for the BMRR beam prior to the September 1992 BMRR core modifications. Preliminary data indicate that these modifications have increased the BMRR beam intensity by 50 percent.

Thus the treatment time comparisons given above may change accordingly once the new BMRR beam is fully characterized. Preliminary data also indicate, however, that the BMRR beam *spectral quality* (as opposed to intensity) has not changed significantly, although this tentative conclusion is still under review.

Figure 109 shows a comparison of RBE-weighted dose depth profiles for the two beams. The data in Figure 109 are based on the assumption of BNCT treatment using BSH, with a realistic blood concentration of 30 mg/Kg (ppm) and a tumor-to-blood ratio of 1.0. In addition, it was further assumed that, as in standard photon therapy, the healthy tissue at a selected critical location is brought to its RBE-weighted tolerance dose (assumed here to be 15 RBE-Gy). The dose-limiting tissue was assumed for this exercise to be the capillary endothelium in normal brain tissue at the location of the peak RBE-weighted dose to healthy tissue. Given this normalization, hypothetical RBE-weighted tumor dose-depth profiles corresponding to the data given in Figure 108 are shown in Figure 109. This provides one consistent, relatively widely-accepted, measure of performance for one beam relative to the other, with all controllable parameters held constant for both. It can be seen that the so-called "advantage depth" (depth at which tumor dose falls below the healthy tissue tolerance dose) is about 1 cm greater for the GTRR beam. By the use of standard radiobiological cell survival models, it can be shown that this difference in advantage depth corresponds to one or two orders of magnitude greater malignant cell killing power for the GTRR beam at all depths of therapeutic interest for primary brain tumors.

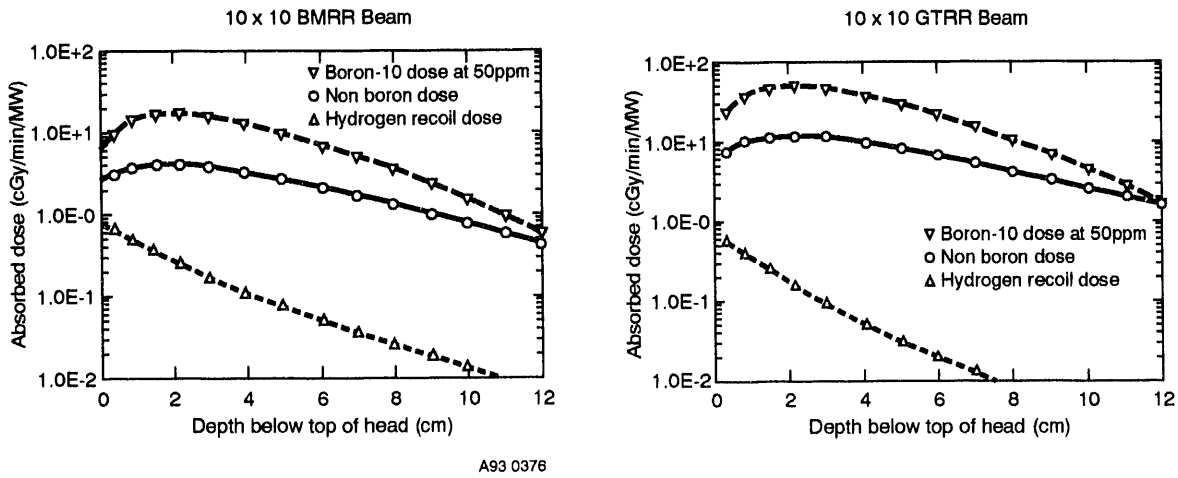

Figure 108. Calculated physical absorbed dose-depth results along beam centerline.

As is always the case with any calculational model, the results presented here are heavily dependent upon the input assumptions. The results will vary with the assumed boron concentration and with the assumed RBE factors for the various dose components. Any reasonable set of these parameters will, however, still show the same qualitative comparison for GTRR tumor-cell killing advantage. The RBE factors assumed in this analysis are based on various data available in the published literature. A factor of 2.3 was used for uniformly-distributed boron in tumor tissue. For the capillary endothelium, a so-called "compound RBE factor" of 0.33 was used. This factor includes the combined effects of both classical RBE and geometric protection (due to high-LET charged particle imbalance) that are characteristic of this tissue with BSH as the boron-carrying agent. The commonly-accepted measured RBE of 2.7 was used for the nitrogen (n,p) reaction in both healthy and malignant tissue. The gamma component of each beam was assigned an RBE of 0.625 to account for cellular repair during irradiation. An RBE value of 5.0 was used for the fast neutron component in both beams. All other components were assumed to have an RBE of 1.0. The nitrogen content of the dose-limiting healthy tissue will also affect the results. A conservative value of about 2.8 percent by weight was used in this exercise. Finally, it may be noted that there is considerable biovariability in healthy tissue tolerance to radiation. The value of 15 RBE-Gy employed here is within the range observed in canine studies, but complications have been observed at lower doses for some human ateriovenous malformation (AVM) patients treated with photon radiation at lower doses.

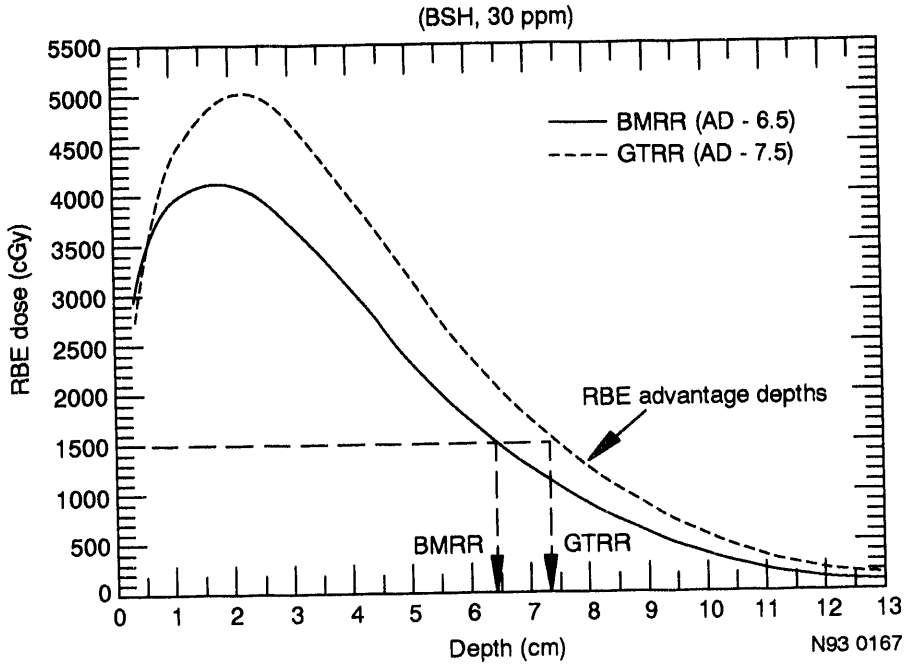

Figure 109. Tumor REB close-depth profiles for GTRR and BMRR.

Conclusions

Considering economics, geographic location, and the physics studies presented here, the proposed GTRR beam offers, overall, the most desirable known source of epithermal neutrons for BNCT that is available, or can be made available, in the U.S., using present reactor or accelerator technology. The best *currently-operating* epithermal neutron source in the U.S. is the BMRR beam, which will continue to see heavy use for BNCT research for the forseeable future. The BMRR beam, however, has a radiobiologically-significant level of fast neutron contamination, which has led to surface tissue damage in some canine experiments. Studies conducted by INEL researchers during the year show that this contamination can be suppressed to a significant extent with the proposed GTRR beam. This would allow some types of advanced animal experimentation to be done without surgically reflecting the scalp. Also, extrapolation of animal BNCT irradiation data for the purpose of deciding whether to proceed to human clinical trials (the ultimate objective of all BNCT research) would be facilitated by the availability of the proposed GTRR beam because this beam has spectral qualities more typical of that required for routine human treatment, should BNCT become a widespread modality. In addition, the GTRR beam, if eventually employed for human clinical trials, would offer patients an improved probability of local tumor control. It would allow treatment of a much larger fraction of those patients who could potentially benefit from BNCT because the ratio of tumor dose (and tumor cell killing) to healthy tissue dose is inherently greater for this beam at all depths of therapeutic interest. The calculations have shown that this is the case for both the best currently-available boron carrier drug (BSH) and, based on the results of the studies conducted during the year, is expected to be even more pronounced with any improved boron drugs that may become available in the future. This is a subject for continued study during Fiscal Year-1993 and beyond.

REFERENCES

1. R. F. Barth, A. H. Soloway, R. G. Fairchild, "Boron Neutron Capture Therapy for Cancer," *Cancer Research, 50*:1061 (1990).

2. M. Javid, G. L. Brownell, and W. H. Sweet, "The Possible Use of Neutron-Capture Isotopes Such as Boron-10 in the Treatment of Neoplasms. II. Computation of the Radiation Energy and Estimates of Effects in Normal and Neoplastic Brain," *J. Clin. Invest., 31*:603 (1952).

3. B. H. Laster, S. B. Kahl, E. A. Popenoe, R. G. Fairchild, *Cancer Research*, Vol 51, pp 4588, 1991.

4. K. Thapar, K. Kovacs, E. R. Laws, P. J. Muller, Pituitary Adendomas: Current Concepts in Classification, Histopathology, and Molecular Biology, *The Endocrinologist*, 3 (1) 39-57, (1993).

5. Y. D. Harker, R. A. Anderl, G. K. Becka, and L. G. Miller, Spectral Characterization of the Epithermal Neutron Beam at the Brookhaven Medical Research Reactor, *Nuc Sci Eng 110*: 355, (1992).

6. J. Furth, E. L. Gedsen, A. C. Upton; ACTH Secreting Transplantable Pituitary Tumors; PROC SOC BIOL MED, Vol 84, pp 235; 1953.

7. I. Ahmad and T. M. Allen, 1992, Antibody-mediated specific binding and cytotoxicity of liposome–entrapped doxorubicin to lung cancer cells *in vitro*. *Cancer Research 52*: 4817-4820.

8. I. Ahmad, M. Longenecker, J. Samuel, and T. M. Allen, 1993, Antibody-targeted delivery of doxorubicin entrapped in sterically stabilized liposomes can eradicate lung cancer in mice, *Cancer Research 53*: 1484-1488.

9. T. M. Allen, 1988, Interactions of liposomes and other drug carriers with the mononuclear phagocyte system, pp. 37-50, *In*: G. Gregoriadis (ed.), *Liposomes as drug carriers: recent trends and progress*, John Wiley & Sons, New York.

10. T. M. Allen and A. Chonn, 1987, Large unilamellar liposomes with low uptake into the reticuloendothelial system, *FEBS Letters 223*: 42-46.

11. T. M. Allen, C. Hansen, F. Martin, C. Redemann, and A. Yau-Young, 1991, Liposomes containing synthetic lipid derivatives of poly(ethylene glycol) show prolonged circulation half-lives *in vivo*, *Biochimica et Biophysica Acta 1066*: 29-36.

12. E. A. Forssen, D. M. Coulter, and R. T. Proffitt, 1992, Selective *in vivo* localization of daunorubicin small unilamellar vesicles in solid tumors, *Cancer Research 52*: 3255-3261.

13. A. Gabizon and D. Papahadjopoulos, 1988, Liposome formulations with prolonged circulation time in blood and enhanced uptake by tumors, *Proc. Natl. Acad. Sci. USA 85*: 6949-6953.

14. G. Gregoriadis, 1988, Fate of injected liposomes: observations on entrapped solute retention, vesicle clearance and tissue distribution *in vivo*, pp. 3-18, *In*: G. Gregoriadis (ed.), *Liposomes as drug carriers: recent trends and progress*, John Wiley & Sons, New York.

15. G. Gregoriadis (ed.), 1988, *Liposomes as drug carriers: recent trends and progress*, John Wiley & Sons, New York.

16. S. K. Huang, K-D Lee, K. Hong, D. S. Friend, and D. Papahadjopoulos, 1992, Microscopic localization of sterically stabilized liposomes in colon carcinoma-bearing mice, *Cancer Research 52*: 5135-5143.

17. S. K. Huang, E. Mayhew, S. Gilani, D. D. Lasic, F. J. Martin, and D. Papahadjopoulos, 1992, Pharmacokinetics and therapeutics of sterically stabilized liposomes in mice bearing C-26 colon carcinoma, *Cancer Research 52*: 6774-6781.

18. K. J. Hwang and P. L. Beaumier, 1988, Disposition of liposomes *in vivo*, pp. 19-35, *In*: G. Gregoriadis (ed.), *Liposomes as drug carriers: recent trends and progress*, John Wiley & Sons, New York.

19. S. Lestavel-Delattre, F. Martin-Nizard, V. Clavey, P. Testard, G. Favre, G. Doualin, et al., 1992, Low-density lipoprotein for delivery of an acrylophenone antineoplastic molecule into malignant cells, *Cancer Research 52*: 3629-3635.

20. B. H. Laster, S. B. Kahl, E. A. Popenoe, D. W. Pate, and R. G. Fairchild, 1991, Biological efficacy of boronated low-density lipoprotein for boron neutron capture therapy as measured in cell culture, *Cancer Research 51*: 4588-4593.

21. D. Liu, A. Mori, and L. Huang, 1992, Role of liposome size and RES blockade in controlling biodistribution and tumor uptake of GM_1-containing liposomes, *Biochimica et Biophysica Acta 1104*: 95-101.

22. L. D. Mayer, M. B. Bally, and P. R. Cullis, 1986, Uptake of adriamycin into large unilamellar vesicles in response to a pH gradient. *Biochimica et Biophysica Acta 857*: 123-126.

23. G. G. Meadows and H. F. Pierson, 1988, Liposomes as a carrier for tyrosine phenol-lyase, pp. 461-472, *In*: G. Gregoriadis (ed.), *Liposomes as drug carriers: recent trends and progress*, John Wiley & Sons, New York.

24. H. F. Pierson and G. G. Meadows, 1981, Properties of stearylamine liposomes containing tyrosine phenol-lyase, *Biochimica et Biophysica Acta 676*: 177-186.

25. R. Perez-Solar and A. R. Khokhar, 1992, Lipophilic cisplatin analogues entrapped in liposomes: role of intraliposomal drug activation in biological activity, *Cancer Research 52*: 6341-6347.

26. D. A. Potter, C. M. Gorschboth, and P. D. Schneider, 1985, Liposome uptake by melanoma: *In vitro* comparison with hepatocytes, *Journal of Surgical Research 39*: 157-163.

27. S. Schmitz, T. M. Allen, and K. Jimbow, 1992, Polyethylene-glycol-medicated delivery of liposome-entrapped pigments into fibroblasts: experimental pigment cells as models for mutator phenotypes, *Cancer Research 52*: 6638-6645.

28. K. Shelly, D. A. Feakes, M. F. Hawthorne, P. G. Schmidt, T. A. Krisch, and W. F. Bauer, 1992, Model studies directed toward the boron neutron capture therapy of cancer: boron delivery to murine tumors with liposomes, *Proc. Natl. Acad. Sci. USA 89*: 9039-9043.

29. S. Vitols, C. Peterson, O. Larsson, P. Holm, and B. Aberg, 1992, Elevated uptake of low density lipoproteins by human lung cancer tissue *in vivo*, *Cancer Research 52*: 6244-6247.

30. F. Zhou, B. T. Rouse, and L. Huang, 1992, Prolonged survival of thymoma-bearing mice after vaccination with a soluble protein antigen entrapped in liposomes: a model study, *Cancer Research 52*: 6287-6291.

31. Personal communication: H. Fankhauser, M.D., Dept. of Neurosurgery, CHUV, Lausanne, Switzerland.

32. Y. Hayashi, H. Furukawa, Y. Kawano, M. Matsurra, A. Harihara, S. Araki, Y. Muraoka, Y. Maeda, T. Yamashita, M. Muto, "Toxicity of sodim monomercaptoundecahydro-closo-dodecaborate by single intravenous injection," Report, Shionogi Research Laboratory, Shionogi & Co., Ltd, Fukushima-ku, Osaka, 553 Japan.

33. P. Marshall, M. Miller, S. Grand, P. Micca, and D. Slatkin, "Toxicities of $Na_2B_{12}H_{11}SH$ and $Na_4B_{24}H_{22}S_2$ in mice," *In*: R. Fairchild, V. Bond, and A. Woodhead, (eds): *Clinical Aspects of Neutron Capture Therapy*, New York: Plenum Press, 1989, pp 333-351.

34. A. Soloway, H Hatanaka, and M. Davis, "Penetration of brain and brain tumor, VII, Tumor-binding sulfhydryl boron compounds," *J. Med. Chem. 10*: 714–717, 1967.

35. W. Sweet, J. Messer, and H. Hatanaka, "Supplementary pharmacological study between 1972 and 1977 on purified mercaptoundecahydrododecaborate," Chapter IV in Hatanaka H. (ed): *Boron Neutron Capture Therapy for Tumors*, Niigata, Japan: Nishimura Co, Ltd, 1986, pp 175-184.

36. K. Yoshino, A. Suzuki, Y. Mori, H. Kakihana, C. Hondu, Y. Mishima, T. Kobayashi, K. Kanda, "Improvement of solubility of p-boronophenylalanine by complex formulation with monosaccharides," *Strahlentherapie und Onkologie*, Volume 165 (1989), No. 213, February/March.

37. P. R. Gavin, S. L. Kraft, C. E. DeHaan, M. L. Griebenow and M. P. Moore, "A Large Animal Model for Neutron Capture Therapy," In: *Progress in Neutron Capture Therapy for Cancer*, B. J. Allen, et al., Eds., Plenum Press, New York, 1992, 479-484.

38. G. W. Kabalka, M. Davis, and P. Bendel, "Boron-11 MRI and MRS of Intact Animals Infused with a Boron Neutron Capture Agent," *Magn. Res. Med., 8*:231 (1988).

39. P. Bendel, M. Davis, B. Berman, and G. W. Kabalka, "A Method for Imaging Nuclei with Short T2 Relaxation and Its Application to Boron-11 Imaging of a BNCT Agent in an Intact Rat," *J. Magn. Res. 88*:369 (1990).

40. T. L. Richards, K. M. Bradshaw, D. M. Freeman, C. Sotak, and P. R. Gavin, "Imaging with ^{11}B of Intact Tissues Using Magnetic Resonance Gradient Echoes," *Strahlenther. Onkol., 165*:179 (1989).

41. K. M. Bradshaw, T. L. Richards, and S. L. Kraft, "*In Vivo* Pharmacokinetic Evaluation of Boron Compounds Using Magnetic Resonance Spectroscopy and Imaging," In: *Progress in Neutron Capture Therapy for Cancer*, B. J. Allen, et al., Eds. Plenum Press, New York, 1992, 325-329.

42. G. H. Glover, J. M. Pauly, and K. M. Bradshaw, "Boron-11 Imaging with a Three-Dimensional Reconstruction Method."

43. A. H. Soloway, H. Hatanaka, and M. A. Davis, "Penetration of Brain and Brain Tumor. VII. Tumor-Binding Sulfhydryl Boron Compounds," *J. Med. Chem. 10*:714 (1967).

44. K. M. Bradshaw, "Development of Magnetic Resonance Technology for Noninvasive Boron Quantification," U. S. Department of Energy Report, EGG-2629 (1990).

45. M. Salcman, E. W. Scott, R. S. Schepp, H. C. Knipp, and R. D. Broadwell, "Transplantable Canine Glioma Model for Use in Experimental Neuro-oncology," *Neurosurgery 11*:372 (1982).

46. K. M. Bradshaw, M. P. Schweizer, G. H. Glover, and J. K. Thomas, "*In Vivo* Pharmacokinetic Data for Boron Neutron Capture Therapy Compounds Obtained by Three-Dimensional Magnetic Resonance Projection Reconstruction Techniques," *11th Society of Magnetic Resonance in Medicine Meeting, Berlin, Germany*, August 1992.

47. K. M. Bradshaw, M. P. Schweizer, G. H. Glover, and J. K. Thomas, "Pharmacokinetics of Borocaptate Sodium in Canine Head Determined by ^{11}B Magnetic Resonance Imaging and Spectroscopy," *Fifth International Symposium on Neutron Capture Therapy for Cancer, Columbus, OH, September 1992.*

48. K. M. Bradshaw, M. P. Schweizer, G. H. Glover, R. H. Tippets, and J. R. Hadley, "Boron MRI: A Rapid *In Vivo* Method for Biodistribution of Boron Compounds," *International Congress of Radiation Oncology, Kyoto, Japan, June 1993.*

49. K. M. Bradshaw, M. P. Schweizer, G. H. Glover, and J. R. Hadley, "Pharmacokinetics of Borocaptate Sodium in Canine Head Determined by ^{11}B Magnetic Resonance Imaging and Spectroscopy," *Proceedings of Fifth International Symposium on Neutron Capture Therapy for Cancer, Columbus, OH, September 1992*, Plenum Press, New York, NY, 1993.

50. K. A. O'Connell and M. Edidin, "A Mouse Lymphoid Endothelial Cell Line Immortalized by Simian Virus 40 Binds Lymphocytes and Retains Functional Characteristics of Normal Endothelial Cells," *J. Immunol. 144*:(2) 521-525, 1990.

51. B. J Allen, D. E. Moore, and B. V. Harrington, *Progress in Neutron Capture Therapy for Cancer*, New York: Plenum Press, 1992.

52. H. Hatanaka (ed.), *Proceedings of the 2nd International Symposium on Neutron Capture Therapy*, Tokyo, Japan, October 1985, Nishimura Co., Ltd., Japan 1985.

53. B. J. Allen (ed.), *The Second Japan-Australia Workshop on Neutron Capture Therapy for Malignant Melanoma, Kobe, Japan, September 1987.*

54. E. S. Gladney, E. T. Jurney, and D. B. Curtis, "Nondestructive Determination of Boron and Cadmium in Environmental Materials by Thermal Neutron-Prompt γ-ray Spectrometry," *Analytical Chemistry, 48*, 1976, 2139-2142.

55. K. Yoshino, M. Okamoto, H. Kakihana, T. Nakanishi, M. Ichihashi, and Y. Mishima, "Spectrophotometric Determination of Trace Boron in Biological Materials After Alkali Fusion Decomposition," *Analytical Chemistry, 56*, 1984, 839-842.

56. J. C. de Andrade, M. Derreira, N. Baccon, and O. C. Bataglia, "Spectrophotometric Determination of Boron in Plants Using Monosegmented Continuous Flow Analysis," *Analyst, 113*, 1988, 289-293.

57. M. A. Z. Arruda and E. A. G. Zagatto, "A Simple Stopped-Flow Method With Continuous Pumping for the Spectrophotometric Flow-Injection Determination of Boron in Plants," *Analytica Chimica Acta, 199*, 1987, 137-145.

58. T. Kobayashi and K. Kanda, "Microanalysis System of PPM-Order ^{10}B Concentrations in Tissue for Neutron Capture Therapy by Prompt-Gamma Ray Spectrometry," *Nuclear Instruments and Methods, 204*, 1983, 525-531.

59. R. G. Fairchild, D. Gabel, B. H. Laster, D. Greenberg, W. Kiszenick and P. L. Micca, "Microanalytical Techniques for Boron Analysis Using the $^{10}B(n,\alpha)^{7}Li$ Reaction," *Medical Physics, 13*, 1986, 50-56.

60. T. Matsumoto and O. Aizawa, "Prompt Gamma-ray Neutron Activation Analysis of Boron-10 in Biological Materials," *Applied Radiation and Isotopes, 41*, 1990, 897-903.

61. J. C. Mills, "An Acid Dissolution Procedure for the Determination of Boron in Coal Ash and Silicates by Inductively-Coupled Plasma Emission Spectrometry with Conventional Glass Nebulizers," *Analytical Chemistry, 183*, 1986, 231-238.

62. E. Kitazume, S. Ishioka, and E. Mitani, "Determination of Traces of Boron in Semiconductor Amorphous Silicon Film by Filament-Vaporization Inductively Coupled Plasma/Atomic Emission Spectrometry," *Analytica Chimica Acta, 199*, 1987, 245-248.

63. B. A. Zarcinas and B. Cartwright, "Acid Dissolution of Soils and Rocks for the Determination of Boron by Inductively Coupled Plasma Atomic Emission Spectrometry," *Analyst, 112*, 1987, 1107-1112.

64. S. R. Tamat, D. E. Moore, and B. J. Allen, "Determination of Boron in Biological Tissues by Inductively Coupled Plasma Atomic Emission Spectrometry," *Analytical Chemistry, 59*, 1987, 2161-2164.

65. D. L. Mann, "Analysis of Boron in Contaminated Shrimp by Inductively Coupled Plasma Spectroscopy," *Spectroscopy, 3*, 1988, 37-39.

66. J. W. Owens, E. S. Gladney, and D. Knab, "Determination of Boron in Geological Materials by Inductively Coupled Plasma Emission Spectrometry," *Analytica Chimica Acta, 135*, 1982, 162-172.

67. F. A. Cotton and G. Wilkinson, *Advanced Inorganic Chemistry*, 4th ed., New York: John Wiley and Sons, 1980, pp 244-245 and 496.

68. A. Montaser and D. W. Golightly (eds.), *Inductively Coupled Plasmas in Analytical Atomic Spectroscopy*, New York: VCH Publishers, Inc., 1987.

69. E. G. Chudinov, I. I. Ostroukhova, and G. V. Varvanina, "Acid effects in ICP-AES," *Fresenius Zeitschrift für Analytiche Chemie, 335*, 189, 25-33.

70. P. W. J. M. Boumans (ed.), *Inductively Coupled Plasma Emission Spectroscopy Part 1: Methodology, Instrumentation and Performance, Volume 90 in the Chemical Analysis Series*, New York: John Wiley and Sons, 1987, 170-178.

71. A. Lorber, Z. Goldbart, and M. Eldan, "Correction for Drift by Internal Reference Methods in Inductively Coupled Plasma Simultaneous Multielement Analysis," *Analytical Chemistry, 56*, 1984, 43-48.

72. W. B. Barnett, V. A. Fassel, and R. N. Kniseley, *Spectrochimica Acta, Part B, 25B*, 1970, 139-161.

73. A. Lorber and Z. Goldbart, "Generalized Internal Reference Method for Simultaneous Multichannel Analysis," *Analytical Chemistry, 56*, 1984, 37-43.

74. R. S. Houk, "Mass Spectrometry of Inductively Coupled Plasmas," *Analytical Chemistry, 58*, 1986, 97A-105A.

75. D. L. Anderson, W. C. Cunningham, and E. A. Mackey, "Determination of Boron in Food and Biological Reference Materials by Neutron Capture Prompt-γ Activation," *Fresenius' Journal für Analytische Chemie, 338*, 1990, 554-558.

76. W. F. Bauer, D. A. Johnson, S. M. Steele, K. Messick, D. L. Miller, and W. A. Propp, "Gross Boron Determination in Biological Samples by Inductively Coupled Plasma-Atomic Emission Spectroscopy." *Strahlentherapie und Onkologie, 165*, 1989, 176-179.

77. W. F. Bauer, D. A. Johnson, K. M. Messick, D. L. Miller, W. A. Propp, S. M. Steele, "Analysis of Boron Containing Biological Samples by ICP," *Workshop on Boron Compounds Suitable for Neutron Capture Therapy for the Treatment of Cancer, Bethesda, MD, May 1988*, Proceeding Published by NCI, 1988.

78. P. R. Gavin, S. L. Kraft, L. R. Wendling, and D. L. Miller, "Canine Spontaneous Brain Tumors - A Large Animal Model for BNCT," *Strahlentherapie und Onkologie, 165*, 1989, 225.

79. J. C. Miller and J. N. Miller, *Statistics for Analytical Chemistry*, 2nd ed., Chichester, UK: Ellis Horwood Limited, 1988, 65-74.

80. N. Maric, S. M. Cahn, P. B. Hoffer, and P. Duray, "Radiolabeled Porphyrin Versus Gallium-67 Citrate for the Detection of Human Melanoma in Mice," *34th Annual Meeting of the Society of Nuclear Medicine, Toronto, Canada, June 1987.*

81. N. Blagojevic, "The Role of ^{10}B and ^{157}Gd Conjugated EDTMP Neutron Capture Therapy for Osteosarcoma and Bone Cancer Metastases," *3rd Australia-Japan Workshop on Neutron Capture Therapy for Malignant Melanoma, Sidney, Australia, December 1988.*

82. J. Ruzicka and E. H. Hansen, "Flow Injection Analysis: Principles, Applications and Trends," *Analytica Chimica Acta, 114*, 1980, 19.

83. D. R. Migneault, "Enhanced Detection of Sulfite by Inductively Coupled Plasma Atomic Emission Spectroscopy with High-Performance Liquid Chromatography," *Analytical Chemistry, 61*, 1989, 272-275

84. P. R. Gavin, C. E. DeHaan, S. L. Kraft, M. P. Moore, L. R. Wendling, and R. V. Dorn, "Acute and Late Reactions Following Boron Neutron Capture Epithermal Neutron Therapy in Dogs With Spontaneous Brain Tumors," *Progress in Neutron Capture Therapy for Cancer*, B. J. Allen et al. eds., New York: Plenum Press, 1992, 507-510.

85. M. D. Wichman, R. C. Fry, and M. K. Hoffman, "Slurry Method for Rapid DCP Atomic Emission Determination of Residual Bone Fragments in Mechanically Separated Turkey," *Applied Spectroscopy, 40*, 1986, 351.

86. G. R. Wellum, E. I. Tolpin, A. H. Soloway, and A. Kaczmarczyk, "Synthesis of μ-disulfido-bis(undecahydro-*closo*-dodecaborate)(4-) and of a Derived Free Radical," *Inorganic Chemistry, 16*, 1977, 2120.

87. R. F. Barth, D. M. Adams, A. H. Soloway, E. B. Mechetner, F. Alam, and A. K. M. Anisuzzaman, "Determination of Boron in Tissues and Cells Using Direct-Current Plasma Atomic Emission Spectroscopy," *Analytical Chemistry, 63*, 1991, 890.

88. W. F. Bauer, P. L. Micca, and B. M. White, "A Rapid Method for the Direct Analysis of Boron in Whole Blood by Atomic Emission Spectroscopy," A. H. Soloway and R. F. Barth, eds., *Proceeding of the Fifth International Symposium on Neutron Capture Therapy*, R. F. Barth, ed., Plenum Press, 1993.

89. A. Kaczmarczyk, J. R. Messer and C. E. Peirce, "Rapid Method for Determination of Boron in Biological Materials," *Analytical Chemistry, 43,* 1971, 271.

90. I. Ikeuchi and T. Amano, "A Colorimetric Determination of Boron in Biological Materials," *Chem. Pharm. Bull., 26,* 1978, 2619-2623.

91. A. Anderson, J. Anderson, J-O. Burgman, J. Capala, J. Carlsson, H. Conde, J. Crawford, S. Graffmann, E. Gruseil, A. Holmberg, E. Johnson, B. S. Larsson, B. Larsson, T. Liljefors. P. Lindström, J. Malmquist, L. Pellettieri, O. Pettersson, J. Pontén, A. Roberti, K. Russel, H. Reist, L. Salford, S. Sjöberg, B. Sternerlöw, P. Strömberg and B. Westermark, "Programme for BNCT With Accelerator-Produced keV Neutrons and Related Chemical and Biological Studies," *Progress in Neutron Capture Therapy for Cancer,* B. J. Allen et al. (eds.), New York: Plenum Press, 1992, 41-52.

92. W. A. Ausserer, Y-C. Ling, S. Chandra, and G. H. Morrison, "Quantitative Imaging of Boron, Calcium, Magnesium, Potassium, and Sodium Distributions in Cultured Cells with Ion Microscopy," *Analytical Chemistry, 61,* 1989, 2690-2695.

93. T. E. Blue, T. C. Roberts, R. F. Barth, J. W. Talnagi, and F. Alam, "Boron-10 Concentration Measurements Using Solid-State Nuclear Track Detector CR-39 and Automatic Image Analysis," *Nuclear Technology, 77,* 1987, 220-226.

94. D. D. Siemer, "Determination of Boron by Methyl Ester Formation and Flame Emission Spectrometry," *Analytical Chemistry, 54,* 1982, 1321-1324.

95. J. R. Castillo, J. M. Mir, C. Bendicho, and C. Martinez, "Determination of Boron in Vegetal Matter by Atomic Absorption Spectroscopy Using Direct Atomization of Methyl Borate as Volatile Phase," *Atomic Spectroscopy, 6(6),* 1985, 152-155.

96. I. Novozamsky, R. van Eck, J. J. van der Lee, V. J. G. Houba, and G. O. Ayaga, "Continuous-Flow Technique for Generation and Separation of Methyl Borate from Iron-Containing Matrices with Subsequent Determination of Boron by ICP-AES," *Atomic Spectroscopy, 9(4),* 1988, 97-99.

97. M. Hosoya, K. Tozawa, and K. Takada, "Rapid Technique for Distillation of Methyl Borate for ICP Atomic-Emission Spectrometric Determination of Boron in Steel," *Talanta, 33,* 1986, 691-693.

98. T. Kumamaru, H. Matsuo, Y. Okamoto, M. Yamamoto, and Y. Yamamoto, "Inductively-Coupled Plasma Atomic Emission Spectrometric Determination of Boron Based on Generation of Methyl Borate," *Analytica Chimica Acta, 186,* 267-272.

99. D. A. Johnson, D. D. Siemer, and W. F. Bauer, "Determination of Nanogram Levels of Boron in Milligram-Sized Tissue Samples by Inductively Coupled Plasma-Atomic Emission Spectroscopy," *Analytica Chimica Acta, 270,* 1992, 223-230.

100. "Boron 10-Mercaptoundecahydrododecaborate Distribution in Human Brain Tumors as Studies by Neutron-Induced Alpha-Auto Radiography," *Boron Neutron Capture Therapy for Tumors,* Chapter VI, MTP Press, H. Hatanaka, ed., Nishimura Co. Lt.d, 1986.

101. G. H. Morrison and S. Chandra, in: *Secondary Ion Mass Spectroscopy SIMS VIII,* A. Benninghoven, K. T. F. Janssen, J. Tumpner, and H. W. Werner, eds., John Wiley & Sons, New York, 1992.

102. N. Thonnard, J. E. Parks, R. D. Willis, L. J. Moore, and H. F. Arlinghaus, *Surf. Interface Anal., 14,* 751, 1989.

103. H. F. Arlinghaus, M. T. Spaar, N. Thonnard, A. W. McMahon, and K. B. Jacobson, in: *Optical Methods for Ultrasensitive Detection and ANalysis: Techniques and Applications,* B. L. Fearey, ed., SPIE, Vol. 1435, 1991.

104. D. L. Pappas, D. M. Hrubowchak, M. H. Ervin, and N. Winograd, *Science, 243,* 64, 1989.

105. M. J. Pellin, C. E. Young, W. F. Calaway, J. E. Shitten, D. M. Gruen, J. B. Blum, I. D. Hutcheon, and G. J. Wasserburg, *Phil. Trans. R. Soc. Lond., A 333,* 133, 1990.

106. C. H. Chen, P. G. Payne, S. Hurst, S. D. Kramer, S. L. Allman and R. C. Phillips, in: *Laser and Mass Spectroscopy,* D. Lubman, ed., Oxford University Press, London, 1990.

107. H. F. Arlinghaus, M. T. Spaar, and N. Thonnard, *J. Vac. Sci. Technol., A8,* 2318, 1990.

108. H. F. Arlinghaus, N. Thonnard, M. T. Spaar, R. A. Sachleben, G. M. Brown, R. S. Foote, F. V. Sloop, J. R. Peterson, and K. B. Jacobson, *J. Vac. Sci. Technol., A9,* 1312, 1991.

109. H. F. Arlinghaus and N. Thonnard, in: *Laser Ablation Mechanisms and Applications,* J. C. Miller and R. F. Haglund, Jr., eds., Springer Verlag, Berlin, 1991.

110. G. W. Kabalka, G. Q. Cheng, P. Bendel, P. L. Micca, and D. N. Slatkin, *Magnetic Resonance Imaging, 9,* 969, 1991.

111. F. Schmittroth, *Nuclear Science & Engineering, 72,* 19 (1978).

112. Y. Harker, et al., *Nuclear Sciences & Engineering, 110,* 355 (1992).

DATE
FILMED
9/17/93

END